

PRODUCTION AND CHARACTERIZATION OF POROUS TITANIUM ALLOYS

A THESIS SUBMITTED TO  
THE GRADUATE SCHOOL OF NATURAL AND APPLIED SCIENCES  
OF  
MIDDLE EAST TECHNICAL UNIVERSITY

BY

ZIYA ESEN

IN PARTIAL FULFILLMENT OF THE REQUIREMENTS  
FOR  
THE DEGREE OF DOCTOR OF PHILOSOPHY  
IN  
METALLURGICAL AND MATERIALS ENGINEERING

OCTOBER 2007

Approval of the thesis:

**“PRODUCTION AND CHARACTERIZATION OF POROUS  
TITANIUM ALLOYS”**

submitted by **ZİYA ESEN** in partial fulfillment of the requirements for the degree  
of **Doctor of Philosophy in Metallurgical and Materials Engineering, Middle  
East Technical University** by,

Prof. Dr. Canan Özgen  
Dean, Graduate School of **Natural and Applied Sciences** \_\_\_\_\_

Prof. Dr. Tayfur Öztürk  
Head of Department, **Metallurgical and Materials Engineering** \_\_\_\_\_

Prof. Dr. Şakir Bor  
Supervisor, **Metallurgical and Materials Engineering, METU** \_\_\_\_\_

**Examining Committee Members**

Prof. Dr. İbrahim Günal  
Department of Physics, METU \_\_\_\_\_

Prof. Dr. Şakir Bor  
Metallurgical and Materials Engineering, METU \_\_\_\_\_

Assoc. Prof. Dr. Kadri Aydınol  
Metallurgical and Materials Engineering, METU \_\_\_\_\_

Assoc. Prof. Dr. Nuri Durlu  
Mechanical Engineering, TOBB ETU \_\_\_\_\_

Assist. Prof. Dr. Arcan Dericioğlu  
Metallurgical and Materials Engineering, METU \_\_\_\_\_

Date : \_\_\_\_\_ 16.10.2007 \_\_\_\_\_

**I hereby declare that all information in this document has been obtained and presented in accordance with academic rules and ethical conduct. I also declare that, as required by these rules and conduct, I have fully cited and referenced all material and results that are not original to this work.**

Name, Last name : Ziya Esen

Signature :

## **ABSTRACT**

### **PRODUCTION AND CHARACTERIZATION OF POROUS TITANIUM ALLOYS**

Esen, Ziya

Ph.D., Department of Metallurgical and Materials Engineering

Supervisor: Prof. Dr. Şakir Bor

October 2007, 211 pages

In the present study, production of titanium and Ti6Al4V alloy foams has been investigated using powder metallurgical “space holder technique” in which magnesium powder were utilized to generate porosities in the range 30 to 90 vol. %. Also, sintering of titanium and Ti-6Al-4V alloy powders in loose and compacted condition at various temperatures (850-1250°C) and compaction pressures (120-1125 MPa), respectively, were investigated to elucidate the structure and mechanical properties of the porous cell walls present due to partial sintering of powders in the specimens prepared by space holder technique. In addition, microstructure and mechanical response of the porous alloys were compared with the furnace cooled bulk samples of Ti-6Al-4V-ELI alloy subsequent to betatizing.

It has been observed that the magnesium also acts as a deoxidizer during foaming experiments, and its content and removal temperature is critical in determining the sample collapse.

Stress-strain curves of the foams exhibited a linear elastic region; a long plateau stage; and a densification stage. Whereas, curves of loose powder sintered

samples were similar to that of bulk alloy. Shearing failure in foam samples occurred as series of deformation bands formed in the direction normal to the applied load and cell collapsing occurred in discrete bands.

Average neck size of samples sintered in loose or compacted condition were found to be different even when they had the same porosity, and the strength was observed to change linearly with the square of neck size ratio.

The relation between mechanical properties of the foam and its relative density, which is calculated considering the micro porous cell wall, was observed to obey power law. The proportionality constant and the exponent reflect the structure and properties of cell walls and edges and macro pore character.

Keywords: Powder metallurgy, Space Holder, Titanium and Ti6Al4V alloy Foam, Mechanical Properties, Heat Treatment

## ÖZ

### GÖZENEKLİ TİTANYUM ALAŞIMLARININ ÜRETİMİ VE KARAKTERİZASYONU

Esen, Ziya

Doktora, Metalurji ve Malzeme Mühendisliği Bölümü

Tez Yöneticisi: Prof. Dr. Şakir Bor

Ekim 2007, 211 sayfa

Bu çalışmada, boşluk yapıcı olarak magnezyum tozu kullanılan toz metalurjisi yöntemi ile % 30-90 arasında gözenek içeren köpüksü titanyum ve Ti-6Al-4V alaşımının üretilebilirliği araştırılmıştır. Ayrıca, boşluk yapıcı kullanılarak üretilmiş köpüklerin kısmi sinterlenmiş hücre duvarlarının yapısını ve mekanik özelliklerini belirlemek için titanyum ve Ti-6Al-4V alaşım tozlarının gevşek durumda değişik sıcaklarda (850-1250°C) ve değişik presleme basınçlarında (120-1125 MPa) sinterlenmesi araştırılmıştır. Buna ek olarak, gözenekli alaşımların iç yapısı ve mekanik davranışları betalaştırma sonrası yavaş soğutulan hacimli Ti-6Al-4V alaşım numuneleri ile karşılaştırılmıştır.

Köpük üretiminde kullanılan magnezyumun titanyumun oksitlenmesini engellediği, magnezyum miktarı ile uzaklaştırma sıcaklığının numunelerin çökme oranını belirleme yönünden önemli olduğu gözlenmiştir.

Üretilen köpüklerin gerilim-gerinim eğrileri doğrusal elastik, plato ve yoğunlaşma bölgelerinden oluştuğu, gevşek durumda sinterlenen numunelerin eğrilerinin ise hacimli numunelere benzerlik gösterdiği belirlenmiştir. Köpüklerde

kesme kopması, uygulanan yüke dik yöndeki deformasyon bantlarının oluşumu ile meydana gelmiş ve farklı bantlarda hücrelerin çökmesi ile gerçekleşmiştir.

Aynı gözenek miktarına sahip gevşek ve preslenmiş durumda sinterlenmiş numunelerde ortalama boyun bölge kalınlıklarının farklı olduğu ve bu numunelerinin dayançalarının boyun bölge kalınlık oranının karesi ile doğru orantılı olarak değiştiği belirlenmiştir.

Üretilen köpüklerin mekanik özellikleri ile mikro gözenekli hücre duvar yapısı dikkate alınarak hesaplanan göreceli yoğunluk arasındaki ilişkinin üssel olarak değiştiği görülmüş, elde edilen empirik denklemlerdeki üs ve oran katsayılarının hücre duvarlarının yapısı ile özelliklerini ve köpüklerdeki makro gözenek özelliklerini yansıttığı sonucuna varılmıştır.

Anahtar Kelimeler: Toz Metalurjisi, Boşluk Yapıcı, Titanyum and Ti6Al4V Köpük, Mekanik Özellikler, Isıl İşlem

To my Family

## ACKNOWLEDGMENTS

I wish to express my deepest gratitude to my supervisor Prof. Dr. Şakir Bor for his firm guidance, his helpful suggestions, prompt feedbacks, endless patience advice, criticism, encouragements and close collaboration throughout the research. This dissertation could not have been completed without his support.

I am grateful to Ebru Saralođlu for her never ending support, encouragement and help throughout the entire period of the study.

I am also grateful to Dr. Elif Tarhan and Dr. Kaan Pehlivanođlu for their precious helps, advice, valuable support and encouragement during the development of the study.

I am indebted to my colleagues and friends; Tufan Gngren, Tarık Aydođmuş, Hasan Akyıldız and Gl İpek Nakaş for their help and patience. Additional thanks go to various friends for their support and encouragement.

Special thanks to my family for their supports. Finally, thanks to all the technical staff of the Metallurgical and Materials Engineering Department for their suggestions, help and comments during this study.

This thesis study has been financially supported by M.E.T.U Resesarch Fund and by TBİTAK through the projects BAP-2005-03-08-05 and 104M121, respectively.

## TABLE OF CONTENTS

ABSTRACT.....	iv
ÖZ.....	vi
DEDICATION.....	viii
ACKNOWLEDGEMENTS.....	ix
TABLE OF CONTENTS.....	x
CHAPTER	
1. INTRODUCTION.....	1
2. THEORY.....	6
2.1. Cellular Materials: Properties, Applications and Production	
Methods.....	6
2.1.1. General.....	6
2.1.2. Properties and Applications of Metallic Foams.....	8
2.1.3. Production Methods of Cellular Metallic Materials.....	11
2.2. Powder Metallurgy.....	14
2.2.1. General.....	14
2.2.2. Pre-consolidation Powder Handling.....	14
2.2.3. Powder Consolidation.....	15
2.2.4. Sintering.....	17
2.2.4.1. Solid State Sintering.....	18
2.2.4.2. Liquid Phase Sintering.....	21
2.2.4.3. Transient Liquid Phase Sintering.....	22

2.2.5. Powder Metallurgy of Ti and Ti Alloys.....	24
2.3. Production of Metallic Foams via Powder Metallurgy.....	27
2.3.1. General.....	27
2.3.2. Production Methods.....	28
2.3.2.1. Loose Powder Sintering of Metal Powders ...	29
2.3.2.2 . Gas entrapment technique.....	30
2.3.2.3. Sintering Slurry Saturated Sponge (Replication Process).....	30
2.3.2.4. Metallic Hollow spheres.....	31
2.3.2.5. Space Holder Technique.....	32
2.3.2.6. Reaction or Combustion Sintering.....	34
2.4. Production of Titanium and Titanium Alloy Foams by Powder Metallurgy.....	35
2.4.1. Titanium and Titanium Foams: Properties and Applications.....	35
2.4.2. Production.....	37
2.4.2.1. Loose Powder Sintering.....	38
2.4.2.2. Space Holder Technique.....	41
2.5. Characterization of Metallic Foams.....	46
2.6. Mechanical Behavior of Metallic Foams.....	48
2.6.1. Stress-Strain Curves.....	48
2.6.1.1. Compressive Response.....	50
2.6.1.1.1. Elastic Region.....	51
2.6.1.1.2. Plastic Collapse and Densification.	52
2.6.1.2. Tensile Response.....	53
2.6.1.2.1. Elastic Region.....	54

2.6.1.2.2. Plastic Collapse.....	55
2.6.1.2.3. Brittle Fracture.....	55
2.6.1.3. Determination of the Mechanical Properties	55
2.6.1.4. Densification strain.....	56
2.6.2. Mechanical Models.....	57
2.6.2.1. Porosity and Pore Character.....	57
2.6.2.2. Proposed Models.....	59
2.6.2.2.1. Minimum Solid Area (MSA)	
Models.....	61
2.6.2.2.2. Special MSA Models.....	75
2.6.2.2.3. Gibson and Ashby Model.....	82
2.6.2.2.4. Stress concentration Models.....	90
3. EXPERIMENTAL PROCEDURE.....	95
3.1. Material Used.....	95
3.2. Experimental Technique.....	98
3.2.1 Loose Powder Sintering.....	98
3.2.2 Cold Compaction and Sintering.....	99
3.2.3 Space Holder Technique.....	100
3.3. Experimental Set-up.....	105
3.4. Sample Characterization.....	107
3.4.1. Particle Size Measurement.....	107
3.4.2. Density Measurements .....	107
3.4.3. Pore Size and Porosity Distribution.....	111
3.4.4. Metallographic Examinations.....	112
3.4.5. X-Ray Diffraction.....	113

3.4.6. Mechanical Testing .....	113
4. RESULT AND DISCUSSION.....	115
4.1. Loose Powder and Cold Compaction Sintering Techniques...	115
4.1.1. Porosity and Pore Characteristics.....	115
4.1.2. Interparticle Neck Size.....	122
4.1.3. Microstructure.....	127
4.1.4. Mechanical Properties.....	131
4.1.4.1. Evaluation of Stres-Strain Curves.....	131
4.1.4.2. Comparison of the Experimental Data with Purposed Models.....	138
4.1.4.3. Effect of Neck Size.....	150
4.2. Space Holder Technique.....	154
4.2.1. Production Details and Pore Characters.....	154
4.2.2. Microstructure.....	169
4.2.3. Mechanical Properties.....	171
4.2.3.1. Stress-Strain Curves.....	171
4.2.3.2. Mechanical Property-Porosity Relations.....	180
5. CONCLUSION.....	191
REFERENCES.....	194
APPENDICES	
A. REACTIONS OF TITANIUM AND MAGNESIUM IN DIFFERENT MEDIUMS.....	203
CURRICULUM VITAE.....	209

## **CHAPTER 1**

### **INTRODUCTION**

Cellular material or solid foam is defined as uniform dispersion of a gas phase in a solid. Natural cellular structured materials such as wood, cork and plant stem include prismatic, honeycomb-like cells. Man made cellular solid structures, i.e. metallic, polymeric or ceramic structures, are mainly one of three types: honeycomb, open or closed cellular structured foams. These materials possess unique combination of properties such as air and water permeability, acoustic properties, good electrical insulating properties, low thermal conductivity, impact energy absorption capacity, high stiffness and very low specific weight.

Among the man made porous metals, titanium based foams have been used as load-bearing sandwich cores in transportation industries and as heat exchanger and catalyst substrate up to 400°C. In addition to these, porous titanium is used as an electrode for producing chlorine and sodium hydroxide by electrolysis of aqueous sodium chloride. Due to its high corrosion resistance it is also used in chemical and polymer industry as a filter, i.e. for a carrier gas inlet section of a gas chromatography apparatus.

Pure titanium and some titanium-based alloys are nowadays the most attractive metallic biomaterials for orthopedic and dental implants due to their excellent mechanical properties, wonderful biocompatibility, and good corrosion resistance. Use of porous titanium permits ingrowths of the new-bone tissues and the transport of the body fluids. Most bulk metallic implants in use today suffer from problem of stress-shielding, which results from biomechanical mismatch of elastic moduli of implant and the bone, and leads to bone resorption. However, strength and the Young's modulus of the cellular materials can be adjusted through the

adjustments of the porosity content to match the strength and the Young's modulus of the natural bone.

Considerable progress has been made recently in the production of metallic foams. The production methods utilized for the production of metallic foams divided mainly into three: Liquid state and solid state processing, and coating techniques. The vast majority of the melt processing research has focused on processing of aluminum foams with open or closed cells because of its low melting point (660°C) and low reactivity with atmospheric gases and mold materials. High melting point (1668°C) and extreme chemical reactivity of titanium with oxygen and nitrogen make liquid processing very difficult. Reactivity of liquid titanium with most of the mold materials and requirement of high vacuum during casting are other limitations appeared in liquid foaming techniques. However, it has been shown that by use of powder metallurgy, highly porous titanium parts with controlled pore structures may be manufactured at much lower temperatures and under less stringent chemical reactivity constraints.

There are mainly two different powder metallurgy production methods that yield different types of porosities in titanium. The first one utilizes the inherent pores between powder particles loosely packed in a suitable crucible under a protective atmosphere without any pressing, i.e. loose powder sintering. The second method of forming porous titanium involves introducing isolated or interconnected bubbles (macro pores), using spacers, inert gas or blowing agents. The resultant structure can be idealized as porous solid built up by various stacking of polyhedra cells with solid struts and walls and pore space inside.

The second group of powder metallurgy methods involves techniques such as that based on expansion of pressurized argon gas or sintering of powders mixed with a gaseous blowing agent (CO<sub>2</sub>-based) or foaming agent like TiH<sub>2</sub>. In these processes the size of the macro pores produced by gas expansion or fugitive particles can not be controlled sensitively so that the foams manufactured are generally composed of macro pores varying in size. Replication process utilizes a pattern, such as polyurethane foams that can be removed by thermal treatment or water soluble pattern made up of sodium chloride (NaCl) or NaF, which is immersed in titanium slurry composed of Ti6Al4V powder, H<sub>2</sub>O and ammonia solution. On the other

hand, frequently used space holder method makes use of spacers, i.e. carbamide (urea) powders, ammonium hydrogen carbonate and polymer granules, which can be removed usually at low temperature without excessive contamination of titanium powders. In some cases water soluble spacer particles such as potassium chloride, potassium sorbate, or a mixture thereof are mixed with titanium and alloy powders. Although it is possible to manufacture highly porous titanium samples with homogenous pore size and structure, the spacer particles having low dissociation or melting point may result in collapse of compact due to insufficient sintering of the powders in the cell walls.

As it is known, fluid permeability, thermal and electrical conductivity, dielectric constant, magnetic permeability, diffusion coefficient, acoustic wave velocities, elastic moduli, yield, rupture or ductile strength of materials are effected by porosity. Various studies has been conducted to determine the influence of pore size, shape and its content on mechanical properties of porous articles. Some of the studies carried out on this subject made use of empirical relations obtained by best fits to experimental data but the physical meaning of such relations were not clear. Theories that have been postulated to define the porosity-property relations of porous materials are divided mainly into three categories: Cross-sectional or minimum solid area model, stress concentration model and effective flaw size approach.

MSA models have been shown to be more accurately correlated with properties than accepted stress concentration models since the interaction of pores is thought to reduce their stress concentrations at non-dilute porosity levels. In the cross-section area model the actual load bearing area or the minimum solid cross sectional area is used to define the mechanical properties. For sintered powder particles MSA is defined as the projection of the actual sintered area (neck diameter) between the particles normal to the stress. For foam type structures, MSA is the projection of the minimum web area between adjacent bubbles parallel to the stress. Whereas, the stress concentration approach is based on the effect of pore shape and the resulting maximum stress concentration. Stress concentrations from pores as well as cracks and inclusions were seen as sources for crack propagation under tensile and compressive loading. The last theory, called effective flaw size approach

is based on the existence of flaws before final failure in the vicinity of a pore or void surface.

All of the theoretical models are normally applied to idealized regular arrays of identical shape and oriented particles, pores, or both. However, foams manufactured by powder metallurgical techniques contain macro pores formed upon removal of spacer particles or gas expansion, and micro pores on cell walls and struts due to partial sintering of powders. Therefore, the derived correlations between properties and porosity cannot usually be extended directly to real materials with pores of irregular shapes, non-uniform size and random distribution. Moreover, in the models proposed, purely geometrical reasoning is used to predict the properties and the microstructure that corresponds to the model predictions is not exactly known. Post-processing phases, grain size and shape, and morphology and distribution of the microstructure ( $\alpha+\beta$  colonies) that determine the mechanical properties and deformation characteristics of  $\alpha+\beta$  alloys are not accounted for in the models.

The aim of the present study can be summarized as:

- i) Production of highly porous titanium and Ti-6Al-4V alloy foams without excessive collapse and contamination via powder metallurgical space holder technique using magnesium spacer, which has very limited solid solubility in titanium.
- ii) Optimization of the space holder process parameters, such as compaction pressure, content of magnesium spacer and its removal temperature, cell wall powder characteristics, i.e. size, shape and type, and sintering temperature.
- iii) Manufacturing porous titanium and Ti-6Al-4V alloy samples simulating the microstructure, neck size and pore structure of the cell walls present in foams produced by space holder method so that the effect of variables such as compaction pressure and sintering temperature on the final

porosity, neck size and mechanical properties of the cell wall can be understood.

- iv) Investigation and comparison of the mechanical response of bulk, porous and foam titanium and titanium alloy samples under compression loading and to find out mechanical property (i.e. Young's Modulus and yield strength) porosity or relative density relations by use of empirical and theoretical relations.

In this study, theoretical background about cellular structured materials and titanium-based foams are given in Chapter Two, which consists of the production techniques employed such as liquid and solid state, destructive and non-destructive characterization methods, the mechanical response of different types of foams, i.e. ceramic, metallic, under compressive and tensile loading, theoretical and empirical relations used to define mechanical property-porosity relations. The preliminary and experimental studies are given in Chapter Three. Experimental results are evaluated and discussed in Chapter Four. The concluding remarks are presented in Chapter Five.

## CHAPTER 2

### THEORETICAL FRAMEWORK

#### 2.1. Cellular Materials: Properties, Applications and Production Methods

##### 2.1.1. General

Cellular solid is made up of an interconnected network of solid struts form the edge and faces of cell. Table 2.1 lists all possible dispersions of one phase in a second one (where each phase can be in one of the three states of matter). Foams are uniform dispersions of a gaseous phase in either a liquid or a solid.

**Table 2.1** Dispersions of one phase into second phase [1].

	Is dispersed in a gas	Is dispersed in a liquid	Is dispersed in a solid
When a gas	Gas mixture	foam	Solid foam or Cellular solid
When a liquid	fog	emulsion	gel
When a solid	smoke	Suspension slurry	Embedded particles

In nature, cellular structured materials are widespread. For example, wood and cork include prismatic, honeycomb-like cells Figure 2.1.(a), while those with polyhedral cells include the inner core in plant stems and trabecular bone, Figure 2.1.(b). Cellular materials also appear as the cores in natural sandwich structures: in long, narrow plant leaves, such as the iris, and in shell-like bones, such as the skull Figure 2.1.(c). Natural tubular structures often have a honeycomb-like or foam-like

core supporting a denser outer cylindrical shell, increasing the resistance of the shell to kinking or local buckling failure such as plant stems and animal quills, Figure 2.1 (d).

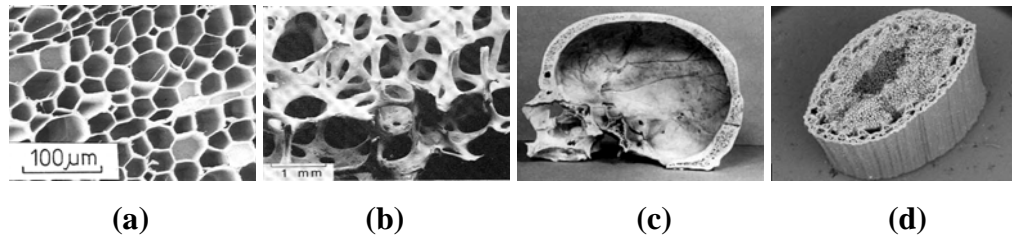


**Figure 2.1** Examples of natural cellular materials, (a) balsa wood, (b) trabecular bone, (c) skull, (d) plant stem [2].

Man made cellular solid structure are mainly three types; two dimensional honeycombs, three dimensional foams with open cells and three dimensional foams with closed cells [3]. Honeycombs, with their prismatic cells, are referred to as two-dimensional cellular solids while foams, with their polyhedral cells, are three-dimensional cellular solids, which are used for lightweight structural components. More familiar man made foams are the polymeric foams used in everything from disposable coffee cups to the crash padding of an aircraft cockpit. Some engineering cellular solids are shown in Figure 2.2.

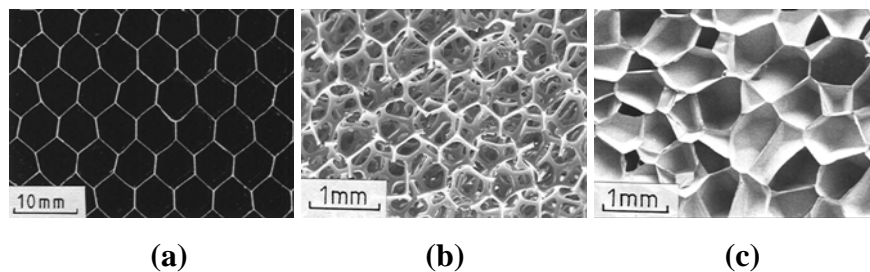


**Figure 2.2** Examples of engineering cellular solids (a) aluminum honeycomb (b) open-cell polyurethane foam (c) closed-cell polyethylene foam [2].

Among man-made cellular materials, polymeric foams are currently the most important ones with widespread applications in nearly every sector of technology. On the other hand, metals and alloys can be produced as cellular materials or foams and their use is becoming widespread. “Metallic foams” generally means a solid foam. The liquid metallic foam is merely a stage that occurs during the fabrication of the material. Solid foams are a special case of what is more commonly called a “cellular solid”.

### **2.1.2. Properties and Applications of Metallic Foams**

The properties of foams generally depend on the pore characteristics, i.e. Type, shape, size, volume percentage, surface area and uniformity of pores, interconnection, which may be quite different in various production techniques [1, 4]. Metallic foams with high porosity ranging from 40 to 98 vol. % have been developed and are growing in use as new engineering materials. These exceptionally light-weight materials possess unique combination of properties such as impact energy absorption capacity, air and water permeability, unusual acoustic properties, low thermal conductivity, good electrical insulating properties and high stiffness in conjunction with very low specific weight [1,3]. Figure 2.3 compares some properties of bulk and foam materials. The enormous extension of properties creates applications for foams, which cannot be easily filled by fully dense solids. However, it is important to notice that the specific mechanical and physical properties of cellular metals always compare badly with their bulk properties. This is true for the elastic modulus, the strength and also the energy absorption ability. That is, the use of cellular materials can only be efficient if the structural properties are explicitly used.

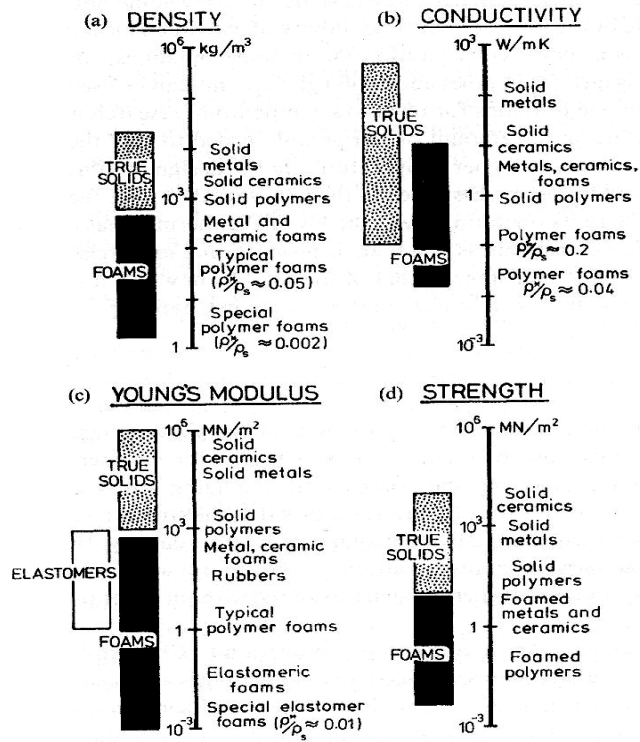


**Figure 2.3** The range of properties of foams [3].

The most prominent property of foamed material is its low density. Because of that cellular materials are finding an increasing range of applications. These applications can be divided into three main categories namely; Structural applications, functional applications and decorative applications. Table 2.2 summarizes the subgroups of such applications.

**Table 2.2** Some selected applications of cellular materials.

<b>Structural Applications</b>	Automotive industry, aerospace industry, ship building, railway industry, building industry, machine construction, sporting equipment, biomedical industry
<b>Functional Applications</b>	Filtration and separation, heat exchangers and cooling machines, supports for catalysts, storage and transfer of liquids, fluid flow control, silencers, spargers, battery electrodes, flame arresters, electrochemical applications, water purification, acoustic control
<b>Decoration and arts</b>	Furniture, clocks, lamps

Many applications require that a medium, either liquid or gaseous, be able to pass through the cellular material. In this case open porosity is required for high rate of fluid flow. Figure 2.4 shows the requirements in the type of porosities in various applications.

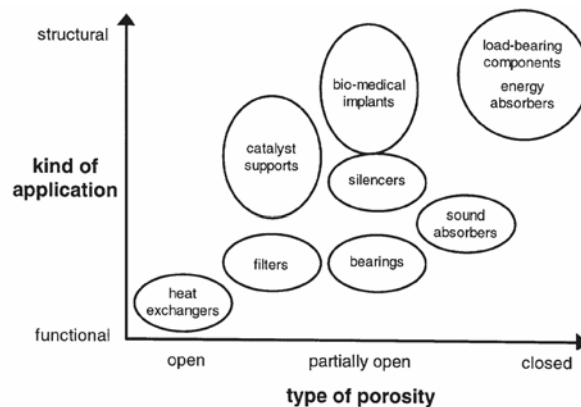


**Figure 2.4** Applications of cellular metals grouped according to the degree of “openness” needed and whether the application is more functional or structural [1].

Some selected applications of metallic foams are shown in Figure 2.5:

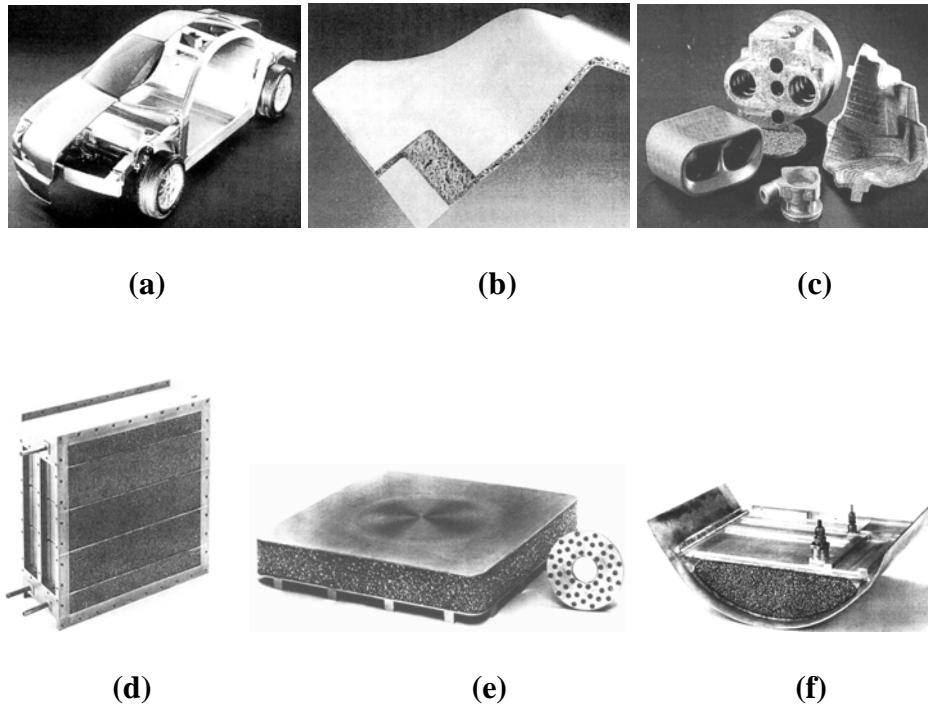


**Figure 2.5** Some potential applications of aluminum foams (a) A concept design of vehicle in which the firewall and trunk are made of three-dimensional aluminum foam panels, (b) Foam metal components with integral skins, (c) Pressed porous panel, (d) Aluminum foam used as the heat exchange medium for the space shuttle atmospheric control system, (e) Aluminum foam used as the structural core of a lightweight composite mirror, (f) Aluminum foam used as the structural core, heat exchanger and anti-slosh baffle in a lightweight conformal tank [5].

### 2.1.3. Production Methods of Cellular Metallic Materials

As the engineering applications of cellular metals grow, many methods for their manufacture are being developed. They result in materials that can be classified by the size of their cells, variability in cell size, the pore type and the relative density of the structure [6]. None of the available manufacturing techniques can be applied to any metal; each is appropriate for one or other base metal [7].

Porosities and pore structures in porous materials may be fully open, less open or closed. The amount and character of the porosity is directly related to the surrounding solid, which is determined by manufacturing method. Production techniques utilized are given in Figure 2.6 and the resultant pore structure and distribution of porosities in those manufacturing methods are presented in Table 2.3.

**Table 2.3** Some of porous material fabrication processes and pore structures and their distribution in those methods.

Pore Structure	Distribution of pores	Production method
CLOSED	Random pore distribution	Cymat/Hydro (Al, Mg, Zn)
		ALPORAS
		Sintering hollow spheres
		Alulight/Foaminal
	Graded pore distribution	Plasma spraying
OPEN	Homogenous pore distribution	Vapor deposition
		Orderly oriented wire mesh
		Ferromagnetic fiber arrays
		Rapid Prototyping
	Non-homogenous pore distribution	Sintering of metal powders and fibers
		Gas entrapment technique
		Space holder technique
		Replication method
		Combustion synthesis
		Slurry foaming technique
	Functionally graded pore distribution	Electric field assisted powder consolidation
		Rapid prototyping

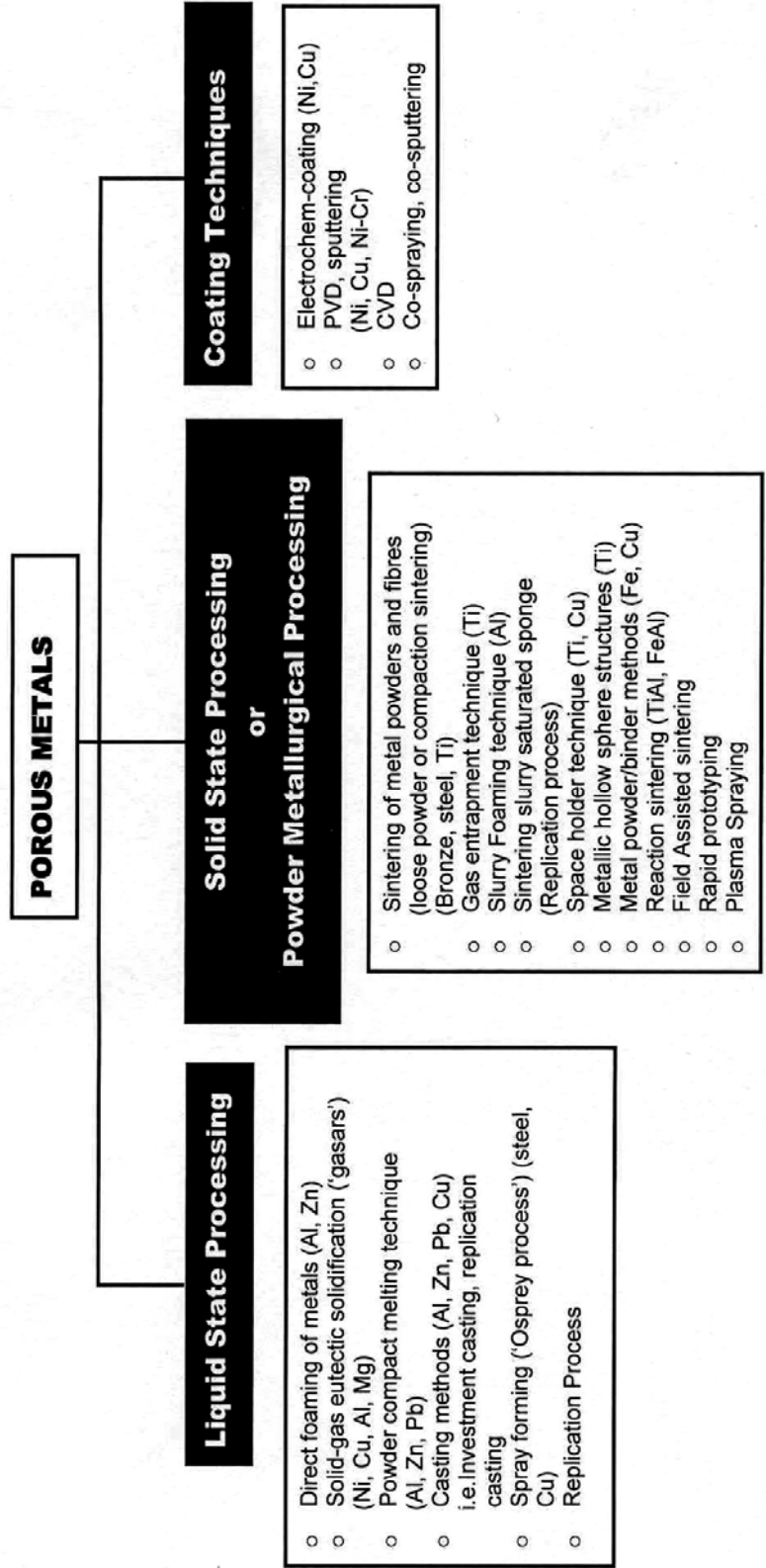


**Figure 2.6** Metallic foam production techniques.

The methods other than the powder metallurgical technique, liquid processing and coating techniques, have difficulty in controlling the pore size and process variables in the production of foams of high melting metals such as Cu, Fe, Ti or Ni-based. However, in powder metallurgical process solid metal in powdered form can be used for making cellular metallic structures using low temperatures under less chemical affinity with atmospheric gases [8].

The powder remains solid during the entire process and merely goes through a sintering treatment or other solid-state operations. This is crucial for the morphology of the resulting cellular structure since only in the liquid state surface tension does cause a tendency towards the formation of closed pores, whereas sintered porous products show the typical open morphology of isolated, more or less spherical particles connected by sinter necks.

## **2. 2. Powder Metallurgy**

### **2.2.1. General**

Powder metallurgy is processing of metal powders into useful engineering components. Powder metallurgy involves firing or sintering of a shaped article from finely divided powders in a furnace so as to develop satisfactory strength in the component without losing the essential shape imparted during initial molding.

### **2.2.2. Pre-consolidation Powder Handling**

The precompaction steps include classification, blending, mixing, agglomeration, deagglomeration and lubrication [9].

Blending and mixing are to combine powders into a homogenous mass prior to pressing.

Agglomeration provides a coarser particle size, which flows easily in automatic forming equipment. Attritioning and deagglomeration are useful in those instances when a fine, discrete powder is needed. Finally, lubricant of a powder using organic molecules provides for easier part ejection from compaction tooling and longer die life. It is essential to reduce friction between the pressed compact and the rigid tool components when compacting metal powders in steel or carbide tooling. The lubricants are usually mixed with the metal powder as a final step before pressing. For metal powders, stearates based on, Al, Zn, Li, Mg, or Ca, are in common uses. Besides the stearates, other lubricants include waxes and cellulose additives.

### **2.2.3. Powder consolidation**

Compaction (consolidation) relies on an external source of pressure for deforming the metal powders into a high-density mass, while providing shape and dimensional control to the powder. For loose powder, there is an excess of void space, no strength and a low coordination number. As pressure is applied, the first response is rearrangement of the particles, giving a higher packing coordination [9].

Subsequently, the point contacts deform as the pressure increases [10]. Plastic flow is localized to particle contacts at low pressures, whereas it occurs homogeneously throughout the compact as the pressure increases. Eventual fragmentation causes densification and an increase in the compacts surface area, but the strength of the compact shows little improvement.

In the compaction of metal powders when the pressure is transmitted from bottom and top punches, the process is termed double action pressing alternative to single action pressing. These type of pressure applications determines the density gradients in the compact and hence its strength. As can be seen in Figure 2.7 in

single ended pressing, the density is highest at the top of the compact and decreases towards the bottom. However, in double-ended pressing the minimum density is achieved at the center of the compact and the density distribution is more homogeneous than that of the single ended pressing.

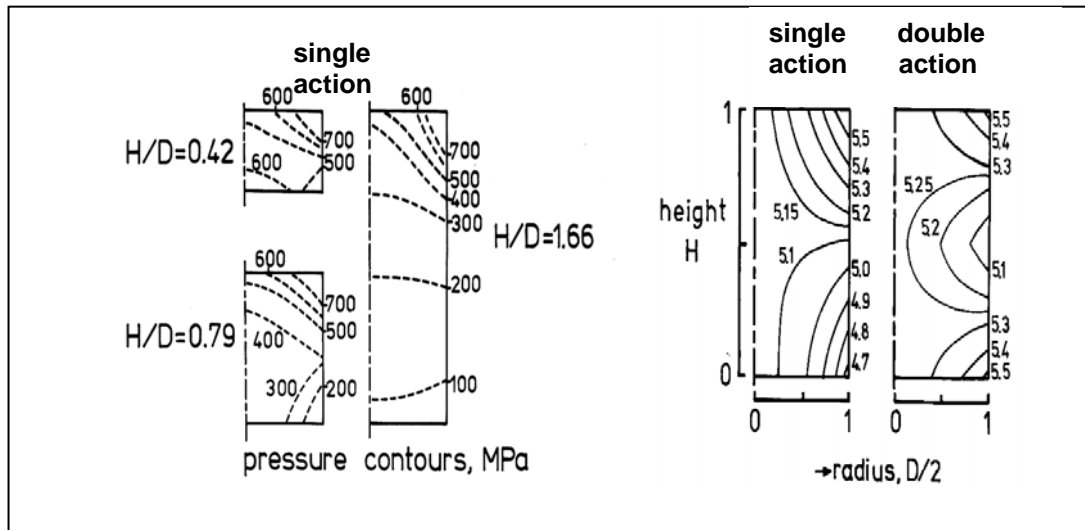


**Figure 2.7** Pressure distributions in single-ended and density distribution in both type of pressing.

The height to diameter ratio of the compact also plays an important role in the densification. With the increasing height to diameter ratio, density gradients in a compact will increase and this causes a decrease in the overall compact density, as shown in Figure 2.7. However, pressure transmissions can be improved by reducing the frictional effects using suitable lubricants such as paraffin wax, stearic acid and various stearates on die walls [11].

## 2.2.4. Sintering

To produce a useful body, packed powders are bonded together when heated to temperatures in excess of approximately half of the absolute melting temperature, which is termed sintering [12].

In addition to causing particle bonding, sintering can also lead to the following important effects: 1) chemical changes, 2) dimensional changes, 3) relief of internal stress, 4) phase changes and 5) alloying. Figure 2.8 summarizes the sintering processes.

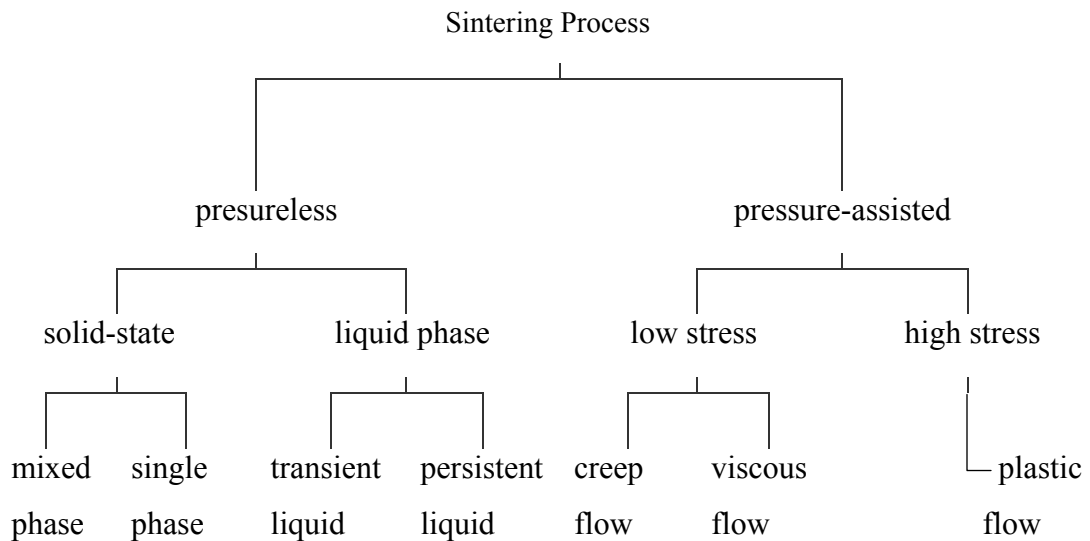


**Figure 2.8** Sintering processes [13].

Most sintering is performed without an external pressure (pressureless sintering). A major distinction among pressureless sintering techniques is between solid-state and liquid phase processes. Among the solid-state processes, single phase treatments are applicable to pure substances such as nickel, alumina, or copper. On the other hand, mixed phase sintering occurs in an equilibrium two-phase field.

Many sintering cycles generate liquid. It may be present momentarily or may persist during much of the sintering cycle. The liquid improves mass transport rates. It also exerts a capillary pull on the particles that is equivalent to a large external pressure. There are two main forms of liquid phase sintering. Persistent liquid phase exist throughout the high-temperature portion of the sintering cycle and can be formed by use of prealloyed powder. Alternatively, transient liquid-phase sintering has a liquid that disappears during the sintering cycle, due to dissolution into the solid or formation of a new phase.

#### 2.2.4.1. Solid State sintering

Various stages and mass transport mechanisms that contribute to sintering have been proposed. These stages are summarized in Figure 2.9.

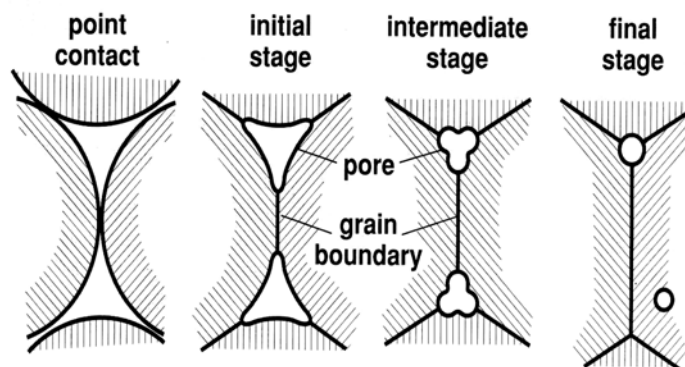


**Figure 2.9** Solid state sintering stages [13].

In the intermediate stage, the pore structure becomes smooth, interconnected and approximately cylindrical. The concomitant reduction in curvature and surface area slows down sintering with time.

When the porosity has shrunk to approximately 8 % somewhat cylindrical pores collapse and pinch off into lenticular or spherical pores indicating the final stage of sintering and slow densification.

Major transport mechanisms involved in sintering are shown in Figure 2.10. These mechanisms are activated by the curvature dependent chemical potential,  $\mu$ , and therefore solubility,  $C$ , reduction at the neck, which can be represented by the relations, respectively,

$$\Delta\mu = \frac{\gamma \cdot V}{\rho} \quad (2.1)$$

$$\Delta C = \frac{\gamma \cdot V}{R.T \cdot \rho} C_o \quad (2.2)$$

where,  $\Delta\mu$  is the chemical potential difference,  $\gamma$  is the surface tension,  $\rho$  is the radius of curvature at the neck,  $V$  is the atomic volume,  $\Delta C$  is the concentration difference of vacancies or solute atoms and  $C_o$  is the equilibrium concentration of vacancies or solute atoms under a flat surface.

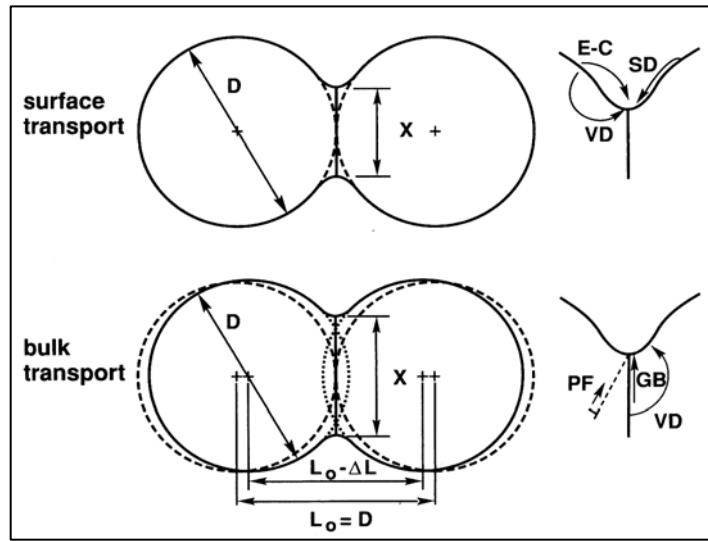


**Figure 2.10** Two classes of mass transport mechanisms during sintering applied to the two-sphere model (E-C; Evaporation-Condensation, SD; Surface Diffusion, VD; Volume Diffusion, PF; Plastic Flow, GB; Grain Boundary Diffusion) [13].

The solution of the flow problem for different transport mechanisms yields the following relationships between the radius of the neck,  $x$ , radius of the sphere,  $r$ , time,  $t$ , and temperature,  $T$ , [14-18]:

$$\frac{x^n}{r^m} = A(T) \cdot t \quad (2.3)$$

Where  $A(T)$  is a function of temperature only, and

$n=2, m=1$  for viscous and plastic flow

$n=3, m=1$  for evaporation and condensation

$n=5, m=2$  for volume diffusion

$n=7, m=3$  for surface diffusion

### 2.2.4.2. Liquid Phase Sintering

Liquid phase sintering has been widely used because liquid provides faster atomic diffusion than the concomitant solid-state processes [19]. The classic liquid phase sintering system densifies in three overlapping stages and densification in each step is different as shown in Figure 2.11.

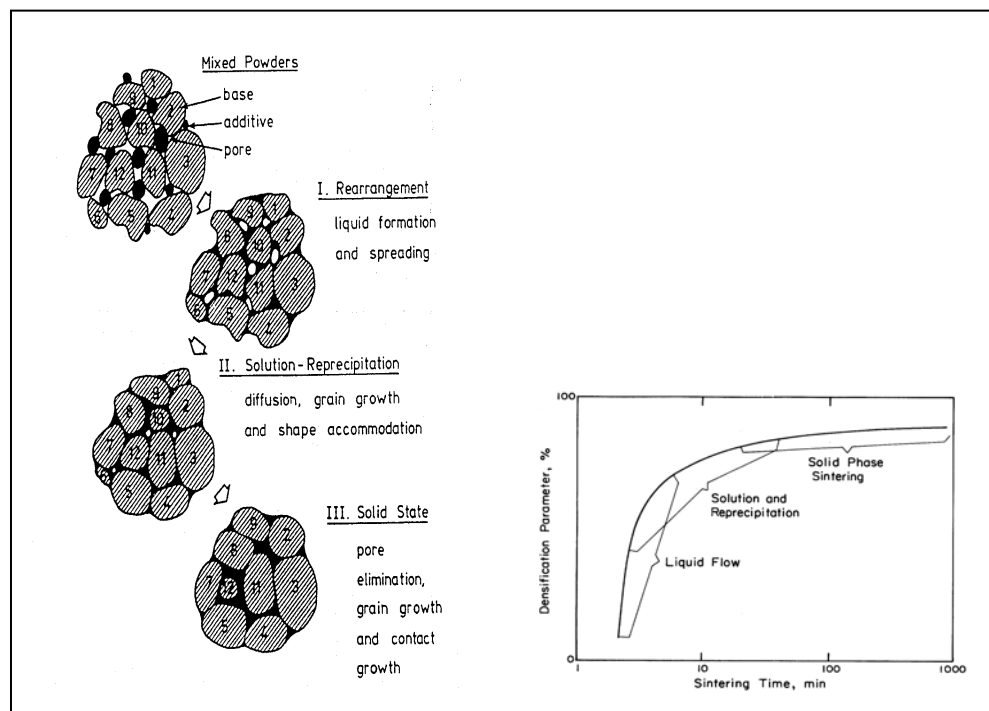


**Figure 2.11** Stages and their effects on densification behavior in liquid phase sintering [12, 13].

In liquid formation, there is rapid initial densification due to capillary forces exerted by the wetting liquid on solid particles. During the rearrangement, the compact responds as a viscous solid to the capillary action. The elimination of porosity increases the compact viscosity. Consequently, the densification rate continuously decreases. Usually finer particles give better rearrangement.

Generally, most successful persistent liquid phase sintering systems exhibit eutectic behavior [20]. The formation of liquid film has the benefit of a surface tension force acting to aid densification and pore elimination [9]. This criteria is met when the liquid form a film surrounding the solid phase, thus wetting the solid. The capillary force due to a wetting liquid promotes rapid densification without the external pressure [20, 21].

#### **2.2.4.3. Transient Liquid Phase Sintering**

An interesting variant to traditional liquid phase sintering involves a transient liquid, which solidifies by diffusional homogenization during sintering. Transient liquid forms between mixed ingredients during heating to the sintering temperature. The phase diagrams of two examples of systems, which could be processed using a transient liquid, are given in Figure 2.12. Unlike the persistent liquid phase sintering, the liquid has a high solubility in the solid and disappears with sintering time. Transient liquid phase sintering is advantageous due to the easy compaction of elemental powders as opposed to prealloyed powders and excellent sintering without the coarsening difficulties associated with a persistent liquid. However, because the liquid content depends on several processing parameters, transient liquid phase sintering is sensitive to processing conditions [22, 23].

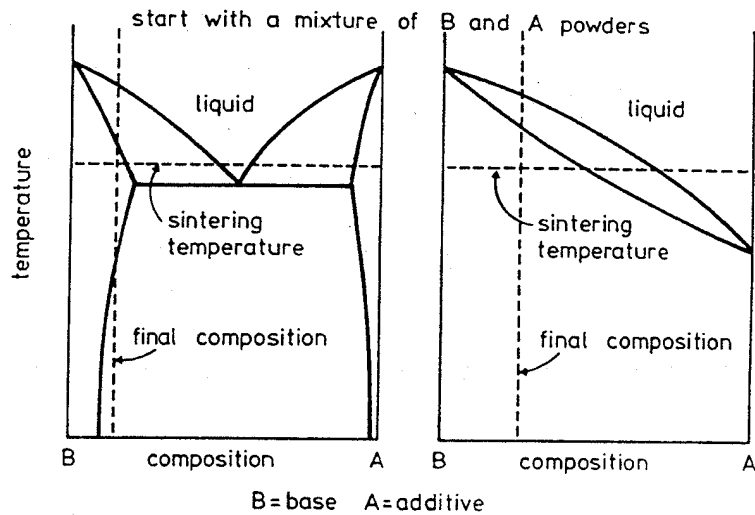


**Figure 2.12** Two binary phase diagrams in transient liquid phase sintering [12].

Transient liquid phase sintering is highly sensitive to processing conditions since the liquid content depends on several processing parameters. The requirements for transient liquid phase sintering include mutual intersolubility between the components with the final composition existing within a single-phase region. Furthermore, the liquid must wet the solid. Under these conditions rapid sintering is anticipated when liquid forms. Generally, the observed steps are as follows [24, 25]:

- 1) Swelling by interdiffusion prior to melt formation (Kirkendall porosity),
- 2) Melt formation,
- 3) Spreading of the melt and generation of pores at prior additive particle sites,
- 4) Melt penetration along solid-solid contacts,
- 5) Rearrangement of the solid grains,
- 6) Solution-precipitation induced densification,
- 7) Diffusional homogenization,
- 8) Loss of melt,
- 9) Formation of a rigid solid structure.

The actual steps depend on the process variables, including particle sizes, amount of additive, heating rate, and maximum temperature.

### 2.2.5. Powder Metallurgy of Ti and Ti-Alloys

Titanium and titanium alloys are the design choice for many applications in aerospace, medical and marine industry because they offer low density, excellent corrosion resistance, and good mechanical properties at room and moderately elevated temperatures. Titanium P/M fabrication offers the potential for true net shape capability combined with mechanical properties that are equal to or exceed cast and wrought products due to lack of texture and segregations and the fine, uniform grain structure inherent to titanium P/M products. Regardless of variety of all compositions, well over 90% of the powder metallurgy developmental efforts have employed on Ti-6Al-4V [26-29].

Because of the high affinity of titanium for oxygen and other atmospheric interstitials, all compaction of titanium alloy powders must be done in vacuum or in an inert environment. The available methods for Ti powder metallurgy are as follow;

#### 1) Metal Injection Molding(MIM):

Metal Injection molding, also known as MIM, is an analog of plastic injection molding. It is a high volume technology, where powdered metal is mixed with a binder and injected into a mold, de-bonded, and sintered to produce small complex parts at low cost.

#### 2) Traditional Powder Metallurgy Methods:

Traditional powder metallurgy methods include press and sinter, elastomeric bag cold isostatic pressing (CIP), and ceramic mold or metal can HIP. Firstly, powder is consolidated at room temperature using pressures up to 410 MPa to produce shapes with green densities 85-90 %. This is done using either of two common powder metallurgy techniques; mechanical pressing or cold isostatic pressing. In mechanical pressing, loose powder is pressed in a die using a relatively simple mechanical hydraulic press. On the other hand, since the mold material is elastomeric (as opposed to hard punch and die tooling) in CIP process, no lubricant

is needed, eliminating a pre-sinter stage for lubricant removal and avoiding lubricant contamination of titanium [30]. At the end of compaction process parts are sintered in vacuum furnace or under protective atmosphere such as high purity Ar gas. Generally, the use of cold walled vacuum furnaces is preferred. The furnace should be equipped with a diffusion pump that has a sufficient capacity to accommodate out-gassing during heatup and maintenance of high vacuum (133 mPa, or  $1 \times 10^{-3}$  mmHg) at peak temperatures. Due to its reactivity, titanium adheres to most metals. Molybdenum, which has very low solubility in titanium, can be used as support material. At lower temperatures (1000-1080°C) high-density graphite, coated with a wash of yttrium oxide, can be used. As a measure against contamination of the parts being sintered, some loose titanium powder may be included with each load to act as a getter for gases. In vacuum sintering the most preferred temperature ranges from 1000 to 1300°C. Lower temperatures are usually used for porous and commercially pure products, and high temperatures are used to produce alloy products. Alternative to vacuum sintering use of purified argon atmosphere is another technique. Argon gas can be purified by passing over titanium chips kept at 800-900°C. The use of temperature cycling through  $\alpha$ - $\beta$  transformation (880°C) for unalloyed titanium can promote densification. The effect is the most significant when heating from  $\alpha$  to  $\beta$  which lasts about 2 minutes [31].

In addition to normal sintering hot isostatic pressing cycle can also be used to improve density and mechanical properties. The most satisfactory container appears to be carbon steel, which reacts minimally with the titanium, forming titanium carbide, which then inhibits further reaction. In HIP process by simultaneously applying temperature and pressure, full density in the part is attained. The shrinkage depends on the packing density of the powder, which depends in turn on the shape and size distribution of the particles. Since in this process applied pressure is isostatic, the shrinkage is approximately uniform in small parts. The HIP operation can be carried out either above or below the beta transus temperature. Above transus consolidation requires shorter cycle time and lower pressure, but the resultant microstructure consists of large prior beta grains and continuous grain boundary alpha which reduces the fatigue strength of the alloy (Ti-6Al-4V). For alloys

consolidation in  $\alpha + \beta$  region is more commonly used. Although can method give satisfactory results it appears that cold-chamber and Fluid die techniques are better [32].

### 3) New P/M Research and Development:

Significant efforts in P/M research continue on numerous fronts such as *spray* forming, rapid solidification, laser forming, mechanical alloying, and vapor deposition. All of these research initiatives are aimed at exploiting the outstanding characteristics of titanium and its alloys [33, 34].

As it is known titanium undergoes a phase transformation (hcp- $\alpha$  to bcc- $\beta$ ) at 882°C. Titanium with other group IVB elements exhibits diffusion anomalies. It shows anisotropy in the hcp phase. During sintering different transport mechanisms may be operative, which result in activation energies of titanium self-diffusion to be different. In the high temperature bcc range, it exhibits a curved Arrhenius plot with  $Q$  (for self-diffusion) increasing with temperature. The reported activation energies for self diffusion in  $\alpha$ -Ti change between 169 and 192 kJ/mol. Studies to determine the rate controlling mechanism of shrinkage have shown that lattice self-diffusion and grain boundary diffusion are the dominant mechanism in low temperature sintering [35, 36]. Table 2.4 lists the activation energies measured in a study carried out on titanium powder sintering.

**Table 2.4** Activation energies for various processes in titanium sintering.

Material	Process	Q(kJ/mol)
$\alpha$ -Ti	Sintering	184.1 $\pm$ 12
	Grain growth	165.2 $\pm$ 7
	Lattice self-diffusion	123-303
	Grain boundary self-diffusion	97.187
$\beta$ -Ti	Sintering (900-1050°C)	158 $\pm$ 11
	1050-1250°C	92.5 $\pm$ 8
	Grain growth	34.3 $\pm$ 8
	Lattice self diffusion	131-328
	Grain boundary self diffusion	135

## 2. 3. Production of Metallic Foams via Powder Metallurgy

### 2.3.1. General

As mentioned, there are many ways to manufacture cellular materials. Powder metallurgy processes has become increasingly popular since it is possible to produce near net shape foam components with desired porosity content and distribution, and graded porosity. As in the liquid state techniques, no stabilizing particles have to be added and since the technique is carried out at solid state (at relatively low temperatures) reactivity of powders are limited and no mold material is needed for production. Moreover, powder processing makes composite foam production and also production of foams with a metal skin possible.

In general, the production of porous structures consists of various steps: powder fractioning and preparation, compaction or molding, binder and fugitive or spacer material removal and sintering.

During foaming, the powder remains solid during the entire process and merely goes through a sintering treatment or other solid-state operations. This is

crucial for the morphology of the resulting cellular structure since only in the liquid state surface tension does cause a tendency towards the formation of closed pores, whereas sintered products show the typical open morphology of isolated, more or less spherical particles connected by sinter necks.

Resultant pore structures and distribution, and its content depends on powder metallurgical process variables and the type of the process utilized. Figure 2.13 shows the pore types obtained using some of the powder metallurgical processes,

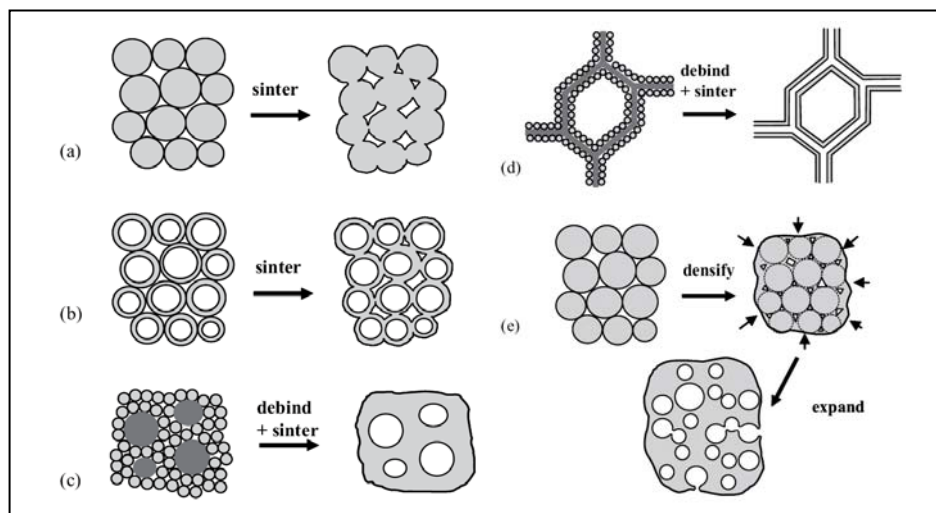


**Figure 2.13** Pore morphologies obtained by powder metallurgical processing techniques, (a) sintering of powders, (b) sintering of hollow spheres, (c) space holder technique, (d) sintering slurry saturated sponge or replication process, (e) gas entrapment technique [8].

### 2.3.2 . Production Methods

In this section, some of the selected production techniques utilized for the production of porous metals and metal foams are summarized.

### **2.3.2.1. Loose Powder Sintering of Metal Powders**

According to mechanisms of sintering, contacts between powder particles are established and grow by the action of capillary or surface tension forces during the time that the powder particles are being heated in contact with each other. Application of pressure facilitates but is not essential for sintering. Therefore, the metal powders of any shape can be filled into mould and then sintered. Axial die-compaction, iso-static pressing or roll compaction of the powders prior to sintering may be employed to increase the strength of the green part. By this method parts with fine porosity can be produced. Loose powder sintering is most commonly used to produce bronze filters, and porous nickel membranes used as electrodes for alkaline storage batteries and fuel cells. A binder is often added with the particular purpose of holding particles together. This ensures a greater area for mass transport between the particles in the solid-state diffusion process. The fraction of porosity is controlled by neck and particle size. The neck size or the size of inter-particle bond region can be controlled by compaction prior to sintering, sintering temperature and time. The limitation in loose powder or compaction& sintering technique is that the pore size and shape are dictated by the powder size and shape. Generally, in spherical powder sintering porosity is limited to 50 % and the shape of the pores is highly non-spherical and the open porosity may be attained [37]. Making porous metals from aluminum and aluminum alloy powders or granules is difficult because aluminum is usually covered by a dense oxide layer, which prevents the particles from sintering together. Usually this oxide layer is broken by pressing or sintering aids are utilized such as copper, silicon or magnesium powders that form a low eutectic alloy. Prior to loose powder sintering aluminum and those sintering aids are generally ball-milled to induce alloying [1].

### 2.3.2.2. Gas entrapment technique

In this method, usually elemental powders are compressed in a compact form in a container and an inert gas allowed to be entrapped into compact during pressing. Then, during heating, expansion occurs due to the internal pressure created by the gas in the compact. So, this process requires high pressure and temperature equipment and necessitates two separate heat treatment steps: during powder compaction and for bubble expansion. Extensive studies on this subject have been carried out for the production of highly porous titanium and titanium alloys containing isolated highly spherical pores for use in aircraft industry [5, 8]. Schematic representation of the process is shown Figure 2.14.

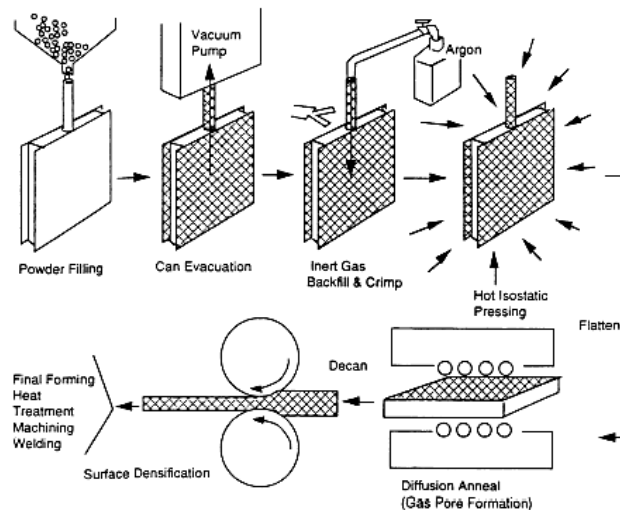


**Figure 2.14** Schematic representation of gas entrapment technique [1].

### 2.3.2.3. Sintering Slurry Saturated Sponge (Replication Process)

For producing of metallic foams method utilizes a temporary support, which may be a sponge-like organic material such as a natural or synthetic plastic sponge

[4], polyurethane foams [37] and in some cases sintered structures of NaCl or NaF [7]. Temporary support is initially soaked into slurry containing desired metal powder, water and organic liquid and kept at that slurry until saturation is achieved. Then, the saturated support is dried and heated to pyrolyse the organic support. After sintering highly porous material with interconnected porosity is obtained. If the NaCl or NaF is used as a support, they are removed in water after sintering process. Use of salt patterns is limited due their low melting point so that only porous structures of aluminum and lower melting point alloys can be manufactured. On the other hand, NaF could potentially be used at temperatures greater than 900°C. Mainly three types of pore structure are observed in foams produced by this technique: primary pores on the surface of the hollow struts, secondary porosity at the core of the hollow struts previously occupied by the temporary support, and open tertiary porosity between struts.

#### **2.3.2.4. Metallic Hollow Spheres**

In this method, highly porous structures are obtained by bonding metal hollow spheres together by sintering or transient liquid phase sintering with the help of powdered additive, and hot isostatic pressing (HIP).

The hollow-sphere structures can be made from gas-atomized hollow powders, coaxially sprayed slurries, coated Styrofoam spheres or by cementation and sintering

Foams produced by sintering hollow spheres contain uniform size of porosity so that the mechanical properties are more predictable than other foams containing random pore size. Another advantage of that technique is that full range of materials such as superalloys, titanium alloys and intermetallics can be foamed.

### 2.3.2.5. Space Holder Technique

The space holder method is a fabrication process that can produce porous metal samples of high porosities or relative densities lower than 0.4 [37].

The metal powder is filled into a dry bulk of fillers or a suitable solvent or even an organic binder may be used to mix the space holders and the metal powders. Ceramic particle or hollow spheres, polymeric grains or hollow polymer spheres, salts or even metals can be used as space holders.

Initially, metal powders and appropriate space holder material is mixed and the mixture is compacted either uniaxially or isostatically to form a green compact to give sufficient mechanical strength, Figure 2.15. Space holder is generally removed by a thermal treatment, leaching or by use of an aqueous solvent. By choosing the size, shape and quantity of the space holder used the mechanical properties of the foam can be adjusted.

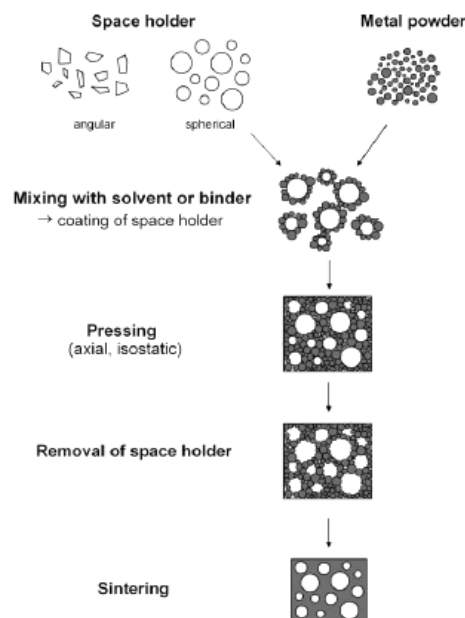


**Figure 2.15** Process steps in space holder foaming technique [1].

The general difficulty in this process is the removal of space holder material. Since the quantity of spacer particles is generally high in the compact care should be taken for slow removal of spacer to prevent collapsing and distortion of the powder compact. In addition, in some cases to prevent high temperature contamination of powders spacers having low dissociation/melting point should be chosen [37]. Good results can be achieved with carbamide,  $(\text{NH}_2)_2\text{CO}$ , (urea), which can be removed below temperatures of  $200^\circ\text{C}$ . Porous structures from aluminum, stainless steel 316L, nickel based superalloys, and titanium has been made this way. However, in some cases low decomposition temperatures leads to collapse of the porous metal structure before strong bonding between the metal particles is formed at the sintering temperature. It is also hard to control the cell shape because of the significant shrinkage involved.

Space holder method utilizing carbamide particles of varying shape and size was used by Jiang et al. [38, 39] for production of aluminum foams with tailored porosity. Instead of thermal decomposition, they dissolved the carbamide particles in water kept at  $80^\circ\text{C}$  prior to sintering. The remainder of the carbamide was removed during the sintering stage. They obtained aluminum foams with 50-80 % porosity and the samples were containing both open and closed type spherical and strip-shaped pores formed as a result of removal of carbamide. Aluminum foams can also be manufactured by a sintering dissolution process (SDP) by use of NaCl spacer particles as carried out by Zhao and Sun [40]. In this process, NaCl spacers were removed after the sintering of Al-NaCl compact. The main limitations of SDP are that it is time consuming to eliminate NaCl completely and any residual NaCl can lead to contamination or corrosion of the base metal.

In a study carried by Bakan [41] highly porous 316L stainless steel samples with 70% porosity were manufactured by water leaching of carbamide at room temperature and sintering the 0.5 % boron added powder by liquid phase sintering. The use of water as a leaching agent eliminates the environmental drawbacks related to the removal of organic space holders and does not involve the anisotropic thermal expansion associated with typical organic substances.

As mentioned, spacer holder method is also utilized to yield highly porous copper samples. In this case space holder material may be PMMA polymer [42] or

$K_2CO_3$  powder [43]. Both of these powders are thermally decomposed and removed, and sintering is carried out at high temperatures, i.e. 950°C.

Ammonium tetrachloride can be used as space holder in the manufacture of filters of iron, nickel or copper. For manufacture of nickel membranes methyl-cellulose is preferred [4].

Studies, specific to production of titanium foams via space holder technique, will be presented in the later chapters.

#### **2.3.2.6. Reaction or Combustion Sintering**

Due to different diffusion coefficients of multi-component systems porous structures can be obtained in some systems such as Ti-Al, Fe-Al, Ni-Al, Ti-Si and Ti-Ni. A compacted powder blend is heated to ignite the reaction between the elemental powders, which results usually in the formation of intermetallics [44]. In reaction sintering particle fusion is obtained by an extremely rapid exothermic reaction due to large heat released. Initially elemental powders with predetermined quantities were mixed together and cold compacted. Then, compact is ignited by a laser beam, electrical heating, or by an electric discharge under a controlled atmosphere. Upon heating of compact to sufficiently high temperature compacts ignites and a strong exothermic reaction propagates as a combustion wave throughout the entire mixture, without requiring additional energy.

Extensive studies have been carried out for the production of porous nitinol (NiTi). Due to low exothermic characteristics (67 kJ/mol) prior to the ignition powder mixture compact is heat to a temperature of 550°C using a tungsten coil element. The general characteristic of the porous compacts is that the pore channels in the compact formed along the propagation direction of the combustion wave. Presence of transient liquid phase, volatilization of impurities and the escape of adsorbed gases affect the final porosity of the compact [37].

## **2.4. Production of Titanium and Titanium Alloy Foams by Powder Metallurgy**

### **2.4.1. Titanium and Titanium Foams: Properties and Applications**

Titanium and titanium alloys exhibit excellent mechanical properties, low density, high chemical resistance and good biocompatibility.

Titanium based foams have potential engineering applications for load-bearing sandwich cores in the aerospace, naval, and ground transportation industries [45]. Titanium's high melting point also allows for the use of titanium foams at elevated temperatures (e.g. for sandwich core or as heat exchanger and catalyst substrate), limited to ca. 400°C due to low oxidation resistance of titanium [8].

Titanium based electrodes are exclusively used in modern electrolytic equipment for producing chlorine and sodium hydroxide by electrolysis of aqueous sodium chloride [46]. Moreover, in partially sintered compact form titanium is used as a filter in chemical and polymer industry due to its corrosion resistance (filters for a carrier gas inlet section of a gas chromatography apparatus), a powder feeder in a polymer electrolyte membrane type water electrolyzer, a current collector in a solid polymer fuel cell and in addition a liquid dispersion plate, especially an ink dispersion plate for an ink jet printer and like [47].

Titanium foams are also used as porous implants in biomedical industry as they possess excellent biocompatibility and fatigue properties [45, 48-51].

Pure titanium foam is generally used for dental implants. On the other hand, its alloys can be used in bone replacements. However, elastic modulus mismatch of implant material and bone results in stress-shielding, which eventually leads to bone resorption.

$\alpha$ - $\beta$  titanium alloys used to reduce the extent of stress shielding have elastic modulus approximately half of the stainless-steels or CoCr-based alloys. However, the modulus of Ti-6Al-4V and related  $\alpha/\beta$  alloys is still high (110 GPa) compared to human bone's (1-40 GPa). For minimizing the elastic moduli metastable  $\beta$ -titanium alloys such as Ti-13Nb-13Zr having elastic modulus ranging from 74 to 88 GPa

have been presented. Among  $\beta$ -type alloys Ti-Nb-Zr-Ta has been used with moduli of 20-25% lower than other available alloys [6, 50].

But, there is still a mismatch in mechanical properties of these materials and natural bone. In addition to these, reliable bone/implant fixation is another problem. One way to alleviate the stress shielding problem is to reduce Young's modulus of metallic materials by introducing pores, thereby minimizing damages to tissues adjacent to the implant and eventually prolong device life time. In addition, bone/implant fixation is achieved by inter-digitation between bone and porous implant matrix [37, 51-53].

The morphology, pore size, porosity, purity, biocompatibility and the mechanical properties are the basic influencing factors in determining the correct porous material in biomedical applications. Studies on porous bone substitutes showed that the optimum pore size for attachment and growth of osteoblasts and vascularization is approximately in the range 100-500  $\mu\text{m}$ . The optimum porosity content was between 30 % and 50 % with open cellular structure. Some studies have shown that pore size down to 50  $\mu\text{m}$  is useful for effective bone ingrowth into porous coatings [54] and for the formation of an osteonal bone structure [55].

Moreover, the ideal bone substitute material should be osteoconductive in order to allow as rapid as possible integration with host bone, biodegradable and bioresorbable at a preferred rate in order to be replaced by newly formed natural bone, and strong enough to fulfill required load-bearing functions during the implantation period [56].

The porous bioactive ceramics and polymeric materials promote bone or tissue ingrowth into pores of the implants, thereby allowing rapid return to the physiologically acceptable state of function. However, because of their extremely weak mechanical properties, the porous bioactive ceramics might fracture if a sudden force is applied to them during healing stage. They are often not appropriate for load bearing applications. However, metallic foams can exhibit mechanical properties adjusted to be very close to those of human bone. Metallic foams can not only overcome the mechanical weakness of the bioactive ceramics and polymeric materials, but they can also eliminate problems of interfacial instability with host tissues and biomechanical mismatch of the elastic moduli [57]. As porous metallic

implant materials titanium and its alloys are mostly preferred due to their excellent biocompatibility, fatigue properties and corrosion resistance.

#### **2.4.2. Production**

High melting point and extreme chemical affinity of titanium and its alloys to atmospheric gases (i.e. oxygen and nitrogen), which dissolve rapidly above 400°C, make liquid processing very difficult. In addition to these, liquid titanium is highly reactive with respect to most mold materials and casting of bulk titanium objects requires high vacuum, high temperature processing equipment. Powder metallurgy, on the other hand, can produce porous titanium parts at much lower temperatures and under less stringent chemical reactivity constraints. Moreover, it is also possible to control the pore size and process variables more precisely through using powder metallurgical techniques.

High porosity titanium parts can be manufactured either by use of conventional loose powder sintering or by electric field assisted powder consolidation techniques such as spark plasma sintering (SPS) [58, 59], electro-discharge compaction (EDC) [60], environmental electro-discharge sintering (EEDS) [61, 62] and plasma spraying [63, 64]. Porous surfaced compacts are produced by the latter techniques [65]. Compaction and sintering is another method that utilizes CIP, HIP or conventional pressing prior to or during sintering. For methods, loose powder sintering and cold compaction & sintering, starting materials may be titanium powders with varying shapes or titanium hollow spheres [66, 67]. The resultant pore size and shape are determined by the powder size and shape.

In the reaction sintering (combustion synthesis), which is extensively used for the production of highly porous nickel titanium, particle fusion and pores are obtained through an extremely rapid self-sustaining exothermic reaction driven by the large heat released in the synthesis [37, 68-70]. Replication process utilizes a removable pattern, such as polyurethane foams [37, 71-74] that can be removed by thermal treatment or leachable pattern (water soluble) made up of sodium chloride (NaCl) or NaF, which is immersed in titanium slurry (i.e. comprising Ti-6Al-4V powder, H<sub>2</sub>O and ammonia solution. The slurry impregnated pattern is subsequently

dried and the process is repeated until a homogenous coating obtained. Then, pattern is removed by thermal evaporation or by leaching prior to sintering and binder removal.

Other production technique involves the sintering of non-uniform powder preforms made with a gaseous blowing agent (CO<sub>2</sub>-based) [75] or foaming agent like TiH<sub>2</sub> [51] and low density polyethylene [76]. Large pores are produced by gas expansion or addition of fugitive particles followed by sintering. In the processes based on expansion of pressurized bubbles, i.e. argon gas, titanium foam is obtained through the use of creep expansion process (argon expansion process, low-density core process) or superplastic expansion process (thermal cycling around the allotropic transformation of Ti and Ti64) [77-82]. The space holder method is a fabrication process that can produce porous metal samples of greater porosity. The process begins by mixing the metal powders with a binder, CMC (carboxymethyl cellulose), collodion or poly vinyl alcohol, or water or organic solvents) and an appropriate space holder material which can be removed usually at low temperature without excessive contamination of titanium powders. The possible spacer holder particles are carbamide (urea) powders, ammonium hydrogen carbonate, polymer granules and magnesium powders. In some cases water soluble spacer particles (Potassium chloride, potassium sorbate, or a mixture thereof) are mixed with titanium and alloy powders and compacted. These leachable particles are removed in water prior to sintering [8].

The detailed description of some of the manufacturing methods of titanium foams by powder metallurgy and powder metallurgy methods of interest in the present study can be summarized as follows;

#### **2.4.2.1. Loose Powder sintering**

As mentioned previously, solid state sintering consists of three stages initial, intermediate (densification) and final (grain growth) stages. Generally, porous titanium compacts are manufactured through the use of initial stage sintering only, where there is no considerable particle size and shape change.

In powder sintering, pore size and shape (spherical, angular) are determined by titanium or alloy powder size and shape. For example, the shape of the pores is non-spherical and porosity is limited to 50 % for monosized powders. Particle contamination during sintering by oxidation or some other surface contaminant would hinder particle bonding. As mentioned previously, loose powder sintering of titanium powders is carried out under vacuum or inert gas atmosphere (Argon) without application of pressure. The sintering temperature greatly affects the sintering rate, neck size and the strength of the product and it is chosen with respect to  $\alpha$ - $\beta$  transition temperature (at which hexagonal closed packed  $\alpha$ -phase changes into body centered  $\beta$ -phase). The transition temperature in titanium and titanium alloy is greatly influenced by the oxygen content of the alloy and it is around 882°C and 975°C for grade 4 titanium and Ti-6Al-4V-ELI alloy, respectively. Sintering is enhanced above transition temperature since the self diffusion coefficient in beta phase is orders of magnitude higher than that in alpha titanium (at 1000°C;  $D_{\alpha-Ti}=10^{-15}$  m<sup>2</sup>/s,  $D_{\beta-Ti}=10^{-13}$  m<sup>2</sup>/s). Sintering may also be enhanced through the alloy additions, i.e. silicon, to the titanium powder, thereby increasing the sintering rate by formation of transient liquid phase. Another method aiming higher sintering rate utilizes cyclic sintering (thermal cycling) around  $\alpha$ - $\beta$  transition temperature. Densification in such sintering technique is attributed to the transformation-mismatch plasticity, which is responsible for transformation superplasticity.

As a result, by controlling the process variables such as initial powder particle size, distribution, shape, compaction pressure, sintering temperature and time, alloy additions and cycles of sintering (if cyclic sintering is to be used) porous titanium specimens with varying porosity contents and pore shape can be manufactured.

There are several studies carried out for manufacturing of porous titanium and titanium alloys using loose powder sintering. A patent [47] invented by Sumitomo Corporation workers for porous titanium to be used especially as filter makes use of sintering of angular and spherical titanium and titanium alloy powders or titanium sponge powders in loose condition. Powders were filled into cylindrical alumina vessels by vibration screening. Porosities in samples sintered between temperatures of 650 and 1200°C argon atmosphere changed between 35-55 %.

Powders with different particle diameters were used to control the porosity content and to produce material graded porosity. Similarly, in a patent [83] invented by Tetjukhin V.V. and Bashkirov A.M. titanium powders were filled in a die by gravity and sintered at temperatures between 1300 and 1500°C for a period between 0.5 and 2.5 hrs.

Oh et al. [52] produced porous pure titanium compacts pressing the powders before and during sintering to be used in human cortical bone replacement. They used spherical titanium powders with three different sizes: 65, 189 and 374  $\mu\text{m}$ , and pressed the powders at room temperature between graphite punches at around 70 MPa prior to sintering. Some of the powders were also pressed at 5-10 MPa during sintering stage. Sintering was conducted in vacuum of  $10^{-3}$  Pa at temperatures of 1173, 1223, 1373 and 1573 K, above the  $\alpha$ - $\beta$  transition, for two hrs. The resultant specimens contained porosities between 5-37 % and had comparable mechanical properties to human cortical bone. In another study, Oh et al. [84] applied the same technique to titanium powders with particle sizes in the range 300-500  $\mu\text{m}$  and achieved porosities between 19 and 35 %.

Similarly, Nomura et al. [85] used powder sintering technique to achieve desired porosities in  $\beta$ -type Ti alloy. Ti-15Mo-5Zr-3Al alloy powders were placed in BN lubricated graphite punches and powders were hot pressed under applied uniaxial pressure of 1 to 30 MPa at 1223 K for 2 hrs in a vacuum of  $10^{-3}$  Pa. Porosity up to 33% was achieved and the pores were irregular and interconnected morphology.

As a biomedical application, dental implants with graded porosity are preferred to satisfy both mechanical and biocompatible property requirements [86-88]. Thieme et al. [86] tried to produce porous titanium samples to be used for orthopaedic implants and used five fractions of unalloyed titanium powder within the range of 180-1000  $\mu\text{m}$  to get desired graded pore size distribution. Initially, powders were pressed and initial sintering was carried out 1150°C under vacuum. Subsequently, silicon powder (1.5 wt. %) was added by infiltration of ethanolic suspensions. In this study silicon had been chosen as an additive for the sintering of coarse titanium powders based on eutectic at 1330°C, 8.4 wt. % Si, which could be utilized for liquid phase sintering. The volume fraction and pore size varied from 22

% and 48  $\mu\text{m}$  for the finer powder layer to 45 % and 200  $\mu\text{m}$  for the coarser powder layer.

In some cases, for biomedical applications, hydroxyapatite (HAP), principle component of bones and teeth, is mixed with titanium powder and packed into the mold to obtain a gradient in concentration. The specimens are compressed using CIP and sintered at around 1300°C by high frequency induction heating in argon gas. [87, 88].

Powder sintering may also be utilized for porous coating of surgical implants for their fixation by bone ingrowth into a three dimensional matrix. Amigó et al. [89], firstly, attached the titanium beads with an average size of 307  $\mu\text{m}$  on Ti-6Al-4V femoral stem hip implants by use of binder. Then, sintering was carried out at about 1400°C under vacuum to obtain porosities between 35-40 %. In this study, post sintering cooling rate was adjusted to control the final substrate microstructure, which determines the fatigue properties.

Similar sintering studies was also conducted on Ti-6Al-4V alloy powders by Cirincione et al. [90] in which alloy powders were sintered at 1000°C above transition temperature for times between 0.5 and 24 hrs and resultant porosities were between 41 and 55 %.

#### **2.4.2.2. Space Holder Technique**

The space holder method can produce titanium and titanium alloy foams using an appropriate space holder material, usually removed at low temperature without excessive contamination of titanium. The use of space holders allows control over the pore properties, including pore density, size, distribution and shape. The pore properties in the final article are determined primarily by the properties of spacer particle and, thereby, are tailored by the selection of the extractable particulate. When choosing a suitable space holder to be used in titanium foam production following criteria should be considered: The spacer should not leave undesired residue in the final part, it should not react with matrix material, and it should have adequate strength so as not to be deformed during processing, such as

compaction. It also preferred to have low melting or dissociation point compared to titanium and titanium alloys.

Ceramic particles or hollow spheres, polymer grains or hollow polymer spheres, salts or even metals can be used as space holders. The possible space holder particles that have been utilized are carbamide (urea) powders, ammonium hydrogen carbonate, polymer granules and magnesium powders, which are removed by thermal treatment. In some cases, binders such as carboxymethyl cellulose and polyvinyl alcohol that can be removed thermally may be used for manufacturing of porous titanium samples. Water soluble spacers such as sodium chloride, potassium chloride, potassium sorbate, or a mixture thereof have also been utilized to yield porous titanium samples. Hydroxypropylmethyl cellulose powder may be used to produce porous titanium in metal injection molding process [91].

The process starts by mixing of titanium powder/ space holder and solvent or even and organic binder using V-blending, jar mill or hand blending. Homogenizing aids are generally used to get homogenous mixture of spacers and titanium powders and include polyethylene glycol (PEG), which reduces segregation and is removable in a water bath prior to thermal processing, and higher alcohols or isoparaffinic solvents, as well as organic liquids such as acetone, which can easily be removed by evaporation prior to or after compaction. Binders such as PEG4000, methycellulose or CMC (carboxymethyl cellulose), polyolefins such as polyethylene or polypropylene, ethylene vinyl acetate, styrene group resins, cellulose derivatives, various types of wax, collodion or polyvinyl alcohol, or water or an organic solvent are used for homogenous covering of spacer particles with titanium powder and also they are used for efficient powder packing during compaction by reducing the friction between powders and between powder/die surfaces. Powder mixture obtained is then pressed at room temperature or, if the space holders are heat resistant, pressed at elevated temperatures to improve compaction and to start sintering process. Removal of space holder material can be achieved by thermal treatment, leaching in water or in a solution, or by use of an aqueous solvent. When using water to dissolve the spacer particle, the water bath should be deoxygenated to reduce or eliminate the potential for oxidation of the metal powder in water. This can be done by bubbling nitrogen through the water, or other known deoxygenating

means. Finally, sintering is carried under argon atmosphere or in vacuum furnace at high temperatures, i.e. 1200-1400°C, for further densification.

Various studies can be found in literature about the production of titanium foams by space holder technique. Bram et al. [92] used spherical and angular carbamide particles as spacers in varying amounts of 60, 70 and 80 %. After pressing the carbamide/titanium powder mixtures at 166 MPa the space holder material was removed using a thermal treatment below 200°C. Then, spacer removed samples were sintered between the temperatures of 1200 and 1400°C for one and two hrs under vacuum ( $10^{-3}$  Pa). Porosities between 60-80 % were achieved and depending on the shape and size distribution of the space-holder particles, angular and spherical pores, in the range of 0.1-2.5 mm with a homogenous distribution, were produced, Figure 2.16.

In the coating step of the carbamide particles with titanium powder carbamide spacers may be moistened with petrolether to obtain homogenous distribution of titanium powders on carbamide particles.

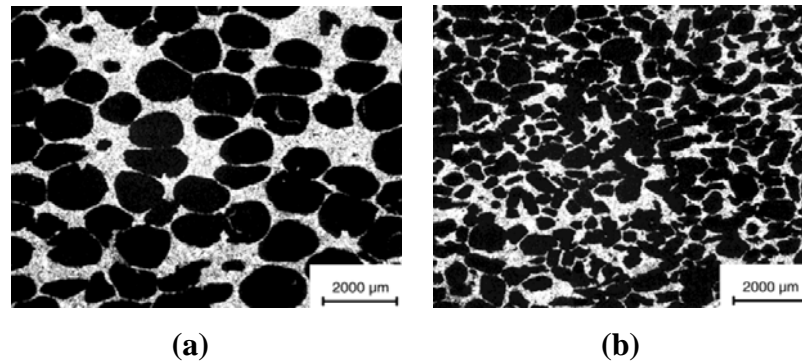


**Figure 2.16** Structure of titanium foams produced using (a) spherical carbamide, (b) angular carbamide [92].

Wen et al. used carbamide, ammonium hydrogen carbonate [57, 93] and both together [56] in the production of titanium foams to be used as an implant with mechanical properties similar to human. In a study carried by these authors [56] both ammonium hydrogen carbonate and carbamide (urea) powders having a size in the

range 200-600  $\mu\text{m}$  were used to mix with titanium powders ( $<45\mu\text{m}$ ) in an agate mortar. In the experiments, spacers from samples compacted at 100 MPa were removed by keeping the samples for 2 hrs at 200°C. Finally, they manufactured titanium foams having porosity around 78 % with an interconnected morphology. There existed two types of pores: Macro pores left by removal of spacer and micro pores on cell walls due to partial sintering of titanium powders. Most of the macro pores were in the range 200-500  $\mu\text{m}$ .

Later, these authors [57, 93] produced titanium foams using ammonium hydrogen carbonate with a wide range of strength and stiffness showing a good match to human bone. Titanium foams had an open cellular morphology and contained porosities between 35 and 80 % and pores with size in the range 200-500  $\mu\text{m}$ . Similarly, ammonium hydrogen carbonate powders were also used by Imwinkelried [94] for production of open-pore titanium foams. Ammonium hydrogen carbonate powders (425-710  $\mu\text{m}$ ) in the range 50-80 % were mixed with titanium powders in a proprietary process using tumbling glass bottles. Then, green bodies were pressed using cold-isostatic and uniaxial pressing. The space holder material was removed from the compact at a lower temperature, 95°C during 12 hrs in a convection furnace. Then, the parts were sintered under argon atmosphere at 1300°C for 3 hrs. By this way, titanium foams having pore size in the range 100-500  $\mu\text{m}$  and porosities between 50 and 80 % were manufactured.

In another study, Wen et al. [95] utilized the same technique to produce Ti-Zr alloy foams to be used in biomedical applications. Initially, elemental powders of titanium and Zirconium were subjected to mechanical alloying (MA) using planetary ball mill to synthesize Ti-Zr alloy under argon atmosphere with the addition of stearic acid. Then, Ti-Zr/ammonium hydrogen carbonate powder (200-500  $\mu\text{m}$ ) mixtures were compacted at 200 MPa and heat treated in a vacuum furnace. Spacer was removed keeping the samples for 5 hrs at 200°C and following the removal step sintering was carried out at 1300°C for 2 hrs. The Ti-Zr alloy foams displayed an interconnected porous structure resembling bone and the pore size ranged from 200 to 500  $\mu\text{m}$ .

Similarly, Li and Zhu [96] manufactured titanium foams with controlled porosity and pore size using carbamide (urea) as spacer particles by heating the titanium-urea powder compacts at 200°C (2 hrs) and sintering at 1200°C for 4 hrs under argon atmosphere.

Polymeric spacer particles may also be used in porous titanium manufacturing, however, their use is limited mainly due to contamination of titanium by side products that form during decomposition and removal step. Rausch and Banhart [7] utilized polymer granules as spacer particles. Polymer granules in titanium-polymer mixture compact were removed by a chemical process at temperatures around 130°C. After removal of spacer, samples were sintered in vacuum at temperatures of 110-1250°C to yield porosities 55-80 %. Average macro pore diameter was in the range 200-3000 μm. They concluded that micro porosity on the cell walls might be reduced by changing the sintering parameters and/or partially replacing titanium powder by titanium hydride.

Metallic space holder is first used by Wheeler et al. [97] to produce titanium and Ti-6Al-4V alloy foams. Limited solid solubility of magnesium in titanium, Figure 2.17, made it possible to use magnesium as spacer particle.

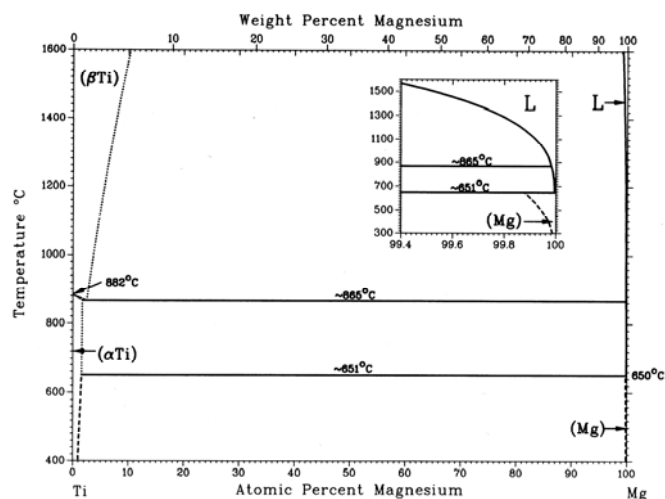


**Figure 2.17** Ti-Mg Binary Phase Diagram [98].

Firstly, magnesium-titanium powder mixtures were hot pressed well below melting point of magnesium. Then, magnesium was removed at 1000°C, which is below the evaporation point (1090°C) and samples were sintered at 1400°C to yield porosities in the range 25-82 %. Magnesium was also used as spacer particle in the manufacturing of porous titanium coatings for surgical implants [46]. Mixture of titanium or titanium alloy and magnesium in an amount 5-75 % and of particle size 100-200 µm and a binder, i.e. polyvinyl alcohol was prepared and the resultant paste was applied to the surface of the substrate. Then, the coated articles were heated to temperatures between 650 and 800°C in vacuum or under an inert gas so as to form a sinter of the Ti/Mg, which firmly adheres to substrate. Removal of magnesium was achieved by heating the article up to 1000°C or by immersion in an acid solution.

Tuchinskiy and Loutfy [99] recently used a different variation of space holder method. Firstly, they extruded the rods consisting of a fugitive core and shell made of titanium powder and polymer binder. After compaction, the core material and binder were removed at low temperature and the powder vacuum-sintered at 1200-1300°C, resulting in a titanium foam containing elongated secondary pores.

As thermally removed spacer particles may cause degradation of titanium compacts it is advantageous in some cases to use water soluble spacers. Potassium sorbate and potassium chloride are some of the water soluble spacer particles that can be used in manufacturing of titanium foams [91]. These spacer particles with different size and shape are used in the production of titanium foam. Initially, powder mixtures are pressed using a cold isostatic press and then, the spacer particles, potassium chloride or potassium sorbate, are removed in a water bath kept between 30 and 60°C. Water is replaced several times to remove any traces of the extractable particulate. After removal from the water bath the compact is dried in air at a temperature between 40 and 50°C. Then, the article is sintered around 1300°C.

## **2.5. Characterization of Metallic Foams**

Cellular metals and alloys are characterized by different methods to obtain the mechanical or physical properties or to evaluate the technological applicability.

Various production methods result in characteristic structures, densities and also imperfections. The most important parameters to characterize a cellular structure are the morphology of the cell (cell geometry, open or closed cell), the topology, the relative density, the mean cell size, its distribution, the properties of the cell wall material mechanical properties (yield and tensile strength, Young's Modulus), and corrosion behavior of the metal foams, Table 2.5. On the other hand, imperfections can be wavy distortions of cell walls, variations in cell wall thickness or non-uniform cell shape, etc. [100].

**Table 2.5** Characterization methods for metallic foams [1].

Type	Testing Method	Aim
<b>Non-Destructive</b>	Density Measurement (Archimedes')	Overall density
	Dye penetration measurement	Surface defect determination
	X-Ray radiography and radioscopy	2-D imaging of pore distribution
	X-Ray computed tomography	3-D imaging of foam
	Eddy-current sensing	Relative density, pore size
	Acoustic measurements	Porosity level and type
	Vibrational analysis	Young modulus
	Porosimetry and permeametry (Mercury porosimetry, gas absorption technique, permeametry, bubble point method)	Pore size and distribution, surface area, internal structure
	Elect. & Conductivity measurement	Electrical resist. & thermal cond.
	X-ray and neutron small angle scattering	Pore size distribution
	Ultrasonic imaging	Internal structure imaging
<b>Destructive</b>	Optical image analysis	Morphology, microstructure, size and distribution of pores
	Mechanical Testing	Fatigue life, elastic modulus, yield and tensile strength
	Corrosion testing	Corrosion behavior

Mechanical testing of cellular metals is the prerequisite for any applications. The characterization methods are, in principle, the same as for other non-cellular materials. However, sometimes some modifications of the test procedures are

necessary to account for the specific nature of cellular materials. One such specialty concerns statistics: if metal foam of a given alloy were tested, the resulting mechanical properties of a number of samples with the same overall density would show a much larger scatter than usually found in testing conventional materials. The reason can be different mass distribution or heterogeneous microstructure, which distinguish various samples of the same density from each other. Therefore, a large number of samples may be necessary for comparison. Moreover, as in cellular materials the length of macroscopic heterogeneities is sometimes in the range of millimeters, the sample dimensions in mechanical tests might have to be enlarged compared to existing standards.

In the mechanical testing of metal foams following factors should be considered:

Type of applied stress: Uniaxial, biaxial, multiaxial or hydrostatic. Uniaxial test is the most common test type.

Mode of Loading: Compression, tension, shear, bending, torsion. Compression tests are the ones most frequently carried out.

Time Dependence of Load: Constant, slowly increasing (quasi-static), dynamic, cyclic. Most of the work found in literature was obtained under quasi-static conditions ( $\dot{\epsilon} \sim 10^{-3} \text{ s}^{-1}$ ).

## **2.6. Mechanical Behavior of Metallic Foams**

### **2.6.1. Stress-Strain Curves**

The stress/strain responses (Figure 2.18) exhibited by low relative density cellular metals establish two aspects of their engineering utility: Firstly, their relatively high stiffness and yield strength achievable at low density creates an opportunity for ultra-light structures, with integrally bonded dense face sheets. Secondly, large compressive strains achievable at nominally constant stress impart a

high-energy absorption capacity at force levels relevant to crash and blast amelioration systems [101].

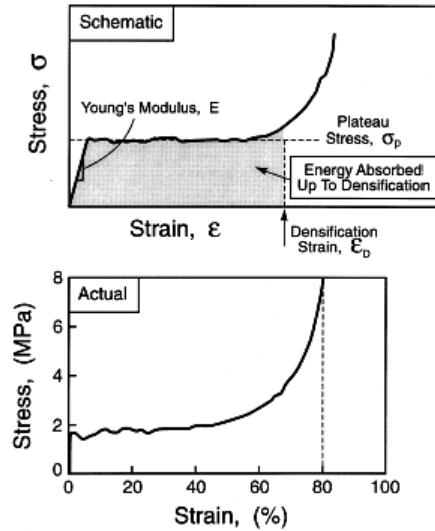


**Figure 2.18** Ideal and actual compression stress-strain curves for a closed cell Al alloy.

Initial structural analysis for the mechanical response of cellular solids employed unit cells such as a hexagon in two dimensions or a dodecahedron or tetrakaidecahedron in three dimensions. The simple geometry of the unit cell makes the analysis tractable but may not give an exact representation of the real material, i.e. foams. For example, Gibson and Ashby used a simple strut model, which use a cubic cell to illustrate the argument [2, 3, 101]. An even simpler approach is to use dimensional analysis to model the mechanisms of deformation and failure observed in the cellular material without specifying the exact cell geometry. This approach assumes that the cell geometry is similar in foams of different relative densities. It can represent the dependence of the properties, on foam parameters in terms of some empirical constants, but requires experimental determination of the constants related to the cell geometry. A third approach is to use finite element analysis of either regular or random cellular structures.

Based on deformation behavior metallic foams can be divided into three main groups; elastomeric, elastic-plastic, elastic-brittle, Figure 2.19, each of which posses different mechanical responses under compressive and tensile loading.

### 2.6.1.1. Compressive Response

All types of foams, including honeycomb structures, show three different deformation regions: linear elasticity at low stresses; long collapse plateau region; densification in which the stress raises steeply, Figure 2.19. Depending on the structure of the foams (open, closed or partially open) different deformation stages are controlled by different mechanisms.

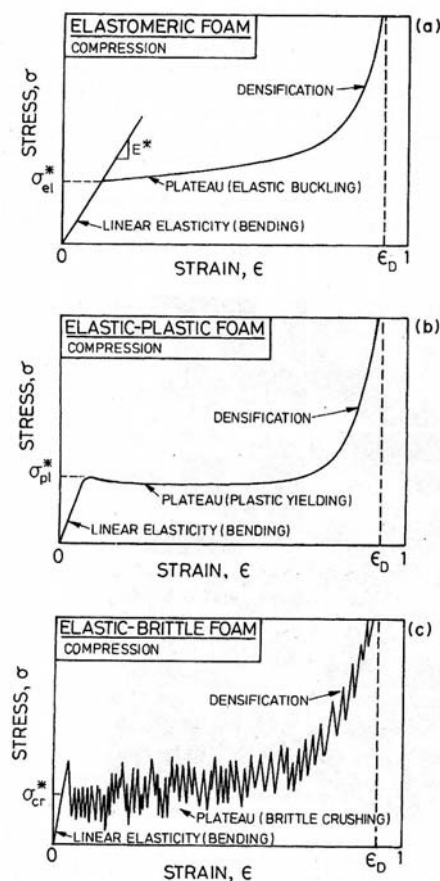


**Figure 2.19** Schematic compressive stress-strain curves for foams [3].

In these structures, linear elasticity is controlled by cell wall bending or by cell face stretching if the cells are closed. When loading is compressive the plateau is associated with collapse of the cells; by elastic buckling in elastomeric foams (rubbers, for example), by the formation of plastic hinges in a foam which yields (such as a metal); and by brittle crushing in a brittle foam (such as a ceramic). When the cells have almost completely collapsed, opposing cell walls touch each other and further strain compresses the solid itself, giving the final region of increasing stress (density of the material increases). Increasing the relative density of the foam increases Young's modulus, raises the plateau stress and reduces the strain at which densification starts.

#### 2.6.1.1.1. Elastic Region

The mechanism of linear elasticity of metal foams depends on whether the cells are open or closed. At low relative densities, open cell foams deform primarily by cell edge/wall bending, Figure 2.20.

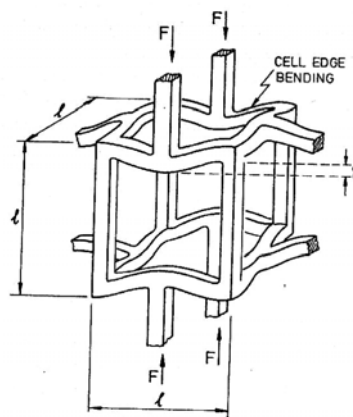


**Figure 2.20** Cell Edge bending during linear-elastic deformation [3].

As the relative density ( $\rho^*/\rho > 0.1$ ) of the foams increased the contribution of simple extension or compression of the cell walls becomes more significant. In

closed-cell foams the cell edges both bend and extend or contract, while the membranes which form the cell faces stretch, increasing the contribution of the axial cell-wall stiffness to the elastic modulus.

Linear elasticity is limited to small strains, typically 5 % or less. In compression tests, the stress-strain curve shows an extensive plateau at a stress, *elastic collapse stress*. This kind of deformation is seen in elastomeric foams, Figure 2.19 (a). The elastic buckling of the cell walls causes elastic collapse in foams. The elastic collapse stress and the post-collapse behavior depend on whether the foam has open or closed cells. Open cell foams such as polyurethanes, collapse at almost constant load, giving a long flat plateau. In closed-cell foams (polyethylene) the compression of the gas within the cells, together with the membrane stresses, which appear in the cell faces, give a stress-strain curve, which rises with strain.

#### **2.6.1.1.2. Plastic Collapse and Densification**

Foams made from materials, which have a plastic yield point (rigid polymers or metals, for instance) collapse plastically when loaded beyond the linear-elastic regime. This kind of behavior is seen in elastic-plastic type of foams, Figure 2.19 (b). Plastic collapse gives a long horizontal plateau to the stress-strain curve. Like elastic buckling, the failure is localized in a band transverse to the loading direction, which propagates throughout the foam with increasing strain. Plastic collapse in open-cell foam occurs when the moment exerted on the cell walls exceeds the fully plastic moment creating plastic hinges. Closed cell foams are more complicated since the plastic-collapse load may be affected by the stretching as well as the bending of the cell walls.

### 2.6.1.2. Tensile Response

Tensile responses of different foams are shown in Figure 2.21. The initial linear elasticity is caused by cell wall bending, plus stretching if the cells are closed. In elastomeric foam larger strains rotate the cell edges towards the tensile axis, increasing the stiffness of the structure.

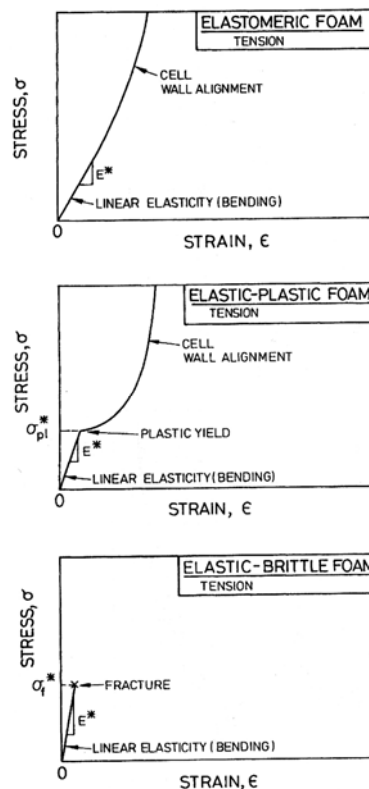


**Figure 2.21** Schematic tensile stress-strain diagrams of foams [3].

In the plastic foams, rotation towards the tensile axis, gives a yield point followed by a rising stress-strain curve, which is ultimately truncated by fracture. In the brittle foam a crack nucleates at a weak cell wall or pre-existing flaw and propagates catastrophically, giving fast brittle fracture. Some of the foams (rigid polymer foams are examples) are plastic in compression but brittle in tension. This

is because stress-concentrating effect of crack, which can cause cell wall failure and fast fracture when loaded in tension, but which is less damaging in compression.

### 2.6.1.2.1. Elastic Region

The small elastic modulus of foam in tension is the same as that in compression. The moduli of open-cell foams are determined by cell-edge bending; those of closed-cell foams by edge bending and face stretching. The buckling, which gives non-linear elasticity in compression is not possible in tension. Cell-edges, which lie at an angle to the tensile axis, rotate towards this axis, and the bending moment acting on them decreases, Figure 2.22.

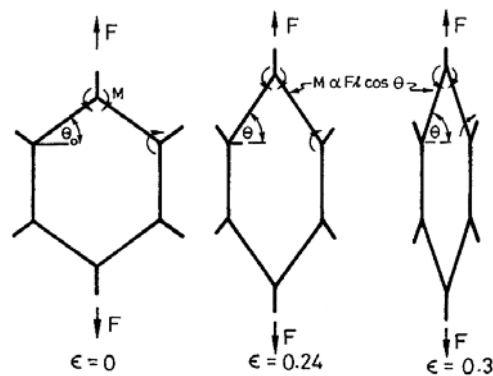


**Figure 2.22** Alignment of the cell edges during tensile loading [3].

Initially elastic response is dominated by cell-edge bending but as the cell walls rotate the stiffness rises. Experiments on real foams suggest that as the edges become aligned, stretching, rather than bending, dominates the deformation.

#### **2.6.1.2.2. Plastic Collapse**

A plastic foam yields in tension by the same mechanism as in compression. But, the post yield behavior is rather different. In tension, rotation of the cells reduces the bending moment so that after a strain of 1/3 the cell walls are substantially aligned with the tensile axis; then further strain requires the plastic extension of the cell walls themselves.

#### **2.6.1.2.3. Brittle Fracture**

Brittle fracture in tension is quite different from that in compression. In compression, the foam crushes progressively; in tension, it fails by the propagation of a single crack.

#### **2.6.1.3. Determination of the Mechanical Properties**

In general, the form of the stress-strain curves and the corresponding mechanical properties of manufactured foams are related to their densities or porosity contents, pore type, i.e. open, closed or partially open, and structure of the cell walls. Determination of accurate strength or elastic moduli values has been a fundamental issue in correlating the mechanical properties of foams to their densities or porosities. Therefore, various procedures have been used to define the strength of the foams due to uncertainty in the compression strength values. In some cases, upper or lower yield points are used for determination of strength or their average is taken. When no such upper and lower yield points are observed and the plateau region is rather smooth extrapolation of the plateau region to zero strain level gives compression strength. It is also possible to define the strength at a certain deformation level [102]. To determine the strength levels 0.2 % offset-method yield strength values are also used in defining mechanical property-relative density relation.

The Young's Modulus of a foam sample is not a material constant and depends on the architecture of the foam. For porous materials it can be measured using static and dynamic tests such as using direct measurement of strain as a function of stress, by external LVDT's placed between the loading platens, or by an extensometer mounted directly on the specimens [5]. Measurement of the resonance frequency of the material, ultrasonic methods and dynamic mechanical analysis can also be used to get information about elastic properties [103]. Use of direct measurement of strain as a function of stress may lead to measure the elastic moduli lower than the expected value. Because, in metal foams three types of imperfections degrade the stiffness and strength: cell edge curvature, material concentrated at cell nodes rather than cell edges, and non-uniform foam density. Although all the deformation is considered to be totally elastic in the linear section, presence of stress concentrations in some locations results in early yielding of some cell walls and edges in the elastic region.

#### **2.6.1.4. Densification strain**

The sharp increase in the compressive stress vs. strain curve at a nominal strain is termed as densification strain [3]. Densification strain of foams depends on cell topology. In some cases, it is defined as the strain at which the slope of the tangent is equal to that of the elastic regime. On the other hand, some authors [104, 105] defined this strain as the intersections of the tangents to the stress plateau regime and densification regime. Since the deformation mechanisms in open and closed cells are different, dissimilar densification strains are expected. Chan and Xie [104] defined the densification strain, ( $\epsilon_d$ ) for metal foams with open and closed cells considering tetrakaidecahedron cell geometry by the equations 2.4 and 2.5, respectively;

$$\epsilon_d = 1 - \alpha_c \frac{\rho^*}{\rho} \quad (2.4)$$

$$\varepsilon_d = 1 - \alpha_o \left( \frac{\rho^*}{\rho} \right)^{\frac{1}{2}} \quad (2.5)$$

where,  $\rho^* / \rho$  is the initial relative density and the  $\alpha_c$  and  $\alpha_o$  are the constants that depends on the foam structure and the cell wall material.

## 2.6.2. Mechanical Models

### 2.6.2.1. Porosity and Pore Character

Porosity in materials affects physical properties such as fluid permeability, thermal and electrical conductivity, dielectric constant, magnetic permeability, diffusion coefficient and acoustic wave velocities as well as the mechanical properties such as elastic moduli, yield, rupture or ductile strength [106].

As mentioned previously, it is possible to achieve various types of porosities using different powder metallurgical production techniques and the amount, type and distribution of porosity throughout the sample strongly influence the mechanical properties. Many of the models proposed to predict the mechanical behavior make use of various ideal stacking of powder particles or pores. Accordingly, it would be appropriate to give the pore types prior to discussing the mechanical models based on different type of pore morphologies.

As explained, there are mainly two different basic production methods that yield different types of porosities. The first one utilizes the inherent pores between packed particles, within various degrees of bonding, i.e. loose powder sintering. Here, the amount of porosity and pore character are related to both the size and the packing of the particles and their degree of bonding. The structure can be idealized as stacking of spherical particles with various degrees of sintering bonds within the confines of imagined space-filling polyhedral cells with the particles in the center of the cells (Figure 2.23). The second method of forming porous solids involve

introducing isolated or interconnected bubbles, using space holders removed during subsequent sintering or other rigidization of the structure. The structure can be idealized as building up porous solids by various stacking of polyhedra cells with solid struts and walls and pore space inside, Figure 2.24.

Porosities and pore structures obtained may be fully open, less open or closed. The amount and character of the porosity is directly related to the surrounding solid. Porous materials can be characterized considering the size, shape and coordination number ( $C_n$ ) of the pores and the solid particles or ligaments that define them, whether the porosity is open or closed, inter- or intragranular, single or multi-modal, and its size and shape distributions and the overlap (or bond) area of the pores (or surrounding particles). Table 2.6 lists some of the packing types of solid spherical particles and resultant maximum porosities and also shape of the final article subsequent to sintering.

**Table 2.6** Coordination number, grain shape and resultant maximum porosities of various powder-packing types [107].

Stacking	Coordination No, $C_n$	Resultant dense grain shape	Porosity (%) (Maximum)
Simple cubic	6	Cube	47.6
Orthorhombic	8	Hexagonal Prism	39.5
Tetragonal	10		30.0
Rhombohedral	12	Rhombic dodecahedron	26.0
BCC	8		32.0
	14	Tetrakaidecahedron	6.0

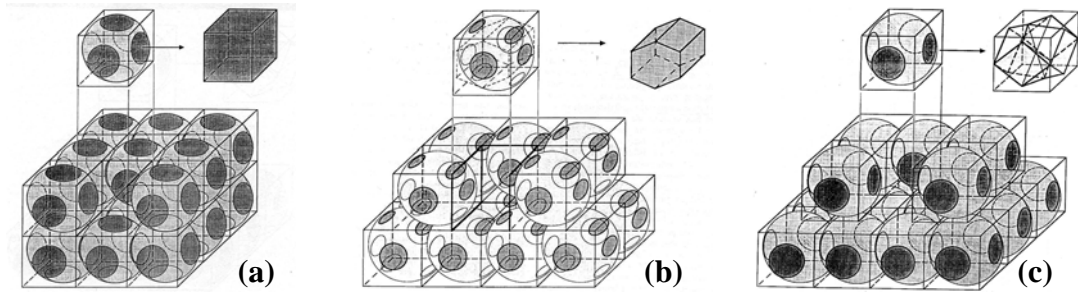


**Figure 2.23** Idealized stacking of uniform solid spheres (or pores) in, (a) cubic, (b) orthorhombic, (c) rhombic arrays and the resultant grain shape at full density for sintered sphere [108].

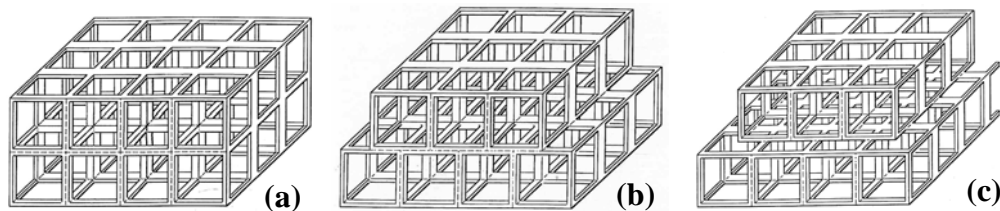


**Figure 2.24** Idealized stackings of uniform foam cells, (a) cubic, (b) orthorhombic, (c) rhombic [108].

### 2.6.2.2. Proposed Models

To describe the dependence of mechanical properties of materials to their porosities, numerous empirical and theoretical relations have been proposed. The empirical relations attempt to best-fit the experimental data, but the physical meaning of the relations is unclear. Some of these equations relate the constants with pore geometry. However, this has not significantly aided predictability. There are two reasons why many of these previous curve-fitting studies have not been successful. Firstly, the data they used were often variable in quality. The second and most fundamental reason is the use of fixed character of porosity (e.g. all bubbles, or all pores between particles of fixed shapes and stackings). However, most porous bodies manufactured using powder metallurgical techniques contain more than one type of porosity, e.g. partially sintered bodies of various particle sizes and packings

result in varying porosity character. Moreover, pore character in materials is not uniform and changes with the amount of porosity, e.g. as sintering occurs, the coordination number of the particles increases from around 6-8 in the starting materials to 12-14 at high densities. Thus, models based on single, fixed type porosity will commonly deviate from actual data, due to neglecting the actual geometry and distribution of porosity, or its change with porosity content [108]. However, the theoretical models are based on some idealized microstructures, e.g. uniform spherical, cylindrical or cubic pores are arranged in a cubic array.

Theories that have been postulated to characterize the mechanical properties of porous materials can be classified into three categories;

- 1) Cross-sectional area models
- 2) Stress concentration models
- 3) Effective flaw size approach

In the cross-sectional area model, the actual load bearing area or the minimum solid cross sectional area is used as the critical parameter. Whereas, the stress concentration approach is based on the effect of pore shape on the resulting maximum stress concentration. Stress concentrations from pores as well as cracks and inclusions were seen as sources for crack propagation under tensile and compressive loading. It was observed that under compressive loading the crack propagation from pores would be greatly inhibited until much higher stresses are reached, allowing pores to act as stress concentrators to active slip and twinning.

The compressive failure of brittle materials was said to be the result of cumulative damage from a number of crack generation-linkage-propagation events. In some studies stress concentrations from pores as well as cracks and inclusions were seen as sources for crack propagation under tensile and compressive loading.

The last theoretical approach, called effective flaw size approach is based on the existence of flaws before final failure in the vicinity of a pore or void surface [109].

### 2.6.2.2.1. Minimum Solid Area (MSA) Models

MSA models have been shown to be more accurately correlated with properties than an accepted stress concentration model because interaction of pores reduces their stress concentrations, leaving the minimum solid areas as the main carrier of stress.

In MSA models the fraction of the zero porosity property values as a function of the volume fraction porosity is equated to either the average or, more commonly, the minimum, fraction of solid area of the total body area normal to the reference (stress) axis. For sintered particles, MSA is the projection of the actual sintered area (neck diameter) between the particles normal to the stress or flux, Figure 2.25 (a). For foam type structures, it is the projection of the minimum web area between adjacent bubbles parallel to the stress or flux, Figure 2.25 (b).

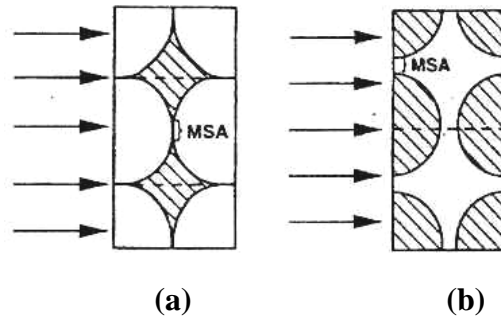


**Figure 2.25** Schematic illustration of minimum solid area (MSA) in, (a) partially sintered powders, (b) foam samples.

According to proposed model, physical properties such as mechanical properties (elastic properties, tensile and compressive strength, and hardness) and electrical and thermal conductivity, i.e. properties determined by the local flux or fields in the material, changes with minimum solid area. These properties depend on both volume fraction and type of porosity. MSA normal to the stress (or conductive flux) should dominate the transmission of stress (i.e. strain, fracture toughness or

energy, or strength) or conductive (thermal and electrical) fluxes through a body. Properties not predictable with such models are those mainly determined by mass (e.g. heat capacity) in which case a simple rule of mixtures of the property values for the solid and pore (e.g. air or vacuum) volume fractions should be appropriate. In the MSA models, the minimum, rather than the average, fractional solid area is more logically the controlling factor and has been most commonly used. However, in a few special cases, the average and minimal solid cross-sectional areas are equal, e.g. for any type of long, parallel cylindrical or prismatic pores with the stress or flux parallel to pore axis.

MSA models were developed for idealized structures containing uniform spherical pores, cubical pores (stressed, normal to various orientations), solid spherical particles (simple cubic, orthorhombic, and rhombic stacking), and aligned cylindrical pores. Proposed models for foams assume mechanical properties are determined by the properties and dimensions of the struts or webs between the pores rather than the thicker cross-sections, i.e. the junction of two or more webs or struts, which also neglects stress concentrations at such junctions [96, 108, 110, 111].

Minimum solid area fraction for cubic, orthorhombic and rhombohedral packing of solid particles was calculated first by Knudsen [112]. An idealized specimen was assumed to be composed of systematic arrangement of equal-sized spheres. At some stage in the fabrication of the specimen they are presumed to coalesce in the following manner: 1) The spheres draw together on their centers without changing their relative angular orientation with respect to one another. 2) Each sphere flattens at the bond areas of contact with its neighbors. 3) Each deforming sphere maintains its original volume, the displaced material redistributing itself evenly over the residual curved surfaces. 4) As the porosity of the specimen decreases, the size of the flattened areas of contact increases, until the original spheres eventually become polyhedrons at zero specimen porosity. In the theoretical specimen models, the contact areas are represented as flat junctions between perfect truncated spheres. In idealized specimen models, the curved surfaces of adjacent grains meet to form a sharp angle at the grain junction. In the actual coalescence of most grains this sharp angle is filled by forces akin to surface tension and the junction of the curved surface is meniscus shaped instead of angular. This

phenomenon increases the size of the contact area and, as can be seen in Figure 2.26, the proportionate increase is greatest in the initial stages of sintering. This concept is the basis for the hypothetical dashed curves in Figure 2.27.

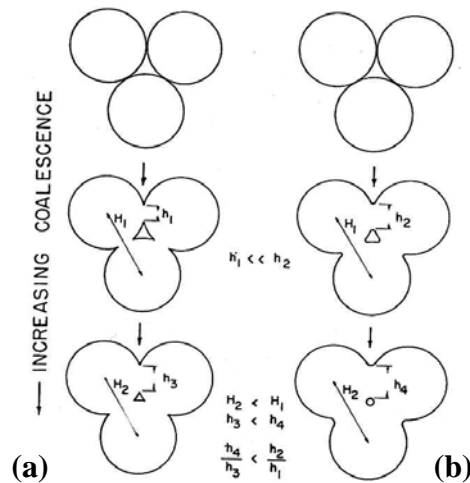


**Figure 2.26** Schematic coalescence of (a) grains idealized geometry, (b) lens shaped contact [112].

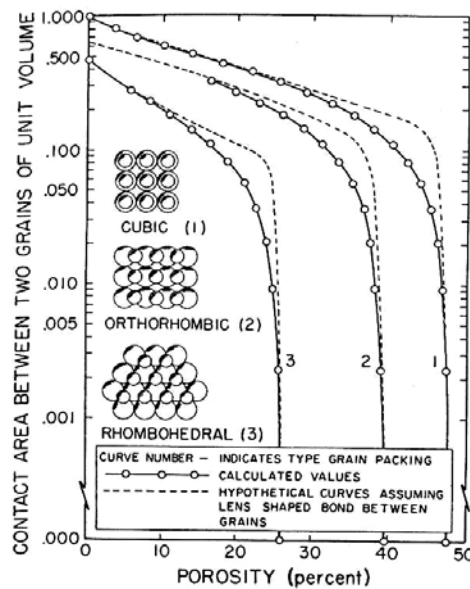


**Figure 2.27** Relation between porosity and contact area between two adjacent spheres within different packing arrangement of coalescing spheres [112].

Euler [113] used MSA concept to determine relative property-porosity relations considering a simple cubic arrays of porous spheres in solid matrix. It was assumed that the repeat distance of the lattice is  $2h$  and the sphere radius is  $r$  as shown in Figure 2.28 (a).

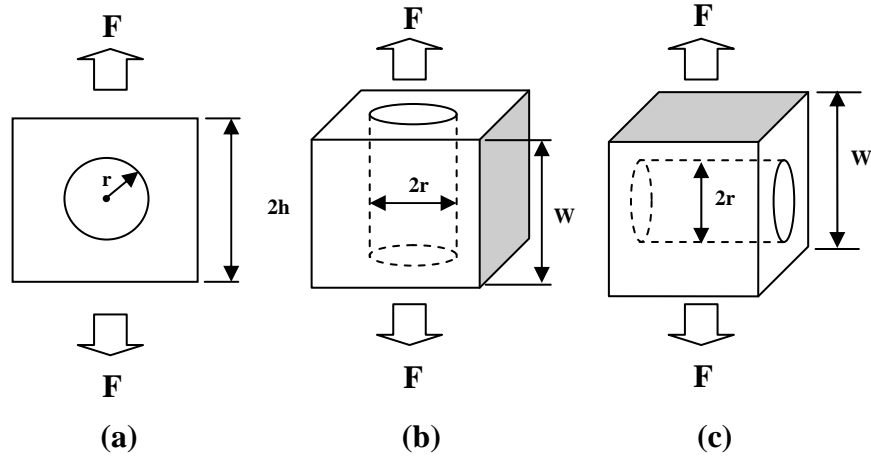


**Figure 2.28** Schematic drawings of the load-bearing area model for bulk samples with, (a) spherical pores in cubic arrangement, (b) cylindrical pores parallel to the tensile direction, (c) cylindrical pores perpendicular to the tensile direction.

Minimum load carrying area is defined as  $(2h)^2 - \pi r^2$  and the total bulk (non-porous) area is  $(2h)^2$ . Then, based on MSA models relative property of interest,  $M/M_o$ , is equal to fraction of minimum load carrying area, which is given below;

$$\frac{M}{M_o} = \frac{(2h)^2 - \pi r^2}{(2h)^2} = 1 - \frac{\pi}{4} \left( \frac{6}{\pi} \right)^{2/3} p^{2/3} = 1 - 1.21p^{2/3} \quad (2.6)$$

where  $P$  is the porosity fraction and defined as  $\frac{1}{6} \pi \left( \frac{r}{h} \right)^3$ . The form of the equation changes when  $r > h$  (or  $p > \pi/6 = 0.524$ ) as the spheres begin to coalesce. Above

this porosity level transition from isolated and closed to open and interconnected porous structures occurs.

Similar calculations can be done for cylindrical pores arranged parallel or perpendicular to the testing direction. In the case of cylindrical pores arranged parallel to the loading direction the porosity, ( $p$ ), can be calculated as;

$$p = \pi \left( \frac{r}{W} \right)^2 \quad (2.7)$$

The minimum load-bearing area is  $W^2 - \pi r^2$ . Then using MSA concept in which relative property is approximated to the fraction of load-bearing area one can obtain following relation;

$$\frac{M}{M_o} = 1 - p \quad (2.8)$$

In a similar way, the relative property can be predicted for materials with cylindrical pores with simple stacking arranged perpendicular to the testing direction, Figure 2.28 (c) and cylindrical pores with hexagonal stacking arranged perpendicular to the testing direction, respectively [114];

$$\frac{M}{M_o} = 1 - 1.13p^{1/2} \quad (2.9)$$

$$\frac{M}{M_o} = 1 - 1.05p^{1/2} \quad (2.10)$$

Figure 2.29 shows calculated ratios of minimum bond area per cell to the cell cross-section for different solid and pore stacking. As shown in Figure 2.29, each curve of MSA model has three characteristics: beyond the initial, approximately linear decrease of the minimum solid area (and hence the property value of interest) on a semi-logarithmic plot versus porosity, the property of interest starts decreasing

more rapidly, then, going to zero at a critical porosity,  $P_c$ , the percolation limit, is where the bond area (or web area) between particles (or pores) goes to zero. For pores in a matrix, it is the point at which the minimum web areas between particles go to zero.

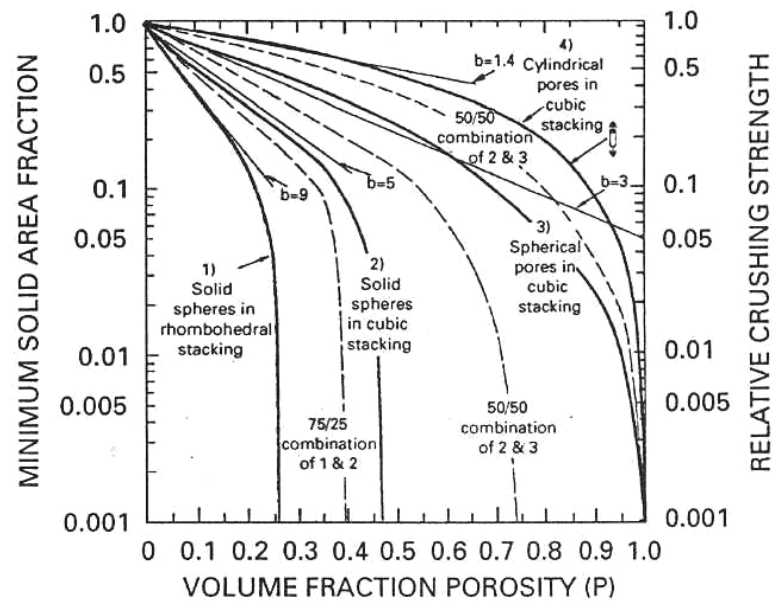


**Figure 2.29** Models from the literature showing calculated ratios of minimum bond area per cell to the cell cross-section for various solid sphere and pore stackings [108].

If there is heterogeneous porosity in the material, combined effects can be calculated in three different ways, Figure 2.29;

- 1) Rule of mixture (upper (Voight) limit);

$$M = p_1 M_1 + p_2 M_2 \quad (2.11)$$

where,

M : property of interest

$p_1, p_2$  : volume fractions of different porosities

$M_1, M_2$  : Materials properties for different type and amount of porosities.

2) Lower (Reuss) bound;

$$M = \frac{M_1 M_2}{p_1 M_2 + p_2 M_1} \quad (2.12)$$

3) Use of combination of upper and lower bonds

In some MSA models relative solid area ( $A/A_0$ ) and hence the property of a material ( $M_c/M_s$ ) has also been derived using an empirical exponential function in the form of  $e^{-bp}$  [96, 106-120];

$$\frac{A}{A_0} = \frac{M_c}{M_s} = e^{-bp} \quad (2.13)$$

$A, A_0$ : Solid areas of porous and pore free material, respectively

$b$  : constant that depends on geometry of pores

$p$  : fraction of porosity

The constant ‘b’ in Equation 2.13 is used to account for the porosity dependence of mechanical properties in the low porosity range as shown in Figure 2.29 and corresponds to the slope of the initial approximately linearly decreasing MSA, or property, with porosity on a semi-log plot corresponding to a given particle stacking, and hence pore structure. This exponential relation was first proposed by Duckworth [121] considering strength. Spriggs [122] used this exponential function to define the relationship between porosity and relative Young’s Modulus.

The disadvantage of Equation 2.13 is that it can be used for only low values of porosity ( $p \leq 0.30$ ) since the boundary condition that property should be equal to zero when porosity fraction is equal to 1 is not satisfied. Moreover, it is not zero

when  $p \rightarrow p_c$  (critical porosity that corresponds to the percolation limit of the solid phase). According to ‘Percolation Theory’ two critical porosity levels may exist in the material. When the porosity reaches first critical value ( $p_{c1}$ ) transition from closed porosity to interconnected porosity with complex shape occurs. Finally, the effective strength or elastic modulus vanishes when the porosity reaches the second critical value ( $p_c$ ) or percolation threshold. For powder materials,  $p_c$  is the tap porosity before sintering. The value of the percolation threshold is a function of powder size, shape, their distribution and the preparation method [123, 124]. Knudsen [112] obtained the theoretical  $p_c$  values for solid spherical particles arranged in cubic, orthorhombic and rhombohedral arrays as 0.476, 0.397 and 0.26, respectively.

Use of Equation 2.13 may have three basic advantages. First, it is a reasonable approximation for the actual case. Second, there are extensive data for which the ‘b’ values have already been determined. Third, it provides a single parameter, b, which can be correlated with pore character and can be readily adapted for pore combinations via a weighted average of the b values. Some of the calculated ‘b’ values for different stackings are presented in Table 2.7. As shown in Figure 2.29 there is approximately linear decrease region of the minimum solid area (and hence the property value of interest) on a semi-log plot versus porosity. Rice [107, 108, 110] has reported that in the low porosity range by use of this exponential function it becomes possible to define the pore type and the mechanical behavior of the manufactured porous samples. Use of exponential function is represented in Figure 2.29 by linear lines having different ‘b’ values.

**Table 2.7** Calculated ‘b’ values in Equation 2.13 for different stackings of solid spheres and pores

Value of ‘b’ in Equation 2.13	Stacking type of solid spheres or pores
9	solid spheres in rhombohedral packing
5	solid spheres in cubic packing
3	cylindrical pores in cubic stacking normal to stress direction
1.4	cylindrical pores in cubic stacking parallel to stress direction

This exponential form has also potential for being combined with the similarly derived expression pertinent only for higher porosity levels, which has the form;

$$1 - e^{-b'(1-p)} \quad (2.14)$$

Variations in pore character, so the 'b' value, is related to powder used and processing. Die pressing of powder results in random stackings of particles. Such random stacking is similar in density to simple cubic stacking of uniform spheres (b~5). If very high compaction pressure were used, lamination becomes increasingly common. Such laminar porosities have b values similar to cylindrical pores of similar orientation. Significantly lower b values are obtained for much larger spherical or (approximately oriented) cylindrical voids obtained introducing bubbles or fugitive particles or due to particle bridging. Moreover, use of particles with a tendency to form chains is commonly obtained in dealing with sols such that these leave significant interstices between the entangled chains. Another factor for low b value is the use of extrusion which can lead aligned cylindrical porosity due to possible alignment of some particle bridges, and especially the stringing out of larger pores or binder material. Use of higher and uniform pressure result in denser packing of particles. Extrusion at high pressure reduces particle bridging and the extent of binder stringers. Samples formed by deposition of particles such as slip, tape or pressure casting have higher densities. Similarly, hot pressing or HIP (hot isostatic pressing) results in higher densities.

Using Knudsen's assumptions, Wang [125, 126] calculated the minimum solid area for simple cubic array of solid spherical particles to define elastic modulus-porosity relation. He found a similar expression to that of Duckworth's [121] and Spriggs's [122] relation, which uses an exponential equation. However, his model is valid over a wider range of porosity. Proposed approximate solution in terms of coefficients a and b, and with a quadratic exponent is as follows;

$$E = E_o \cdot e^{-(bp+cp^2)} \quad (2.15)$$

It was found that additional higher order terms, i.e.  $dp^3$ , can be included for the region where the density is very close to packing density.

There are also several other studies that utilizes porosity to define mechanical properties of porous materials. In an approach called Generalized Mixture Rule (GMR) used for mechanical characterization, porous material is taken as a class of two-phase composite composed of pore and solid material [106]. According to theory, any specific property of a material (M) can be expressed using the formula given below;

$$M_c^J = \sum_{i=1}^N (V_i M_i^J) \quad (2.16)$$

Where;

M: specific property

i : i<sup>th</sup> phase

J : Scaling fractal parameter controlled by shape, size and distribution of the phases. (  $0 < J \leq 1$  )

Taking  $M_{\text{pore}}$  as zero, Equation 2.16 turns into;

$$\frac{M_c}{M_s} = V_s^{1/J} = \left( \frac{\rho_c}{\rho_s} \right)^{1/J} = (1 - p)^{1/J} \quad (2.17)$$

$M_c$ : Specific property of composite

$M_s$ : Specific property of solid material

p : porosity fraction

$V_s$  : volume fraction of solid material

$\rho_c$  : density of the composite (in this case porous material)

$\rho_s$  : density of solid material

The exponent ‘J’ in Equation 2.17 depends on the geometrical shape, spatial arrangement, orientation and size distribution of pores and in turn on the materials and the fabrication method, (i.e. cold pressing, sintering or HIP), e.g., J=1 for porous materials with long cylindrical hexagonal pores aligned parallel to the stress direction. Generally scaling parameter, J, for intergranular, continuous and channel pores cavities is smaller than the parameter used for intragranular, isolated and rounded pores.

One of the most popular power law empirical equation similar to GMR models was defined first by Balshin [127];

$$\frac{M_c}{M_s} = (1 - p)^m \quad (2.18)$$

Constant ‘m’, equivalent to 1/J of Equation 2.17, is defined as adjustable parameter and M in Equation 2.18 may represent any mechanical property [115-117, 128].

When the material has porosities in the range  $p_{c1}$ - $p_c$  of the ‘Percolation Theory’ mentioned previously, mechanical properties of materials cannot be represented by Equation 2.18 [106]. Thus, p in equation 2.18 for this intermediate porosity region may be replaced reasonably by the effective porosity ( $p/p_c$ ) due to interconnection of pores. The relation containing critical value of porosity,  $p_c$ , to explain property-porosity relation was proposed first by Phani [117, 129];

$$\frac{M_c}{M_s} = \left(1 - \frac{p}{p_c}\right)^m \quad (2.19)$$

Where, m is defined as a parameter dependent on grain morphology and pore geometry.

Such normalization compresses the MSA model curves into a single universal MSA property-porosity curve as indicated by dashed region in Figure 2.30. There is very limited of normalization for tubular pores aligned with the

stress axis and somewhat more for spherical pores, then more for tubular pores aligned normal to the stress axis, and still progressively, more for pores between particles of various packings sintered to various degrees. The consolidation to a single curve suggests that there is a basic microstructural character to porous structures that underlies the diversity of porosity dependence of various structures.

Above equations fit the porosity trends near the percolation limits well, but this couldn't always be reliably done over a wide range. One of the basic problems with these equations is that the parameters all interact in one term.

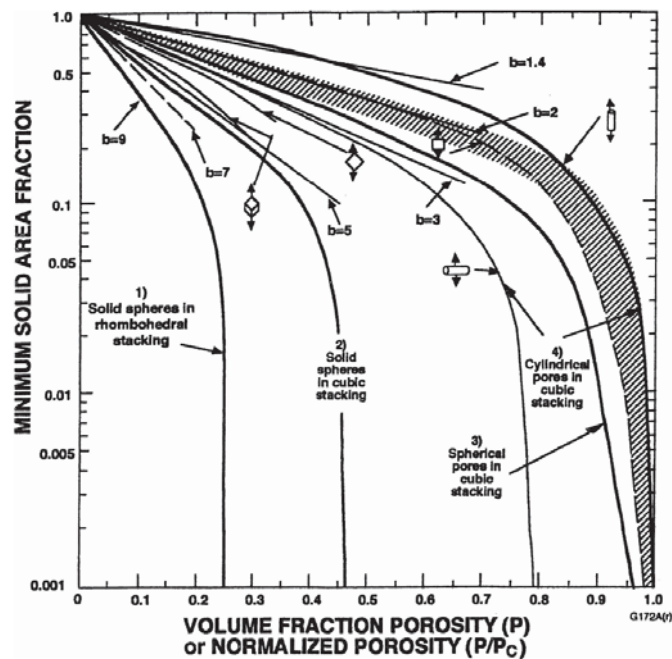


**Figure 2.30** Minimum solid area curves with and without porosity normalization [130].

Some models currently used for various foam structures are essentially specialized minimum solid area models since they assume mechanical properties are determined by the properties and dimensions of the struts or webs between the pores rather than the thicker cross-sections, i.e. at the junctions of two or more webs or struts, which also neglects stress concentrations at such junctions [110].

Models of Gibson and Ashby for elastic properties, toughness and strength of very porous, cellular materials (porosities higher than 70 %) are basically load-bearing models and neglect stress-concentrations [131].

Considering the linear-elastic deflection of open-cell foams, Gibson and Ashby [2, 3] proposed a simple relation for the Young's modulus of the cellular materials resembling to Balshin's equation and GMR model;

:

$$\frac{E_c}{E_s} = C \left( \frac{\rho^*}{\rho_s} \right)^n = C(1-p)^n \quad (2.20)$$

where;

$E_c$ : Young's modulus of porous material

$E_s$ : Young's modulus of pore free material

$\rho^*$  : density of the porous material

$\rho_s$  : density of solid material

They found  $n=2$  by fitting the available experimental data. For a porous material with honeycomb structure parallel to the direction of pores they showed that  $n$  value is equal to 1 and it is 3 when the direction is perpendicular. The detailed explanation about Gibson and Ashby study will be given in the following sections.

There are also some studies on MSA models, which made use of direct measurement of contact area between sintered powders. Danninger [132] used load bearing cross-sections to characterize the Young's moduli, yield strength, fracture strength and fatigue limit of sintered iron at different temperatures and soaking times. Load bearing cross-sections were measured on surfaces fractured using liquid nitrogen. It has been found that there is linear relationship between yield strength, cyclic properties and cross-section. For the fatigue limit, it was observed that one of the decisive parameter was crack initiation. The crack initiation occurred at the

largest clusters containing interconnected pores. The probability of the occurrence of clusters increased with decreasing load bearing area.

A similar study was carried out by Yeheskel et al. [133] on sintered prealloyed  $\gamma$ -TiAl powder. They used BET measurements to determine the contact area between the powders instead of optical or scanning electron microscopy. Plot of elastic moduli versus the specific surface area showed a smooth and monotonic increase with the increase of the contact area. They also found that there may be shift in the properties for the same porosity levels for different production techniques (CIP+sintering or HIP). This suggests that factors other than the contact area, such as the nature of the inter-particle contact might contribute in determining the properties.

MSA model assumes that different properties (E, G, B) have the same dependence on porosity, it predicts a similar evolution of the MSA and the considered property. However, in some studies [111] a deviation and fluctuation have been shown for toughness and fracture energy. Rice [110] explained the deviation from MSA models by crack branching and crack bridging mechanisms, which appear for large cracks due to pore interactions. On the other hand, Reynaud [111] attributed this behavior to the variation of grain size with porosity. As the grain size gets smaller fracture mode became more transgranular.

The basic data quality problem in applying MSA models is the issue of the homogeneity of the porosity. All properties dependent on MSA will be affected by porosity heterogeneities. Test of the homogeneity of the samples is to compare different directions of measurement (e.g. of elastic or conductivity properties) or comparison of inter-related properties. Thus, comparison of Young's Modulus with shear or bulk or both is very useful. In particular, calculation of the Poisson's ratio and its dependence on porosity can be of considerable value, since it is fairly sensitive indicator of differences, e.g. between E and G.

Moreover, MSA models do not consider the effect of anisotropy or other non-uniformities. Knudsen [112] calculated bond areas for three different sphere stackings, but only for one direction, essentially  $\langle 100 \rangle$ , for each of these stackings. In general, bond areas normal to the reference (e.g. stress, flux, etc.) direction play a

major role in supporting load, heat conduction, etc. Areas at intermediate angles play an intermediate role and areas parallel to such direction play even a lesser role.

In the MSA models, purely geometrical reasoning is used to predict the properties on the weakest points within the structure. The microstructure that corresponds to the MSA predictions is not exactly known [119].

#### 2.6.2.2.2. Special MSA Models

There are some special MSA models studies used to determine the mechanical property-neck size relation of partially sintered powders, which have irregular porosities between them. They are based on the dimension of bonded cross section (neck area) between powder particles that carry load.

During sintering atomic diffusion leads to formation of interparticle bonding and shrinkage. Sinter bonding is the result of multiple transport mechanisms. For example, in high temperature sintering bulk transport mechanisms are active and induce densification. Strength of such compacts comes from further neck growth, densification (removal of pores), and a higher coordination number for each particle.

So, in sintered compacts bonds between particles or grains determine the strength [134, 135]. Nice and Shafer [136] derived a relation between strength and neck size ratio of the interparticle bond;

$$\frac{\sigma}{\sigma_0} = A \left( \frac{X}{D} \right)^2 \quad (2.21)$$

Where;

$\sigma_0$  : wrought material strength

A : empirical constant

X/D : neck size ratio (average interparticle neck diameter divided by average particle diameter)

This empirical relation is then, developed by studies of German [137, 138] and Xu et.al. [134, 139]. Consider the geometry shown in Figure 2.31 with monosized spherical particles with diameter  $D$ , interparticle neck diameter  $X$  and the angle  $\alpha$  between interparticle bond and the horizontal compression planes.

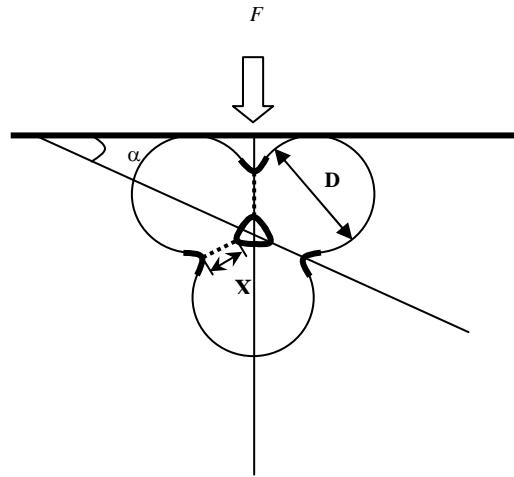


**Figure 2.31** Schematic representation of clustered monosized spherical particles

In mechanical testing, initially, an effective bond area perpendicular to compression axis was defined as;

$$A_{\text{eff.}} = \text{Bond Area} \times \text{Cos}\alpha \Rightarrow A_{\text{eff}} = \pi \left( \frac{X}{2} \right)^2 \cdot \text{Cos}\alpha \quad (2.22)$$

There are several interparticle bonds per particle. However, not all of those contribute to the strength. So, effective number of bonds that contribute the strength was defined as;

$$N_{C,\text{eff}} = \frac{N_C}{\pi} \quad (2.23)$$

where,

$N_C$  : average particle packing coordination number and it is defined as;

$$N_c = 14 - 10.3(1 - V_s)^{0.38} \quad (2.24)$$

$V_s$ : fractional density

Then, total effective bond area per particle is;

$$A_{\text{eff,total}} = X^2 \text{Cos}\alpha \left( \frac{N_c}{4} \right) \quad (2.25)$$

The ratio (R) of total effective bond area to the projected particle area (Load bearing area fraction) is;

$$R = \frac{A_{\text{eff,total}}}{A_{\text{particle}}} = \frac{X^2 \text{Cos}\alpha \left( \frac{N_c}{4} \right)}{\pi \left( \frac{D}{2} \right)^2} = \left( \frac{N_c}{\pi} \right) \left( \frac{X}{D} \right)^2 \text{Cos}\alpha \quad (2.26)$$

Where,  $A_{\text{particle}}$  is the projected area of a particle on horizontal plane.

There are many particles having various orientations relative to compression axis. The ratio R can be computed as;

$$\int_0^{\pi/2} \left( \frac{N_c}{\pi} \right) \left( \frac{X}{D} \right)^2 \text{Cos}\alpha \cos \alpha \, d\alpha = \left( \frac{N_c}{\pi} \right) \left( \frac{X}{D} \right)^2 \quad (2.27)$$

Due to load bearing area, the nominal strength can be approximated as  $\sigma_0 V_s$ , where  $\sigma_0$  is the strength of wrought material and  $V_s$  is the fractional density.

The presence of shoulders, threads and holes results in a localized high stress known as stress concentration. In sintered compacts, failure at lower loads than expected is associated with the stress concentrations at the inter-particle necks. The

stress concentration factor is defined as the ratio of the peak stress in the neck region to the nominal stress. Then the strength of porous material can be approximated as;

$$\sigma = \sigma_o V_s \frac{N_c}{K\pi} \left( \frac{X}{D} \right)^2 \quad (2.28)$$

Stress concentration effects are generally significant in brittle materials such as ceramics and glasses failing from pores, i.e., when isolated (large) pores act as the fracture origin [140].

The stress concentrations decrease when going from homogeneous uniaxial tension, to tension, from bending to homogeneous uniaxial compression. Thus, upon loading of a porous material in compression stress concentration may have very little effect on yield and ultimate strength of the material. In fact, there is no concentration of the compressive stress for spherical pores, only the occurrence of a localized tensile stress whose maximum equals the value of the applied compressive stress [141].

Average neck size ratio, (X/D), between the powder particles may be determined by direct measurement of bonded area and average particle size in fracture surfaces of powder samples by use of optical or scanning electron microscopes or can be estimated by the formula given (for neck size ratio smaller than 0.5) below;

$$\left( \frac{X}{D} \right)^2 = 4 \left[ 1 - \left( \frac{V_0}{V_s} \right)^{1/3} \right] \quad (2.29)$$

Similarly, Krasulin et al. [142] also studied the neck size (load bearing cross-section) effect on the mechanical properties of sintered stabilized zirconia microspheres. They derived the following formula for the strength of these partially sintered samples;

$$\sigma = \sigma_o \frac{3(1-P_C)(1-P)^{2/3}}{K_\sigma} \left( \frac{X}{R} \right)^2 \quad (2.30)$$

Where;

$$K_\sigma : \text{stress concentration factor, } K_\sigma = K_t K_b \left( \frac{\rho}{\rho + 2y} \right)$$

$\rho$  : density

$P_C$  : critical porosity level

$P$  : porosity fraction

$X$  : neck size

$R$  : powder particle diameter

As can be seen from studies of both Xu et al. [139] and Krasulin et al. [142] studies a linear relation is expected between strength and square of neck size ratio,  $(X/R)^2$ .

In a recent study, Mizusaki et al. [143] used a model in which electrical conductivity is described in terms of densification during sintering of porous ceramic green ware. In another work, Mukhopadhyay and Phani [144] used the same model for developing a relationship between the normalized minimum contact area fraction of solid and Young's modulus of porous ceramics. Then, they [145] tried to find out a relation between normalized ultrasonic velocity ( $v/v_o$ ) and the volume fraction of pores of some ceramic systems based on minimum solid area of contact model.

These models predict the change in the relative density,  $\rho/\rho_{th}$ , with the progressive sintering. The thickening of the neck area is formulated using two sine-wave functions. The model considers the gradual change in the minimum solid area of contact between neighboring grains with the progress of densification for an idealized simple cubic arrangement of equivalent spheres, Figure 2.32. The final shape of the three dimensional array of spheres turn into a rod of diameter  $a_f$  as shown below,

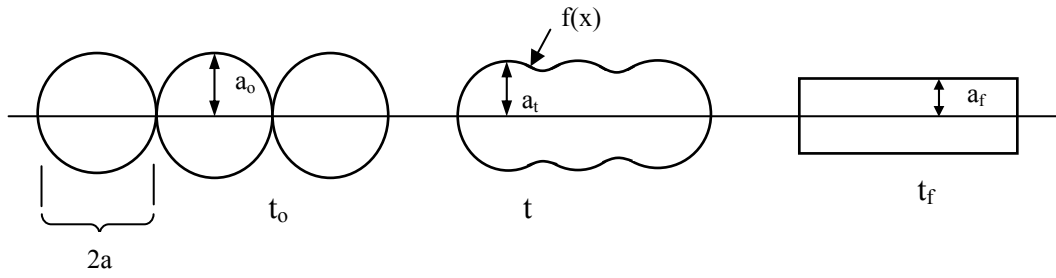


**Figure 2.32** Proposed model for the calculation of the relationship between relative density and relative property [143].

The volume of such string of spheres with a contour is expressed by a sine-wave function with a period  $2a$ . Then, the volume of the rod for one period,  $V_a^0$ , is given by,

$$V_a^0 = \int_0^{2a} \pi a_t^2 dx = 2\pi a_t^2 a \quad (2.31)$$

Then relative density can be obtained as;

$$\rho/\rho_{th} = V_a/V_a^0 = \int_0^{2a} \left[ \frac{f(x)}{a_t} \right]^2 dx \quad \text{where,} \quad -1 \leq (f(x)/a_t) \leq 1 \quad (2.32)$$

Change in the shape of the neck area between two particles during sintering, Figure 2.33, has been modeled by a combination of two sine-wave functions;

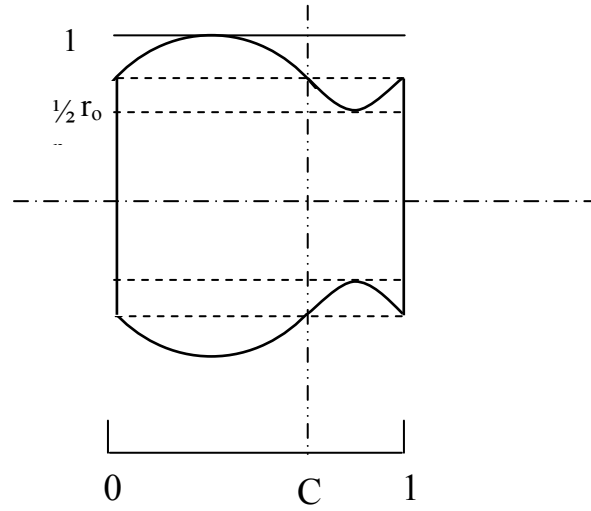


**Figure 2.33** Sine-wave functions for the approximations of a partially deformed sphere and the developing neck area between two neighboring spheres during sintering [144].

In the above figure,  $r_0$  stands for the ratio of the minimum diameter at the neck to the maximum diameter of the rotating body. When defined sine-wave functions for  $0 \leq x \leq C$  and  $C \leq x \leq 1$  are inserted into relative density equation, one can obtain;

$$\rho/\rho_{th} = [a^2 - (4ab/\pi 4 + (b^2/2) + (8abc/\pi 8)] \quad (2.33)$$

where,  $a = (1+r_0)/2$  and  $b = (1-r_0)/2$

The minimum contact area (MCA) in the above figure is found at  $x = (1+C)/2$ . Then, MCA becomes,

$$MCA = (\pi\pi/4)_1^2 r_0^2 \quad (2.34)$$

Normalized minimum contact area (NMCA) can be found dividing the MCA equation by its value at fully sintered condition ( $r_0 = 1$ ), then  $NMCA = r_0^2$ . Finally,

$$NMCA/P = \left[ \frac{r_0^2}{l} \right] \left\{ 1 - \left[ a^2 - (4ab/\pi 4 + (b^2/2) + (8abc/\pi 8) \right] \right\} \quad (2.35)$$

where, P is the porosity fraction and can be represented by  $1 - \rho/\rho_{th}$ .

### 2.6.2.2.3. Gibson and Ashby Model

Another specific MSA model purposed by Gibson and Ashby [2,3] used a simple bending strut model and they derived elastic moduli and collapse strength formula of foams considering both open and closed cell morphology.

#### 1. Open Cellular Foam

##### 1.1. Linear Elasticity

Open cells are modeled as cubic array, Figure 2.34, having length l and square cross-section of t as shown below,

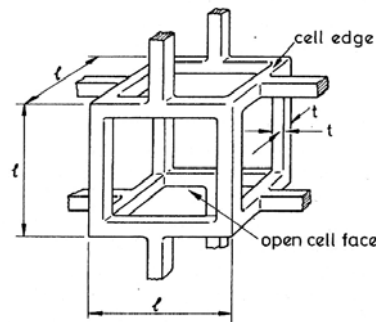


**Figure 2.34** A cubic model for an open-cell foam [3].

When a foam is loaded, the cell walls bend causing struts to deflect by  $\delta$ , which may be calculated according to beam theory as

$$\delta = \frac{CF.I^3}{12E_s.I} \quad (2.36)$$

Where C is a resolution factor dependent on the details of cell geometry,  $E_s$  is Young's modulus of the cell strut material, F is the force acting on the cell wall, and I is the second moment of area of cell wall. The Young's modulus of the cellular material ( $E^*$ ) was found to be;

$$\frac{E^*}{E_s} \cong \left(\frac{t}{l}\right)^4 \quad (2.37)$$

And the relative density  $\left(\frac{\rho^*}{\rho_s}\right)$  is given by;

$$\frac{\rho^*}{\rho_s} \cong \left(\frac{t}{l}\right)^2 \quad (2.38)$$

where  $\rho^*$  is the density of the foam and  $\rho_s$  is the density of cell strut material. Combining Equations 2.37 and 2.38 Gibson and Ashby [3] obtained Young's Modulus of cellular material as [2, 5, 146-148];

$$\frac{E^*}{E_s} = C_1 \left(\frac{\rho^*}{\rho_s}\right)^2 \quad (2.39)$$

where,  $C_1$  is a geometric constant dependent on the geometry of the micro-mechanical model used and it is generally taken as one.

The mechanical properties of foam samples differ in tension and compression testing. Before cell edge buckles upon axial loading, axial load exerts an additional moment on the bent edge. In compression this beam-column

interaction lowers the modulus. Part of the stress-strain curve is not truly elastic, but is concave downwards and Young's modulus is smaller in compression than tension.

## 1.2. Plastic Collapse and Densification

The long stress plateau is exploited in foams for crash protection and energy-absorbing systems. Plastic collapse in an open-cell foam occurs when the moment exerted on the cell walls exceeds the fully plastic moment creating plastic hinges, Figure 2.35. Plastic collapsing of closed cell foams is more complicated because plastic collapse load may be affected by the stretching as well as the bending of the cell walls, and by the presence of a fluid within the cells.

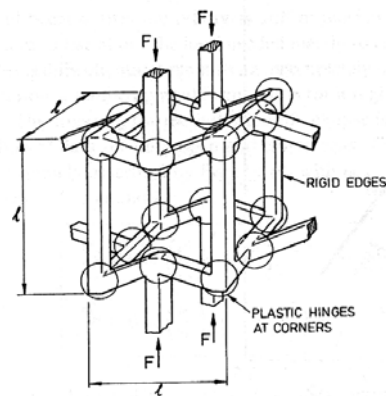


**Figure 2.35** The formation of plastic hinges in open-cell foam [3].

The plastic collapse stress,  $\sigma_{pl}^*$  is found by equating the applied moment,  $M$ , on a strut from a transverse force  $F$  to the plastic moment,  $M_p$ , required to form plastic hinges:

$$M \propto F.l \propto \sigma_{pl}^*.l^3 \quad (2.40)$$

$$M_p \propto \sigma_{ys}t^3 \quad (2.41)$$

Giving

$$\frac{\sigma_{pl}^*}{\sigma_{ys}} \propto \left(\frac{t}{l}\right)^3 = C_3 \left(\frac{\rho^*}{\rho_s}\right)^{3/2} \quad (2.42)$$

where,  $\sigma_{ys}$  is the yield strength of the solid cell wall material and  $C_3$  contains all of the constants of proportionality and it is found to be 0.3 from experimental data analysis. In a similar manner brittle crushing strength is found as [2, 3, 146-148];

$$\frac{\sigma_{cr}^*}{\sigma_{fs}} = C_4 \left(\frac{\rho^*}{\rho_s}\right)^{3/2} \quad (2.43)$$

where,  $\sigma_{fs}$  is the modulus of rupture of the solid cell wall material. By experimental data evaluation  $C_4$  is found as ~0.2.

## 2. Closed-Cellular Foam

### 2.1. Linear Elasticity

In closed cell foams, stretching of the cell faces also contributes to the mechanical response. The contribution of the faces to the overall mechanical response depends on the fraction of the solid in the faces.

In Gibson and Ashby theorem closed-cell structure is considered to contain  $\phi$  fraction of solid in the cell edges, and the remaining solid fraction  $(1- \phi)$  is in the faces which have a thickness  $t_f$ . Young Modulus of closed cell structures were calculated considering three effects: cell edge bending, compression of the cell fluid and membrane stresses in the cell faces.

Since cell faces are thin the bending stiffness of them is usually not very important. When we consider cell edge bending, its contribution to modulus can be calculated as above for open cellular materials by factor of  $\phi \cdot C_1 \cdot \left(\frac{\rho^*}{\rho_s}\right)^2$ .

The closed cells in materials may contain air, liquid or a gas. As the volume of the cell decreases during compression, the pressure of the enclosed gas within the cells increases according to the ideal gas law, contributing to the overall stress required to deform the foam. If the foam material having a gas is compressed axially by a strain  $\varepsilon$ , then the contribution of the gas to the elastic modulus,  $E_g^*$  of the foam is:

$$E_g^* = \frac{dp'}{d\varepsilon} = \frac{p_0(1-2v^*)}{(1-\rho^*/\rho_s)} \quad (2.44)$$

When  $p_0$  is atmospheric pressure its contribution is small. If the cell fluid is a liquid, then the contribution cannot be neglected since incompressible response of the fluid requires additional cell wall stretching.

When a compressive load is applied cell edges deflect by amount of  $\delta$ , Figure 2.36 and work  $(1/2.F.\delta)$  is done against the restoring force caused by cell edge bending and face stretching.

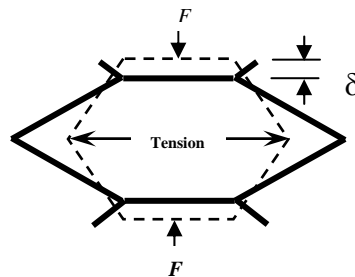


**Figure 2.36** Stretching of the faces of closed-cell foam in compression [3].

Cell edge bending is proportional to  $\frac{1}{2}S\delta^2$  and face stretching is proportional to  $\frac{1}{2}E_s\varepsilon^2V_f$

where ,

S: stiffness of the cell edge ( $S \propto E_s I/l^3$ )

$\varepsilon$ : strain caused by stretching of cell face ( $\varepsilon \propto \delta/l$ )

$V_f$ : volume of the solid in a cell face ( $V_f \propto l^2 t_f$ )

$t_f$  : thickness of the cell face

$$\frac{1}{2}F\delta = \frac{\alpha E_s I \delta^2}{l^3} + \beta E_s \left(\frac{\delta}{l}\right)^2 l^2 t_f, \quad (I \propto t_e^4 \text{ and } E^* \propto (F/l^2)/(\delta/l)) \quad (2.45)$$

$$\frac{E^*}{E_s} = \alpha \frac{t_e^4}{l^4} + \beta \frac{t_f}{l} \quad (2.46)$$

Then, the equation describing both cell-edge bending and cell-face stretching;

$$\frac{E^*}{E_s} = C_1 \varphi^2 \left(\frac{\rho^*}{\rho_s}\right)^2 + C_1' (1-\varphi) \frac{\rho^*}{\rho_s} \quad (2.47)$$

where,  $C_1$  and  $C_1'$  are proportionality constants and they are usually taken as 1.

Finally, elastic modulus of closed cells, including membrane stresses and gas pressure can be described by,

$$\frac{E^*}{E_s} = \varphi^2 \left(\frac{\rho^*}{\rho_s}\right)^2 + (1-\varphi) \frac{\rho^*}{\rho_s} + \frac{\rho_0(1-2\nu^*)}{E_s(1-\rho^*/\rho_s)} \quad (2.48)$$

To conclude,  $\phi$  is the volume fraction of the solid contained in the cell edges and the remaining fraction  $(1-\phi)$  is in the face and  $\nu^*$  is the Poisson's ratio.

The parameter  $\phi$  is defined as a distribution constant and it is bounded by;

$$\frac{\rho^*}{\rho_s} \leq \phi \leq 1 \quad (2.49)$$

The first term in Equation 2.48 is the contribution of cell edge bending while the second contribution is from membrane stresses in the cell faces. The third is that caused by the compression of the cell fluid. When the initial  $P_0$  is the atmospheric pressure (0.1 MPa) the third term can be neglected since its contribution is small. [2, 3, 146-148]

## 2.2. Plastic Collapse and Densification

Closed cells have membranes spanning their faces. Plastic collapse causes the membranes to crumple in the compression direction. Since membranes are thin, the force required to crumple them is small. In the right angles to compression axis, membranes are stretched as shown Figure 2.37, and the plastic work required to extend them contributes to the yield strength of the foam.

When a compressive load of  $F$  is applied, work is done by the plastic displacement of  $\delta$ . The angle of rotation at the four plastic hinges is then proportional to  $\delta/l$ , and the plastic work done at these hinges is proportional to  $M_p \delta/l$ . The cell face is stretched by a distance, which is again proportional to  $\delta$  and the work done is  $\sigma_{ys} \delta t_f l$ . Then;

$$F\delta = \alpha M_p \frac{\delta}{l} + \beta \sigma_{ys} \delta t_f l \quad (2.50)$$

where  $\alpha$  and  $\beta$  are constants, and  $F = \sigma l^2$ ,  $M_p = \sigma_{ys} t_e^3/4$

$$\frac{\sigma_{pl}^*}{\sigma_{ys}} = \frac{\alpha}{4} \left( \frac{t_e}{l} \right)^3 + \beta \left( \frac{t_f}{l} \right) \quad (2.51)$$

where,  $\frac{t_f}{l} = 1.4(1-\phi) \frac{\rho^*}{\rho_s}$  and  $\frac{t_e}{l} = 0.93\phi^{0.5} \left( \frac{\rho^*}{\rho_s} \right)^{0.5}$

Then, we obtain;

$$\frac{\sigma_{pl}^*}{\sigma_{ys}} = C_5 \left( \phi \frac{\rho^*}{\rho_s} \right)^{3/2} + C_5' (1-\phi) \left( \frac{\rho^*}{\rho_s} \right) \quad (2.52)$$

When  $\phi = 1$  (open cells),  $C_5=0.3$ , and in the other limit of  $\phi = 0$ ,  $C_5'=1$ . If there is a fluid in the cells, its contribution must be added to above equation. If the cell fluid is a gas at atmospheric pressure the contribution is small since  $\sigma_{ys} \gg p_{atm}$ . But if the cells contain fluid at a pressure  $p_0$  much larger than atmospheric, this pressure must be added.

$$\frac{\sigma_{pl}^*}{\sigma_{ys}} \approx 0.3 \left( \phi \frac{\rho^*}{\rho_s} \right)^{3/2} + (1-\phi) \frac{\rho^*}{\rho_s} + \frac{p_0 - p_{atm}}{\sigma_{ys}} \quad (2.53)$$

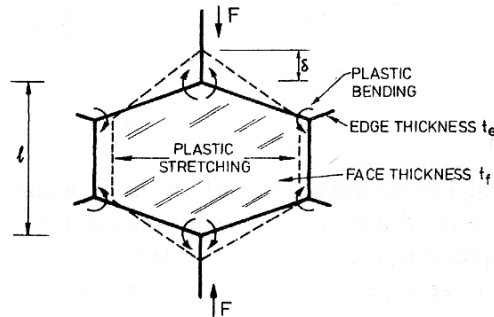


**Figure 2.37** Plastic Stretching of the cell faces of a closed-cell foam [3].

One needs to note that Gibson and Ashby's model is generally good for cellular materials of relatively high porosity, typically above 70 %.

#### 2.6.2.2.4. Stress Concentration Models

As MSA models stress concentration approach is also based on idealized geometries and their generalization. Both stress concentration and minimum solid area concepts are normally applied to idealized regular arrays of identical shape and oriented particles, pores, or both. The solid load bearing area clearly plays a basic role in not only mechanical but all physical properties. Stress concentrations may play a role only in mechanical properties [107].

Rossi [149] modified Hashin's [150] equation for predicting Young's Modulus of porous ceramics as a function of concentration of spherical pores at low values;

$$E = E_0(1 - np) \quad (2.54)$$

Rossi's modification was based on the observation that coefficient 'n' partially reflected the stress concentration associated with spheres, Figure 2.38 and he calculated it as  $n \cong 5a/4c + 3/4$ .

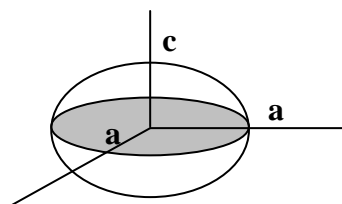


**Figure 2.38** Pore shape used in Rossi's Modification [107].

As previously stated Balshin [127] proposed an empirical relation to describe the variation of property with the porosity as follows;

$$M = M_o (1 - p)^m \quad (2.55)$$

where,  $m$  is the empirical constant and it depends on the materials and the fabrication method. The exponent  $m$ , originally purposed as an empirical constant, has recently been identified as the stress concentration factor originated at the pores.

Boccaccini et al. [151] used this equation to define the strength and suggested that this empirical constant  $m$  is related to stress concentration around the pores and called it  $K$  [114]. The stress concentration factor depends on pore geometry, its orientation relative to loading direction and elastic constants of material under consideration. It was stated that for uniaxial stresses, the maximum stress concentration factor, which occurs at the pore boundary, was identified as the key parameter in predicting the mechanical property, i.e., Young's modulus and fracture strength and it is expressed by;

$$K = \frac{\sigma_{\max}}{\sigma} \quad (2.56)$$

where  $\sigma_{\max}$  is the maximum value of the stress and can be defined under tensile loading by the following equation for an elliptical pore having radius parameters of  $a$  and  $b$  [152], Figure 2.39;

$$\sigma_{\max} = \sigma \left(1 + 2 \frac{a}{b}\right) \quad (2.57)$$

When cylindrical pores are oriented perpendicular to the loading direction parameter 'a' becomes equal to 'b', so that value of  $K$  approaches 3. If cylindrical pores aligned parallel to the tensile direction, since  $b$  becomes infinite, the value of  $K$  approaches unity. In this case, reduction of mechanical properties is only due to

reduction of load-bearing area and mechanical property follow MSA model predictions. For spherical pores the theoretical stress concentration factor is 2.

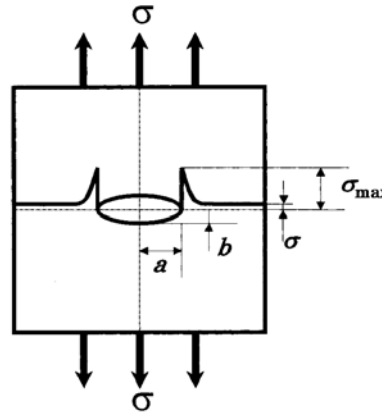


**Figure 2.39** Stress concentration in the vicinity of elliptical pores under tensile loading [114].

This concept was used to predict the strength of porous ceramics containing dilute (non-interacting) porosity when the pores are identified as the fracture origin. Interactions between neighboring pores at high-porosity volume fractions were found to make the stress concentration calculations unsuitable [140].

Rice [141] suggested that pore-stress concentration effects on the mechanical property-porosity relation are rather limited and three sets of arguments have been presented to show these limitations:

- 1) variable nature of stress concentrations for isolated pores
- 2) the interactive nature of stress concentrations as porosity increases so pores are no longer isolated
- 3) interactions of pores and cracks

Rice [141] has calculated that at porosity values as low as 5-10 %, interactions between pores begin to be of concern and minimum surface to surface

spacing between pores must be at least  $\sim 1$  pore diameter for these to be considered isolated.

It was stated that in dilute concentrations of pores stress concentrations of individual pores were clearly defined. Such stress concentrations vary in their limits with pore shape and the orientation of such shapes relative to the stress axis, as well as around the pore. They also vary with the nature of the stress and with the proximity of the pore to the surface. A summary of the limiting stress concentrations for cylindrical pores (perpendicular to the loading direction) and spherical pores for different state of stress in polar (P) and equatorial (E) directions (Figure 2.40) is presented in Table 2.8.

**Table 2.8** Maximum stresses on spherical and cylindrical pores [141].

	Spherical pore	Cylindrical pore
Uniaxial tension	$\sim 2$ (E)	3(E); 1(P)
Uniaxial compression	-1 (P)	-1(P)
Bi-axial tension	-	2(P); 2(E)
Bi-axial comp./tension	-	4(P); 4(E)

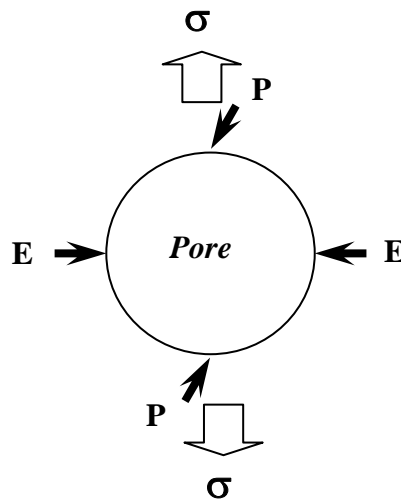


**Figure 2.40** Locations of the maximum stresses during tension [141].

As can be seen, stress concentrations decrease when going from homogenous uniaxial tension to homogenous uniaxial compression. In fact, there is no concentration of the compressive stress for spherical pores; instead of a localized tensile stress whose maximum equals the value of the applied compressive stress appears.

Rice [141] also showed that most stress concentrations decrease with increasing number of pores and decreasing pore spacing (non-dilute porosity, i.e.  $p > 10\%$ ). However, three-dimensional elasticity for the interaction effect of neighboring cavities show that stress concentrations around a pore may increase by proximity of a second pore for porosities higher than 40%.

On the other hand, for pore-crack interactions relative size of cracks and pores are important. If the pore and crack sizes begin to approach one another, stress-concentration effects from pores will become more significant. If the cracks act as the fracture origin, the effect of pore stress-concentration will be decreased. Then, stress-concentration approach becomes invalid for mechanical property reduction [140].

## CHAPTER 3

### EXPERIMENTAL PROCEDURE

#### 3.1. Materials Used

Starting powders were gas atomized spherical titanium and Ti-6Al-4V alloy powders distributed in the range of 45 to 150  $\mu\text{m}$  with a mean diameter of 74  $\mu\text{m}$  and 107  $\mu\text{m}$ , respectively. Although the spherical Ti-6Al-4V alloy powders follow the log-normal (Gaussian) distribution, pure titanium powders exhibit bi-modal distribution, Figure 3.1 (a) and 3.1 (b). Moreover, angular Ti-6Al-4V alloy powders having a size of -200 mesh ( $<74 \mu\text{m}$ ) with an average particle size of 54  $\mu\text{m}$  were also used in foaming experiments. Titanium and Ti-6Al-4V powders shown in Figure 3.2 (a), 3.2 (b) and 3.2 (c) were conforming to ASTM F 1580-01 specifications designed for coating of surgical implants, Table 3.1, and supplied from Phelly Materials. Magnesium powder with 99.8 % purity supplied from Alfa-Aesar with a particle size between -20+100 mesh was used as a spacer particle. Prior to foaming experiments sieving was performed to obtain magnesium powders in the limited range of 425-600  $\mu\text{m}$ . However, particle size analyses of magnesium powders revealed a wide range of distribution (300-1500  $\mu\text{m}$ ) with an average particle size of 660  $\mu\text{m}$ ., Figure 3.1 (d). Presence of some highly elongated (ligamental) powders is the main reason of the powders sieved from mesh openings smaller than the particle size. As a binder and lubricant to reduce the friction between the powders and powder/die surface PVA (Poly vinyl alcohol) solution (2.5 %<sub>w</sub> PVA([ -CH<sub>2</sub>CHOH- ]<sub>n</sub>) + water) prepared using a magnetic stirrer was added to some of the powders and powder mixtures.

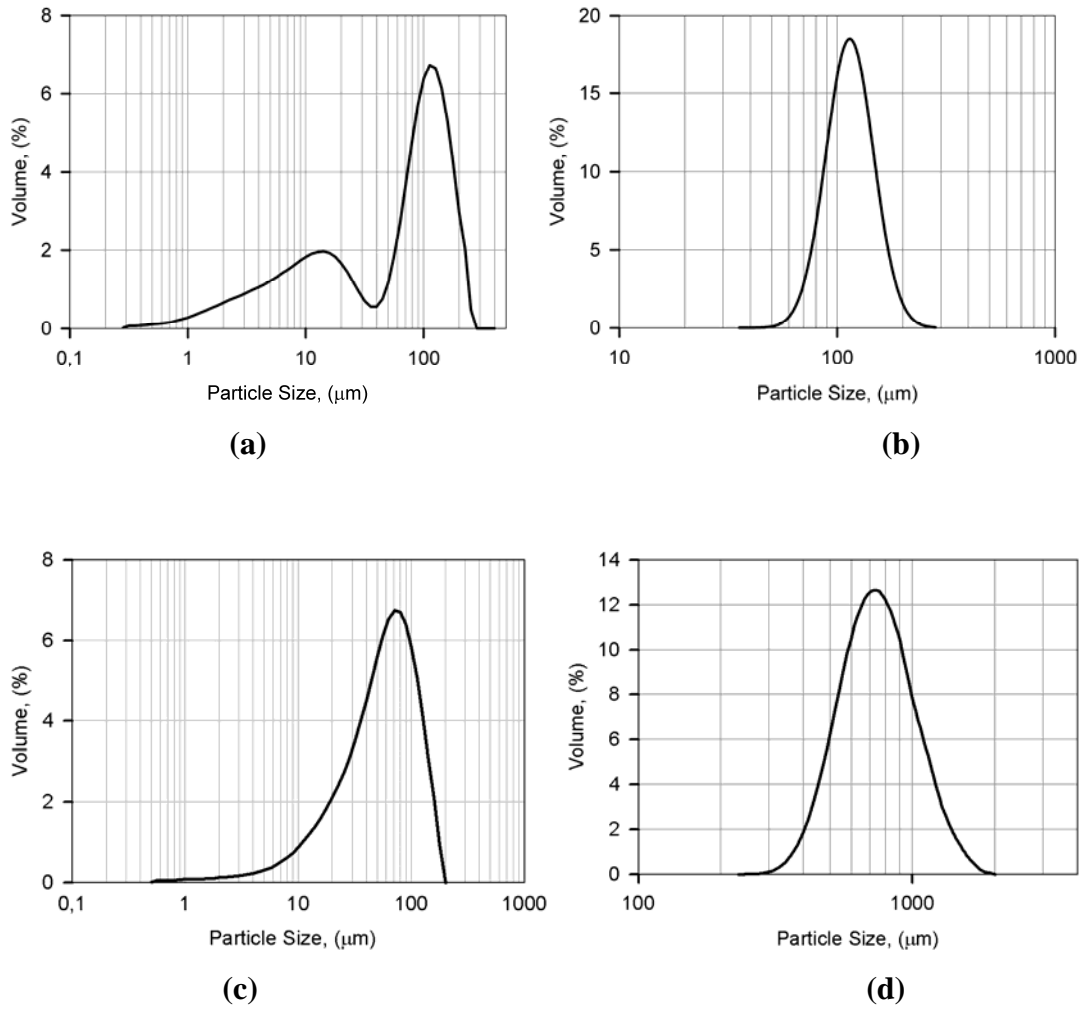


**Figure 3.1** Partical size distribution of the powders used; (a) Spherical titanium, (b) Spherical Ti-6Al-4V, (c) Non-Spherical Ti-6Al-4V, (d) Rounded Magnesium.

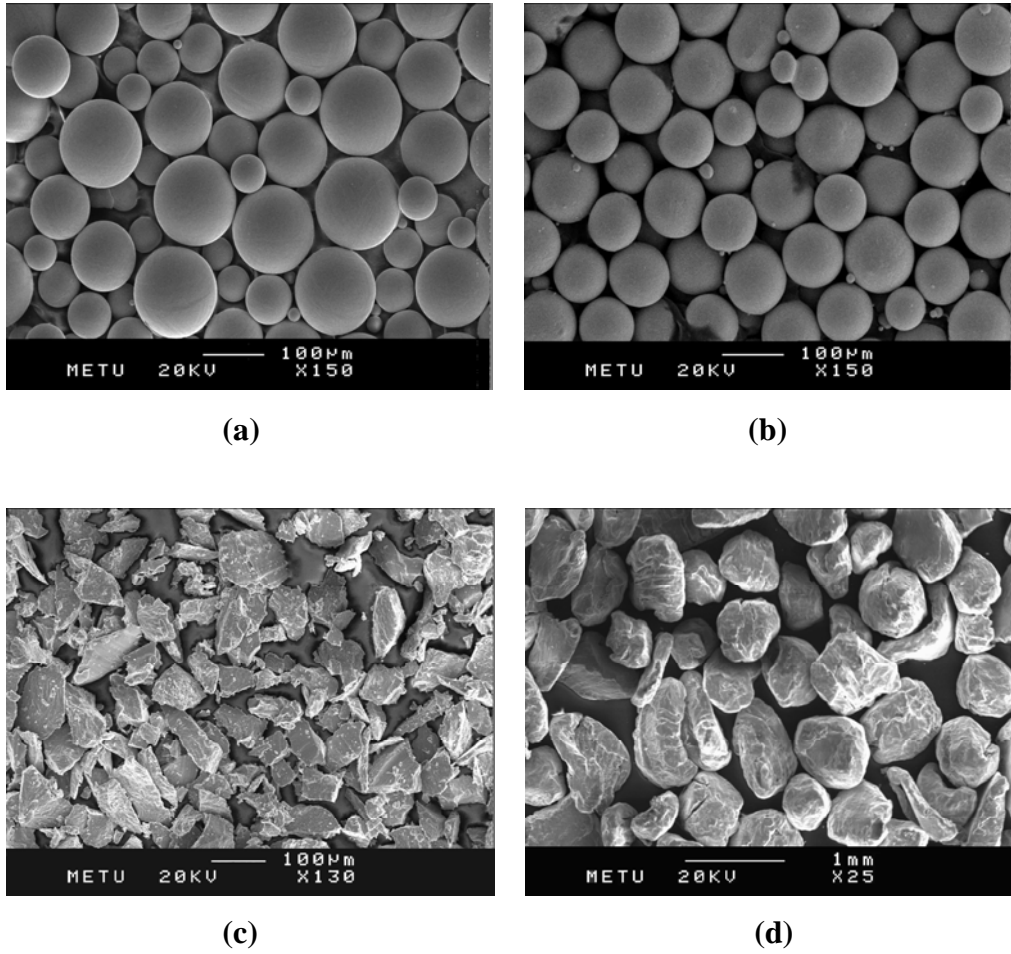


**Figure 3.2** Powders used in experiments; (a) Spherical titanium, (b) Spherical Ti-6Al-4V, (c) Angular Ti-6Al-4V, (d) Rounded magnesium.

**Table 3.1** ASTM 1580-01 Standart Specification [153] (Chemical requirements).

Element	Unalloyed Ti Powder, (wt. %)		Ti-6Al-4V Powder, (wt. %)	
	Min	Max	Min	Max
Al			5.50	6.75
V			3.50	4.50
O		0.40		0.20
Fe		0.50		0.30
C		0.10		0.08
H		0.05		0.015
N		0.05		0.05
Cu				0.10
Sn				0.10
Si		0.04		
Cl		0.20		
Na		0.19		
Ti		Balance		Balance

Bulk Ti-6Al-4V-ELI (extra low impurity) alloy in the form of round bars with 18.0 mm diameter conforming to ASTM F136-98 standart (Table 3.2) with beta transus temperature of 974.9°C has been used to compare the microstructure and mechanical properties of bulk alloy with that of porous Ti-6Al-4V alloys. As recieved alloy had an alpha+beta microstructure obtained as a result of air cooling subsequent to one hour annealing at 730°C.

**Table 3.2** ASTM F136-98 Standart [154], (Chemical requirements) and composition of the corresponding alloy.

Chemical Composition, (wt. %)							
	C	V	Al	O	N	H	Fe
Min.		3.50	5.50				
Max.	0.08	4.50	6.50	0.13	0.05	0.012	0.25
Result	0.01	4.10	6.20	0.10	0.01	0.004	0.06

### 3.2. Experimental Technique

Three different production techniques, namely; loose powder sintering (no pressure), cold compaction and sintering and space holder method were used to get desired level of porosity and pores of various size and morphologies in both pure titanium and Ti-6Al-4V alloys.

#### 3.2.1 . Loose Powder Sintering

For loose powder sintering (sintering with no prior compaction), 30 mm long and 5.6 mm diameter cylindrical Quartz crucibles have been used to fill the spherical powders in under vibration until tap density is attained. Use of quartz crucibles and the absence of compaction eliminated the density variations caused due to die wall friction and it was also eliminated the use of binders, which may detoriate the powder. Samples of both pure titanium and Ti-6Al-4V alloys were sintered for one

hour under high purity argon gas atmosphere. While pure titanium powders were sintered at 850, 950, 1000 and 1050°C, which correspond to both below and above the  $\alpha/\beta$  transition temperature of 882°C, sintering of Ti-6Al-4V alloy powders has been carried out at 1000, 1050, 1100, 1150, 1200 and 1250°C corresponding to around and above the  $\alpha/\beta$  transition temperature of  $1000 \pm 20^\circ\text{C}$ . Maximum applicable sintering temperatures were limited by the reactivity of titanium and Ti-6Al-4V powders with the quartz crucibles. A thin layer of dark gray reaction product having composition of 1.1 %<sub>w</sub> Si and 98.9 %<sub>w</sub> Ti as determined from EDS analyses was observed to appear on the crucible wall with increasing sintering temperatures.

### **3.2.2 . Cold Compaction and Sintering**

Conventional cold compaction and sintering experiments were conducted to study the conditions for lower porosity levels and especially to simulate the cell wall structure that exists in specimens prepared by space holder method.

5 wt. % PVA (poly vinyl alcohol) solution (2.5 wt. % PVA ( $[-\text{CH}_2\text{CHOH}]_n$ )+water) added spherical titanium and Ti-6Al-4V powders were compacted at different pressures, Table 3.3, using 30 tons capacity manual hydraulic press. Cold pressing of cylindrical compacts with 10 mm. diameter and 7-8 mm height was conducted using double-ended compaction technique to minimize density gradients. Die wall frictions causing a density gradient along the sample height limited the H/D ratio of samples to 0.7-0.8. Prior to heating to sintering temperature, samples were kept at 600°C for one hour for complete dissolution and removal of PVA solution. Compacts heated to sintering temperature of 1200°C in 45 min were sintered for one hour.

**Table 3.3** Compaction pressures applied to spherical titanium and Ti-6Al-4V powders prior to sintering at 1200°C.

Powder Type	Compaction Pressure, (MPa)				
	120	375	510	750	1125
Spherical Titanium	✓	✓	✓	✓	-
Spherical Ti-6Al-4V	-	✓	✓	✓	✓

Additionally, to see the enhancement of densification with sintering temperature, spherical titanium and Ti-6Al-4V powders wetted with 5 wt. % PVA solution and compacted at pressures of 750 and 1125 MPa, respectively, were sintered for one hour under high purity argon gas at about 1310°C subsequent to binder removal at 600°C for one hour.

### 3.2.3. Space Holder Method

Production steps involved in space holder technique are summarized in Figure 3.3. To obtain homogenous titanium or Ti-6Al-4V-magnesium powder mixtures by cold pressing, PVA solution was added to cover the surfaces of magnesium powders prior to compaction. This facilitated homogenous attachment of titanium powders on spacer magnesium powders. In general, the quantity of binder added to powder mixture depends primarily on the relative amount of magnesium. As the volume percent of magnesium powder in mixture increases, the amount of binder needed to cover all the powder surfaces also increases. However, in the present study, the weight percent of PVA solution was kept at about 5 wt. % in all powder mixtures. PVA solution not only aids to bind powder particles together, but also acts as a lubricant, which reduces the friction between particles as well as at the particle/die wall surface. In the second step of production, different quantities of

titanium or Ti-6Al-4V powders (either spherical or angular) were added to PVA coated magnesium powders. Then the powders were mixed together for 30 min to ensure homogenous titanium/Ti-6Al-4V agglomerate formation on magnesium powders. Size and shape of the powder to be coated on magnesium directly affect the final structure of the foam and determine the maximum achievable porosity levels together with the maximum magnesium content in investigated systems. Third step involved the powder compaction for shaping and to enhance the subsequent densification. Finally, sintering has been done at elevated temperatures after binder removal below the melting point of magnesium (650°C).

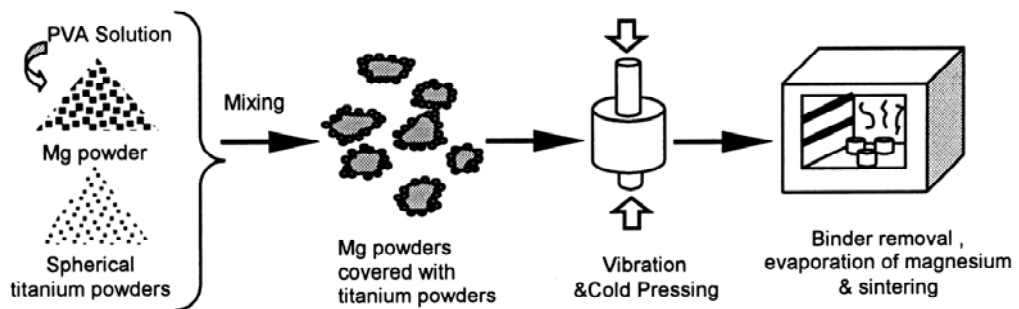


**Figure 3.3** Schematic representation of space holder technique.

Prior to production of cellular titanium and Ti-6Al-4V using space holder technique summarized in Figure 3.3, preliminary experiments had been conducted to investigate the effect of parameters such as compaction pressure and sintering temperature on porosity content and properties of the samples and to determine their optimum values. In addition, to reveal the evaporation behavior of magnesium some preheating experiments were done for one hour at various temperatures using spherical titanium and magnesium powder compacts containing 60 vol. % magnesium, Table 3.4.

**Table 3.4** Parameters investigated in preliminary space holder method studies.

Compaction Pressure, (Mpa)	83	255	510	765	-
Sintering Temperature, (°C)	1150	1200	1250	1300	-
Preheating Temperature (°C)	600	650	700	800	900

Figure 3.4 shows the evaporation data obtained from the magnesium powder containing compacts (Ti-60 vol. % Mg) used in the experiments and the vapor pressure data collected from literature. As can be seen, at 600°C, which is below the melting point of magnesium only ~1.8 vol. % evaporation takes place. As passing through the melting point (650°C) fraction evaporated increases sharply to 17 vol. % and reaches to 43 vol. % at a preheating temperature of 900°C. Observed collapse of the compacts directly sintered at higher temperatures is believed to be mainly due to combined effect of melting and sudden evaporation of the space holder. It is thought that the collapse of the samples may be prevented if some of the magnesium could be removed below the melting point or the powder mixture could be compacted at very high pressures. The latter is found to be technically unfeasible due to distortion of both the spacer and titanium particles. In experiments it was seen that the collapse of low pressure compacted samples may be prevented by waiting at temperatures near the melting point of magnesium (600°C) long enough to allow evaporation of some magnesium slowly.

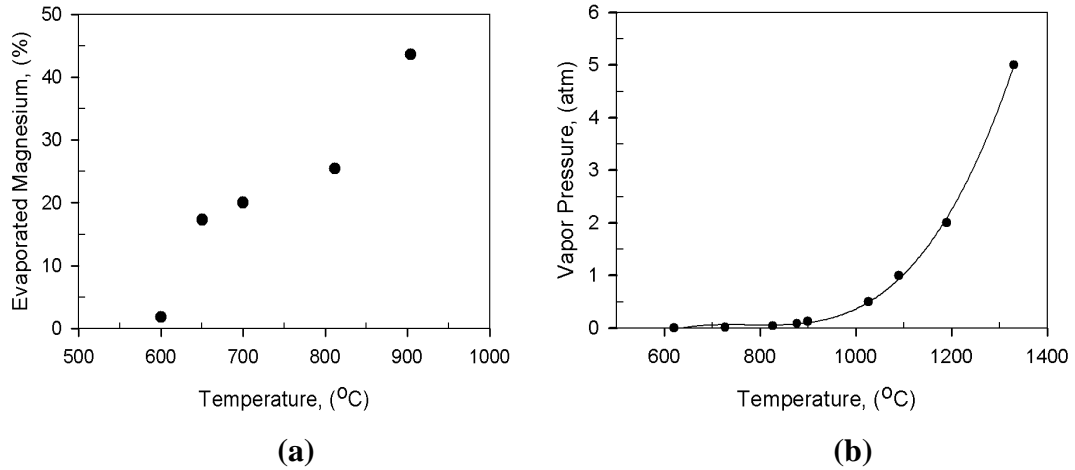


**Figure 3.4** Evaporation behavior of magnesium, (a) percentage of magnesium evaporated during experiments, (b) Vapor pressure data collected from literature.

The effect of compaction pressure on final porosities is presented in Figure 3.5 (a) for Ti-60 vol. % Mg powder mixtures sintered at 1200°C for one hour after holding at 600°C for one h. The resulting porosity contents were between 60.8-65.3 vol. %, which were higher than the amount of magnesium powder in the mixture because of the additional porosity present in the cell walls due to incomplete sintering of titanium powders. Lower compaction pressures (83 and 255 MPa) caused subsequent collapse and non-homogenous shrinkage throughout the sample, whereas very high compaction pressures (765 MPa) deformed magnesium powders plastically and resulted in smearing of magnesium on the surface of compact. Based on these observations, 510 MPa has been chosen as the optimum pressure for compaction of Ti-60 vol. % Mg powder mixture.

Sintering temperature is more effective than the time in obtaining denser compacts. As shown in Figure 3.5 (b), Ti-60 vol. % Mg samples compacted at 510 MPa and then sintered for one hour at temperatures between 1150 and 1300°C revealed porosity content in the range of 61.7 and 62.6 vol. %. Further shrinkage could not be achieved by sintering above 1250°C. Considering the high oxygen affinity of titanium and Ti-6Al-4V alloy at high temperatures and the total heating time to high temperatures, optimum sintering temperature was determined as 1200°C.

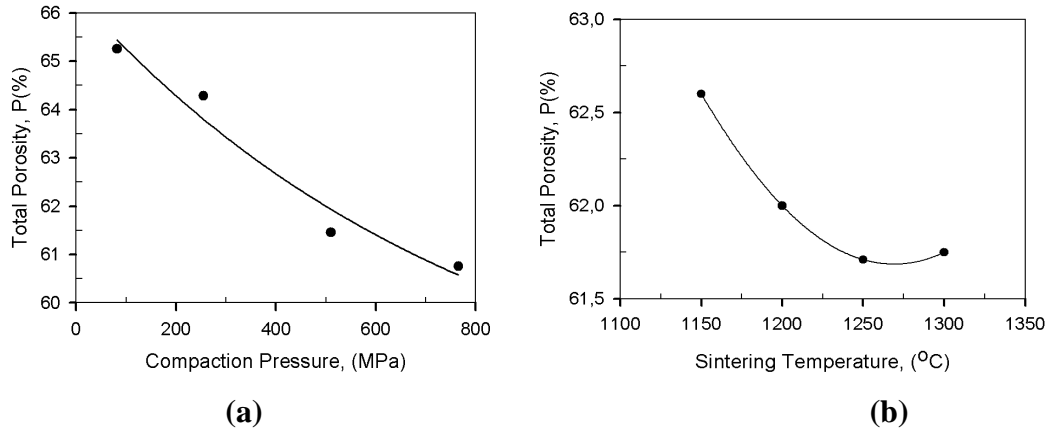


**Figure 3.5** Total porosity change in Ti-60 vol. % Mg compacts, (a) with compaction pressure, (b) with sintering temperature.

Based on the preliminary studies, titanium or Ti-6Al-4V-magnesium powder mixtures prepared with magnesium content in the range 30 to 90 vol. %, Table 3.5, were then cold pressed at 510 MPa in a double-ended die to obtain compacts 10 mm in diameter and 7-8 mm in height. Initially, the compacts were heated to 600°C (below the melting point of Mg, 650°C) with a heating rate of ~50°C/min and held at that temperature for one hour to remove PVA solution and to acquire sufficient strength by sintering to prevent the subsequent collapse of the compacts during melting and evaporation of magnesium. Afterwards, binder removed samples were heated with a rate of 15-20°C/min to the sintering temperature of 1200°C, which is above the boiling point of magnesium, 1090°C. Holding at that temperature for one hour allowed to evaporate and remove all magnesium and resulted in full strengthening of the compacts by sintering.

**Table 3.5** Prepared Ti/Ti-6Al-4V powder mixtures.

POWDER TYPE	MAGNESIUM CONTENT, VOL ( %)						
	30	40	50	60	70	80	90
Spherical Titanium	-	✓	✓	✓	✓	✓	-
Spherical Ti-6Al-4V	✓	✓	✓	✓	✓	-	-
Angular Ti-6Al-4V	-	-	✓	✓	✓	✓	✓

In addition to powder sintering and foaming experiments, bulk Ti-6Al-4V-ELI Alloys were cooled slowly (8°C/min) after betatizing at 1020°C for one hour to simulate the microstructure in porous alloy samples.

### 3.3. Experimental Set-up

Preliminary sintering studies were started with pure titanium and Ti-6Al-4V compacts under argon gas. Visual inspections after sintering at 600°C and 900°C revealed dark, violet and black colored components identified as various oxides, on the surfaces and even in the interior regions of the compacts, Figure 3.6.

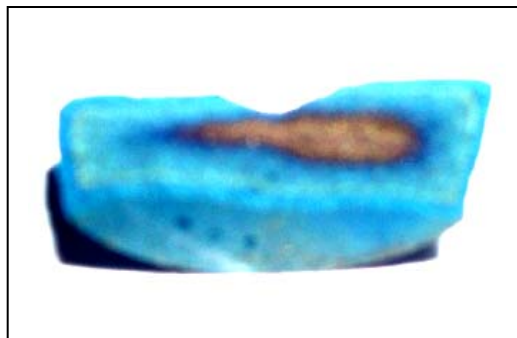


**Figure 3.6** Cross-section of oxidized titanium during sintering.

Titanium is a very reactive metal and form various oxides such as TiO, TiO<sub>2</sub>, Ti<sub>2</sub>O<sub>3</sub> and Ti<sub>3</sub>O<sub>5</sub> as can be seen in Appendix A. Based on observations involving physical properties, titanium oxides formed on the samples in the present study was concluded to be TiO, Ti<sub>2</sub>O<sub>3</sub> and Ti<sub>3</sub>O<sub>5</sub>. Prevention of oxidation was one of the main concerns of the present study, which involved sintering temperatures as high as 1200°C. For this purpose, oxygen partial pressure in the sintering atmosphere should be reduced to below 10<sup>-24</sup> atm and this is not attainable physically by vacuum systems. As an alternative, using hydrogen gas as a reducing agent as in the case of conventional sintering of some copper alloys is found not to be applicable due to extensive solubility of hydrogen in titanium. Hydrogen solubility in β-phase titanium can reach to a value as high as 50 at.% at temperatures above 600°C and about 7 at.% in α-phase at temperatures about 300 °C. As a result, an inert gas, high purity argon, was used as the sintering atmosphere.

All of the sintering and foaming experiments were performed in a vertical tube furnace (Figure A.1) with two type-K thermocouples. One of the thermocouples was connected to the PID type controller while the other thermocouple placed just above the specimen was used to measure the sample temperature. Titanium crucibles were used to hold the compacts during sintering to prevent excessive reaction of the magnesium to be vaporized from the compacts with the crucible material. Considering the reactivity of titanium, oxygen and water vapor in the high purity argon gas (N<sub>2</sub>: 8.0 ppm, O<sub>2</sub>: 2.0 ppm, Humidity: 1.5 vpm) were kept under close control. As can be seen in appendix A, Figure A.1 sintering furnace was designed with a gas-cleaning unit containing copper chips (to remove oxygen in gas) and silica gel or CaCl<sub>2</sub> (to eliminate the water vapor). After removal of water vapor, argon gas pass through copper chips heated to 500°C, at which partial pressure of oxygen in the argon gas may be reduced down to 10<sup>-16</sup> atm., while the oxidation rate is sufficiently high. At lower temperatures, oxidation kinetics will be insufficient and at higher temperatures equilibrium oxygen partial pressure will be higher as shown in Ellingham diagram (Figure A.2). Since the attained oxygen partial pressure is far from the desired level of oxygen partial pressure (10<sup>-24</sup> atm) for sintering of titanium at 1200°C, porous or sponge titanium was placed as sacrificial material on the top of the crucible and around the samples during the

foaming and sintering experiments. In addition to these, having more affinity for oxygen compared to titanium makes magnesium itself a self-protector. During the sintering experiments, at 1200°C, the partial pressure of oxygen in the crucible was calculated to decrease down to  $10^{-32}$  atm. due to the presence of magnesium vapor. Oxidized copper chips were occasionally changed with fresh ones rather than cleansing by H<sub>2</sub> gas passed through the heated chips to break down the copper oxide because of practical reasons.

### **3.4. Sample Characterization**

#### **3.4.1. Particle size measurement**

Particle size characterization of as-received and sieved powders were done using Malvern Mastersizer 2000, which is capable of using Mie scattering technique and has the flexibility of allowing wet and dry measurements. Analyser make use of Helium neon laser as a source for red light in size determination of coarser particles and solid state light source to produce blue light for finer particle size measurement. Based on the test results frequency versus log-particle size graphs were obtained.

#### **3.4.2. Density Measurements**

The density measurements of the samples were carried on the basis of Archimedes' principle, which states "When a body is immersed in a fluid, the fluid exerts an upward force on the body equal to the weight of the fluid that is displaced by the body."

The weight of a specimen, W, could be given as,

$$W = m_{\text{specimen,air}} \times g \quad (3.1)$$

where  $m$  is the mass of the body and  $g$  is gravitational acceleration and the small buoyant force of air is neglected. The specimen experiences an upward buoyant force,  $F$ , equal to the weight of water displaced, when it is immersed in water. This force is,

$$F = V \times \rho_w \times g \quad (3.2)$$

where  $V$  is the volume of the specimen and  $\rho_w$  is the density of the water ( $1 \text{ g/cm}^3$ ).

The actual weight of the specimen decreases when it is immersed in water and cause overflow of water. The difference between the actual weight of the specimen and the weight of the water that is overflowed gives the upward buoyant force,  $F$

$$F = W_{\text{actual}} - W' = (m_{\text{specimen,air}} \times g) - (m_{\text{specimen, water}} \times g) \quad (3.3)$$

where  $W_w$  is the weight and  $m_w$  is the mass of the water, that is overflowed when the specimen is immersed in the water. During the density measurements the actual weight,  $W$ , and the reduced weight,  $W_w$ , of specimen were determined using a sensitive balance. Using these measured values, the density of the specimen could be obtained easily combining above equations as follows:

$$V = (W_{\text{actual}} - W_w) / (\rho_w \times g) \quad (3.4)$$

$$V = (m_{\text{specimen,air}} - m_{\text{water}}) \times g / (\rho_w \times g) \quad (3.5)$$

As  $\rho_w = 1 \text{ gr/cm}^3$ , then;

$$V = (m_{\text{specimen}} - m_w) \quad (3.6)$$

Once the volume of the specimen is found, the density was calculated according to the equation below;

$$\rho_{\text{specimen}} = m_{\text{specimen,air}} / V \quad (3.7)$$

During density measurements temperature of the medium and the type of fluid to be used should be chosen and controlled carefully. Since densities of water and ethanol change with the test temperature, correct density value of the corresponding liquid should be incorporated in calculations. Moreover, balance unit should be very well insulated against air convection when conducting the density measurements.

In the present study, density measurements were carried out using a Sartorius precision balance (model CP2245-OCE) equipped with a density determination kit. Fractions of open and closed porosity were determined by impregnation with two different fluids depending on the pore size of the sample. For loose powder sintered samples and samples produced using compacting followed by sintering technique, in which the pore size is relatively small a highly volatile xylol ( $\text{CH}_3\text{C}_6\text{H}_4\text{CH}_3$ ) solution with a density of  $0.861 \text{ g/cm}^3$  was used, while liquid paraffin was used in samples produced by space holder technique. In the former technique samples were dipped in xylol for 36 hours to allow impregnation of the solution into open pores. Based on the below equations volume, density, open and closed porosities were calculated as follows;

$$V = \frac{(m_{\text{specimen,air/xylol}} - m_{\text{specimen,xylol/xylol}})}{\rho_{\text{xylol}}} \quad (3.8)$$

where V is the volume of the sample. Then, density ( $\rho$ ) of the porous material is;

$$\rho = \frac{m_{\text{specimen,air}}}{V} \quad (3.9)$$

$$P\%(\text{total}) = \left( 100 - \left( \frac{\rho}{\rho_{\text{titanium or Ti6Al4V}}} \right) \times 100 \right) \quad (3.10)$$

$$P\%(open) = \frac{\text{Volume of xylol in pores}}{V(\text{specimen})} = \frac{\left( \frac{m_{\text{specimen,air/xylol}} - m_{\text{specimen,air}}}{0.861} \right)}{V(\text{specimen})} \quad (3.11)$$

$$P\%(closed) = P\%(total) - P\%(open) \quad (3.12)$$

where,

$m_{\text{specimen,air/xylol}}$  : Mass of the xylol impregnated specimen in air

$m_{\text{specimen,xylol/xylol}}$  : Mass of the xylol impregnated specimen in xylol

$m_{\text{specime,air}}$  : Mass of the dry specimen in air

$P\%(total)$  : percentage of the total porosity

$\rho_{\text{xylol}} = 0,861 \text{ gr/cm}^3$

$\rho_{\text{titanium}} = 4,507 \text{ gr/cm}^3$  and  $\rho_{\text{Ti6Al4V}} = 4,43 \text{ gr/cm}^3$

$P\%(open)$  and  $P\%(closed)$  are the percentages of open and closed porosities, respectively.

Xylol solution is not appropriate for density and the porosity determination of porous samples produced by space holder method in which the pore size reaches to 1500-2000  $\mu\text{m}$ , due to flow out problem during weighing in air. Several methods, one of which uses the impregnation of oil into pores conforming to ASTM B 328-92 standard [155] may be used in porosity determination experiments. However, in the present study fractions of open and closed porosity were found by weight measurements prior to and after dipping the samples in boiling paraffin at 170°C for two hours. A correction factor has been taken into account during density calculations since about 7.5 % volume change occurs during melting of paraffin.

$$V = \frac{\left( m_{\text{specimen,air/paraff}} - m_{\text{specimen,water/paraff}} \right)}{\rho_{\text{water}}} \quad (3.13)$$

$$\rho = \frac{m_{\text{specimen,air}}}{V} \quad (3.14)$$

$$P\%(total) = \left( 100 - \left( \frac{\rho}{\rho_{\text{titanium or Ti6Al4V}}} \right) \times 100 \right) \quad (3.15)$$

$$P\%(open) = \frac{\left( \frac{m_{\text{specimen, air/paraff}} - m_{\text{specimen, air}}}{\rho_{\text{solid paraff}}} \right) \times 1,075}{V(\text{specimen})} \quad (3.16)$$

$$P\%(closed) = P\%(total) - P\%(open) \quad (3.17)$$

where,

$m_{\text{specimen,air/paraff}}$  : mass of the paraffin impregnated specimen in air

$m_{\text{specimen,water/paraff}}$  : mass of the paraffin impregnated specimen in water

$m_{\text{specime,air}}$  : mass of the dry specimen in air

$V$  : Total volume of the specimen, (cm<sup>3</sup>)

$\rho$  : density of the specimen, (g/cm<sup>3</sup>)

$\rho_{\text{solid paraffin}} = 0,826 \text{ gr/cm}^3$

Subsequent to density measurements, after allowing paraffin to melt and flowout of the pores at about 80-100°C, paraffin left in small pores was removed by dipping of samples in xylol solution for 24 h. Since xylol is soluble in ethanol the final cleaning was carried out in ethanol bath by the help of an ultrasonic cleaner.

### 3.4.3. Pore Size and Porosity Distribution

Mainly two types of characterization methods were used for determination of pore size and porosity distribution. Size and distribution characteristics of pores left

from incomplete sintering of spherical powders in loose and pressed condition were examined using mercury porosimetry, whereas linear quantitative metallographic analysis was applied for pore size determination in samples produced by space holder method with pores larger than 200-250  $\mu\text{m}$ .

Gas and mercury porosimetry are complementary techniques with the latter covering a much wider pore size range. Although the nitrogen porosimetry is effective in measuring the pores in the range of 0.002-0.4  $\mu\text{m}$ , it is possible to examine pores between 0.002  $\mu\text{m}$  and 1000  $\mu\text{m}$  using mercury porosimeter.

In the present study Quantachrome mercury porosimetry equipped with high (0-maximum psi) and low (0-50 psi) pressure ports has been used. Incomplete sintered samples were pressurized up to 50 psi with a contact angle of 140°.

#### **3.4.4. Metallographic Examinations**

For metallographic examinations of samples, an epoxy resin was impregnated into the pores for ease of sample preparation and to reveal the pore shape more accurately. Micrographs were taken by using Nikon FDX-35 camera connected to Nikon Optiphot-100 type microscope. Porous samples produced using different techniques were examined both in polished and etched conditions. Etchant used was Kroll's Reagent (3 ml HF+6 ml HNO<sub>3</sub>+100 ml H<sub>2</sub>O).

Scanning electron microscope studies were carried out using a Jeol 6400 Scanning Electron Microscope equipped with "Northern Tracor" EDS analysis system.

Apart from these, to correlate the mechanical properties to neck and pore size, quantitative metallography studies were also done using an image analyser to calculate average neck size and porosity. At least 70 necks and also their neighbour particles were measured from optical or SEM micrographs, Figure 3.7 for a statistically reliable evaluation.

Average grain sizes of furnace-cooled bulk Ti-6Al-4V (ELI) samples were determined using linear quantitative analysis.

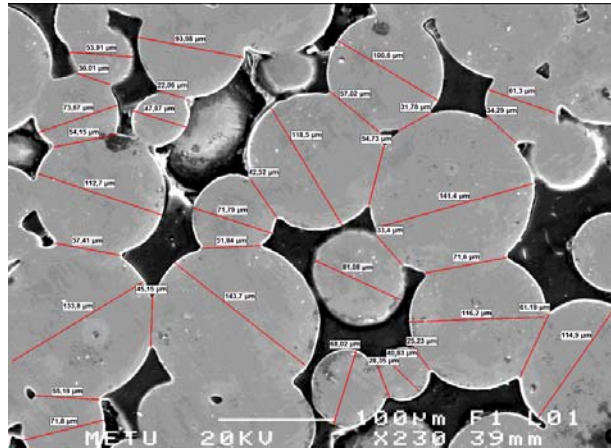


**Figure 3.7** An example of neck and the particle size measurement in powder sintered in loose condition.

### 3.4.5. X-Ray Diffraction

To determine the residual magnesium in porous titanium and Ti-6Al-4V alloy samples after sintering and also to examine the resultant phases in both porous and bulk Ti-6Al-4V-ELI alloy samples, X-Ray diffractograms were taken by continuous scanning at 40 kW between 25° to 90° 2θ angles using Rigaku D/Max 2200/PC model X-Ray Diffractometer.

### 3.4.6. Mechanical Testing

For the compression tests carried out with Shimadzu ACS-J 10 kN capacity universal tension-compression test machine at a cross-speed of 0.5 mm/min, loose powder sintered specimens were cut to 8.4 mm length by a diamond saw to obtain H/D (height to diameter) ratio of 1.5 and both surfaces of the specimens were mechanically ground to render them parallel. Teflon tapes stuck on the die surfaces of compression testing unit were employed to reduce the friction. High strength samples such as bulk Ti-6Al-4V-ELI and compacted and sintered ones were

characterized using Dartec 9500 250 kN capacity universal tension–compression test machines at a crosshead-speed of 0.5 mm/min.

H/D ratio of samples produced using cold compaction & sintering and space holder technique was limited to 0.7-0.8 due to limitation in pressing a homogenous compact even when double-pressing is employed. At high H/D ratios, although both ends of the specimen, top and bottom, have equal density, in the center the density turns out to be considerably smaller. Surface roughness of the porous specimens was very high due to large pores present on both surfaces. Using teflon tapes during compression testing, especially in samples produced by space holder method, was not effective to reduce the friction since specimens tore them. As a result, movement of the surfaces facing the die in the lateral direction is being precluded. Grease was applied on both of the die surfaces to reduce the friction and prevent barrelling to a certain extent during compression.

Elastic modulus of the specimens were calculated from curves fitted to the linear elastic regions of the stress-strain curves. 0.2 % offset method is used to determine compression yield strength values. Finally, based on the results of experiments comparisons were made with empirical and analytical models used for characterizing porosity-elastic moduli and porosity-yield strength relations.

## CHAPTER 4

### RESULTS AND DISCUSSION

#### 4.1. Loose Powder and Cold Compaction Sintering Techniques

##### 4.1.1. Porosity and Pore Characteristics

Porosity contents achieved by loose powder sintering of spherical titanium and Ti-6Al-4V powders are shown in Figure 4.1. One hour sintering of pure titanium and Ti-6Al-4V alloy powders under argon gas exhibited interconnected pores and porosities with amounts systematically decreasing from 36 % to about 30 % with sintering temperature increasing from 850°C to 1250°C.

Tap density of the powders used, i.e., the highest packing density possible without application of pressure, was measured as 2.77 and 2.71 g/cm<sup>3</sup> for spherical titanium and Ti-6Al-4V alloy, respectively, which means that the initial porosity contents prior to sintering were about ~ 38.5 % and ~39.0 %. These maximum porosity levels, i.e. tap porosity, and the pore character are related to the particle size distribution, so does the packing characteristics of powders, i.e. orthorhombic, rhombohedral stacking. As previously stated, the calculated upper limit of porosity for simple cubic, orthorhombic and tetragonal stackings of similar sized powders are 47.6, 39.5 and 30.0 % [112].

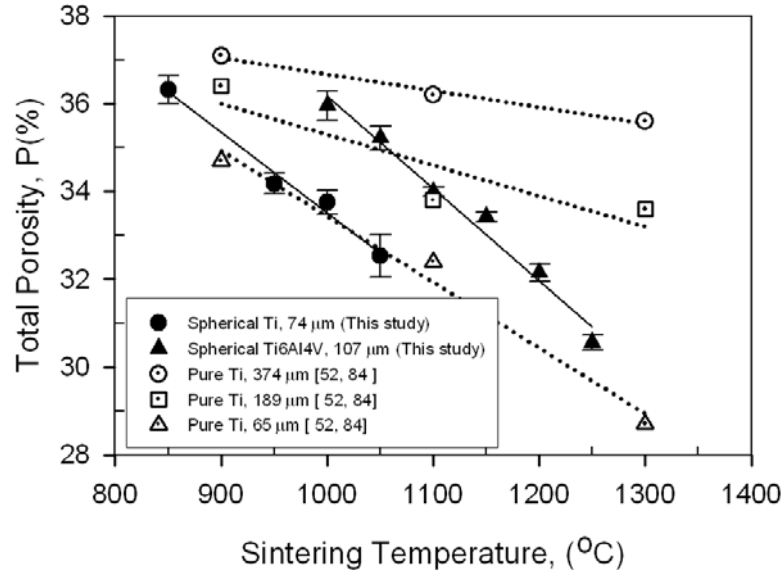


**Figure 4.1** Final porosities of pure titanium and Ti-6Al-4V samples after sintering in the loose condition.

Upon sintering of spherical powders, porosity in both titanium and Ti-6Al-4V alloy samples was observed to decrease linearly with increasing sintering temperature at almost the same rate as shown in Figure 4.1. Equations 4.1 and 4.2 given below represent the temperature dependencies of porosities of titanium and Ti-6Al-4V alloy samples for the range studied, respectively;

$$\text{Porosity (\%)} = 51.9 - 0.018 \times T (\text{°C}) \quad R^2=0.9832 \quad (4.1)$$

$$\text{Porosity (\%)} = 57.2 - 0.021 \times T (\text{°C}) \quad R^2=0.9810 \quad (4.2)$$

Temperature-percent porosity relation obtained for the pure titanium powder in the present study is different from that obtained by Oh et al. [52, 84], which has been superimposed onto Figure 4.1 for comparison. In their study, pure titanium powders with 65, 189 and 374 μm particle size have been pre-pressured at 70 MPa for 0.6 ks and then sintered at 900, 1100 and 1300°C. Both studies verify that, for a given sintering temperature porosity increases as the mean particle size increases since the available surface contacts necessary for sintering decreases. Higher porosity contents observed in Ti-6Al-4V alloy samples compared to pure titanium

samples at the same sintering temperature can be attributed to the bi-modal distribution as well as the relatively smaller mean particle size of the later. Since the compaction pressure is another parameter affecting the sintering response of powder particles in the same sintering temperature range, loose powder sintering with no compaction has been practiced in the present study to maximize the porosity content.

A rather interesting feature observed in Figure 4.1 is that porosity of the pure titanium sample sintered at 850°C, which is below the  $\alpha/\beta$  transus temperature (882°C), also obeys the general trend. It is well known that, due to the close packed structure, self diffusion coefficient of hcp- $\alpha$  titanium is orders of magnitude smaller than that of bcc- $\beta$  titanium [26]. Based on this fact, sintering is expected to be much slower below the  $\beta$ -transus temperature, yielding smaller neck size (interparticle bond size) and higher porosity. The observed inconsistency can be elucidated by the dominance of surface diffusion over the bulk at early stages of sintering.

Further densification of compacts may be achieved through the use of smaller particles, powders with wide range of particle size distribution, higher sintering temperatures with prolonged soaking time or higher cold compaction pressure (above the yield point of the material) before sintering. As previously stated, sintering in titanium and titanium alloys may also be enhanced through the alloy additions, i.e. silicon, to the titanium powder, thereby increasing the sintering rate by formation of transient liquid phase [86]. Another method aiming higher sintering rate utilizes cyclic sintering (thermal cycling) around  $\alpha$ - $\beta$  transition temperature. Densification in such sintering technique is attributed to the transformation-mismatch plasticity, which is responsible for transformation super plasticity [77-80].

Compared to loose powder sintering wider range of mean porosities in the range 14.1-32.5 % and 20.5-31.6 % for titanium and Ti-6Al-4V alloy powders, respectively, were obtained by compaction at various pressures and sintering at 1200°C. Exponential relation between porosity and compaction pressure in the form of  $y = Ae^{-bx}$  was obtained from the experimental data as given by Equations 4.3 and 4.4. Extrapolation of the compaction pressure versus total porosity curves for

spherical titanium and Ti-6Al-4V, Figure 4.2, at zero compaction pressure gives porosities around 38.7 and 38.8 %, which are near to the calculated tap porosities of 38.5 % and 39 % for titanium and Ti-6Al-4V alloy powders, respectively.

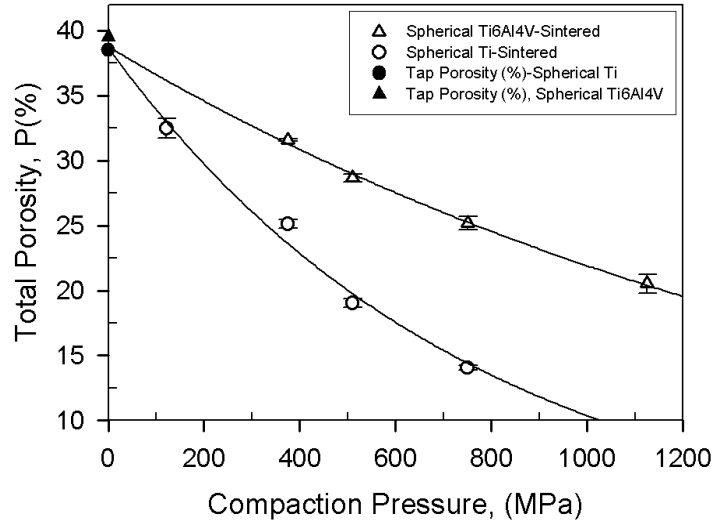


**Figure 4.2** Final porosities of pure titanium and Ti-6Al-4V samples after sintering at 1200°C for one hour subsequent to conventional pressing.

$$\text{Porosity (\%)} = 38.7 \times \exp\{-0.0013 \times \sigma(\text{MPa})\} \quad R^2=0.9833 \quad (4.3)$$

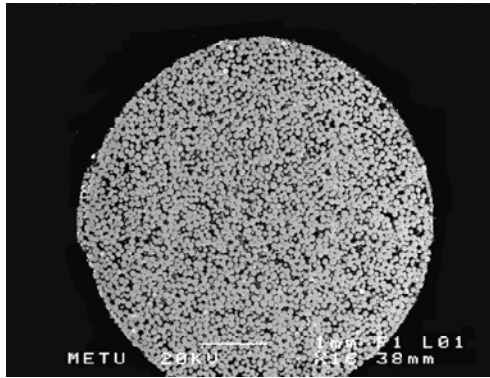
$$\text{Porosity (\%)} = 38.8 \times \exp\{-0.0006 \times \sigma(\text{MPa})\} \quad R^2=0.9972 \quad (4.4)$$

Pressing of powders prior to sintering decreases the porosity in the green compact and enhances the sintering rate due to an increase in the neck area and in dislocation density at higher pressures. At low pressures, plastic flow is localized to particle contacts, while at high pressures homogenous plastic flow occurs and powder particles become work hardened [13]. Moreover, higher compaction pressures result in an increase in density of compact and contact size, while reducing the rate of neck growth. Compaction pressure is limited with the strength of powder particles that higher pressures lead to excessive deformation and fracture of powder

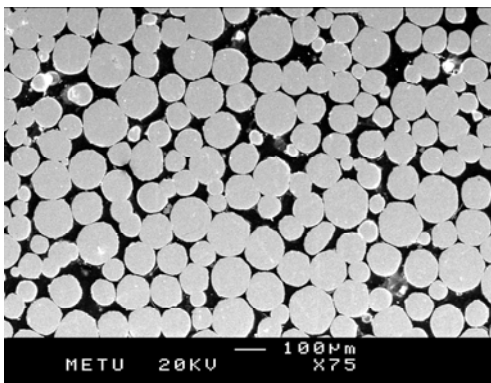
particles. Yield strength of bulk grade 4 titanium and Ti-6Al-4V alloy are around 550 MPa and 1215 MPa, respectively.

Figures 4.3, 4.4 and 4.5, which show the polished cross-sections of pure titanium and Ti-6Al-4V alloy powders sintered in loose and pressed condition, reveal interconnected pores of irregular shape, which may be suitable in biomedical applications. In powder sintering pore size and pore shape are dictated primarily by the powder size, shape and size distribution and by the compaction pressure, sintering temperature and time. For example, the amount of porosity in sintered samples is limited to 50 % for mono-sized powders [8]. Moreover, in pressed and sintered samples as the prior compaction pressure is increased sharp neck curvatures seem to disappear, Figure 4.4 (d) and 4.5 (d).

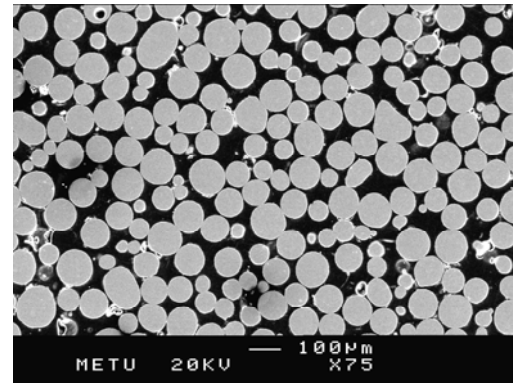
Pore size distributions of sintered samples obtained by mercury porosimeter are presented in Figures 4.6 and 4.7 for maximum and minimum loose powder sintering temperatures and compaction pressures. As can be seen in both pure titanium and Ti-6Al-4V alloy samples sintered either in loose or pressed condition, pore sizes up to 200  $\mu\text{m}$  were observed. For loose powder sintered samples the average pore size was found to be around 30-40  $\mu\text{m}$  and most of the pores were in the range 15-70  $\mu\text{m}$ . Pore size distribution presented in Figure 4.6, also indicates a slight shift to smaller pore size with increasing sintering temperatures. Pressed samples, on the other hand, exhibited relatively smaller average pore sizes around 15-30  $\mu\text{m}$  and an expected shift to smaller pore sizes with increasing compaction pressure.



(a)

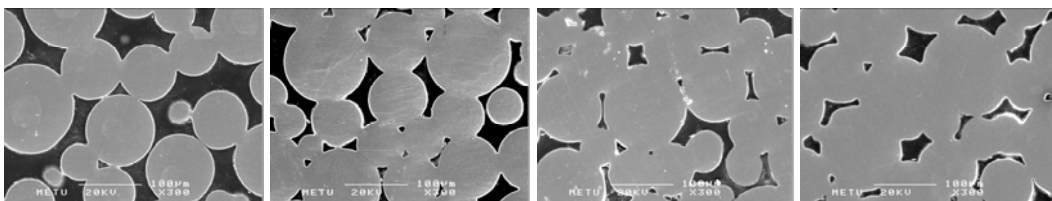


(b)



(c)

**Figure 4.3** Polished cross-section of loose sintered powders at 1000°C, (a) cross-section of titanium compact, (b) Spherical titanium, (c) Spherical Ti-6Al-4V.



(a)

(b)

(c)

(d)

**Figure 4.4** Polished cross-sections of pressed and sintered (at 1200°C) spherical titanium powders, (a) 120 MPa, (b) 375 MPa, (c) 510 MPa, (d) 750 Mpa.

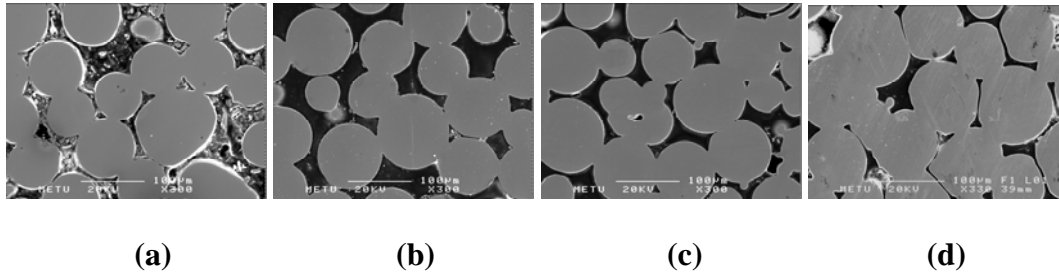


**Figure 4.5** Polished cross-sections of pressed and sintered (at 1200°C) spherical Ti-6Al-4V powders, a) 375 MPa, b) 510 MPa, c) 750 MPa, d) 1125 Mpa.

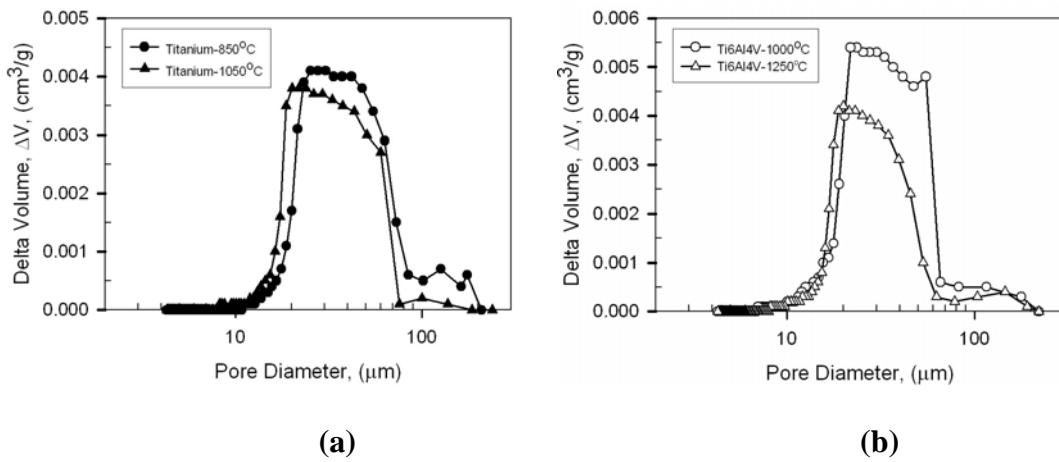


**Figure 4.6** Pore size distribution of loose powder sintered samples for minimum and maximum sintering temperatures, (a) Spherical titanium, (b) Spherical Ti-6Al-4V.

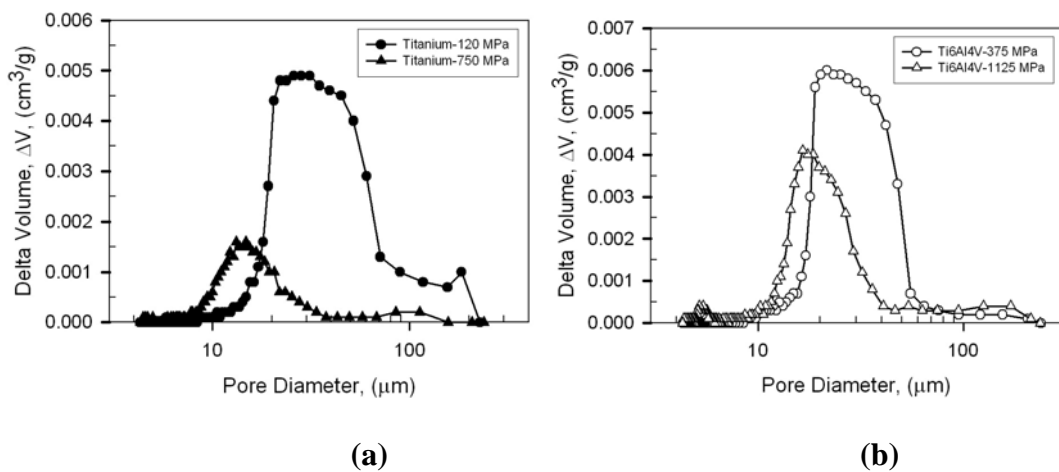
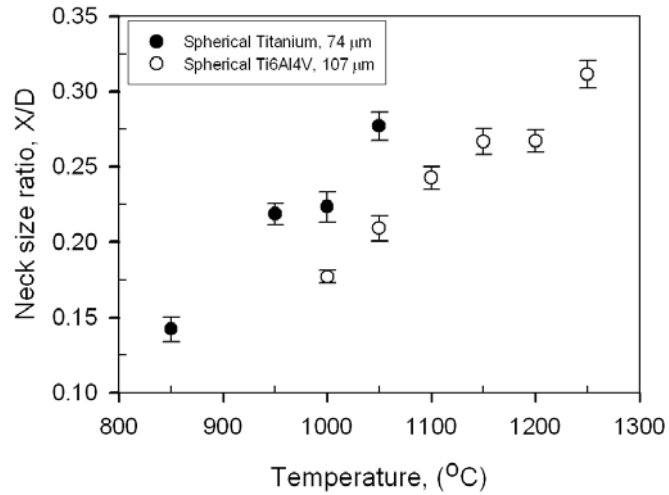


**Figure 4.7** Pore size distribution of pressed and sintered samples for minimum and maximum compaction pressures, a) Spherical titanium, b) Spherical Ti-6Al-4V.

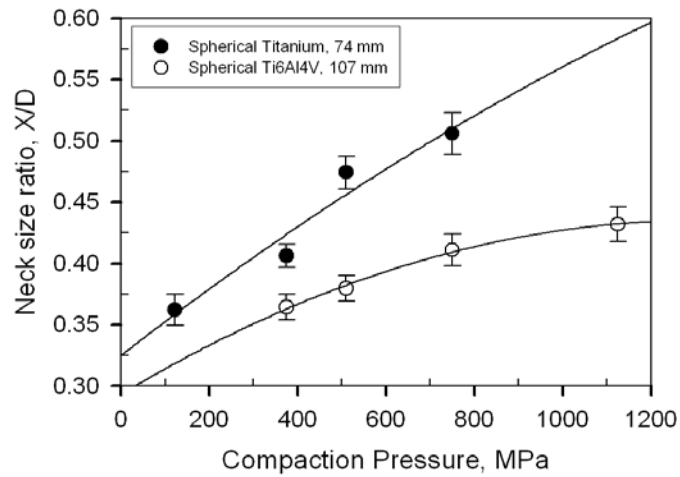
#### 4.1.2. Interparticle Neck Size

In the solid state sintering the degree of sintering can be determined using interparticle neck size, density, porosity or shrinkage measurements. Reduction in surface area also provides a gauge of the degree of sintering. Gas adsorption or gas permeability techniques give information about surface area of the powder compacts. However, interparticle neck growth, with a loss of surface area, can occur without shrinkage depending on the sintering mechanism, which describe the path of atomic motion over the surfaces along the grain boundaries, or through the crystal lattice.

Figure 4.8 (a) and 4.8 (b) show the change of average neck size ratio with sintering temperature and compaction pressures, respectively, for spherical titanium and Ti-6Al-4V powders sintered in loose and pressed condition. Additionally, change of neck size ratio with porosity content is given in Figure 4.9 to compare the neck size-porosity relation in different production techniques. As expected, in loose powder sintering average neck size increases as the sintering temperature increases (with decreasing porosity level). For titanium samples sintering temperatures between 850 and 1050°C resulted in average neck size ratio, ( $X/D$ ), between 0.142 and 0.277. On the other hand, average neck size ratios were found to be 0.177 and 0.312 for Ti-6Al-4V alloy powders sintered in loose condition between 1000 and 1250°C. Compaction at various pressures and sintering at 1200°C resulted in relatively higher average neck sizes in both type of powders. The measured average neck size ratio in titanium samples compacted between 120 and 750 MPa were observed to change between 0.362 and 0.506, while it was between 0.364 and 0.432 for spherical Ti-6Al-4V alloy samples compacted between the compaction pressures of 375 and 1125 MPa.



(a)

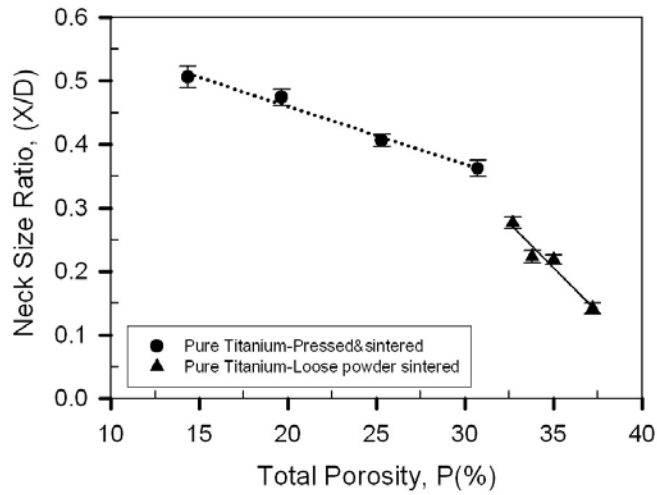


(b)

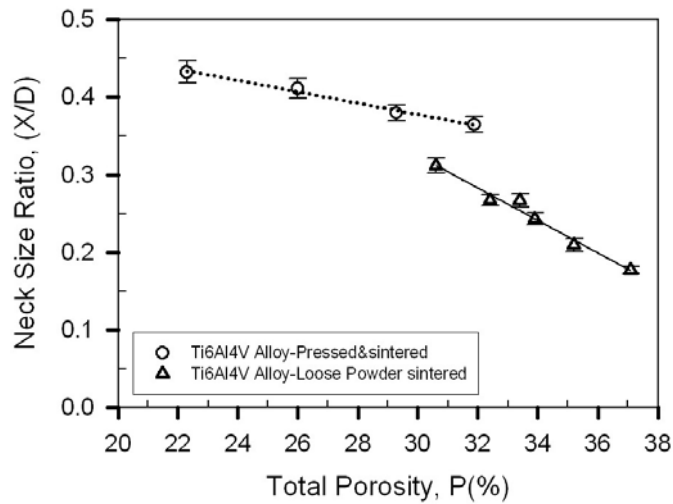
**Figure 4.8** Neck size ratio (X/D) change with (a) sintering temperature (loose powder sintering) and, (b) compaction pressure (samples sintered at 1200°C).

The interesting point in Figure 4.9 is that for similar porosity levels, i.e. around 30 %, average neck sizes of pressed and sintered samples are higher than that of powder samples sintered loose condition. This effect is more pronounced in pure titanium compared to Ti-6Al-4V alloy powders. Lower neck size of loose sintered powders in the same porosity levels can be attributed to lower sintering temperature and the limited contact area prior and during sintering. On the other

hand, relatively high mean particle sizes of Ti-6Al-4V powders as compared to the pure titanium have resulted in smaller average neck size in the same porosity levels.



(a)



(b)

**Figure 4.9** Neck size ratio ( $X/D$ ) change with total porosity in samples sintered in loose and compacted condition, (a) Pure titanium, (b) Spherical Ti-6Al-4V.

In addition to the observed differences in neck sizes in the same porosity range, region neck curvatures of sintered powders in loose and pressed condition were also observed to be different from each other. In the same porosity range,

compared to pressed and sintered samples, very sharp neck curvatures were detected in loosely sintered titanium powders as shown by arrows in Figure 4.10. This is mainly due to dominance of different transport mechanisms in loose and pressed powder sintering.

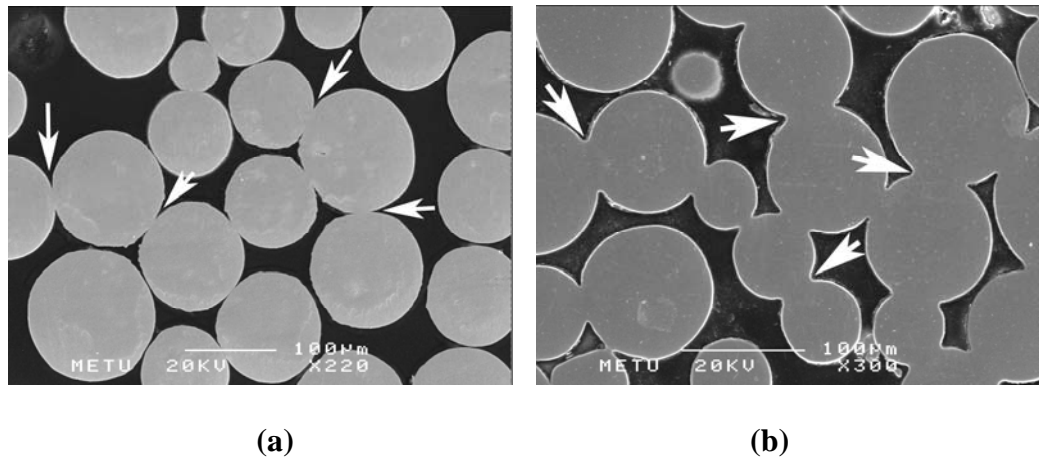


**Figure 4.10** Neck curvature in sintered titanium powders, (a) sintered in loose condition, ( $\sim 31\%$  porosity), (b) sintered in pressed condition, ( $30\%$  porosity).

It is clear that the effect of sintering temperature on the average neck size ratio is higher compared to compaction pressure probably due to dominance of different transport mechanisms as sintering temperature increases. As can be seen from Figure 4.9 (a) and (b) the slope of the line for loose powder sintered samples are higher than that of pressed & sintered samples for both types of powders, i.e. for small changes in the porosity content the change in average neck size ratio is higher in loose powder sintered samples compared to pressed and sintered samples.

As can be seen in Figure 4.9, different production techniques may be utilized to achieve similar porosity levels, however, internal structure of the powders may vary, and the resultant size of the interparticle bond regions will be different. Therefore, mechanical properties of porous samples manufactured with different production techniques but having similar porosity levels may differ considerably.

As it is elucidated, the effect of compaction pressure and sintering temperature on shrinkage is different. Higher compaction pressures contribute to

increase in contact size. Since available surface contacts necessary for sintering increase with compaction pressure a decrease in diffusion distances occurs. Moreover, higher dislocation density results in an initially faster sintering rate. Dislocations in powder compacts can interact with vacancies, and densification rate is improved due to dislocation climb, where the dislocations collect vacancy fluxes being emitted by the pores. The vacancies annihilate at the dislocations and allow the dislocation to climb during initial heating to the sintering temperature [13]. However, the rate of neck growth and also amount shrinkage reduces as compaction pressure increases due to compression limit of the powders. This effect can be seen clearly in Ti-6Al-4V powders shown in Figure 4.8 (b) mainly due to higher mean particle size and narrow particle size distribution of these alloy powders.

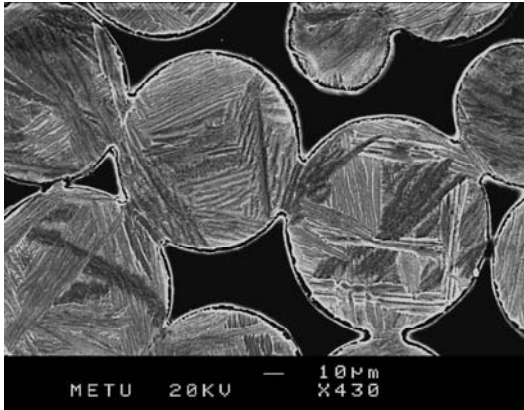
In the loose powder sintering technique, as in all diffusion-controlled phenomena, temperature is the dominant factor affecting the sintering rate. Although the neck size is expected to change with sintering temperature in an exponential manner for constant soaking times, the relation obtained between neck size ratio and sintering temperatures in the present study seems to be linear, Figure 4.8 (a). Also there is a sharp increase in neck size ratio at sintering temperatures around 1050 and 1250°C for loose powder sintered titanium and titanium alloys, respectively.

As mentioned previously, the initial stage of sintering is characterized by rapid growth of the interparticle neck and maximum neck size ratio ( $X/D$ ) in this stage is usually around 0.3. In the intermediate stage, the pore structure becomes smoother and has an interconnected, cylindrical nature. By the final stage pores are spherical and closed, grain growth is evident. Transport mechanisms involved during sintering are surface and bulk transport. Generally, the dominant mechanism at low sintering temperatures is surface transport, while bulk transport mechanisms are more active at higher sintering temperatures. Surface transport mechanisms, i.e. evaporation condensation and surface diffusion, involve neck growth without a change in particle spacing. However, bulk transport mechanisms involving plastic flow, grain boundary diffusion, viscous flow and volume diffusion cause compacts to shrink. The neck size measurements and microstructures (Figures 4.3-4.5 and Figure 4.8) of pure titanium and Ti-6Al-4V powders sintered in the present study indicate that within the applied soaking times, the samples were in the initial stage

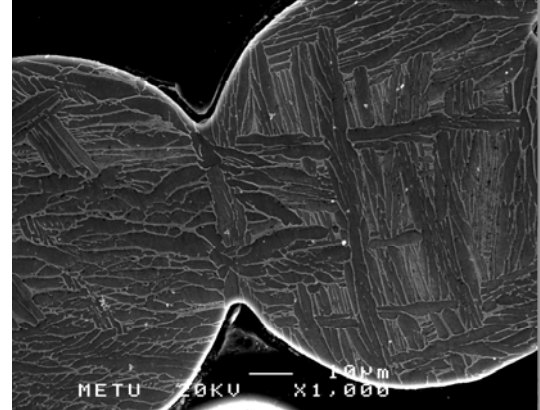
of sintering with partially sintered powders and sharp curvatures in the neck area especially in loose powder sintered samples. The most probable transport mechanisms dominate during sintering of titanium and Ti-6Al-4V alloy powders are, lattice (volume), grain boundary and surface diffusion. The dominance of each mechanism depends on sintering temperature and time.

### 4.1.3. Microstructure

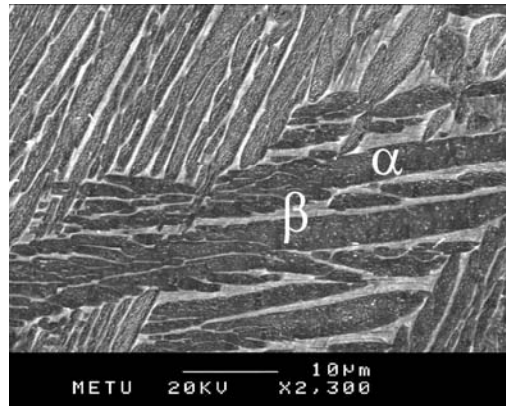
In sintered samples, pore character, average neck size, resulting microstructures as well as the porosity content affect most of the physical and mechanical properties, (e.g. elastic moduli, strength, etc). In  $\alpha+\beta$  alloys, depending on the heat treatment and deformation history of the alloy, fully lamellar, bi-modal and equiaxed type of microstructures may be obtained. The phase transformation upon cooling from  $\beta$ -region to room temperature may be diffusion controlled or diffusionless [28]. The cooling rate at which change from a colony or Widmanstätten type of microstructure to martensitic microstructure occurs is faster than 1000 °C/min for Ti-6Al-4V. In the present study, slow cooling ( $\sim 8^\circ\text{C}/\text{min}$ ) of both bulk and porous Ti-6Al-4V samples from above the  $\beta$ -transus temperature,  $\sim 975^\circ\text{C}$ , under high purity argon gas resulted in a lamellar type Widmanstätten structure, Figure 4.11. The dark regions correspond to the  $\alpha$ -phase and the bright regions, which are depleted from aluminum, are the  $\beta$ -phase. The EDS spot analysis taken from some sintered compacts exhibited about 2.97 wt. % V and 6.58 wt. % Al in  $\alpha$ -phase, and 6.84 wt. % V and 5.25 wt. % Al in  $\beta$ -phase, Figure 4.12 and Table 4.1. In both bulk and porous samples, during slow cooling from the beta phase field, Widmanstätten  $\alpha$ -plates with hcp crystal structure should be grown into bcc- $\beta$  phase with a specific orientation relationship resulting in 12 orientation variants with  $\{110\}_\beta$  habit plane to form plates with their faces parallel to  $\{110\}_\beta$  [30]. In bulk samples, in addition to alpha phase present in the grains primary alpha phase was also observed along the prior beta grain boundaries, Figure 4.13 (a).



(a)

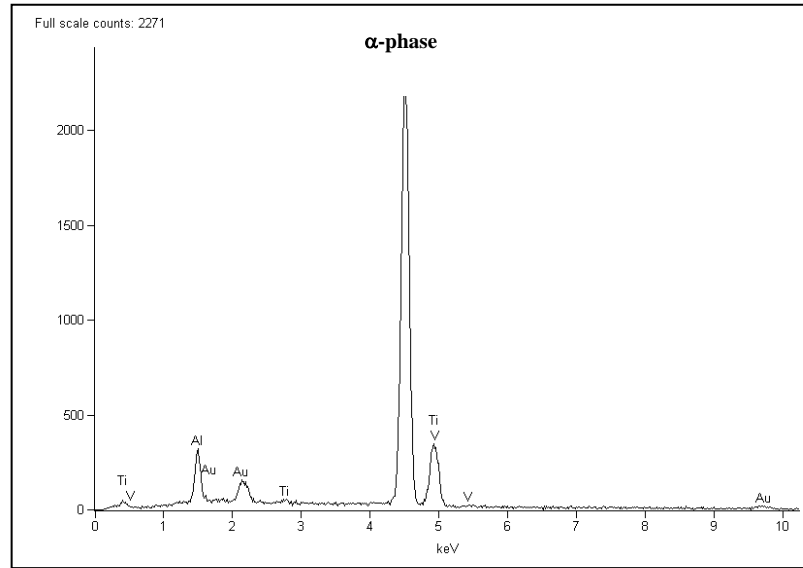


(b)

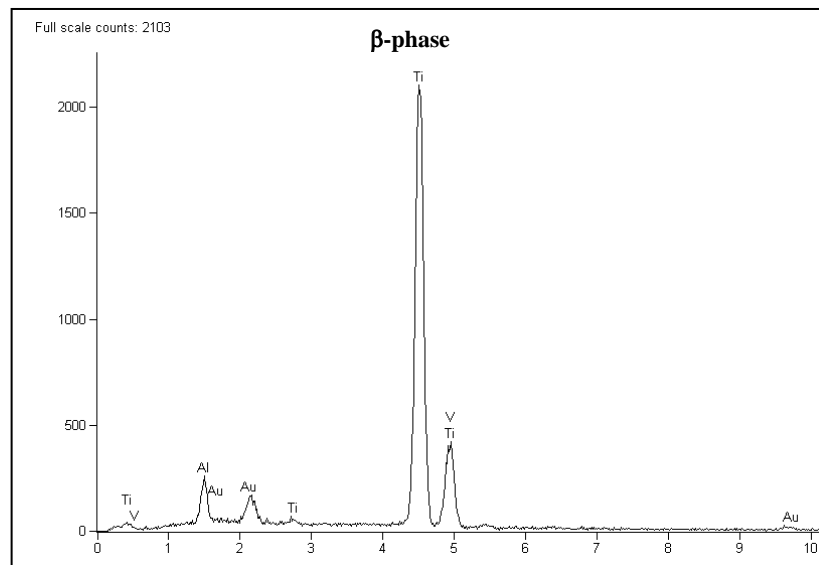


(c)

**Figure 4.11** Microstructure of Ti-6Al-4V alloy samples sintered in loose or compacted condition, (a), (b) partially sintered powders containing Widmanstätten microstructure, (c) Widmanstätten structure containing  $\alpha/\beta$  colonies.



(a)



(b)

**Figure 4.12** SEM EDX Analysis of loose powder sintered Ti-6Al-4V alloy samples, (a)  $\alpha$ -phase, b)  $\beta$ -phase.

**Table 4.1** EDS analysis of the phases present in Ti-6Al-4V alloy sample.

Element	$\alpha$ -phase (% wt.)	$\beta$ -phase (% wt.)
Al	6.58	5.25
Ti	90.44	87.91
V	2.97	6.84

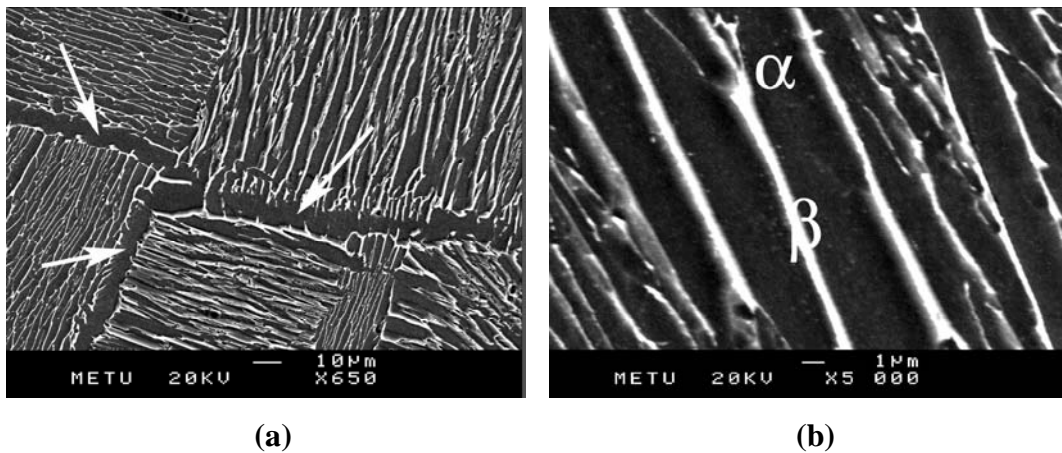


**Figure 4.13** SEM micrograph of furnace cooled bulk Ti-6Al-4V-ELI alloy samples showing, (a) microstructure containing primary  $\alpha$  phase formed on the prior beta grain boundaries, (b) Widmanstätten microstructure containing  $\alpha$  plates and  $\beta$  lathes.

Cooling rate from beta phase region determines the final dimensions of the  $\alpha/\beta$  colony and the thickness of the plates, which play an important role in determining the mechanical properties of the  $\alpha$ - $\beta$  alloys with lamellar microstructure. The strength increases with increasing cooling rate due to refinement of the lamellar microstructure, i.e., reducing the thickness of the plates reduces the slip distance across the plates [162]. In addition, the amount of  $\beta$ -stabilizing elements, i.e. vanadium, directly affect the relative thicknesses and length of the lamellar phases. In the present study, plate thicknesses in slowly cooled specimens of porous and bulk Ti-6Al-4V alloy samples were close to each other. The measured

thicknesses of the  $\alpha$  and  $\beta$  phases in slowly cooled samples were  $\sim 2.95$  and  $0.8 \mu\text{m}$  in foam samples, and  $\sim 3.3$  and  $1.1 \mu\text{m}$  in bulk samples, respectively.

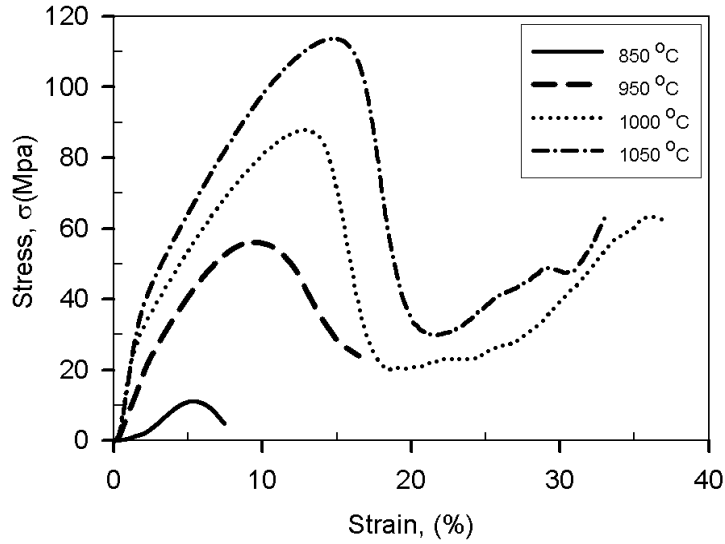
The major distinction between the bulk and powder samples was in the colony size. It was measured to be  $285 \pm 8 \mu\text{m}$  for heat-treated bulk Ti-6Al-4V-ELI samples. Compared to powders with few colonies and maximum size of  $250 \mu\text{m}$ , colonies were couple of times smaller in the sintered compacts, but since the parameter critical in strength is the plate thickness rather than the colony size this difference is assumed to be insignificant.

#### **4.1.4. Mechanical Properties**

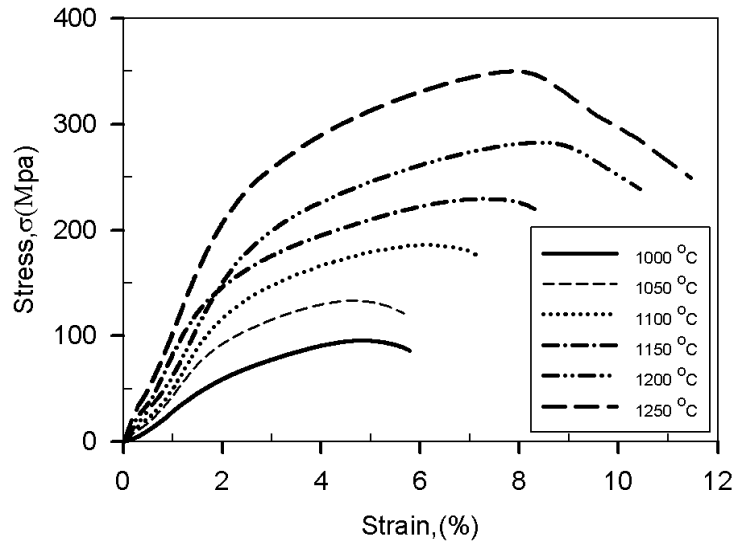
##### **4.1.4.1. Evaluation of Stress-Strain Curves**

All of the stress-strain curves of loose powder sintered pure titanium and Ti-6Al-4V alloy samples, Figure 4.14, exhibited three distinct region of deformation. There is an almost linear elastic deformation region, plastic region with hardening up to a peak stress and plastic region up to fracture. Subsequent to peak stress fracture occurred after different amounts of straining. At maximum stresses, which corresponds to the compressive strength, deformation presumably starts to become non-uniform as two conic shear bands begin to develop along the diagonal axes of the compacts, at  $45^\circ$  to the loading direction, Figure 4.15. Deformation localization in the shear bands, which is called as shear banding, results in a reduction in the load carrying capacity of the deforming compact as can be seen from the stress drops after peak stress. Complete failure occurred by the separation of the bonded particles on the shear bands, starting from the two ends of the cylindrical compact. In some pure titanium samples, i.e. samples sintered at  $1000$  and  $1050^\circ\text{C}$ , although surface crack in the direction of  $45^\circ$  to the compression axis were observed as passing through the peak stress, samples did not fail completely until about 35 % strain. However, the plateau region similar to that of loose powder sintered titanium samples has not been observed in the stress-strain curves of porous

Ti-6Al-4V specimens sintered in the same way, Figure 4.14 (b). These curves with an elastic region followed by plastic region, ultimate stress and fracture are rather similar to those of conventional wrought alloys.



(a)



(b)

**Figure 4.14** Stress-strain curves samples of sintered loosely at various temperatures, (a) Spherical pure titanium powder, (b) Spherical Ti-6Al-4V powder.

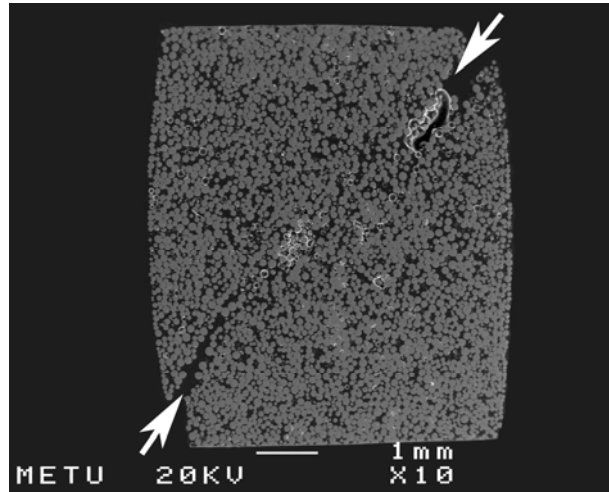
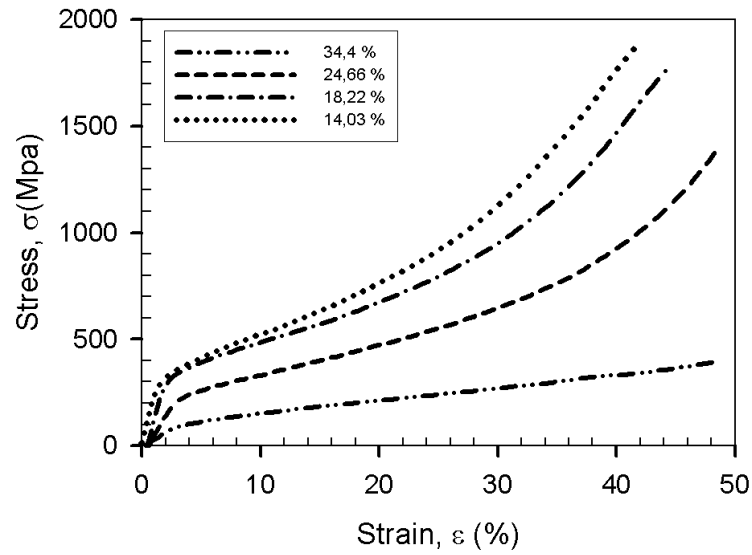


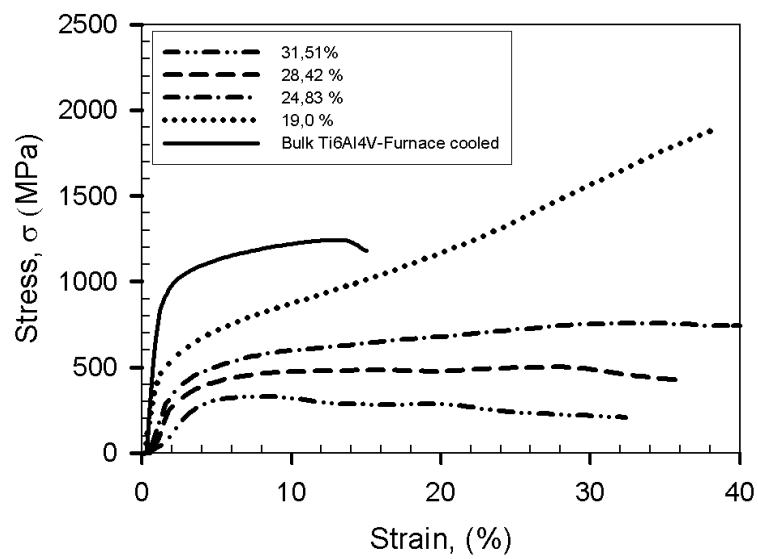
**Figure 4.15** Shear band in loose sintered compact failed during compression-testing.

On the other hand, all of the pressed and sintered specimens of titanium and Ti-6Al-4V alloy, Figures 4.16, have exhibited typical compression stress-strain curves similar to that of highly porous elastic-plastic foams. The curves consist of a linear elastic region at the beginning of deformation, a long plateau stage with nearly constant flow stress to a large strain, and occasionally a densification stage, where the flow stress increases sharply. For the elastic-plastic behavior, it is stated that linear elasticity is controlled by cell wall bending and the plateau is associated with the collapse of the cells. Subsequent increase in stress is a consequence of the compression of the solid itself after complete collapsing of opposing cells. As can be seen from Figures 4.16, both types of pressed and sintered samples possess high energy absorption capacities due to very large strains at even low stresses. In both types of the samples there are plateau regions with nearly constant stresses up to large strains especially for high porosity samples. As the porosity content of the samples decrease the plateau regions start to disappear and subsequent to yielding an increase in the flow stress was observed with strain, i.e., strain hardening is observed in samples with limited porosity. Such effect is seen more clearly in pure titanium samples mainly due to lower porosity content, Figure 4.16 (a). Compared to loose powder sintered samples, the presence of such plateau regions in pressed and

sintered samples may be related to the lower H/D (height to diameter) ratio of these samples.



(a)



(b)

**Figure 4.16** Stress-strain curves of compacted and sintered samples having varying amounts of porosity contents, (a) Spherical pure titanium powder, (b) Spherical Ti-6Al-4V powder.

As can be seen in Figure 4.17, except the pure titanium specimen having highest porosity level (34.4 %) none of the pressed and sintered titanium samples failed completely. Only surface cracks are formed at different directions. However, the results in Ti-6Al-4V alloy samples were different in that complete failure occurred in samples having porosities between ~35 % and 25 % by formation of surface cracks and propagation of these cracks in the direction  $45^\circ$  to the compression axis, Figure 4.18. Cracks were initiated at the surface of the compacts where maximum tensile stress is present in compression, and these cracks propagated predominantly along inter-particle boundaries. Moreover, as it can be seen that different deformation behaviors exhibited by pure titanium and Ti-6Al-4V alloy samples. Higher fracture strain values of porous titanium samples compared to that of Ti-6Al-4V alloy may be attributed to the ductile nature and higher degree of inter-particle bonding. Similar relation was also observed for loose powder sintered samples. In powders sintered in loose condition, maximum strain value at which failure started was about 16 % for titanium samples while it was only 12 % for Ti-6Al-4V alloy samples, Figures 4.14.

The reason of such different compression stress-strain curves of loose powder sintered samples compared to pressed samples can be attributed to the sintering degree, which may be estimated from average neck sizes. As it has been pointed out and shown in Figure 4.9, for similar porosity levels, average neck size ratio of loose powder sintered samples are lower than that of pressed & sintered ones.

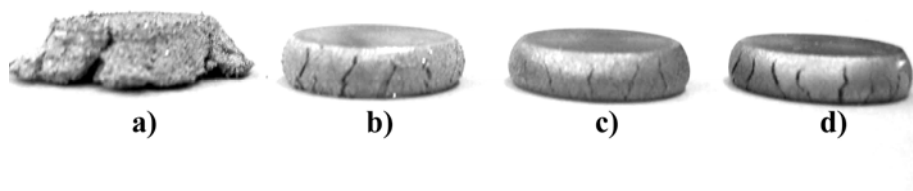


**Figure 4.17** Pressed&sintered pure titanium samples with different porosities after compression testing , (a) 34.4 %, (b) 24.66 %, (c) 18.22 %, (d) 14.03 %.

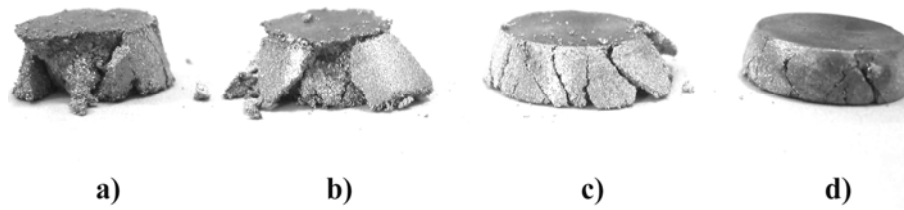


**Figure 4.18** Pressed&sintered Ti-6Al-4V alloy samples with different porosities after compression testing, (a) 31.51 %, (b) 28.42 %, (c) 24.83 %, (d) 19.0 %.

Bulk Ti-6Al-4V alloy having Widmanstätten microstructure is known to have 829 MPa yield and 897 MPa tensile strength values [156]. In this study, compression tests on Ti-6Al-4V-ELI alloy having lamellar structure with  $\sim 3.3$  and  $1.1 \mu\text{m}$  alpha and beta phase thickness, respectively, and average grain size of  $285 \pm 8 \mu\text{m}$  revealed yield and compression strength values around 864 and 1215 MPa. In addition, the typical response of bulk Ti-6Al-4V-ELI alloy under compression loading is plotted for comparison in Figure 4.16 (b). As can be seen, compression stress-strain curves of bulk Ti-6Al-4V-ELI alloy exhibited linear elastic behavior at small strains, followed by yield and strain hardening up to an ultimate stress. Subsequent to a maximum or peak stress fast fracture occurred after small straining. Internal damage such as voids or cracks may cause the material softening after the peak stress. When bulk Ti-6Al-4V-ELI alloy specimens were deformed to a strain level around 14 %, shearing failure occurred along a plane of maximum shear stress at an angle of about  $45^\circ$  to the compression axis. Depending on the microstructure, reported critical strain values for Ti-6Al-4V alloys increase from martensitic to lamellar microstructure. The critical strain values at which shear banding starts change between 8 and 16 % [156].

In all of the porous samples, sintered either in loose or pressed condition, large shear stresses developed in the neck region caused fracture by tearing of the necks as marked with arrows in Figures 4.19 (a) and 4.19 (b). Ductile nature of failure is manifested by dimples in the fracture surfaces. In some studies [157], it has been shown that the growth and coalescence of voids initiated at alpha platelets and beta/alpha interface are the main reason of macrocracks and the separation of neck regions. Moreover, during compression testing originally non-contacting powder

particles developed contacts with neighboring particles during deformation and as a result of particle inelastic deformation the contact areas between powder particles increased over the interparticle bond areas as shown marked as A in Figure 4.19 (d).

Figure 4.19 (e) shows the SEM fractograph of compression tested bulk Ti-6Al-4V-ELI alloy, which contains both sharp and shear ductile dimples. Shear ductile dimples were observed to occur in regions near to the surface of the sample, where maximum tensile stresses develop.

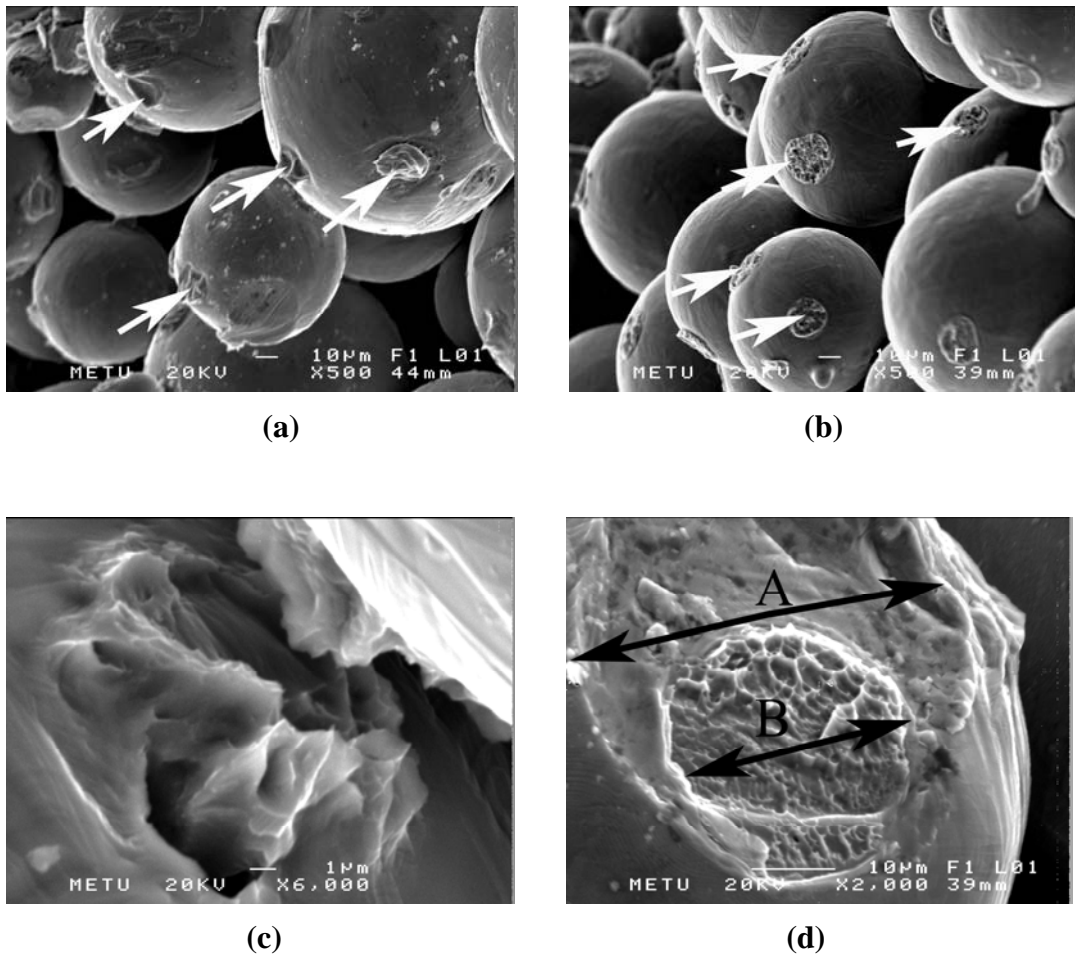
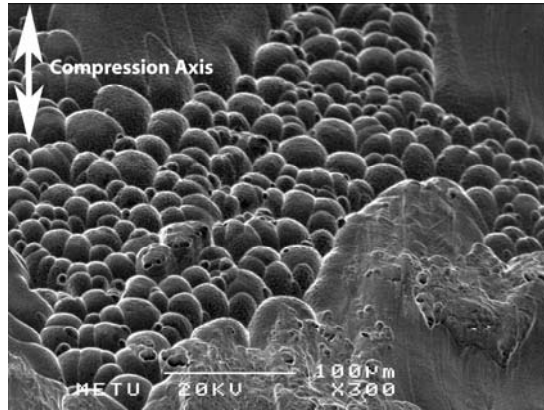


**Figure 4.19** Fractures surfaces of compression tested porous samples, (a) separated interparticle bond regions in titanium samples, (b) separated interparticle bond regions in Ti-6Al-4V samples, (c) dimples in neck region (titanium), (d) dimples in neck region (Ti-6Al-4V), (e) fracture surface of bulk Ti-6Al-4V-ELI alloy containing both sharp and shear ductile dimples.



(e)

**Figure 4.19 (cont.)** Fractures surfaces of compression tested porous samples, (a) separated interparticle bond regions in titanium samples, (b) separated interparticle bond regions in Ti-6Al-4V samples, (c) dimples in neck region (titanium), (d) dimples in neck region (Ti-6Al-4V), (e) fracture surface of bulk Ti-6Al-4V-ELI alloy containing both sharp and shear ductile dimples.

#### 4.1.4.2. Comparison of the Experimental Data with the Proposed Models

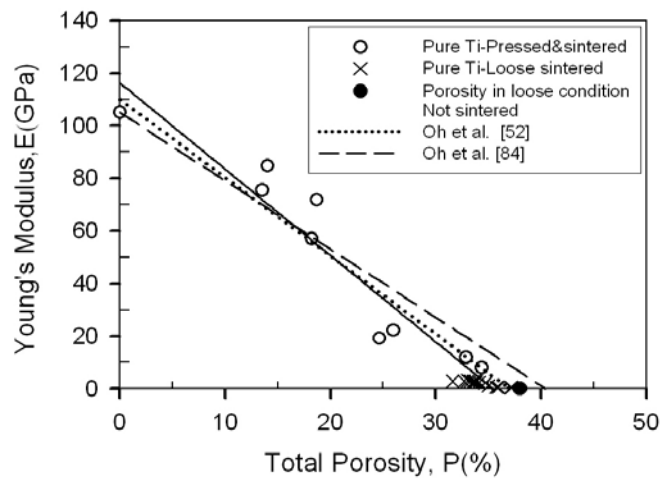
Mechanical properties (Young's Modulus and yield strength) determined from compression stress-strain curves of porous titanium and titanium alloys are presented in Table 4.2, for samples containing minimum and maximum amount of porosities. As expected, mechanical properties of porous Ti-6Al-4V samples are better than the porous titanium samples in the same porosity range. Moreover, regardless of the pore content, the compacts of titanium or titanium alloy sintered in pressed condition possess higher elastic moduli and yield strength values compared to powders sintered loosely. This effect is more evident in pure titanium samples sintered loosely having elastic moduli and yield strength values 60 % lower than that of pressed ones in the same porosity range. As previously discussed in the beginning of this chapter, differences in sintering characteristics and the number of contacts formed before and during sintering may be the reason for such a difference. As higher compaction pressures contribute to the increase in contact size, available surface contacts necessary for sintering increase with compaction pressure and a decrease in diffusion distances occurs.

**Table 4.2** Young's Moduli and Yield strength values for minimum and maximum porosities obtained from sintered samples in loose and pressed conditions.

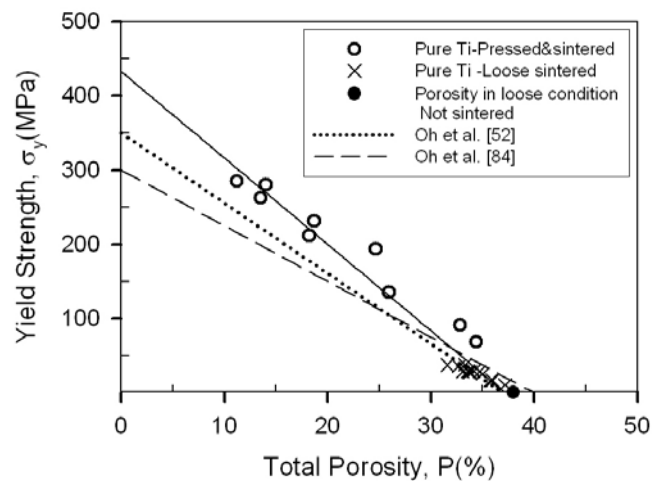
Powder	Sintered condition	Porosity, %	E, (GPa)	$\sigma_y$ , (MPa)
Titanium	Loose	31.6	2.9	37.6
		37.2	0.36	10.6
	Pressed	13.5	75.4	280.0
		34.4	8.0	68.8
Ti-6Al-4V	Loose	30.2	14.1	238.3
		37.1	3.9	58
	Pressed	14.6	64	620
		31.5	11.1	260

There are several studies on sintering of titanium powders in which the effect of porosity content on mechanical behavior has been investigated. However, only a few cover a wide enough range of porosity. Oh et al. [52] used Grade 2 spherical titanium powder having average particle size of 374  $\mu\text{m}$  relatively higher compared to powders used in the present study, about 74  $\mu\text{m}$ . They applied pressure to powders prior or during the sintering. In another study carried out by Oh et al. [84] spherical titanium powders of the same grade with various particle sizes (65, 189, 374  $\mu\text{m}$ ) have been utilized to obtain wider range of porosity with the application of same technique. Best fits obtained by least square method for elastic moduli and yield strength-porosity relation for the present and for their study are shown in Figure 4.20 (a) and 4.20 (b), respectively. Almost the same behavior, i.e. Young's modulus and yield strength decreasing linearly with increasing porosity, is observed both in study of Oh et al. [52] and in the present study. However, the slopes of the lines are different so that extrapolation to zero porosity level gives different elastic modulus and yield strength values. This result may be usual for the yield strength-porosity relation because of the lower bulk yield strength value of Grade 2 titanium, which is around 275 MPa, compared to titanium used in this study. The difference in

elastic modulus-porosity relation may arise from the production technique utilized and the size differences of powder used in these studies. Wide range of porosity levels may be obtained by changing the initial particle size of the powders as done by Oh et al. [52]. It is also possible to achieve similar porosity level by using powders having different average size. However, different inter-particle bond (neck) diameters are obtained for those powders so that the resulting mechanical property-porosity relation may be misleading.



(a)

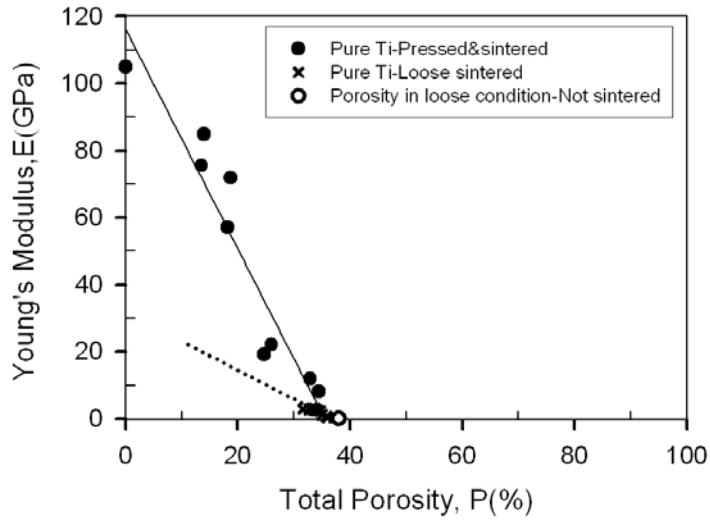


(b)

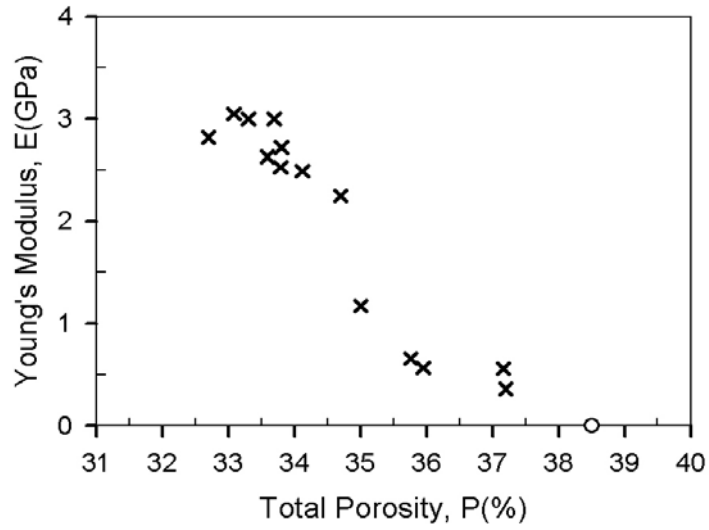
**Figure 4.20** Comparison of mechanical properties of porous pure titanium compacts produced with the literature data, (a) Young's modulus-porosity relation, (b) Yield strength-porosity relation.

Figures 4.21 and 4.22 show the change of Young's modulus with porosity in porous titanium and Ti-6Al-4V alloy samples sintered either in loose or pressed condition. As can be seen clearly, Young's modulus is inversely proportional to porosity content and approaches to nil at the percolation limit, where the material no longer behaves as a solid. Similar trend has also been observed in yield strength-porosity relations, Figure 4.23 and 4.24. The maximum attainable porosity in powder sintering is limited to tap porosity (porosity of powders in loose condition before sintering), which depends primarily on the shape and the size distribution, (packing type, i.e. cubic stacking or rhombohedral stacking) characteristics of initial powders. As can be seen, the porosities at which the Young's Moduli and yield strength values are zero correspond to tap porosities of ~38.5 and ~39.0 % for spherical titanium and Ti-6Al-4V alloy powders, respectively, which are called critical porosities ( $P_c$ ) in Percolation Theory and generalized mixture rule (GMR) [106].

As stated previously and seen especially in Figures 4.21 (a), 4.22 (a) and 4.23 (a), in the same porosity range, mechanical property-porosity relations of loose powder sintered samples, shown by dashed lines, seem to be different than that of samples sintered in pressed condition. As it has been shown in Figure 4.9, in the same porosity level neck size of loose powder sintered samples are lower compared to pressed and sintered samples. Moreover, neck curvature in loose powder sintered samples is very sharp, which may result in early yielding at very low loads due to the presence of stress concentrations leading to elastic moduli that are lower than expected.

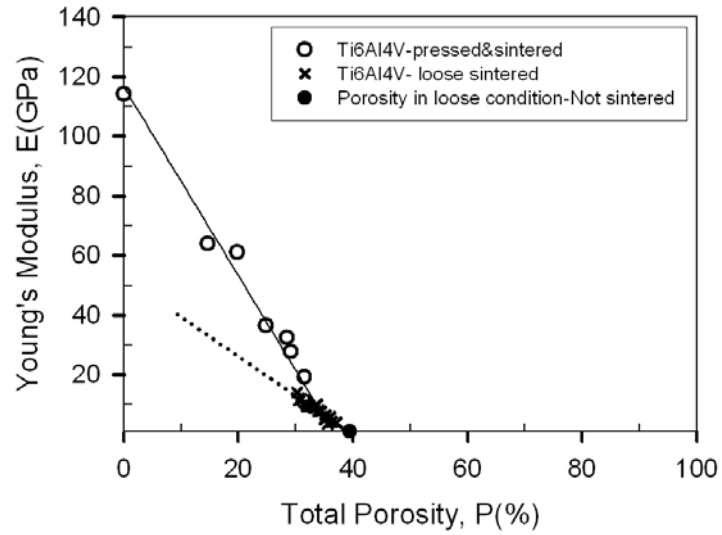


(a)

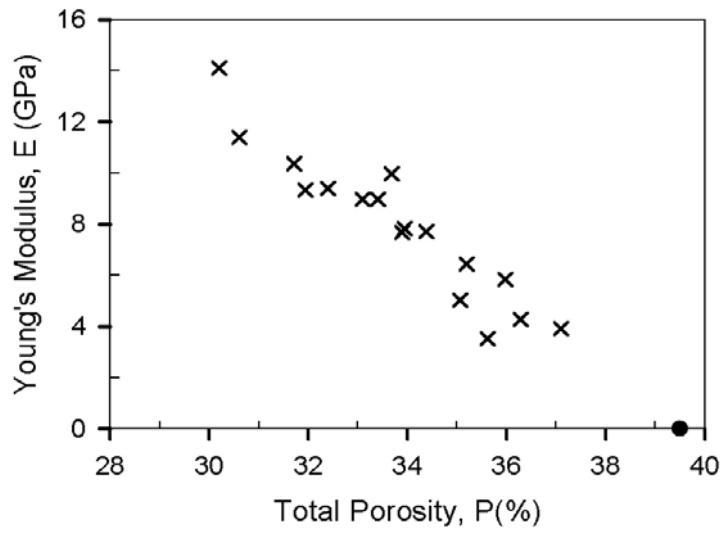


(b)

**Figure 4.21** Change of Young's Modulus with porosity, (a) Pure titanium (sintered in loose and pressed condition), (b) Pure titanium (loose powder sintered).

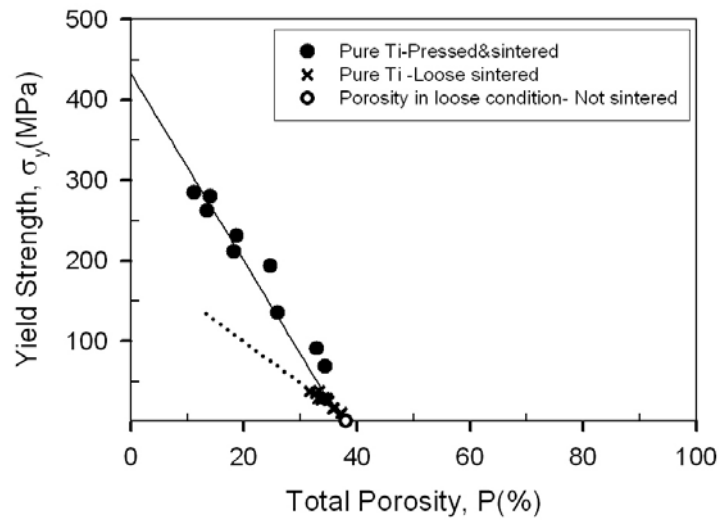


(a)

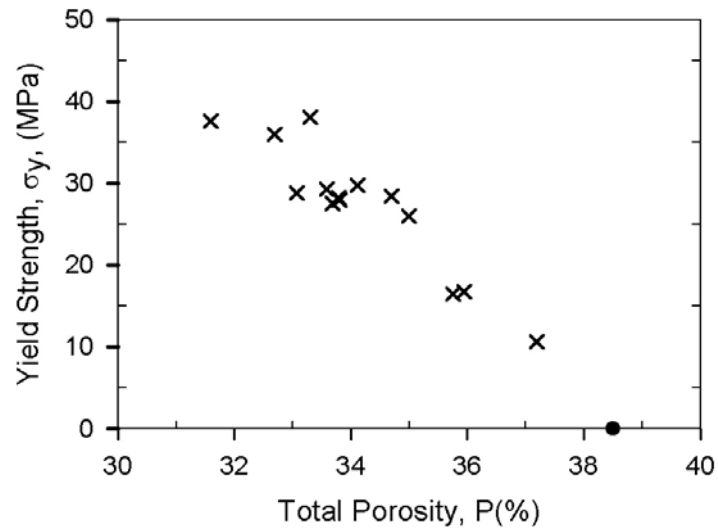


(b)

**Figure 4.22** Change of Young's Modulus with porosity, (a) Ti-6Al-4V (sintered in loose and pressed condition), (b) Ti-6Al-4V (loose powder sintered).

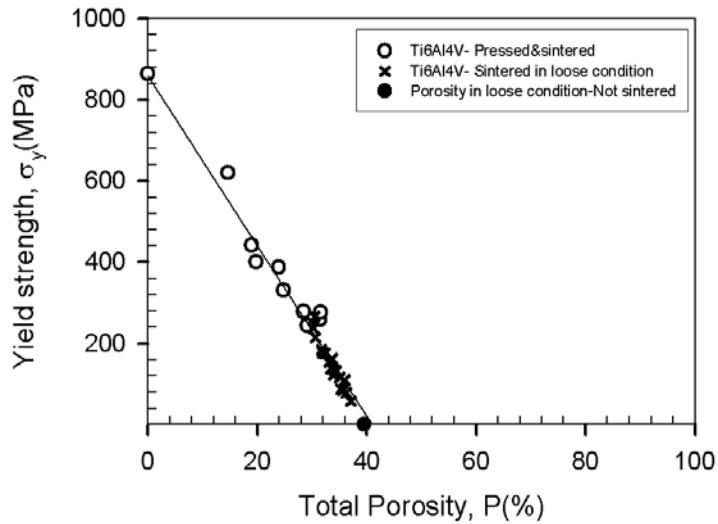


(a)

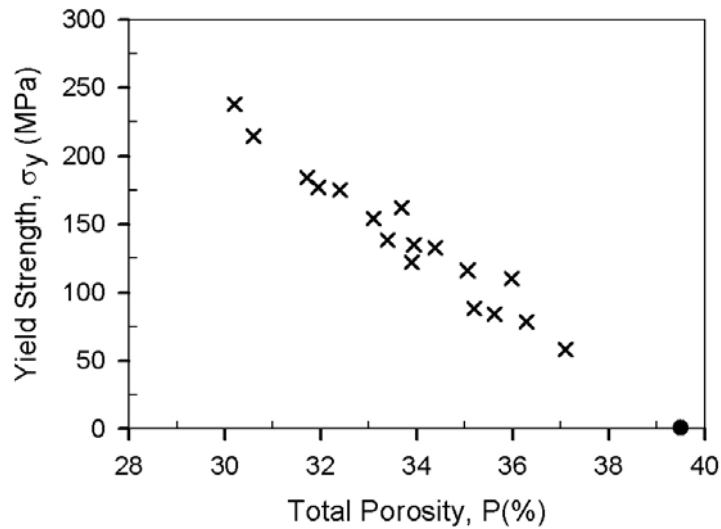


(b)

**Figure 4.23** Change of yield Strength change with porosity, (a) Titanium (sintered in loose and pressed condition), (b) Titanium (loose powder sintered).



(a)



(b)

**Figure 4.24** Change of yield Strength change with porosity, (a) Ti-6Al-4V (sintered in loose and pressed condition), (b) Ti-6Al-4V (loose powder sintered).

As summarized previously in Section 2.6.2, minimum solid area model, stress concentration approach and the effective flaw size approach [109] have been utilized to investigate the mechanical property-porosity relation. Moreover, some studies on this subject have focused on the empirical relations, which contain constants related with pore geometry, stacking type of powders, etc. and obtained by

fitting of curves using regression analysis on experimental data. However, most porous bodies contain more than one type of porosity, e.g. partially sintered bodies of various particle sizes and packings result in varying porosity character. Moreover, pore character in materials is not static and changes with the amount of porosity as sintering occurs and the co-ordination number of the particles increases. Thus, models based on a single, fixed, porosity may deviate from actual data, due to neglecting the original geometry, the initial mix of porosity (tap porosity), or its change with porosity.

The use of stress-concentration models in the present study is not appropriate since they were derived for highly porous materials having porosities up to 90-95 %, such as the materials produced by space holder technique. Properties obtained experimentally will be compared with the theoretical in the following and empirical relations predicted in literature to determine the best relation indexing the mechanical property and porosity.

In literature, the power law relation defined by Phani [117, 129] is mostly used for indexing the relative property with respect to porosity and given as;

$$\frac{M}{M_o} = \left(1 - \frac{P}{p_c}\right)^n \quad (4.5)$$

M : property of porous material

M<sub>o</sub> : property of bulk material

P : porosity fraction

P<sub>c</sub> : critical porosity fraction

n in equation 4.5 is defined as a parameter that depends on pore shape, pore distribution. Computational studies predicts n=2.1. However, this characteristic exponent n was found to vary in the range of 1.1-1.7 in most of the best fitting studies. Low value of n was explained by the low strength values of the bonds (necks) created due to high concentration of the surface inhomogeneties, cracks and impurities.

Best fitting curves to experimental Young's Modulus data of samples sintered in loose and compacted condition in the present study give Equations 4.6 and 4.7 for pure titanium and Ti-6Al-4V alloy samples, respectively.

$$E = 115.8 - 3.29 * P(\%) \quad R^2 = 0.945 \quad (4.6)$$

$$E = 113.8 - 3.1 * P(\%) \quad R^2 = 0.973 \quad (4.7)$$

Rearranging of equations 4.6 and 4.7 result in relations similar to Equation 4.5;

$$\frac{E_{\text{titanium}}}{115.8} = 1 - \frac{P(\%)}{35.2} \quad (4.8)$$

$$\frac{E_{\text{Ti6Al4V}}}{113.8} = 1 - \frac{P(\%)}{36.6} \quad (4.9)$$

Similar relations were also obtained for the change of yield strength with porosity content as given by Equations 4.10 and 4.11, for titanium and Ti-6Al-4V alloy samples, respectively.

$$\sigma_y = 432.4 - 11.6 * P(\%) \quad R^2 = 0.96 \quad (4.10)$$

$$\sigma_y = 858.5 - 21.8 * P(\%) \quad R^2 = 0.972 \quad (4.11)$$

Rearranging of Equations 4.10 and 4.11 yields,

$$\frac{\sigma_{y,(Ti\ titanium)}}{432.4} = 1 - \frac{P(\%)}{37.23} \quad (4.12)$$

$$\frac{\sigma_{y,(Ti6Al4V)}}{858.5} = 1 - \frac{P(\%)}{39.4} \quad (4.13)$$

The exponent  $n$  was found to be one, which is defined as the upper limit of the porosity dependence of properties.

The chemical composition of the titanium powders used in the present study is in the range of Grade 3 and Grade 4 titanium. Reported compressive modulus and yield strength values for Grade 3 titanium are 110 GPa and 450 MPa, respectively. Whereas, the corresponding values are 110 GPa and 480-552 MPa for Grade 4 titanium, which has a bit higher oxygen content compared to Grade 3 and similar composition to the powder used in the present study. On the other hand, yield and compressive strength values of Ti-6Al-4V powders used in the present study have been found as 114 GPa and 865 MPa using bulk Ti-6Al-4V-ELI alloy having similar oxygen content and lamellar microstructure.

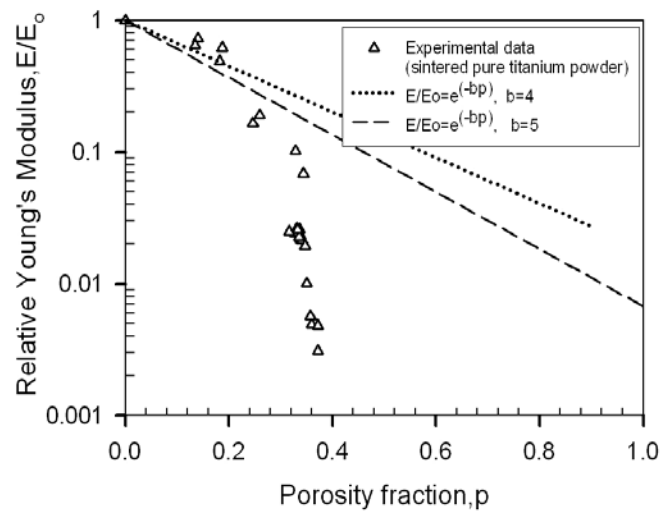
As can be seen from Equations 4.8 and 4.9, elastic moduli values predicted from the data of sintered samples, i.e. 116 and 114 GPa for pure titanium and Ti-6Al-4V alloy, respectively, are similar to that of bulk materials. On the other hand, for the sintered titanium and Ti-6Al-4V alloy, linear extrapolation of yield strength versus porosity data to zero porosity content give values around 432 and 856 MPa for titanium and Ti-6Al-4V, which are close to the strength of corresponding bulk materials. As it can be seen, linear relations derived for the titanium alloy were better, Figure 4.24 (a) and Equation 4.13.

In addition to the empirical models, MSA models may also be used for indexing mechanical property-porosity relation, in which minimum solid are defined as the bond areas between solid particles. In the low porosity range, in some studies variation of relative mechanical property with fractional porosity ( $p$ ) of samples has been shown to obey the relation:

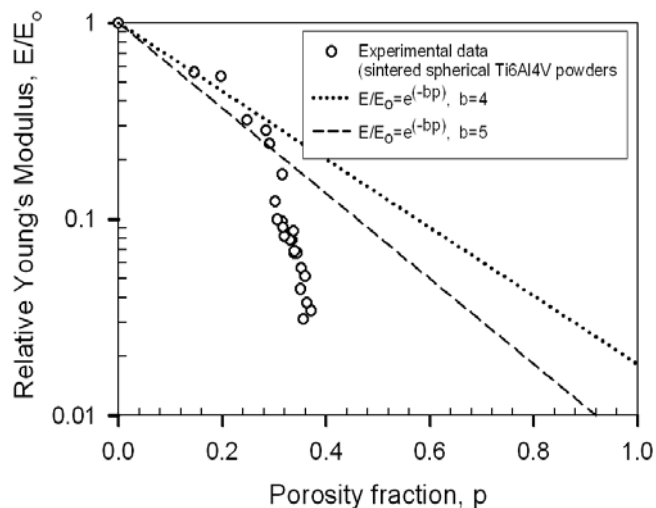
$$\frac{M}{M_0} = e^{-bp} \quad (4.14)$$

where,  $M$  and  $M_0$  are the mechanical properties of porous and bulk metal, respectively. The value of 'b' is varied with assumed idealized packing geometry in bodies. The basic characteristic of the MSA model is that on a semi-log plot of the property versus the porosity ( $p$ ), the minimum solid area (and hence the pertinent

property of interest) decreases first, approximately, along a straight line and then starts decreasing more rapidly, going to zero at a critical porosity ( $P_c$ ). It is obvious that the semi-log plots of Young's modulus and yield strength versus porosity as shown in Figures 4.25 and 4.26 have these features of MSA model. As can be seen, the experimental data lie between the 'b' value of 4 and 5. According to MSA model these values corresponds to solid spheres in cubic stacking.

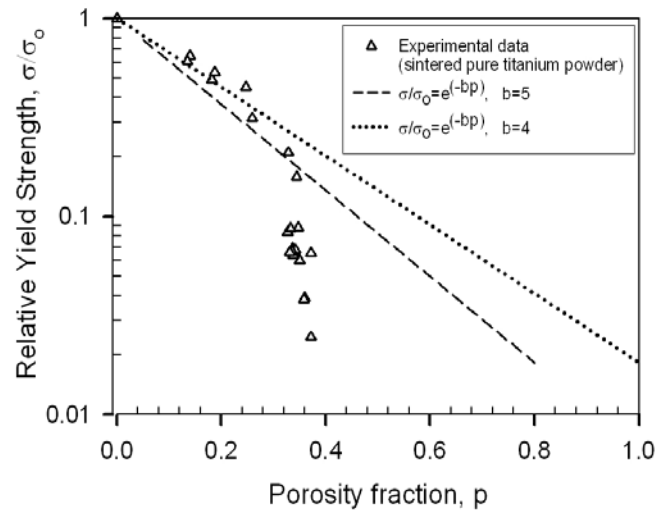


(a)

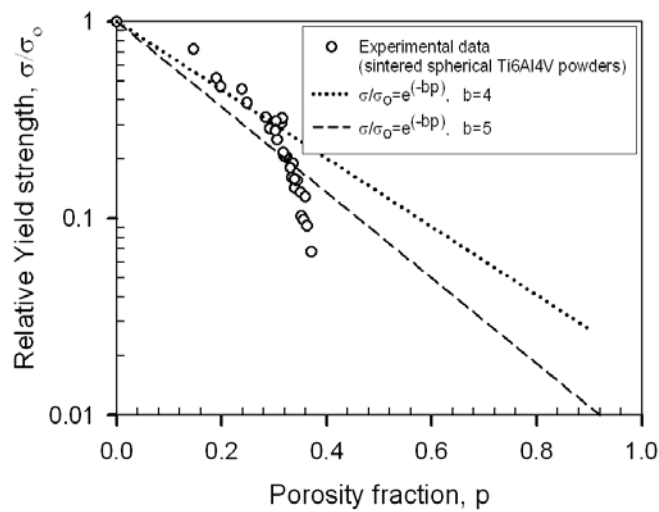


(b)

**Figure 4.25** Comparison of the experimental Young's moduli data with MSA models, (a) spherical pure titanium, (b) spherical Ti-6Al-4V.



(a)



(b)

**Figure 4.26** Comparison of the experimental yield strength data with MSA models, (a) spherical pure titanium, (b) spherical Ti-6Al-4V.

#### 4.1.4.3. Effect of Neck Size

As explained, during sintering inter-particle bonds in metals occur as a result of various transport mechanisms such as surface and bulk transport. Densification (decrease in porosity) is not essential for a material to strengthen. For example, surface diffusion promotes neck growth without densification and leads to an

increase in the compact strength. Therefore, strengths of the powder metallurgy parts arise from the degree of bonding between contacting particles. Sensitive control of sintering temperature and time make it possible to adjust porosity, neck size and the resulting strength values of the metals.

As can be seen from stress-strain curves of porous titanium and Ti-6Al-4V alloy samples, Figures 4.14, investigated mechanical properties, i.e. yield strength, improve as the sintering temperature increase. As previously discussed, in many of the models used for indexing the mechanical properties, porosity content was taken as a single variable affecting the mechanical property. However, such a relation is somewhat misleading since the neck size may be different in the same porosity range because of the differences in sintering characteristics of various sintering techniques, i.e. loose powder sintering, cold compaction and sintering. In the present study, it was shown in Figure 4.9 that the average neck size ratio ( $X/D$ ) of pressed and sintered samples are higher than that of powder samples sintered loosely in the same porosity range, i.e. around 30 %. Pressed and sintered samples' higher neck size ratio compared to loose powder sintering was attributed to the higher contact area prior or during sintering, which result in enhanced diffusion rate. A similar result was obtained in the study of Yeheskel et al. [133], in which they sintered prealloyed  $\gamma$ -TiAl powder using cold and hot isostatic pressing. They have found that there was a shift in the properties in the same porosity levels for different techniques.

As previously stated, when a load is applied to a porous metal deformation localizes on minimum solid area (MSA), which is the projection of the actual sintered area (neck diameter) between the particles normal to the stress. MSA may be calculated either theoretically or by direct measurement of the bond diameter on the fractured surfaces of sintered samples as it was done in the present study. Based on the MSA model porous specimens with higher degree of bonding are expected to have higher strength values leading to a correlation between the strength and the neck size.

As given in previous sections, Nice and Shaffer [136] predicted the sintered strength of porous materials by an empirical model yielding the relation;

$$\sigma = \sigma_0 A \left( \frac{X}{D} \right)^2 \quad (4.15)$$

where  $X/D$  is the neck size ratio (ratio of neck size to particle diameter),  $A$  is an empirical constant, and  $\sigma_0$  is the wrought material strength.

Similar to proposed model and studies carried out on this subject by Yeheskel et al. [133], Danninger [132] and Xu et al. [134] a good linear relationship was obtained between the experimental yield strength and  $(X/D)^2$  values for both pure titanium and Ti-6Al-4V alloy, where the strength goes to zero as  $(X/D)^2$  approaches to nil, Figure 4.27. The corresponding relations between square of neck size ratio and yield strength for pure titanium and Ti-6Al-4V alloy are given in equations 4.16 and 4.17, respectively. The differences in the slopes of these curves may arise from the differences in packing characteristics of powders, i.e., number of contacts, and inherent material properties.

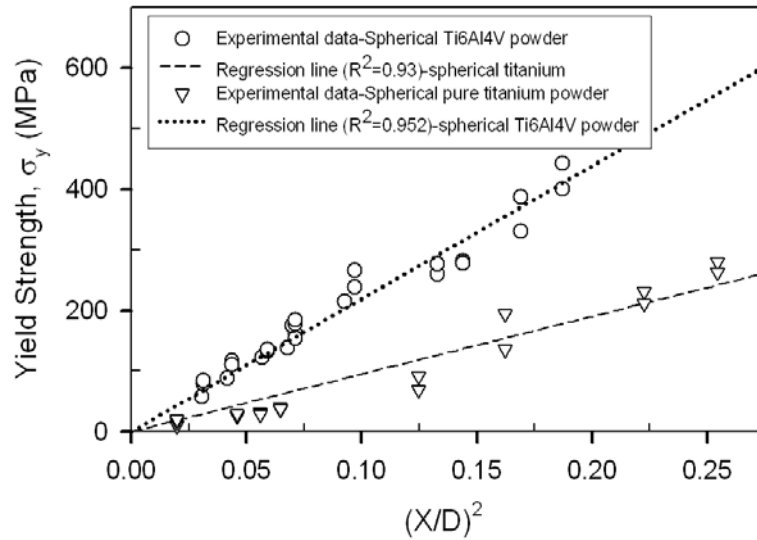


**Figure 4.27** Compressive yield strength versus the square of the neck size ratio  $(X/D)^2$  for porous titanium and Ti-6Al-4V powders.

$$\sigma_y(\text{titanium}) \cong 950.7 \left( \frac{X}{D} \right)^2 \quad R^2=0.93 \quad (4.16)$$

$$\sigma_y(\text{Ti6Al4V}) \cong 2190.3 \left( \frac{X}{D} \right)^2 \quad R^2=0.952 \quad (4.17)$$

The empirical relation given by Equation 4.15 was developed by German [137, 138] and Xu et al. [134, 139] and the proportionality constant A was clarified as;

$$A = \sigma_o V_s \frac{N_c}{K\pi} \quad (4.18)$$

where,

$\sigma_o$  : strength of bulk material

$V_s$  : solid fraction

$N_c$  : coordination number

K: stress concentration factor

By dividing Equations 4.16 and 4.17 by yield strength values of bulk titanium and Ti-6Al-4V alloy, which are about 432 and 864 MPa, respectively, we get similar values for the constants A, i.e., 2.2 and 2.5, which involve the effect of solid fraction, coordination number and stress concentration factor according to proposed model.

Stress concentration effects are significant only in brittle materials such as ceramics and glasses failing from pores, i.e., when isolated (large) pores act as the fracture origin [140]. The stress concentrations decrease when going from homogeneous uniaxial tension, to tension from bending, to homogeneous uniaxial compression. Thus, upon loading of a porous material in compression stress concentration may have very little effect on yield and ultimate strength of the material. In fact, there is no concentration of the compressive stress for spherical

pores, only the occurrence of a localized tensile stress whose maximum equals the value of the applied compressive stress [141].

## **4.2. Space Holder Technique**

### **4.2.1. Production Details and Pore Characters**

As it was explained previously, spacer particles utilized for manufacturing of titanium or titanium alloys are divided mainly into two groups: Thermally removable and water soluble. Carbamide (urea) [56, 92, 96], and ammonium hydrogen carbonate [56, 57, 93, 94] are the most frequently used spacer particles, which are removed by thermal treatment at low temperatures, i.e. at around 200°C. Polymer granules used as space holder, [7] are generally removed by combination of chemical and thermal treatment at around 130°C. Although these spacers dissociate at low temperatures it is not possible to remove all of the spacer without increasing the temperature sufficiently. Hydrogen, oxygen and nitrogen present in these spacer particles start to dissolve in titanium or titanium alloy and cause contamination as temperature is increased, which affects the foaming process and/or the mechanical properties adversely. In addition to these, spacers having low dissolution/melting point may cause the collapse of cell walls during their removal due to insufficient sintering. Similar disadvantages may exist during foaming by water-soluble spacers.

To prevent the oxidation of titanium parts during foaming, oxygen partial pressure in the sintering atmosphere should be reduced to below  $10^{-24}$  atm as seen in Figure A.2, however, this is not attainable physically by vacuum systems. Having more affinity for oxygen compared to titanium makes magnesium itself a self-protector. During the sintering experiments, at 1200°C, the partial pressure of oxygen in the crucible is calculated to decrease down to  $10^{-32}$  atm. due to the presence of magnesium vapor. Apart from these, it becomes possible to produce titanium foams without collapse of the cell walls since magnesium is removed at

higher temperatures compared to urea and ammonium hydrogen carbonate due to its high melting point, 650°C.

In the present study, using magnesium as space holder, highly porous, magnesium free samples of titanium and Ti-6Al-4V alloy were manufactured, Figure 4.28. Diffraction charts showing the indices of peaks of  $\alpha$  and  $\beta$  phases are given in Figures 4.29 and 4.30, for the as-received pure titanium and Ti-6Al-4V powders as well as for the foams manufactured from the corresponding powders. Microstructural examination carried out on the cross-sections of as-received powders of titanium and Ti-6Al-4V alloy revealed only  $\alpha$ -phase, and this is confirmed by XRD patterns shown in Figure 29 (a) and Figure 30 (a). Since Ti-6Al-4V alloy is classified as  $\alpha+\beta$  alloy theoretically calculated  $\beta$  peaks are also shown in Figure 30 (a) for comparison. As a result of binder (PVA) removal at 600°C, and sintering and removal of magnesium at 1200°C neither a binder residue in the form of oxides/nitrides nor free magnesium was detected in the manufactured foam samples.

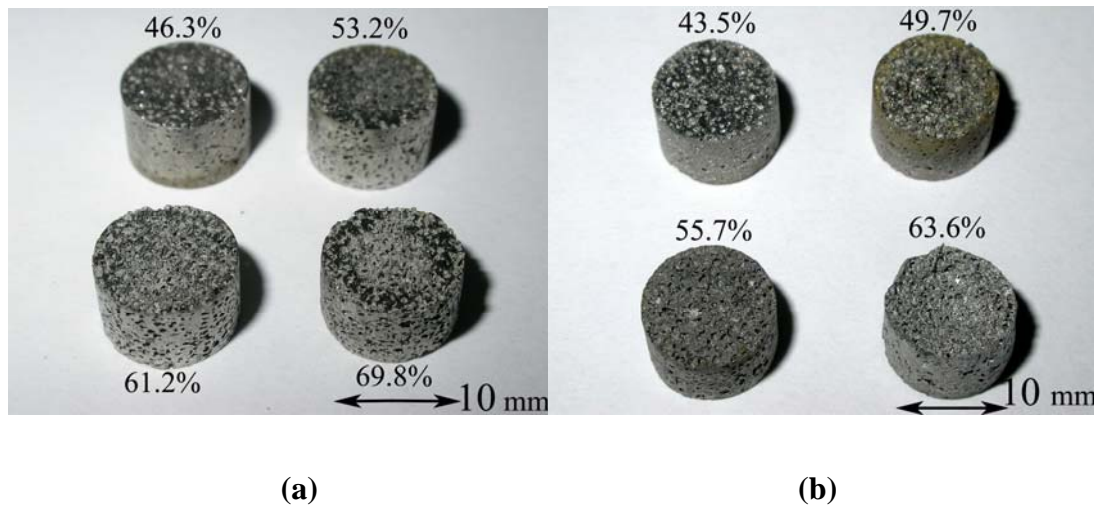
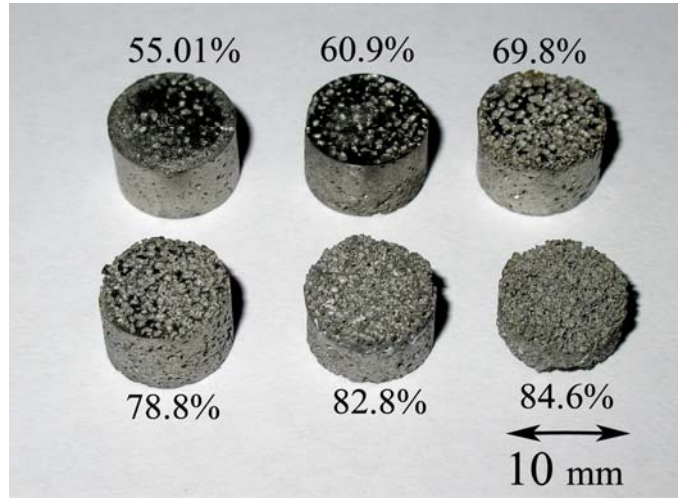
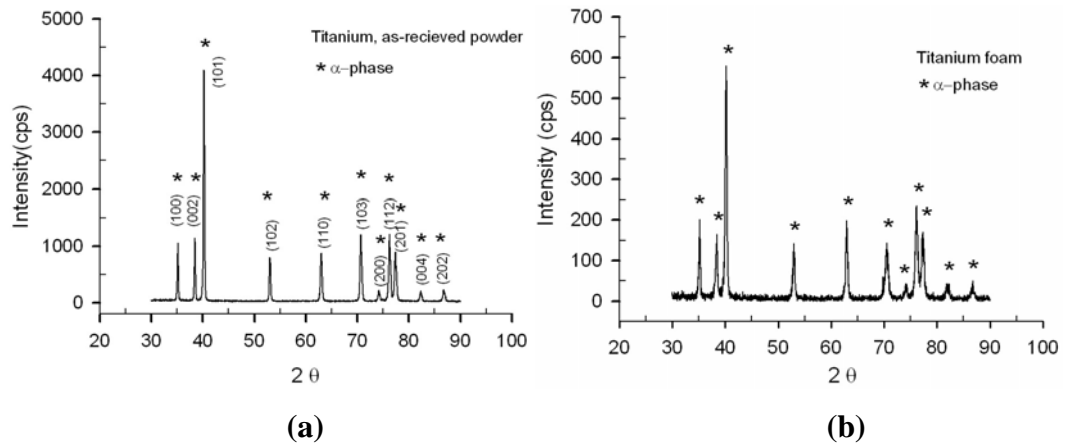


**Figure 4.28** Foams manufactured by space holder technique, (a) Pure titanium, (b) Ti-6Al-4V(spherical), (c) Ti-6Al-4V (angular).



(c)

**Figure 4.28 (cont.)** Foams manufactured by space holder technique, (a) Pure titanium, (b) Ti-6Al-4V(spherical), (c) Ti-6Al-4V (angular).



(a)

(b)

**Figure 4.29** X-Ray Diffraction charts of; (a) As-received titanium powder, (b) Titanium foam manufactured by space holder technique.

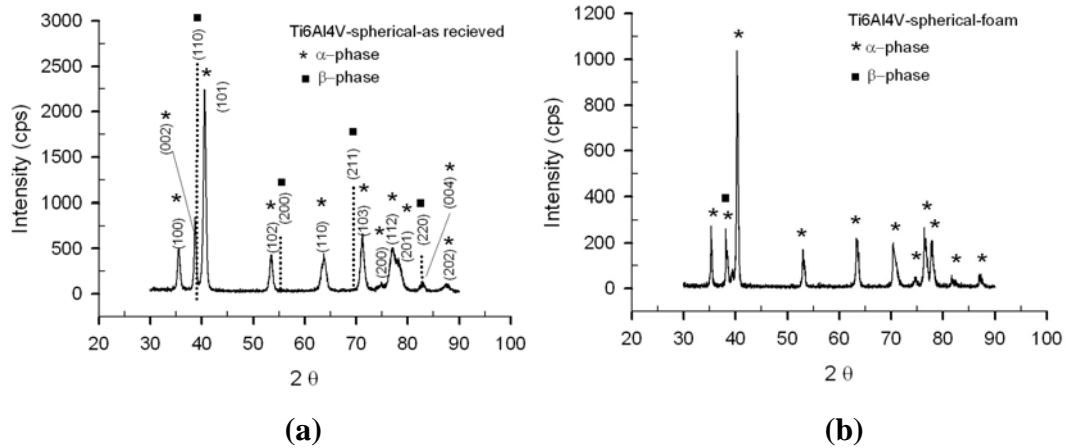


**Figure 4.30** X-Ray Diffraction charts of; (a) As-received spherical Ti-6Al-4V powder, (b) Ti-6Al-4V foam manufactured by space holder technique.

Foams with porosities in the range 45 to 85 % were manufactured from titanium, Ti-6Al-4V Alloy (spherical) and Ti-6Al-4V Alloy (angular) using magnesium powder in the range 30-90 % in volume. Final porosities after removal of magnesium were generally different from the prior magnesium contents present in compacts before foaming experiments. The porosities of the titanium foams produced using urea [56, 92, 96], ammonium hydrogen carbonate [56, 57, 93, 94] or polymer granules [7] are usually limited to 80 % due to excessive collapse of the cell walls at higher spacer particles contents. As mentioned in the previous chapters, higher levels of porosities, i.e. 90-95 %, may be achieved by melt processing foaming techniques. However, extreme chemical affinity of titanium and its alloys with atmospheric gases (i.e. oxygen and nitrogen), which dissolve rapidly above 400°C, makes liquid processing difficult.

Figure 4.31 shows the achieved porosities in compacts of titanium and Ti-6Al-4V alloy containing various amounts of magnesium prior to foaming experiments.

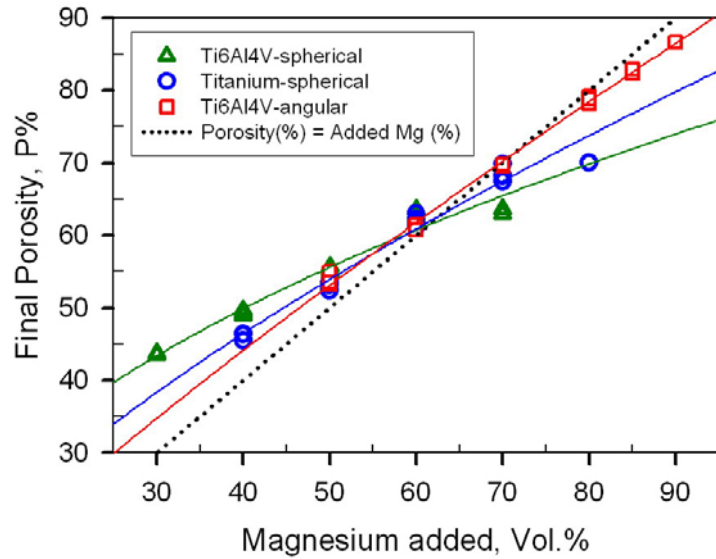


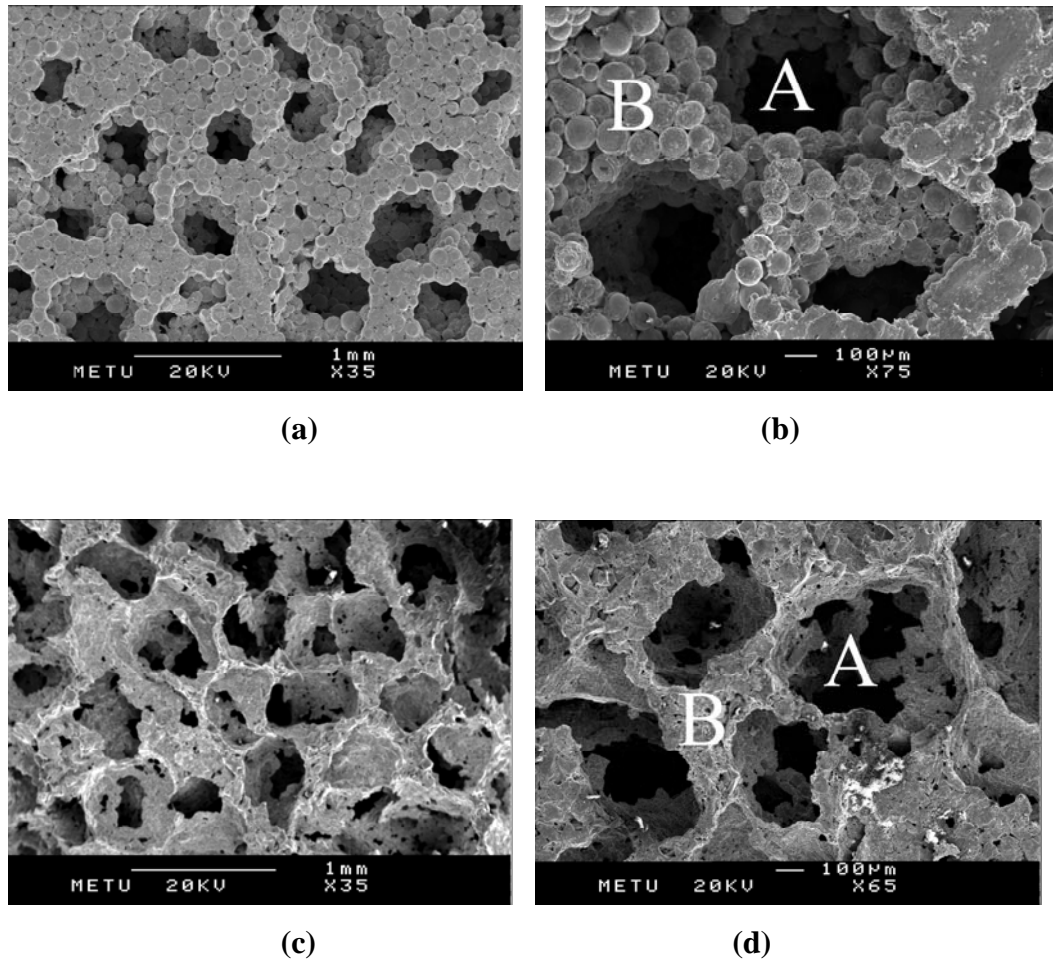
**Figure 4.31** Change of total porosity with initial magnesium content in compacts of different types of powders.

As can be seen, for all samples, i.e. either containing spherical or angular, titanium or Ti-6Al-4V powder, there is a limiting or critical magnesium content, which determines whether the compact will collapse or will have higher porosity than the utilized magnesium content. These critical volume percentages of magnesium were found around 64, 62 and 70 % for spherical titanium, spherical Ti-6Al-4V and angular Ti-6Al-4V alloy powders, respectively. Below the corresponding critical values, the resultant porosities were observed to be higher than the evaporated magnesium volume fraction. The difference between final porosity and evaporated magnesium content is highest for samples containing spherical Ti-6Al-4V powders (with average particle size of 107  $\mu\text{m}$ ) and lowest in the case of angular Ti-6Al-4V powder (with average particle size <74  $\mu\text{m}$ ). The excess amount of porosity was attributed to the pores left from partial sintering of titanium and Ti-6Al-4V powders on the cell walls of foams. As the size of the powders used in cell struts increases, the resultant porosity and pore size in the cell walls and edges also increase due to insufficient sintering. The factors, which determine the critical magnesium content and subsequent total porosity and shape change are the size and the shape of the powders used in cell walls and cell edges.

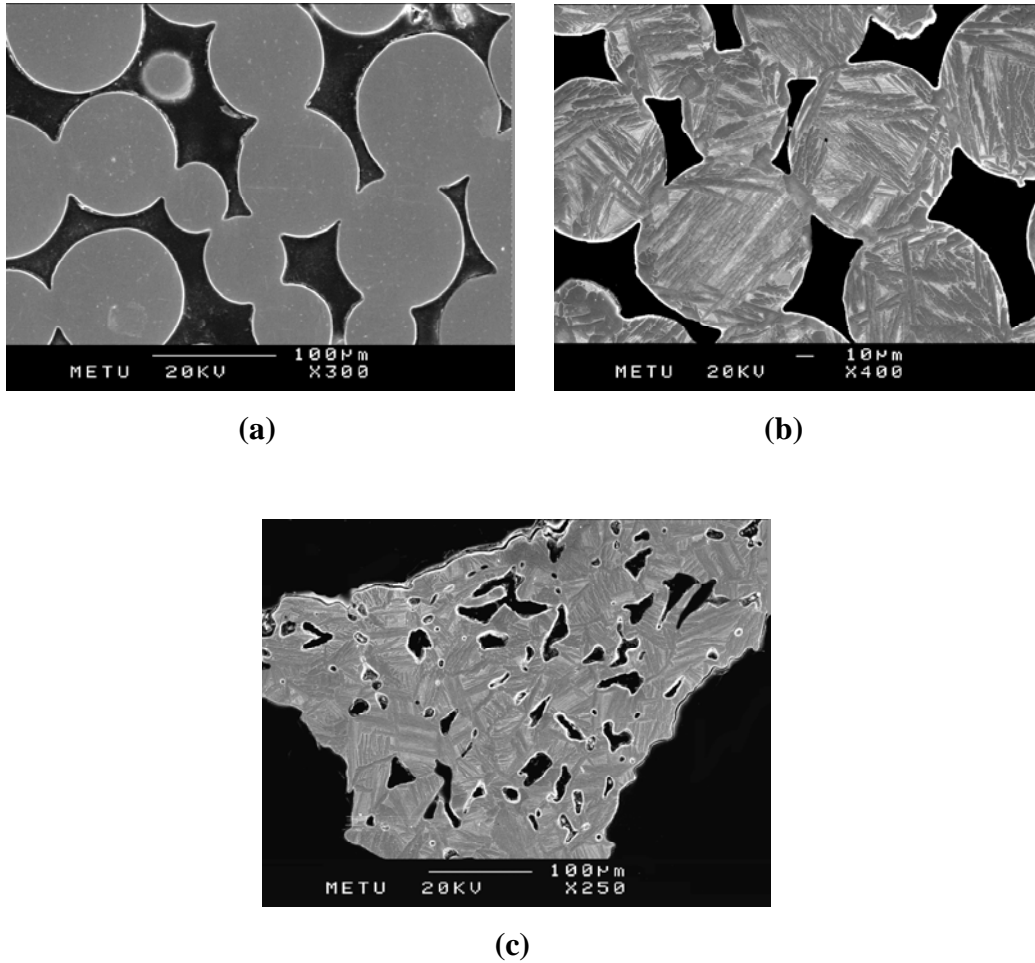
Excessive collapse was observed in the compacts of spherical Ti-6Al-4V powders with 70 % magnesium. On the other hand, collapse of spherical titanium samples was not observed up to 80 % magnesium. However, in samples containing angular powders of Ti-6Al-4V a small homogenous shrinkage was observed even at very high magnesium contents. Normally, as the amount of magnesium increases, titanium/Ti-6Al-4V powder particles becomes insufficient for homogenous coverage of the surface of the magnesium powders as long as the magnesium particles are not very large. Because of that, the powder particles used in foaming experiments should be as small as possible to achieve higher porosities in compacts. Insufficient coverage of magnesium powders or non-homogenous distribution, which is observed especially in powder mixtures containing spherical titanium/Ti-6Al-4V powders lead to collapse of cell walls and edges. Collapse in samples is mainly due to combined effect of melting/evaporation of magnesium and sintering shrinkage. If it could be possible to remove some of the magnesium below its melting point, collapsing would be prevented. Preliminary experiments conducted on compacts of Ti-80 vol. % Mg and Ti-6Al-4V(spherical)-70 vol. % Mg powder mixtures, which were observed to collapse, have shown that the degree of collapse may be lowered by keeping the compacts at temperatures around 635-640°C, near the melting point of magnesium, long enough, i.e. ~ 5 hrs. In this way, some of the magnesium, which melts and evaporates at high temperatures, would be removed slowly prior to sintering and evaporation step. Experiments have also shown that compaction pressure had very limited effect on preventing the collapse of samples. Only the surfaces of the compacts gain strength mainly due to frictional effects, while the centers collapse during foaming.

Figure 4.32 shows the structure of the manufactured titanium and Ti-6Al-4V foams. The foams were observed to contain mainly two types of pores: macropores obtained as a result of evaporation of magnesium particles, and micropores on cell walls, due to incomplete sintering of titanium powders. Although the macro pores, region A in Figure 4.32 (b) and 4.32 (d), are isolated from each other in all closed cellular samples, they are in fact connected through the micro pores present between the partially sintered powders in cell walls and edges, region B Figure 4.32 (b) and 4.32 (d) and Figure 4.33. The macro pores become connected above a specific

porosity content, which varies with the type of powder used in cell struts, and amount and size of the magnesium spacer. The terms open and closed porosity will be used for inter-connectivity of macro pores in the rest of this section.



**Figure 4.32** SEM micrographs showing, (a) Structure of titanium foam (61.2% porosity), (b) Macro and micro pores present in titanium foam, (c) Structure of Ti-6Al-4V (angular) foam (78.8% porosity), (d) Macro and micro pores present in Ti-6Al-4V (angular) foam.



**Figure 4.33** Micro pores in the cell walls containing micro pores, (a) Titanium foam, (b) Ti-6Al-4V (spherical) foam, (c) Ti-6Al-4V (angular) foam.

In fact, it is difficult to distinguish the size of the micro and macro pores using quantitative metallographic techniques since it requires several image-processing steps. However, pore size measurements carried out in samples sintered in loose and compacted condition without spacer particles using mercury porosimetry could be used as rough estimates of the upper limit of micro pore size in foams because pore structures and sinter bonds were similar to that cell walls of the manufactured foams. As it has been shown in Figure 4.6 and 4.7 in Section 4.1.1, maximum pore size in samples sintered either in loose or compacted condition may reach up to 220  $\mu\text{m}$ . In this respect, pore size evaluations in samples produced using spacer particles were made in two separate ranges: micro pores in the range of

0-220  $\mu\text{m}$  and macro pores above 220  $\mu\text{m}$ . Figures 4.34-4.36 show the extent of micro and macro pore size distribution observed in some Ti-6Al-4V (angular), Ti-6Al-4V (spherical) and titanium foams, respectively. Since the macro pore structures in samples containing spherical Ti-6Al-4V alloy powders are rather irregular, only the pore morphology, size and porosity content of titanium and Ti-6Al-4V (angular) samples will be evaluated.

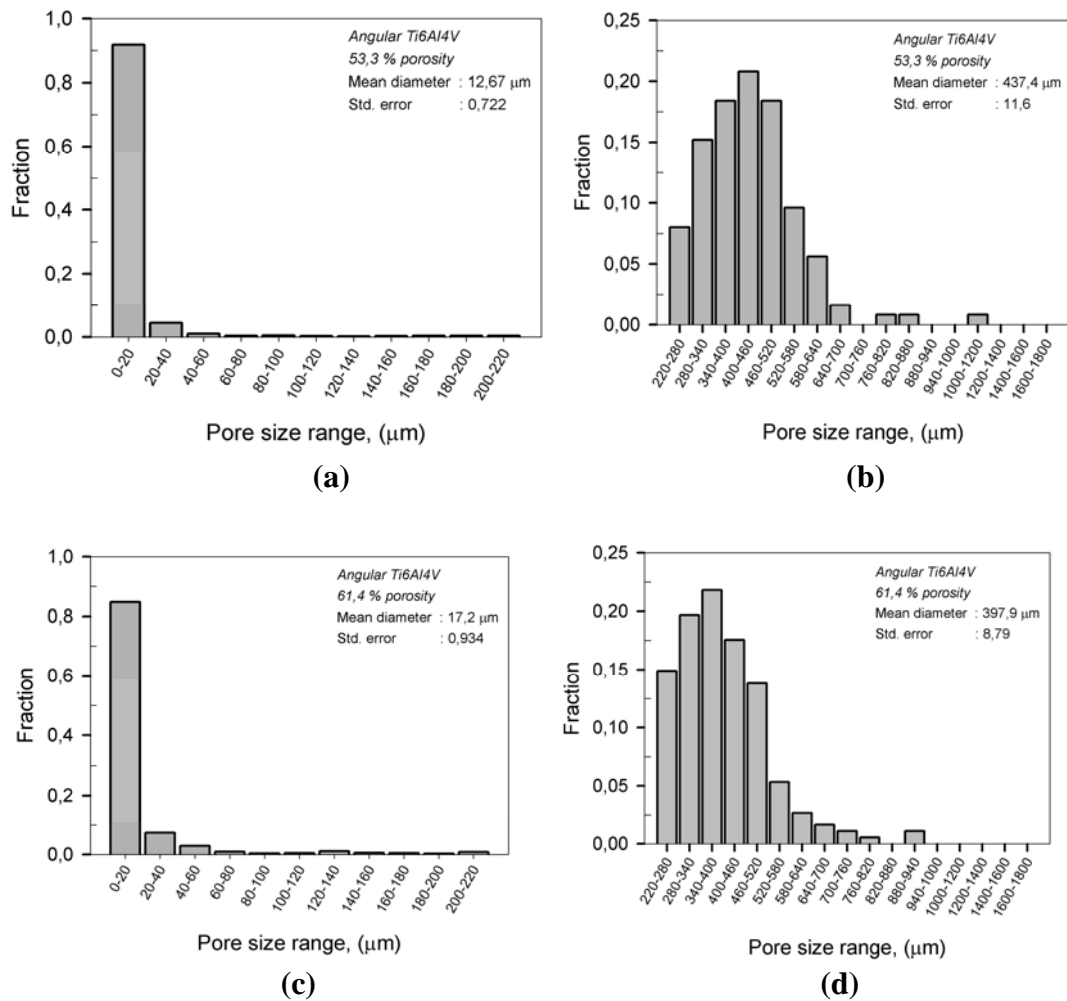
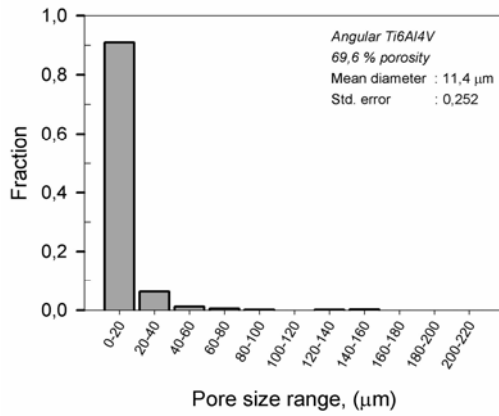
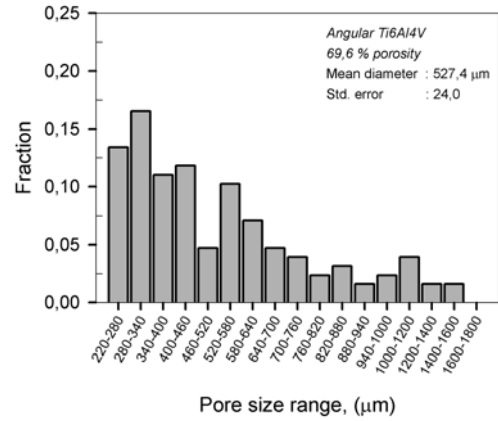


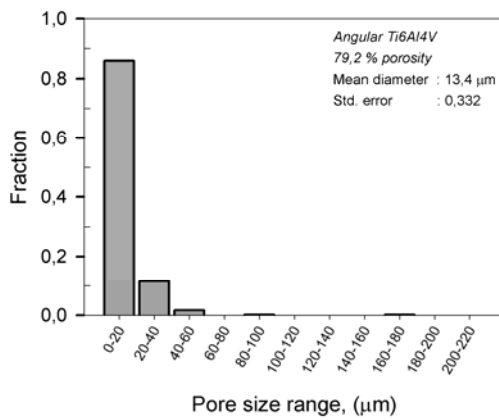
**Figure 4.34** Pore size distribution in Ti-6Al-4V (angular) foams ; (a), (c), (e), (g), (i) Micro pores left from incomplete sintering of angular powders, (b), (d), (f), (h), (j) Macro pores obtained by spacer particles.



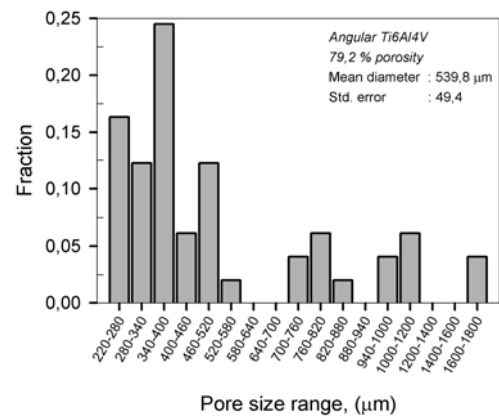
(e)



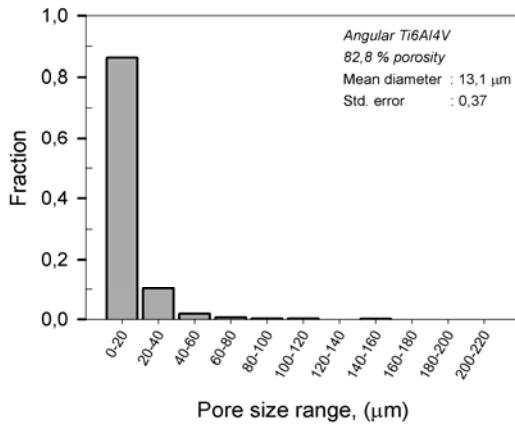
(f)



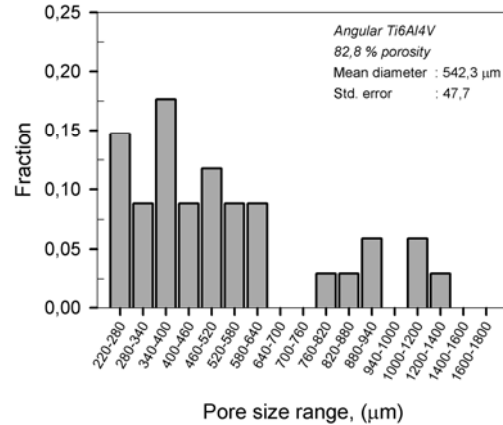
(g)



(h)

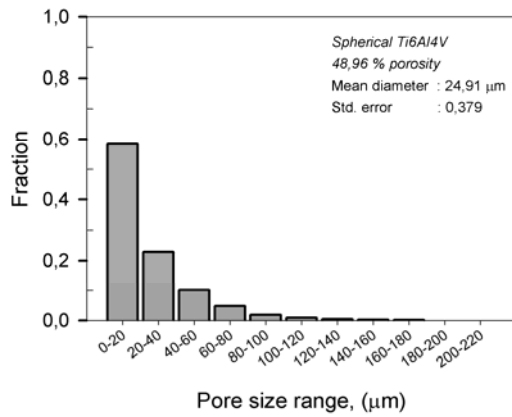


(i)

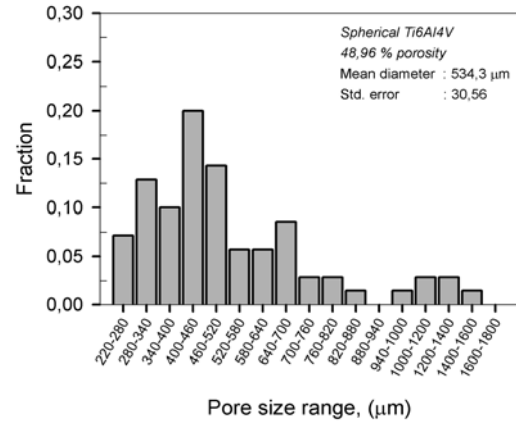


(j)

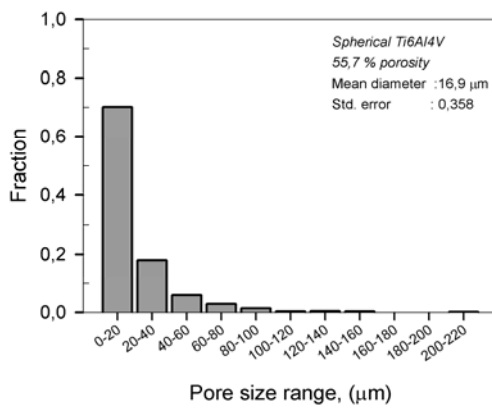
**Figure 4.34 (cont.)** Pore size distribution in Ti-6Al-4V (angular) foams ; (a), (c), (e), (g), (i) Micro pores left from incomplete sintering of angular powders, (b), (d), (f), (h), (j) Macro pores obtained by spacer particles.



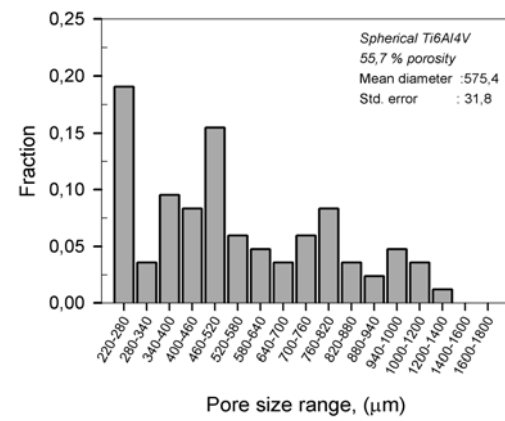
(a)



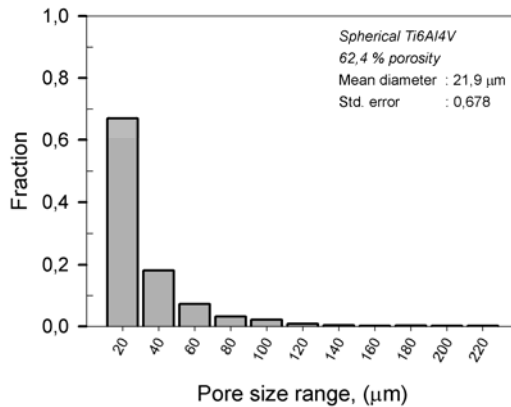
(b)



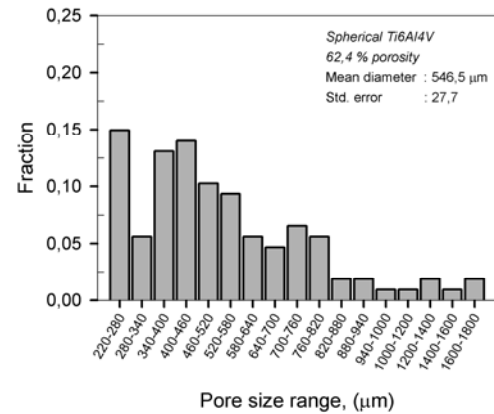
(c)



(d)

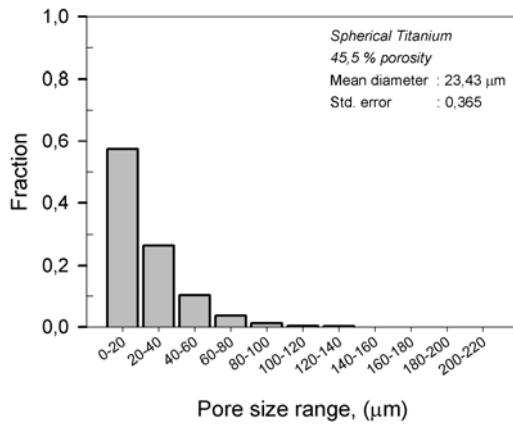


(e)

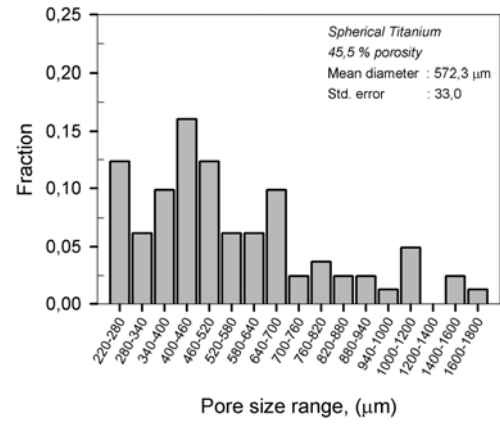


(f)

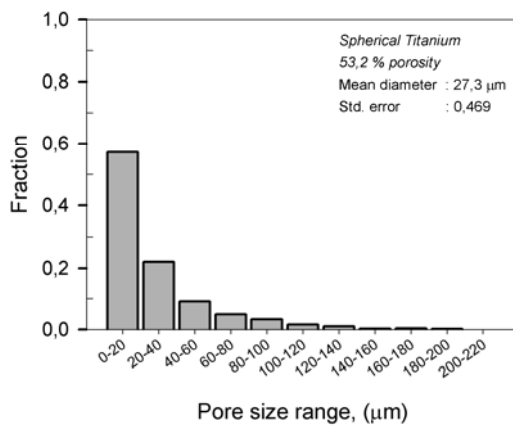
**Figure 4.35** Pore size distribution in Ti-6Al-4V (spherical) foams; (a), (c), (e) Micro pores left from incomplete sintering of spherical powders, (b), (d), (f) Macro pores obtained by spacer particles



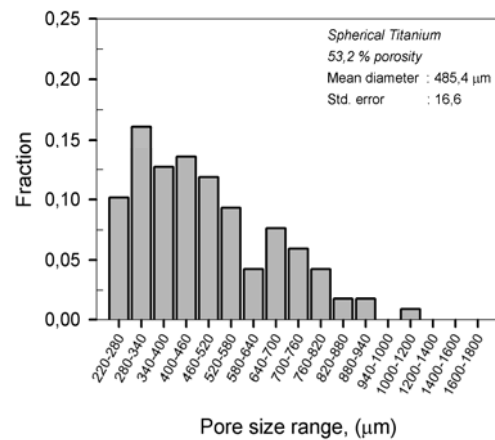
(a)



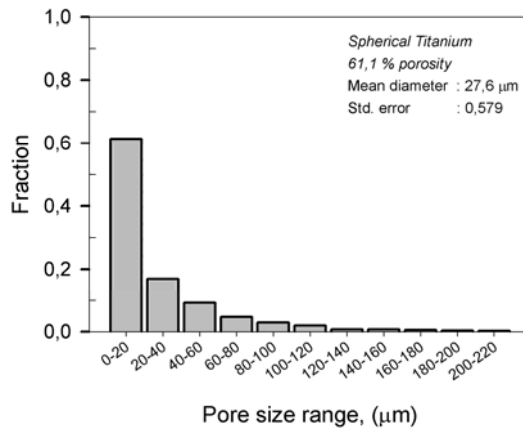
(b)



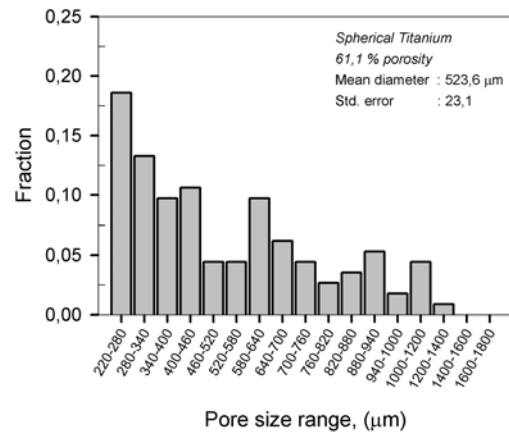
(c)



(d)



(e)



(f)

**Figure 4.36** Pore size distribution in titanium foams; (a), (c), (e), (g) Micro pores left from incomplete sintering of spherical powders, (b), (d), (f), (h) Macro pores obtained by spacer particles.

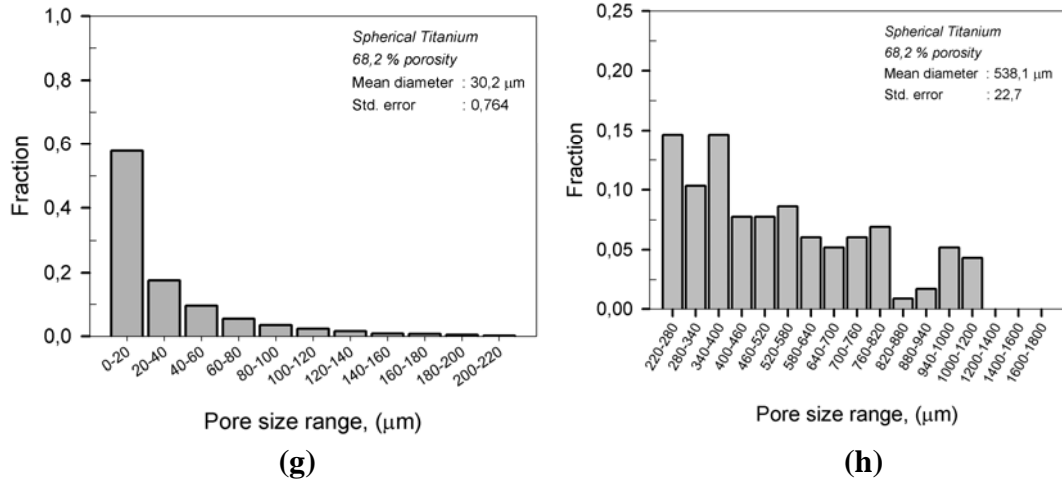


**Figure 4.36 (cont.)** Pore size distribution in titanium foams; (a), (c), (e), (g) Micro pores left from incomplete sintering of spherical powders, (b), (d), (f), (h) Macro pores obtained by spacer particles.

The majority of the micro pores present on the cell walls and edges of the foams were in the range of 0-40 μm. The average micro pore size was found to vary between 12-17, 17-25 and 23-30 μm for foams of Ti-6Al-4V (angular), Ti-6Al-4V (spherical) and titanium having total porosities in the range 53.3-82.8 %, 48.9-62.4 % and 45.5-68.2 %, respectively. As expected, the size of micro pores in cell walls and edges was smallest in samples containing angular Ti-6Al-4V powders because of higher degree of sintering due to smaller powder particle size. On the other hand, resultant average macro pore size was observed to vary depending on the amount of total porosity or initial magnesium content. As a result of connectivity of macro pores, pores as large as 1800 μm were observed to exist in all samples.

As porosity content of Ti-6Al-4V (angular) samples increased the average size of macro pores first decreased to ~397.4 μm (at 61.4 %), then reached to a value as high as ~542 μm as 82.8 % porosity is attained. Probably, in low porosity samples sintering shrinkage in cell walls and edges becomes dominant, while interconnection of macro pores in high porosity samples cause average pore size to be higher than the expected. In low porosity samples of Ti-6Al-4V (angular) alloy (53.3 and 61.4 vol. %), Figure 4.34 (b) and (d), macro pores size occasionally changed between ~ 220 and 700 μm, while macro pores as high as 1800 μm were observed to

exist in high porosity samples (~70-83 vol. %). The increase in the average size of macro pores is the indication of interconnection as seen in micrographs, Figure 4.37 (b).

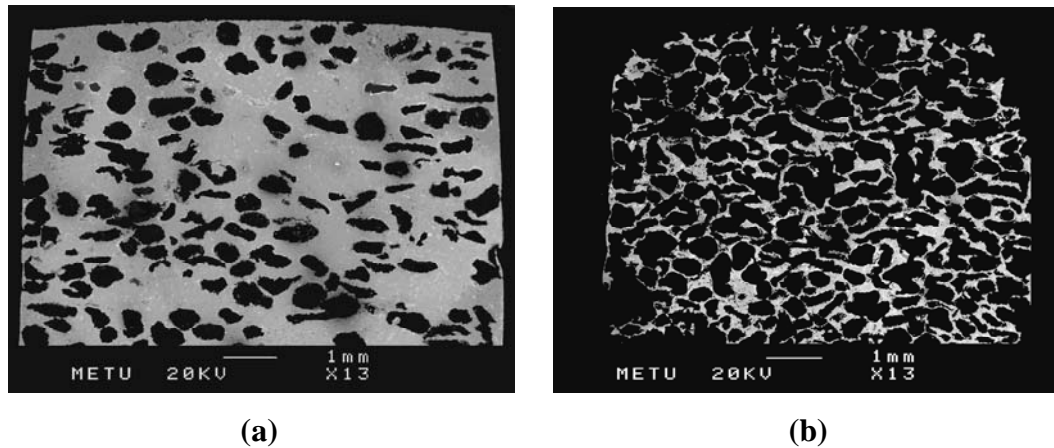


**Figure 4.37** Macro pore structure in Ti-6Al-4V (angular) foams, (a) 53.3 % porosity, (b) 82.8 % porosity.

Similar trend of change of macro pore size with increasing porosity, i.e. an initial decrease of average pore size followed by an increase in the average value, was also observed for pure titanium and Ti-6Al-4V (spherical) foam samples due to interconnectivity of macro pores, Figure 4.38 (b). However, this time broader size distribution, in the range of 220-1400  $\mu\text{m}$ , was observed in all type of samples. Moreover, minimum and maximum average pore size were found to be around 485 and 572  $\mu\text{m}$ , which are well above the average values of Ti-6Al-4V (angular) samples.

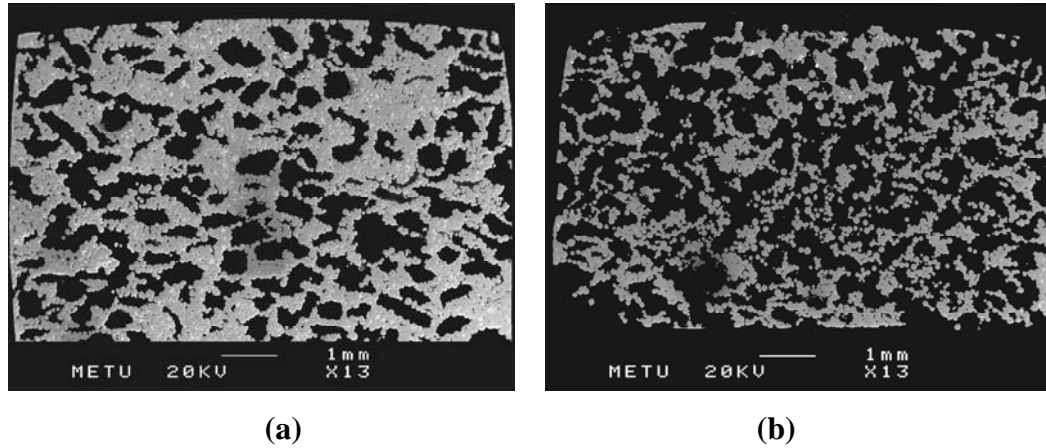


**Figure 4.38** Macro pore structure in titanium foams, (a) 53.2 % porosity, (b) 68.2 % porosity.

During mechanical characterization, two parameters of cellular materials need to be investigated: properties of each pore (size, shape and orientation) and topological properties such as arrangement and neighborhood relations. The volume fraction of material in nodes, edges and walls define the density of cellular materials. The numbers of nodes, cell edges and walls per cell, length, thickness and curvature of cell edges, shape of cell edge have influence on mechanical properties. However, in real foams these parameters are difficult to characterize, so that, agglomeration of solid material is generally tried to be investigated [7]. In the present study, the pore structures (Figure 4.32) in Ti-6Al-4V alloy foams containing angular powders were rather smooth and pores with open and closed morphology were uniformly distributed, and the cell walls were well-defined and had similar thicknesses. However, in samples of titanium and Ti-6Al-4V (spherical) foams, containing partially sintered network of spherical powders on the cell walls, the pore structures are quite irregular and complex. Cell wall and edge features such as thickness, which is important in determining the mechanical properties change with the total pore volume fraction and the size and shape of titanium and Ti-6Al-4V powder used. As expected, the thinnest wall was obtained in angular Ti-6Al-4V alloy samples and the thickness was observed to change from one powder size to several. The struts in manufactured foams generally have an hour-glass shape that the material is concentrated at cell nodes rather than the cell edges and the thickness of the cell

walls and edges were observed to decrease from cell node to cell edge center, Figure 4.39.

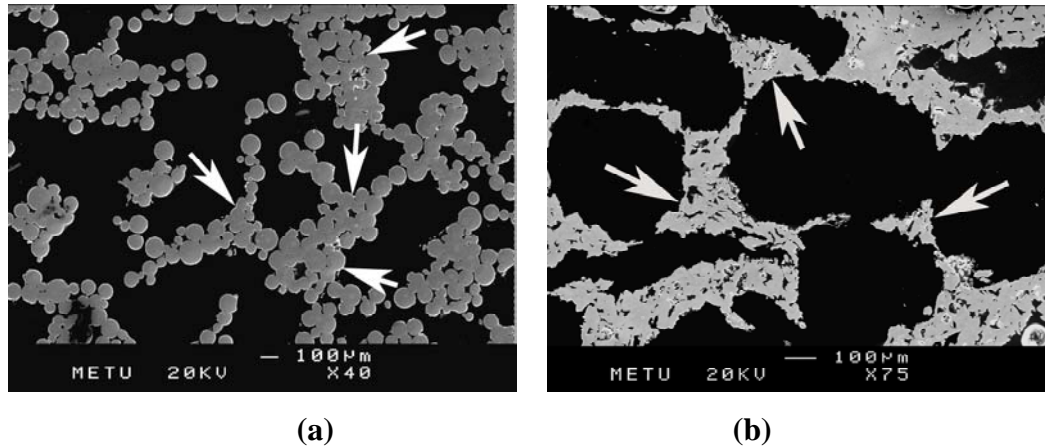


**Figure 4.39** Cell wall and cell node structure in (a) titanium foam, (b) Ti-6Al-4V foam.

#### 4.2.2. Microstructure

Slow cooling of Ti-6Al-4V foams containing either spherical or angular powders subsequent to sintering at 1200°C resulted in a lamellar type Widmanstätten structure, Figure 4.40. The dark regions and the bright regions were defined as  $\alpha$  and  $\beta$ -phase. The EDS spot analysis taken from Ti-6Al-4V foam samples exhibited about 2.09 wt. % V and 6.24 wt. % Al in  $\alpha$ -phase, and 11.17 wt. % V and 4.16 wt. % Al in  $\beta$ -phase, (Table 4.3).  $\alpha$ -phase nucleates within the beta grains as plates with their long dimensions parallel to  $\{110\}_{\beta}$ . As previously mentioned, cooling rate from beta phase region determines the final dimensions of the  $\alpha/\beta$  colony and each of the phase thickness, which play an important role in mechanical properties of  $\alpha$ - $\beta$  alloys. In the present study, the measured  $\alpha$  and  $\beta$  phase thicknesses were similar to that of loose powder sintered samples and it was around 2.95 and 0.8  $\mu\text{m}$  for the alpha and beta phases, respectively.

In partially sintered powders the limiting factor for the  $\alpha/\beta$  colony size is the initial powder particle size. As the powders get smaller, the dimension of colonies also decreases. The dimensions of  $\alpha$ - $\beta$  colony may reach up to 150  $\mu\text{m}$  in samples containing spherical alloy powders, whereas it is limited to 74  $\mu\text{m}$  for the foam samples containing angular alloy powders.

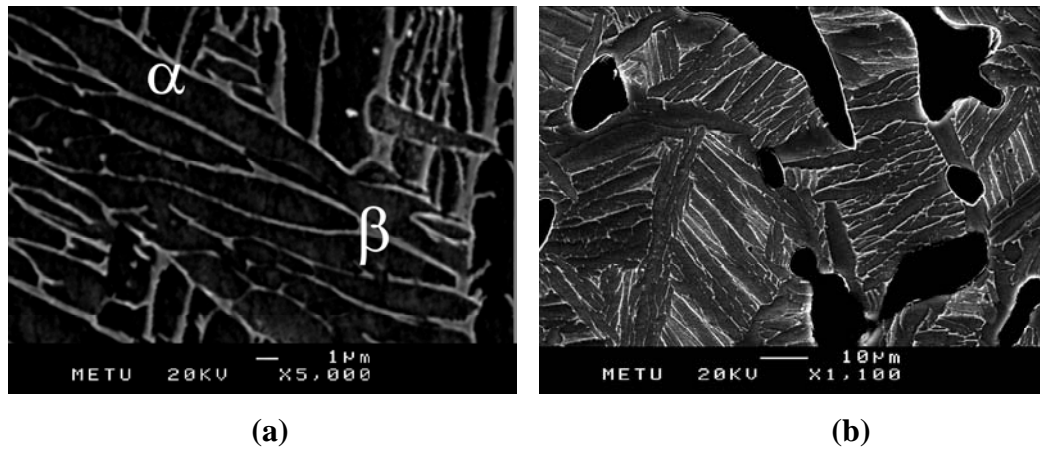


**Figure 4.40** Microstructure of foams containing Widmanstätten microstructure, (a) Ti-6Al-4V (spherical) foam, (b) Ti-6Al-4V (angular) foam.

**Table 4.3** EDS analysis of the phases present in Ti-6Al-4V foams.

Element	$\alpha$ -phase (wt. %)	$\beta$ -phase (wt. %)
Al	6.24	4.16
Ti	91.67	84.67
V	2.09	11.17

### 4.2.3. Mechanical Properties

#### 4.2.3.1. Stress-strain Curves

Figures 4.41, 4.43 and 4.44 show the compression stress-strain curves of manufactured foams having different porosity contents. All the foams exhibited a typical compression stress-strain curves of elastic-plastic foams with three stages of deformation, which consist of a linear elastic region at the beginning of deformation, a long plateau stage with nearly constant flow stress to a large strain, and a densification stage, where the flow stress increases.

Various deformation mechanisms are operative during compression of elastic-plastic foams. Compression loading in the elastic region results in bending and extension/compression of cell edges and cell walls depending on the morphology of the foam. Cell edge bending is the dominant mechanism that controls the linear elasticity in open-cellular foams. If the stresses in the edges and walls exceed the yield stress of the solid, the onset of plastification is reached and the deformation is no longer elastic [3].

Increasing the load on the foam causes to buckle of the cell edges and walls in weaker regions of the foam. A deformation band perpendicular to the loading direction develops, in which plastic collapse of the cells take place. This effect is accompanied by the beginning of the plateau region as seen in the stress-strain curves, (Figures 4.41, 4.43 and 4.44). Plastic collapse in an open-cell foam occurs when the moment exerted on the cell walls exceeds the fully plastic moment creating plastic hinges. However, plastic collapsing of closed cell foam is more complicated that plastic collapse load may be affected by stretching as well as the bending of the cell walls, and by the presence of a fluid within the cells. Depending on the cellular structure and the properties of the solid, the plateau region of the stress-strain curve may not be flat, but a slight slope, or a waviness can occur.

With increasing strain in plateau region, additional deformation bands are formed until most of the cells have collapsed and the densification is reached. Densification region or increase in stress subsequent to plateau region is a consequence of the compression of the solid itself after complete collapsing of

opposing cells. This sharp increase in the compressive stress vs strain curve at a nominal strain, is termed as densification strain [3]. Densification strain of foams depends on cell topology. It is clear from (Figures 4.41, 4.43 and 4.44) in all samples densification started earlier in samples containing lower porosity as expected.

The form of the stress-strain curves of metal foams manufactured through the use of powder metallurgy processing, as in this study, may vary in general with density, density gradient, composition of the foam, microstructure, cell wall geometry, inherent material properties and with the sintering degree of powders in cell walls and edges.

Rather smooth stress-strain curves were observed in foams containing spherical Ti-6Al-4V and titanium powders. It is very clear that pure titanium samples have more clearly defined plateau regions and smooth stress-strain curves at all porosity range compared to Ti-6Al-4V (spherical) foams. The reason of such behavior can be attributed to the ductile nature of pure titanium. Moreover, as expected, the densification strain decreases as the porosity of samples decrease since open cell structure have more opportunity for collapsing during compression.

It is clear from Figure 4.41 that pure titanium samples having higher porosities exhibit more clearly defined plateau regions than those of low porosity samples. As the porosity of the samples decreases, the plateau region starts to disappear and the stress after yielding increases sharply, as observed in titanium foams with 46.3 % and 53.2 % porosity. The increase in stress subsequent to yielding with the increase in strain may be an indication of closed cellular morphology, in which the cell faces carry membrane stress upon loading. Mechanical responses of samples shown in Figure 4.41 are in accordance with the microstructural observations that, as previously stated, at around 55 % porosity there is a transition from closed cellular to open cellular morphology for macropores, as shown in Figure 4.42 for foams with two different porosity contents.

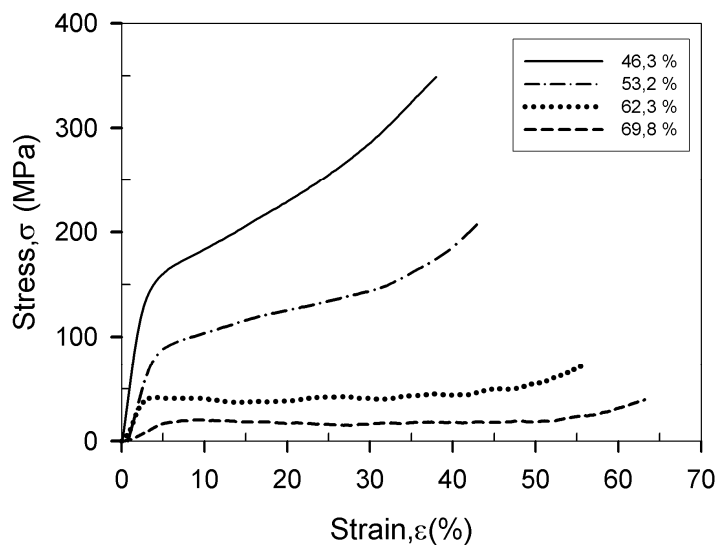


**Figure 4.41** Compression stress-strain curve of foams made up of spherical titanium with different amount of porosities.

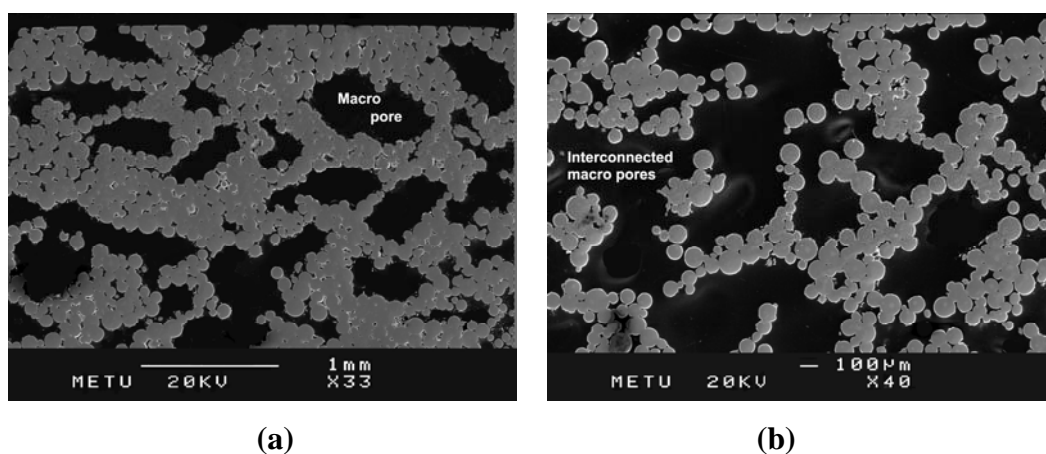


**Figure 4.42** SEM micrographs of titanium foams showing, (a) a closed cellular structure (46.3 % porosity) and (b) the transition to an open cellular structure (53.2 % porosity).

Such behavior, i.e. increase in stress subsequent to yielding with the increase in strain at low porosities, was not observed in Ti-6Al-4V (spherical) alloy samples, Figure 4.43. Also plotted for comparison in Figure 4.43 is the typical response of bulk Ti-6Al-4V-ELI alloy under compression loading. As can be seen, compression

stress-strain curves of bulk Ti-6Al-4V-ELI alloy exhibited linear elastic behavior at small strains, followed by yield and strain hardening up to an ultimate stress. Subsequent to a maximum or peak stress fast fracture occurred after small straining. Internal damage such as voids or cracks may cause the material softening after the peak stress.

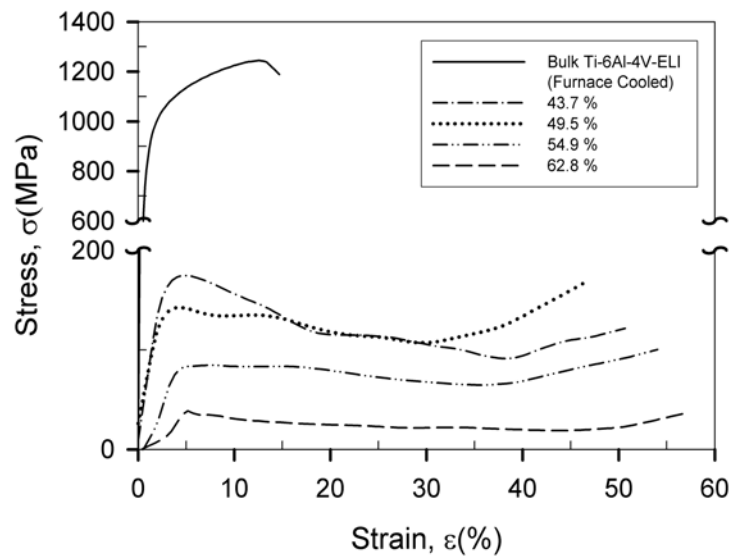


**Figure 4.43** Compression stress-strain curve of foams made up of spherical Ti-6Al-4V with different amount of porosities.

Foams produced using angular Ti-6Al-4V exhibited such a different behavior that they all showed a sudden decrease in stress after the onset of plastic deformation, Figure 4.44. Some serrated regions were observed to exist as the porosity content is decreased. During compression, the cell walls of these foams tended to crack and fracture in a brittle manner. The brittle fractures of cell walls occurred locally and spread to the surrounding regions as compression testing proceeded. In some foam samples, a zig-zag pattern was observed in plateau region, as shown in Figure 4.44 for foam containing 53.55 % porosity. Microscopic examinations carried out and EDX analysis taken from the cross-sections of low porosity foams revealed high fraction of  $\alpha$ -phase regions with equiaxed structure

together with widmanstatten structure, Figure 4.45. This equiaxed alpha, which is an indication of oxidation, may be the cause of zig-zag pattern in stress-strain curves.

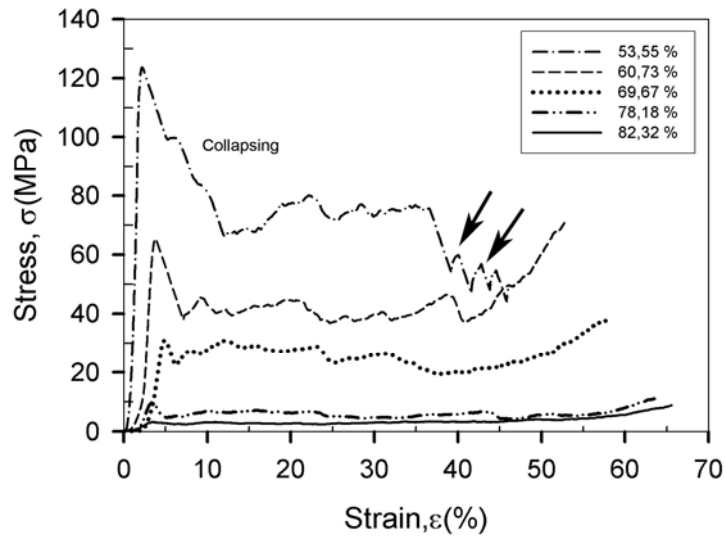
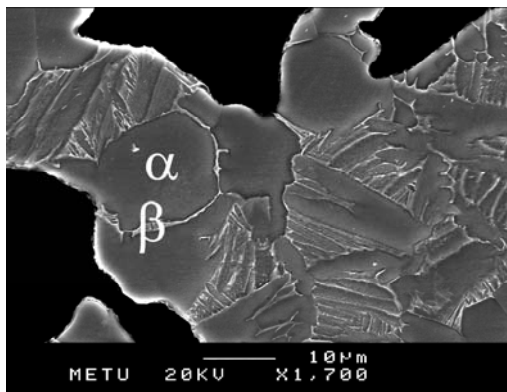


**Figure 4.44** Compression stress-strain curve of foams made up of angular Ti-6Al-4V powder with different amount of porosities.

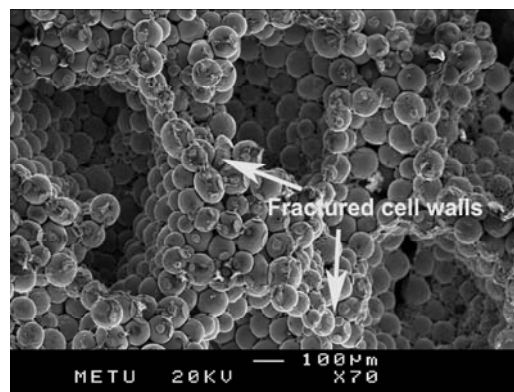


<i>Element</i>	<i>Weight (%)</i>
<b>Al</b>	5.66
<b>Ti</b>	91.71
<b>V</b>	2.63

**Figure 4.45** The regions of equiaxed alpha phase in foams with angular Ti-6Al-4V.

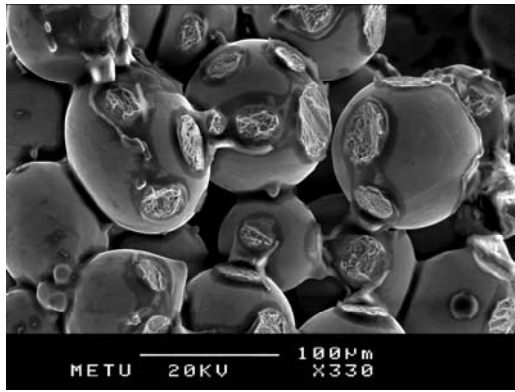
Cell wall geometry and inherent material properties influence the deformation mechanism and plastic response of metal foams under compression loading. Compression of foams made up of titanium and Ti-6Al-4V alloy powders resulted in formation of series of deformation bands in the direction normal to the applied load. Cell collapsing occurs in discrete bands. Probably, a weak cell wall serves as the initiation site for strain localization. Then, the deformation propagates rapidly through the foam resulting in a band of collapsed cells. Once collapsing completed in one region, deformation continues with the new band formation at different positions. As the porosity content of foams decreased propagation of surface cracks combined with large pores at an angle of 45° to the loading direction similar to wrought alloys were detected. This effect was observed mainly in low porosity foams of Ti-6Al-4V alloy with cell walls containing angular powders.

In all foam samples containing either angular or spherical powders, examination of the fracture surfaces revealed ductile dimple features, Figure 4.46 (c) and 4.46 (g). Failure occurred by tearing of the necks between powder particles in cell walls and edges, Figure 4.46 (a) and 4.46 (e).

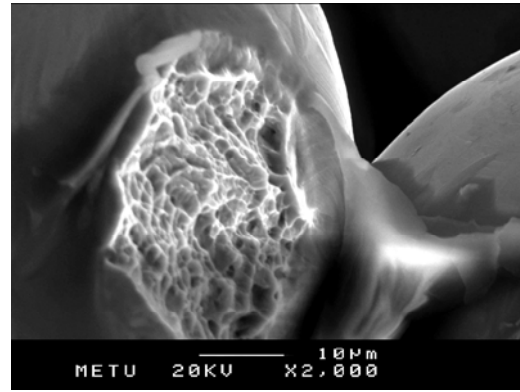


(a)

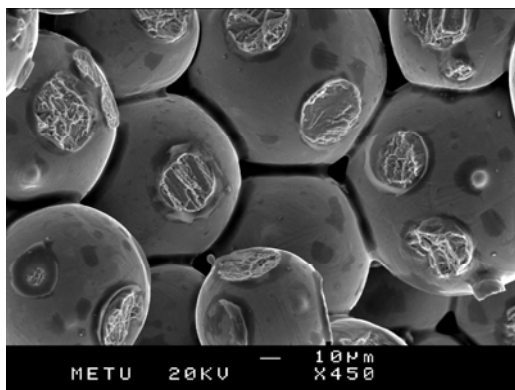
**Figure 4.46** Compression tested foams, (a) Fractured cell walls in Ti-6Al-4V (spherical) foam, (b) fractured surfaces of partially sintered powders on cell walls of Ti-6Al-4V (spherical) foam, (c) Dimples in the neck region of Ti-6Al-4V (spherical) foam, (d) fractured surfaces of partially sintered powders on cell walls of titanium foam, (e) tearing of the neck in titanium foam, (f) fractured surfaces of partially sintered powders on cell walls of Ti-6Al-4V (angular) foam, (g) Dimples in the neck region of Ti-6Al-4V(spherical) foam.



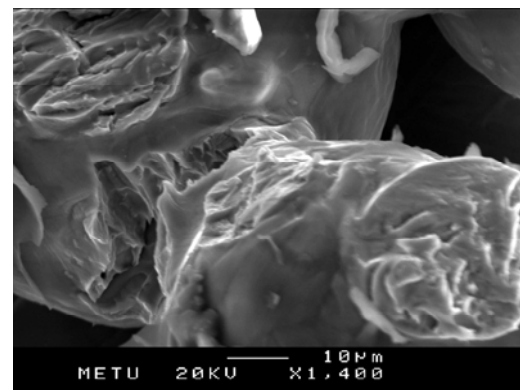
(b)



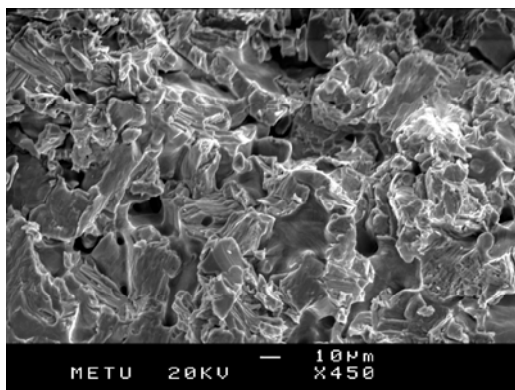
(c)



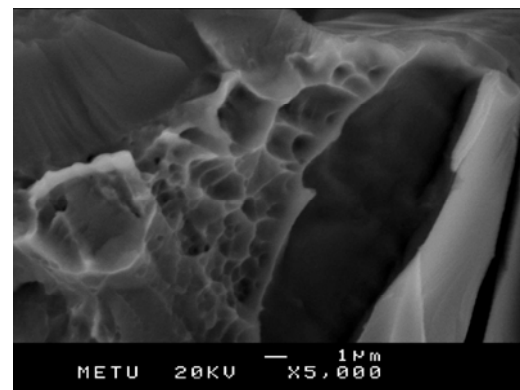
(d)



(e)



(f)

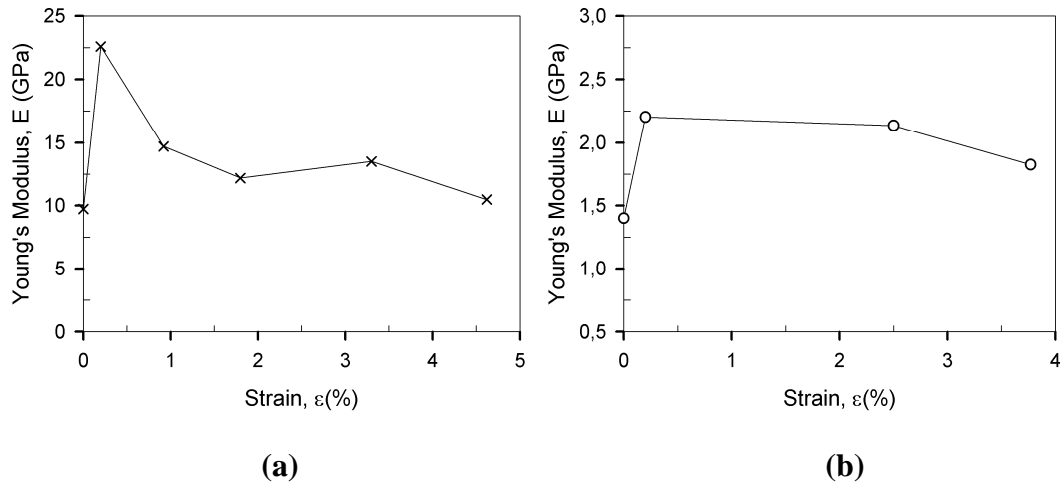


(g)

**Figure 4.46 (cont.)** Compression tested foams, (a) Fractured cell walls in Ti-6Al-4V (spherical) foam, (b) fractured surfaces of partially sintered powders on cell walls of Ti-6Al-4V (spherical) foam, (c) Dimples in the neck region of Ti-6Al-4V (spherical) foam, (d) fractured surfaces of partially sintered powders on cell walls of titanium foam, (e) tearing of the neck in titanium foam, (f) fractured surfaces of partially sintered powders on cell walls of Ti-6Al-4V (angular) foam, (g) Dimples in the neck region of Ti-6Al-4V (spherical) foam.

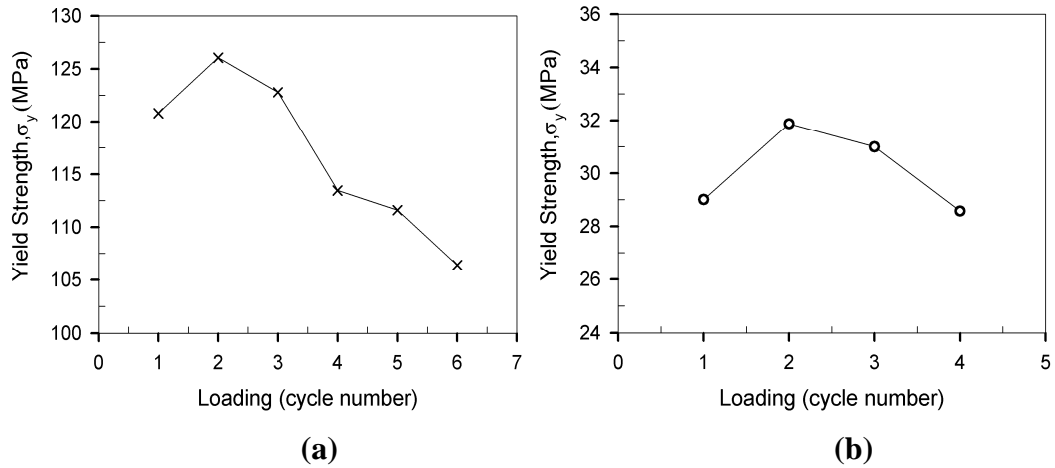
In all of the stress-strain curves of the foams produced, Figures 4.41, 4.43 and 4.44, initial loading appears to be elastic but not ideally linear as some imperfections present in the foam degrade the properties such as stiffness and strength. Cell edge curvature, concentration of materials at cell nodes rather than the cell edges, Figure 4.39, and non-uniform density may be the reason of such degraded properties. The actual modulus is found by measuring dynamically or by loading the foam into the plastic range, then unloading and determining the modulus from the unloading slope. In addition to these, during loading of foams under compression loads presence of stress concentration within the porous structure leads to early yielding at isolated locations resulting in smaller slopes in the elastic regions than expected. Because of that, unloading modulus,  $E$ , after a plastic strain of 0.2 % is expected to be much higher than the initial loading line. Even in bulk polycrystalline materials the measured elastic modulus is lower than the expected value since dislocations motion in some grains is easier than the others. Early yielding of some grains result in a static slope in the elastic region as loading proceeds through the yield point. Consequently, calculated yield point at 0.2 % strain is an average yield point of the grains constituting the material.

Figure 4.47 shows the initial loading and unloading elastic moduli measured at 0.2 % strain and at higher strains for Ti-6Al-4V alloy foams containing partially sintered angular and spherical powders. In each case, the unloading moduli at 0.2 % strain are higher than that of the initial loading value. Because, during first loading cycle weak regions and regions having stress concentrations are eliminated. In contrast, in both type of foam samples, measured unloading moduli decrease as deformation proceeds beyond the 0.2 % strain, since deformation changes the structure of foam by bending, buckling, stretching, and cracking of the cell edges and cell walls. Therefore, the unloading Young's Modulus will change with strain. Generally, Young's Modulus decreases much faster with strain in compression than in tension. Buckling of cell edges and cell walls reduce the stiffness much stronger whereas stretching will increase the stiffness before the initial cracking of cell walls during tension loading.



**Figure 4.47** Unloading moduli change with strain in, a) Ti-6Al-4V (angular) foam, 54 % porosity, b) Ti-6Al-4V (spherical) foam, 63.5 % porosity.

Similar event was also observed in yielding of the foams produced. Figure 4.48 shows the change of yield strength with repeated loading-unloading cycles, in which the second loading corresponds to loading after reaching 0.2 % strain. As expected, in the second loading cycle calculated yield strength value is higher compared to that of first loading and observed to decrease in subsequent loading cycles instead of increase by strain hardening. However, at higher strains at which the plateau region starts to increase; measured yield strength value is expected to increase because of collapsing of cells and compression of the solid itself.



**Figure 4.48** Yield strength change with repeated loading, a) Ti-6Al-4V (angular) foam, 54 % porosity, b) Ti-6Al-4V (spherical) foam, 63.5 % porosity.

#### 4.2.3.2. Mechanical Property-Porosity Relations

There is a direct relationship between mechanical properties and porosity content or relative density. As explained in section 2.6.2, theories that have been used to explain mechanical property-porosity relations are based on load bearing cross-sectional area, stress concentration approach and the effective flaw size approach. In most cases, load bearing or minimum cross-sectional area, the cross-section of cell wall between the macro pores, is used for defining the mechanical properties in porous materials. In this section, experimental mechanical data will be evaluated and compared with some of the theoretical models, and best equation explaining the mechanical property-porosity relation in foam samples will be Determined.

For foam structures having porosities higher than 70 %, a specialized MSA model, which makes use of simple bending strut equations was proposed by Gibson and Ashby [3]. It is frequently used to describe the property-porosity or relative density relations. According to theory, in closed cell foams the cell walls between the cell edges stiffen the structure. When deformed in compression the cell edges bend, and the cell faces carry membrane stresses. Because of that, within the same density range closed cell foam's properties are theoretically higher compared to that

of open-cell foam's. The contribution of the cell face stretching to the overall stiffness and strength of the foam is described by relative density term,  $\rho^*/\rho_s$ , with a linear effect, while the contribution of cell edge bending is non-linear. The relation between yield strength of a foam,  $\sigma_{pl}^*$ , and its relative density,  $\rho^*/\rho_s$ , is given as:

$$\frac{\sigma_{pl}^*}{\sigma_{ys}} \approx 0.3 \left( \phi \frac{\rho^*}{\rho_s} \right)^{3/2} + (1 - \phi) \frac{\rho^*}{\rho_s} \quad (4.19)$$

Where,

$\sigma_{pl}^*$  : Plateau (yield) stress of the foam

$\sigma_{ys}$  : yield strength of the cell wall

$\rho^*$  : density of the foam

$\rho_s$  : density of the cell wall material

$\phi$  : distribution constant or fraction of solid which is contained in the cell wall, it is defined as;

$$\left( \frac{\rho^*}{\rho_s} \right) \leq \phi \leq 1$$

Similarly, the relation between Young's Modulus of a foam and its relative density is defined as:

$$\frac{E^*}{E_s} = \phi^2 \left( \frac{\rho^*}{\rho_s} \right)^2 + (1 - \phi) \frac{\rho^*}{\rho_s} \quad (4.20)$$

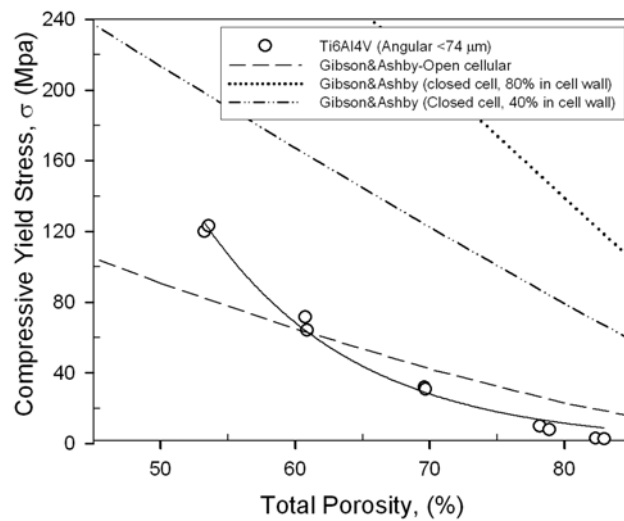
$E^*$  : Young's modulus of the foam

$E_s$  : Young Modulus of the bulk material

$\phi$  : Fraction of solid in cell edges

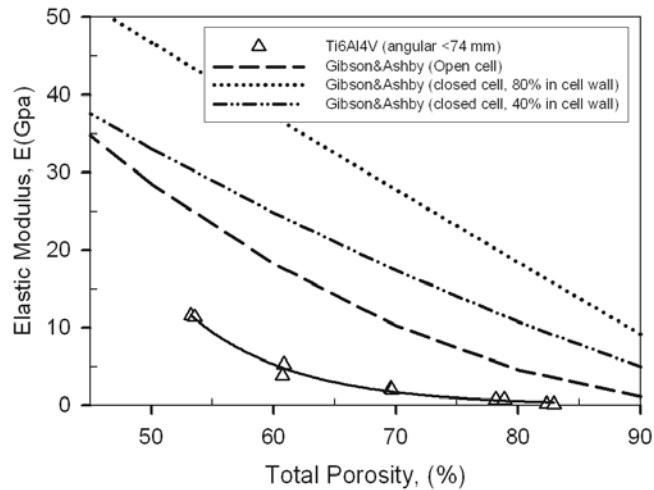
$$\phi = 1 \text{ (open cells)}$$

Comparison between yield strength and elastic modulus values calculated by Gibson&Ashby theory and the experimental data is done considering the total porosity of the foams, Figure 4.49. Comparison between theoretical model and experimental data was carried only for the Ti-6Al-4V (angular) foams because of their acceptable porosity levels, which is in the range of theoretical model calculations, >70%. Theoretical curves for fully open cellular, and closed cellular structures considering 80% ( $\phi:0.2$ ) and 40% ( $\phi:0.6$ ) of the material is in the cell walls were also drawn for the comparison, Figure 4.49.



(a)

**Figure 4.49** Comparison theoretical and experimental mechanical properties of Ti-6Al-4V (angular) foams, (a) Yield strength vs. porosity, (b) Elastic Moduli vs. porosity.



(b)

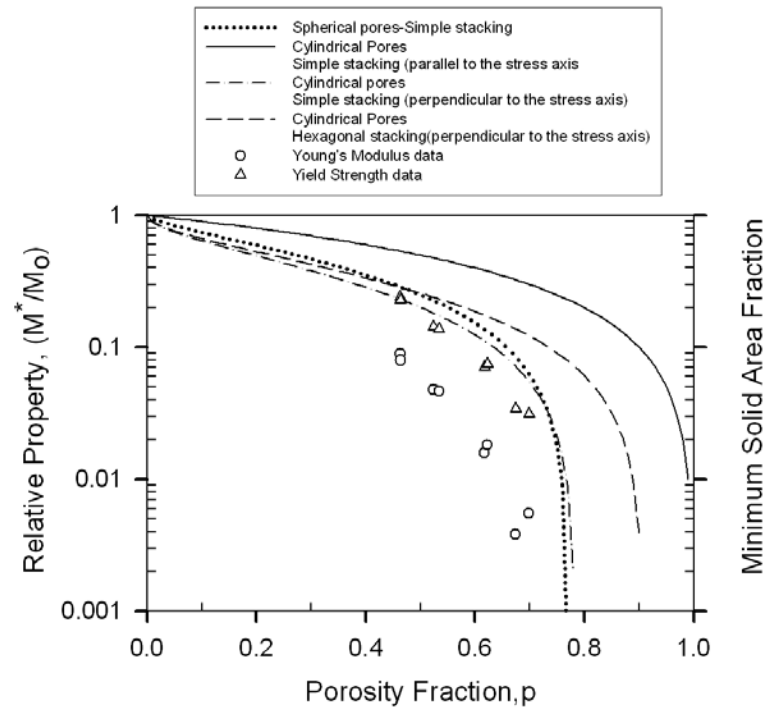
**Figure 4.49 (cont.)** Comparison theoretical and experimental mechanical properties of Ti-6Al-4V (angular) foams, (a) Yield strength vs. porosity, (b) Elastic Moduli vs. porosity.

Both yield strength and elastic modulus exhibited similar exponential decay tendency with increasing porosity. At high porosity levels experimental porosity-yield stress curves become parallel to theoretically calculated curves. However, the experimental elastic modulus and yield strength values are well below the predictions of Gibson&Ashby Model. Three types of imperfections degrade the stiffness and strength; cell edge curvature, large plateau borders (material concentrated at cell nodes rather than cell edges), and non-uniform foam density (redundant solid material and large isolated voids). As indicated previously, initial loading in stress-strain curves appears to be elastic but it is not linear because some cells yield at very low loads due to presence of stress concentration at isolated locations. So, the experimental elastic modulus is less than the true modulus. Moreover, the architecture of the materials also leads to lower elastic modulus than predicted, because struts generally have an hour-glass shape. While some curvature in struts is beneficial, the nodes, where several struts meet contain excess material that does not carry significant load. Moreover, in the calculation of theoretical yield strength and Young's modulus values of foams cell walls were considered as bulk Ti-6Al-4V alloy having Widmanstätten microstructure as used by many researchers,

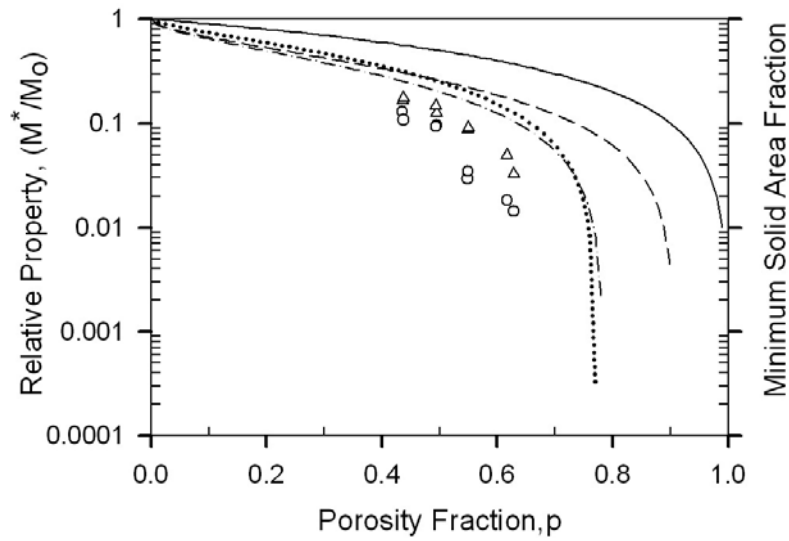
which had yield strength ~864 MPa and Young's Modulus ~110 MPa. However, the cell walls of the foams manufactured via powder metallurgy contain partially sintered powders. So, exact properties are calculated by inserting the density and yield strength of the porous cell wall material. The properties, i.e. porosity, density, elastic modulus and yield strength, of partially sintered cell walls of titanium and Ti-6Al-4V alloy foams will be discussed later in this chapter.

As previously stated, more generalized MSA models, developed for idealized structures containing uniform spherical pores, cubical pores (stressed, normal to one set of cube faces and other orientations), solid spherical particles (simple cubic, orthorhombic, and rhombic stacking), and aligned cylindrical pores, may also be used to describe property-porosity relations of materials. MSA models used for foams structures assume that relative mechanical properties,  $M^*/M_0$ , i.e. relative elastic modulus and yield strength, are determined by the minimum load carrying area fraction, which are the dimensions of the struts or webs between the pores rather than the thicker cross-sections, i.e. at the junction of two or more webs or struts. Figure 4.50 shows the comparison of experimental elastic modulus and yield strength data as a function of porosity and MSA models developed for idealized packing of different type of pores.

As it can be seen, for all type of the foams, the experimental data is well below the theoretical predictions. There may be two reasons of such occurrence. Firstly, as it was mentioned previously, some imperfections such as cell edge curvature, non-uniform pore distribution cause elastic modulus and yield strength to be lower than the expected. Secondly, manufactured foam contains two types of pore: macro pores formed as a result of evaporation of magnesium and micro pores on cell walls due to partial sintering of powders. Because of that, further studies should be carried out to include the effect of micro and macro pores on MSA model predictions. Various MSA model combinations for different stacking types of solid spherical particles and pores may be used.

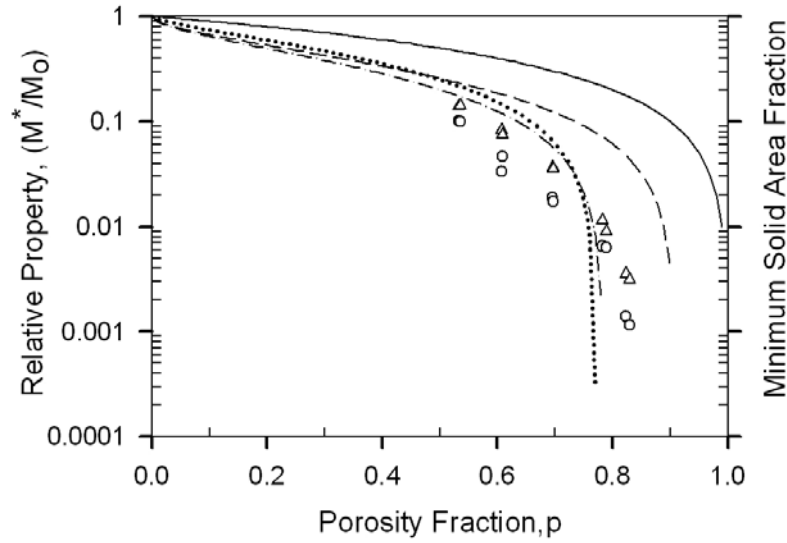


(a)



(b)

**Figure 4.50** Comparison of the experimental data with MSA models applied for various pore packing, (a) titanium foam, (b) Ti-6Al-4V foam (spherical), (c) Ti-6Al-4V foam (angular).



(c)

**Figure 4.50 (cont.)** Comparison of the experimental data with MSA models applied for various pore packing, (a) titanium foam, (b) Ti-6Al-4V foam (spherical), (c) Ti-6Al-4V foam (angular).

As in the Gibson and Ashby Model and in many studies used to characterize the mechanical properties of porous materials, relative density term ( $\rho^*/\rho$ ) is calculated assuming the cell walls and edges of the foams are made up of bulk material as in the foams processed using liquid state foaming techniques. However, as it has been shown, use of bulk properties in powder metallurgy processed foams leads to results or relations that deviate from the theoretical predictions mainly due to presence of partially sintered powders in cell walls. Hence, in this study relative density term was calculated in terms of the density of foams ( $\rho^*$ ) and the density of the micro porous cell walls ( $\rho_{\text{cell wall}}$ ). Based on the quantitative results, the micro porous cell wall densities were calculated as 3.5, 3.2 and 3.5  $\text{g/cm}^3$  for titanium, Ti-6Al-4V (spherical) and Ti-6Al-4V (angular) foams, which are much lower than the densities of titanium (4.5  $\text{g/cm}^3$ ) and Ti-6Al-4V alloy (4.43  $\text{g/cm}^3$ ).

As it has been shown, since many proposed theoretical models are based on idealized pore structures they cannot be directly applied to manufactured foams consisting of irregular pore shape and non-uniform pore size distribution. Accordingly, relation between mechanical property and relative density was found

by best fits to experimental data (Figures 4.51, 4.52 and 4.53). Relations obtained were found to obey a power law relation in the form of  $M^* = M_o \left( \rho^* / \rho_{\text{cell wall}} \right)^n$ , where superscript ‘\*’ denotes the properties of the foam. The proportionality constant,  $M_o$ , and the exponent,  $n$ , reflect the foam properties, such as the structure and properties of cell walls and edges, and macro pore character, i.e. interconnectivity of macro pores. The exponent,  $n$ , especially depends on the geometrical shape, macro pore character, orientation and size distribution of pores, and in turn on the materials and the fabrication method (i.e., cold pressing, sintering, or hot isostatic pressing) [106].

Equations 4.21, 4.23, 4.25 and Equations 4.22, 4.24, 4.26 represent the change of Young’s modulus,  $E^*$ , and yield strength,  $\sigma^*$ , of the manufactured foams with relative density,  $\rho^* / \rho_{\text{cell wall}}$ , respectively.

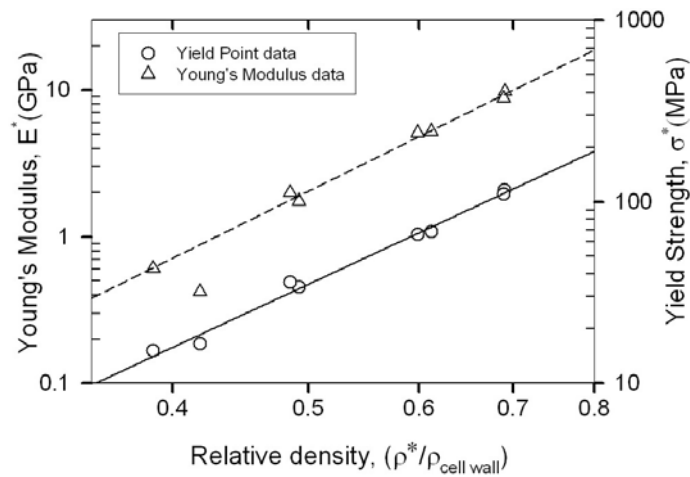


**Figure 4.51** Change of Young’s Modulus and yield strength of titanium foams with relative density.

$$E^* (\text{titanium}) = 53.7(\rho^* / \rho_{\text{cell wall}})^{4.7} \quad R^2=0.9906 \quad (4.21)$$

$$\sigma^* (\text{titanium}) = 423.1(\rho^* / \rho_{\text{cell wall}})^{3.6} \quad R^2=0.9944 \quad (4.22)$$

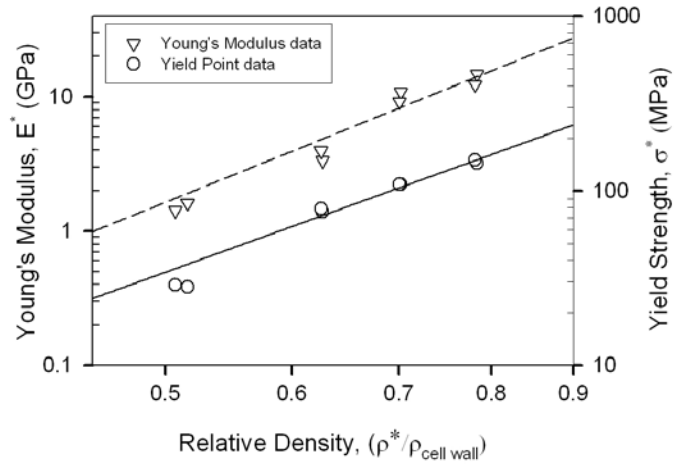


**Figure 4.52** Change of Young's Modulus and yield strength of Ti-6Al-4V (spherical) foams with relative density.

$$E^* (\text{Ti6Al4V, spherical}) = 45.6(\rho^*/\rho_{\text{cell wall}})^{4.8} \quad R^2 = 0.93 \quad (4.23)$$

$$\sigma^* (\text{Ti6Al4V, spherical}) = 336.9(\rho^*/\rho_{\text{cell wall}})^{3.3} \quad R^2 = 0.9809 \quad (4.24)$$

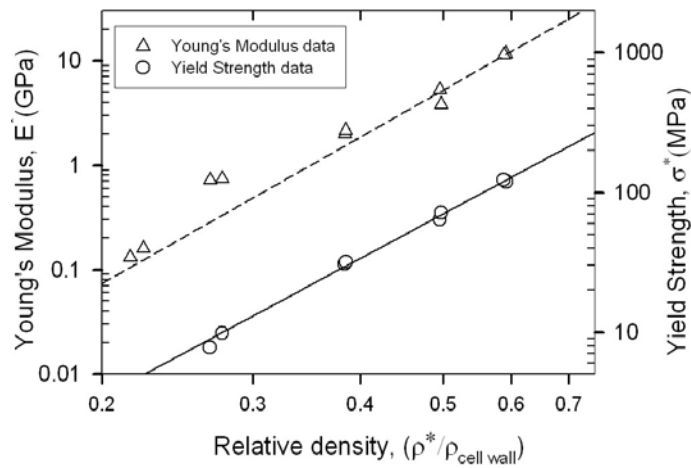


**Figure 4.53** Change of Young's Modulus and yield strength of Ti-6Al-4V (angular) foams with relative density.

$$E^* (\text{Ti6Al4V, angular}) = 131(\rho^*/\rho_{\text{cell wall}})^{4.7} \quad R^2=0.9845 \quad (4.25)$$

$$\sigma^* (\text{Ti6Al4V, angular}) = 692(\rho^*/\rho_{\text{cell wall}})^{3.3} \quad R^2=0.9972 \quad (4.26)$$

In most of the studies, which use a power law relation, similar to relation proposed by Gibson and Ashby, a single exponent value is utilized for open and closed cell morphology. However, exponents calculated in the present study reflect macro pore character consisting of all possible types, i.e. open, closed and partially open. On the other hand, the proportionality constant,  $M_o$ , is directly related to a constant and yield strength ( $\sigma_{\text{cell wall}}$ ), and elastic moduli ( $E_{\text{cell wall}}$ ) of cell walls/edges, which depend on some variables such as coordination number of powders ( $C_n$ ), inherent bulk material properties ( $\sigma_o$ ,  $E_o$ ) and the sintering degree of powders (neck size,  $X$ ).

Cell wall strength of the manufactured foams can be calculated simply by using a special MSA model given in Section 4.1.4.3, which utilizes neck size as the load-bearing cross-section. In many models used for indexing the mechanical properties of sintered articles, porosity content was taken as a single variable. As previously stated, however, use of porosity content as a single variable in defining the properties may lead to misleading results in mechanical property calculations since samples having similar porosity levels may have different interparticle bond region or neck size,  $X$ . Figure 4.54 shows the neck size ratio ( $X/D$ ) change with porosity in titanium and Ti-6Al-4V alloy foams. Neck size ratio ( $X/D$ ) measurements were carried out only on cell walls of foam samples containing spherical powders due to difficulty in measurements of neck size of angular powders. As expected and shown in Figure 4.54 average neck size of powders in cell walls of titanium foam is higher than that of Ti-6Al-4V foam due to having relatively smaller particle size.

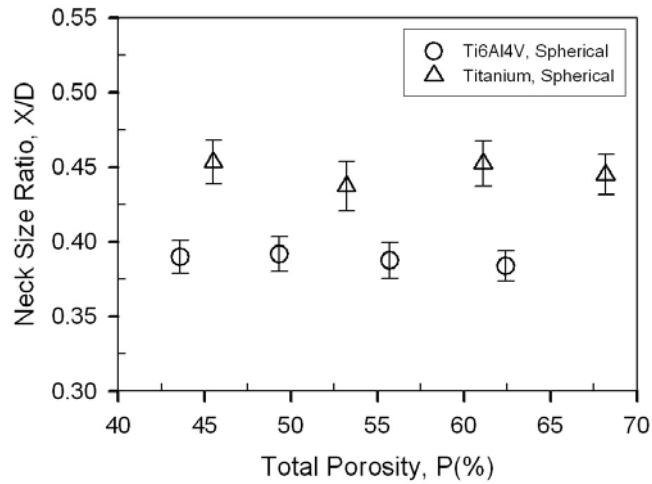


**Figure 4.54** Average neck size in cell walls of titanium and Ti-6Al-4V foams.

Corresponding bulk material strength value of Ti-6Al-4V powders,  $\sigma_o$ , was calculated as ~865 MPa from stress-strain curves of bulk Ti-6Al-4V-ELI samples having Widmanstätten microstructure with similar colony size and  $\alpha$ ,  $\beta$  phase thicknesses to powder samples. The average neck size ratios of powders in cell walls of titanium and Ti-6Al-4V foams were found to be 0.45 and 0.38, respectively. The yield strength of cell walls may roughly be estimated by inserting the calculated neck size ratio of cell walls into equations 4.16 and 4.17. One can find the cell wall yield strength as ~193 and ~330 MPa for titanium and Ti-6Al-4V foams, respectively.

## CHAPTER 5

### CONCLUSION

1. Upon loose powder sintering, porosity content of both spherical titanium and Ti-6Al-4V alloy samples were observed to decrease linearly with increasing temperature at almost the same rate. Porosity content of compacted and sintered samples of spherical titanium and titanium alloy on the other hand changed exponentially with compaction pressure. At the same sintering temperature compacted samples exhibited lower porosity and larger neck size due to the increase in available surface contacts and a decrease in diffusion distances.
2. A change in dependence of neck size ratio,  $X/D$ , on sintering temperature at a specific temperature, as attributed to the dominance of different transport mechanisms in literature, was also observed in the present study.
3. Subsequent to sintering, average neck size of pressed samples were found to be higher than that of the loose powder samples of the same porosity content.
4. Much higher affinity of magnesium for oxygen and nitrogen compared to titanium made it behave as a getter protecting titanium during sintering. In this respect, magnesium was found to have advantages over other spacers like urea and ammonium hydrogen carbonate, which contaminate titanium by dissolution of hydrogen, oxygen and nitrogen present in them.

5. Manufacturing of titanium and Ti-6Al-4V alloy foams without excessive collapse of the cell walls has been optimized by waiting at 600°C for partial evaporation of magnesium. It has been concluded that, even higher levels of porosity may be achieved by allowing evaporation of magnesium closer to its melting point, 630-640°C, long enough to decrease the amount of magnesium that melts as passing through its melting point. Maximum porosity, ~85 %, was attained in samples containing “angular” Ti-6Al-4V powders.
6. The structure of the Ti foams produced in the present study was different compared to samples manufactured by liquid processing techniques. They were observed to contain two types of pores: macropores obtained as a result of evaporation of magnesium particles, and micropores in the cell walls due to incomplete sintering of titanium powders.
7. All of the foams exhibited a typical compression stress-strain curves of elastic-plastic foams with three stages of deformation, which consist of a linear elastic region at the beginning of deformation; a long plateau stage; and a densification stage, where the flow stress increases sharply. However, stress-strain curves of sintered powders in loose condition or conventionally were similar to that of bulk alloy samples.
8. In compression tested bulk Ti6Al4V-ELI alloy and loose powder sintered shearing failure occurred along a plane of maximum shear stress developed, which inclined at an angle of about 45° to the compression axis. Whereas, in foam samples series of deformation bands formed in the direction normal to the applied load and cell collapsing occurred in discrete bands. In all type of samples, failure occurred by tearing of the sinter necks in a ductile manner manifested by dimples in the fracture surfaces.
9. During loading of foams under compression, presence of stress concentration within the porous structure leads to early yielding at isolated locations

resulting in slopes smaller than expected in the elastic region. For this reason, it has been concluded that it is crucial to use the unloading modulus, which is measured after a plastic strain of 0.2 %.

10. Taking porosity as the only variable in indexing the mechanical properties results in misleading relations because, as shown in the present study, the neck size and hence the load carrying area may be different for the same porosity content. The strength of the samples sintered in loose and compacted condition, as well as the cell walls of the foams containing partially sintered powders was found to depend on the neck size and the total porosity, and vary linearly with the square of neck size ratio,  $(X/D)^2$ .
11. The cell wall structure and properties have been found to be effective and very important in determining the foam properties. The empirical relation obtained between mechanical property of foams,  $M^*$ , and their relative density,  $(\rho^*/\rho_{\text{cell wall}})$ , was found to obey a power law in the form of  $M^* = M_0(\rho^*/\rho_{\text{cell wall}})^n$ , where superscript ‘\*’ denotes the properties of foam and the exponent, n, and the proportionality constant,  $M_0$ , reflect the structure of the foam and utilized production technique.

## REFERENCES

1. J. Banhart, *Prog. Mater. Sci.*, 2001; 46: 559.
2. L. J. Gibson, *J. Biomechanics*, 2005; 38: 377.
3. Lorna J. Gibson and Michael F. Ashby, *Cellular Solids; Structure and Properties*, Second Edition, Cambridge University Press, pp. 7, 1988.
4. G. J. Davies, S. Zhen, *J. Mater. Sci.*, 1983; 18: 1899.
5. M. F. Ashby, A. Evans, N. A. Fleck, L. J. Gibson, J. W. Hutchinson, H. N. G. Wadley, *Metal Foams: A Design Guide Butterworth-Heinemann*, Woburn, pp.1-20, 2000
6. Haydn N.G. Wadley, *Adv. Eng. Mater.*, 2002; 4: 10.
7. J. Banhart and G.Rausch, *Handbook of Cellular Metals; Production, Processing, Applications*, edited by Hans-Peter Degischer and Brigitte Kriszt, Wiley-Vch, pp.22, 2002.
8. D. C. Dunand, *Adv. Eng. Mater.*, 2004; 6: 369.
9. R. M. German, *Powder Metall. Sci.*, Metal Powder Industries Federation, Princeton, New Jersey, pp.25, 1984.
10. P. J. James, *Powder Metall. Int.*, 1982; 4: 82.
11. R. L. Sands and C. R Shakespeare, *Powder Metallurgy Practice and Applications*, William and Clowes and Sons Ltd., London, pp. 30, 1966.
12. R.M. German, *Liquid Phase Sintering*, Plenum Press, New York, pp.45, 1985.
13. R.M. German, *Sintering Theory and Practice*, John Wiley and Sons, Inc., New York, pp. 28, 1996.
14. K. S. Hwang, R. M. German, F.V. Lenel, *Powder Metall. Int.*, 1991; 23(2): 86.

15. R. L. Coble, *Kinetics of High Temperature Processes*, Ed. W. D. Kingery, Technology Press and John Wiley, pp. 147, 1959.
16. G. C. Kuczynski, L. Abernethy, J. Allan, *Kinetics of High Temperature Processes*, Ed. W. D. Kingery, Technology Press and John Wiley, pp. 163, 1959.
17. R. L. Coble and J. E. Burke, *Prog. Mater. Sci.*, 1963; 3: 197.
18. R. L. Coble, *J. Applied Physics*, 1961; 32(5): 787.
19. C. Hu, T. N. Baker, *Mater. Sci. Eng. A*, 1995; 190: 125.
20. W. J. Huppmann, *Z. Metallkde.*, 1979; 70: 792.
21. F. Aldinger, *Acta Metall.*, 1974; 22: 923.
22. R.M. German, *J. Metals*, 1986; 38: 26.
23. T. Kohno and M. J. Koczak, *Prog. Powder Met.*, 1982; 38: 463.
24. W. Kehl and H. F. Fischmeister, *Powder Met.*, 1980; 23: 113.
25. F. J. Puckert, W. A Kaysser and G. Petzow, *Sinter Sci.*, 1984; 16:105.
26. C. Leyens and M. Peters, *Titanium and Titanium Alloys: Fundamentals and Applications*, edited by M. Peters and C. Leyens, Wiley-Vch Verlag GmbH&Co. KGaA, Weinheim, pp.258, 2003.
27. G. Lütjering and J. C. Williams, *Titanium*, Springer-Verlag Berlin Heidelberg, pp.89-92, 2003.
28. Matthew J. Donachie, *Titanium: A Technical Guide*, ASM International, Metals Park, pp.113, 1988.
29. Y. Liu, L.F. Chen, H. P. Tang, C. T. Liu, B. Liu, B. Y. Huang, *Mater. Sci. Eng. A*, 2006; 418: 25.
30. F.H. Froes, D. Eylon, G.E. Eichelman, and H.M. Burte, *J. Metals*, 1980; 32(2): 4.
31. ASM Metals Handbook, *Powder Metall.*, volume 7, pp.339, 1984.
32. C. A. Kelto, B.A. Kosmal, D. Eylon and F.H. Froes, *J. Metals*, 1980; 32(8): 17.

33. Brian E. Hurless, *Amptiac Quarterly*, 2000; 6(2): 3.
34. Sumans Das, Martin Wohlert, Joseph J. Beaman, David L. Bourell, *Mater. & Design*, 1999; 20: 115.
35. V. V. Dabhade, B. B. Panigrahi, M. M. Godkhindi, T. R. Rama Mohan, P. Ramakrishnan, *Materials Research Bulletin*, 2006; 41(11): 2111.
36. B. B. Panigrahi, M. M. Godkhindi, K. Das, P. G. Mukunda, P. Ramakrishnan, *Mater. Sci. Eng. A*, 2005; 396: 255.
37. G. Ryan, A. Pandit, D. P. Apatsidis, *Biomaterials*, 2006; 27: 2651.
38. B. Jiang, N.Q. Zhao, C.S. Shi, J. J. Li, *Scripta Mater.*, 2005; 53: 781.
39. B. Jiang, N.Q. Zhao, C.S. Shi, X.W. Du, J.J Li, H.C. Man, *Materials Letters*, 2005; 59: 3333.
40. Y.Y. Zhao, D. X. Sun, *Scripta Mater.*, 2001; 44: 105.
41. H. I. Bakan, *Scripta Mater.*, 2006; 55: 203.
42. E. Zhang and B. Wang, *Int. J. Mech. Sci.*, 2005; 47: 744.
43. Y.Y. Zhao, T. Fung, L.P. Zhang, F.L. Zhang, *Scripta Mater.*, 2005; 52: 295.
44. M. Kobashi and N. Kanetake, *Adv. Eng. Mat.*, 2002; 4: 10.
45. N. G.D. Murray, D. C. Dunand, *Compos. Sci. Technol.*, 2003; 63: 2311-2316
46. UK Patent, 2, 183, 256, 1987
47. Europien Patent 1, 674, 178.
48. W. Pompe, H. Worch, *Mater. Sci. Eng. A*, 2003:1.
49. K. H. Frosch, I. Sondergeld, *J. of Orthopaedic Research*, 2003; 21: 213.
50. M. Long, H. J. Rack, *Biomaterials*, 1998; 19: 1621.
51. R. Ricceri and P. Matteazzi, *Int. J. Powder Metall.*, 2003; 39(3): 53.
52. I. H. Oh, N. Nomura, N. Masahashi, S. Hanada, *Scripta Mater.*, 2003; 49: 1197.
53. R. M. Pillar, *Int. J. Powder Metall.*, 1998; 34(8): 33.

54. J. Bobyn, R. M. Pillar, H. Cameron, G. Weatherly, *Clin. Orthop.*, 1980; 150: 263.
55. A.I. Itälä, H. O. Ylanen, C. Ekholm, K. H. Karlsson, H. T. Aro, *J. Biomed. Mater. Res.*, 2001; 58: 679.
56. C.E. Wen, M. Mabuchi, Y. Yamada, K. Shimojima, Y. Chino and T. Asahina, *Scripta Mater.*, 2001; 45: 1147.
57. C.E. Wen, Y. Yamada, K. Shimojima, Y. Chino, H. Hosokawa, M. Mabuchi, *J. Mater. Res.*, 2002; 17: 2633.
58. K. A. Khor, L. G. Yu, O. Andersen, G. Stephani, *Mater. Sci. Eng. A*, 2003; 356: 130.
59. K. Asaoka and M. Kon, *Mater. Sci. Forum*, 2003; 426-432(4): 3079.
60. J. Qiu, J. T. Dominici, M. I. Lifland and K. Okazaki, *Biomaterials*, 1997; 18: 153.
61. Y. B. An, N. H. Oh, Y. W. Chun, Y. H. Kim, J. S. Park, K. O. Choi, T. G. Eom, T. H. Byun, J. Y. Kim, C. Y. Hyun, D. K. Kim, C. S. Byun, J.-H. Sok, J. J. Kwon, W. H. Lee, *Scripta Mater.*, 2005; 53: 905.
62. W. H. Lee and C. Y. Hyun, *J. Mater. Process. Tech.*, 2007; 189: 219.
63. H. Hahn, W. Palich, *J. Biomed. Mater. Res.*, 1970; 4: 571.
64. M. Takemoto, S. Fujibayashi, M. Neo, N. Suzuki, T. Kokubo, T. Nakamura, *Biomaterials*, 2005; 26: 6014.
65. Y. B. An, N. H. Oh, Y. W. Chun, D. K. Kim, J. S. Park, K. O. Choi, T. G. Eom, T. H. Byun, J. Y. Kim, C. S. Byun, C. Y. Hyun, P. J. Reucroft, W. H. Lee, *Surface Coatings and Technology*, 2006; 200(14-15): 4300.
66. D. J. Sypeck, P. A. Parrish, H. N. G. Hayden, in *Porous and Cellular Materials for Structural Applications*, edited by D. S. Schwartz, D. S. Shih, H. N. G. Wadley, A. G. Evans, MRS, Pittsburg, pp. 205, 1998.
67. O. Andersen, U. Waag, L. Schneider, G. Stephani, B. Kieback, *Adv. Eng. Mater.*, 2000; 2: 192.
68. Y. H. Li, L. J. Rong, Y. Y. Li, *Intermetallics*, 2000; 8: 881.
69. B. Y. Li, *Acta Mater.*, 2000; 48: 3895.

- 70.** C. L. Chu, C. Y. Chung, P. H. Lin, S. D. Wang, *Mater. Sci. Eng. A*, 2004; 366, 114.
- 71.** Patent WO 02/066693 A1.
- 72.** J. P. Li, S. H. Li, K. de Groot, P. Layrolle, *Key Eng. Mater.*, 2002; 218: 51.
- 73.** J. P. Li, S. H. Li, C. A. Van Blitterswijk, K. de Groot, *J. Biomed. Mater. Res. A.*, 2005; 73: 223.
- 74.** D. Kupp, D. Claar, K. Flemmig, U. Waag, H. Goehler, *Processing and Properties of Lightweight Cellular Metals and Structures*, edited by A. Ghosh, T. Sanders D. Claar, TMS, Warrendale, pp.61, 2002.
- 75.** C. S. Y. Jee, N. Özgüven, Z. X. Guo, and J. R. G. Evans, *Metall. Mater. Trans. B*, 2000; 31: 1345.
- 76.** J-P. St-Pierre, M. Gauthier, L-P. Lefebvre, M. Tabrizian, *Biomaterials*, 2005; 26: 7319.
- 77.** M. W. Kearns, P. A. Blenkinsop, A. C. Barber, T. W. Farthing, *Metals Mater.*, 1987; 3: 85.
- 78.** M. W. Kearns P. A. Blenkinsop, A. C. Barber, T. W. Farthing, *Intern. J. Powder Metall.*, 1988; 24: 59.
- 79.** D. C. Dunand and J. Teisen, *Porous and Cellular Materials for structural Applications* edited by D. S. Schwartz, D. S. Shih, H. N. G. Wadley, A. G. Evans, MRS, Pittsburg, pp.231, 1998.
- 80.** N. G. Davis, J. Teisen, C. Schuh, D. C. Dunand, *J. Mater. Res.*, 2001; 16: 1508.
- 81.** R. L. Martin, R. J. Lederich, *Metal Powder Report*, 1992, 30
- 82.** D. M. Elzey, H. N. G. Wadley, *Metall. Mater. Trans. A*, 1999; 30: 2689.
- 83.** Russian Patent, 2, 026, 154
- 84.** I. Oh, N. Nomura and S. Hanada, *Mater. Trans.*, 2002; 43(3): 443.
- 85.** . N. Nomura, T. Kohama, I. H. Oh, S. Hanada, A. Chiba, M. Kanehira, K. Sasaki, *Mater. Sci. Eng. C*, 2005; 25(3): 330.
- 86.** M. Thieme, K.-P. Wieters, F. Bergner, D. Scharnweber, H. Worch, J. Ndop, T.J. Kim, W. Grill, *Journal of Mat. Sci.; Materials in Medicine*, 2001; 12: 225.

- 87.** Fumio Watari, Atsuro Yokoyama, Mamoru Omori, Toshio Hirai, Hideomi Kondo, Motohiro Uo, Takao Kawasaki, *Compos. Sci. and Tech.*, 2004; pp.1.
- 88.** Fumio Watari, Atsuro Yokoyama, Fuminori Saso, Motohiro Uo and Takao Kawasaki, *Composites*, 1997, pp.5.
- 89.**V. Amigó, M. D. Salvador, F. Romero, C. Solves, J. F. Moreno, *J. Mater. Process. Techn.*, 2003; 141: 117.
- 90.** R. Cirincione, R. Anderson, J. Zhou, D. Mumm, W. O. Soboyejo, in *Processing and Properties of Lightweight Cellular Metals and Structures* edited by A. Ghosh, T. Sanders and D. Claar, TMS, Warrendale, pp. 189, 2002
- 91.** US patent 0,002,810.
- 92.** M. Bram, C. Stiller, *Adv. Eng. Mater.*, 2000; 2(4): 196.
- 93.** C. E. Wen, Y. Yamada, K. Shimojima, Y. Chino, T. Asahina, M. Mabuchi, *J. Mater. Sci.: Materials in Medicine*, 2002; 13: 397.
- 94.** T. Imwinkelried, *J. Biomed. Mater. Res. A*, 2007; 81: 964.
- 95.** C. E. Wen, Y. Yamada, P. D. Hodgson, *Mater. Sci. Eng. C*, 2006; 26: 1439.
- 96.** C. Li and Z. Zhu, *J. Porous Mater.*, 2006; 13: 21.
- 97.** K. R. Wheeler, M. T. Karagianes, K. R. Sump, in *Conf. Titanium Alloys in Surgical Implants*, edited by H. A. Luckey, F. Kubli, ASTM, Philadelphia, 1983, 41.
- 98.** Nayeb-Hashemi and J.B. Clark, *Phase diagrams of magnesium alloys*, ASM international, pp 324, 1988.
- 99.** L. Tuchinskiy, R. Loutfy, *Materials and Processes for Medical Devices* ASM, Metals Park pp. 1, 2003.
- 100.** C. Körner and R. F. Singer, *Metal Matrix Composites and Metallic Foams*, Euromat volume 5, edited by T. W. Clyne and F. Simancik, Wiley-Vch Verlag GmbH, Weinheim, pp.1, 2000.
- 101.** A.G. Evans, J.W. Hutchinson, M.F. Ashby, *Prog. Mat. Sci.*, 1999; 43: 171.
- 102.** J. Banhart and J. Baumeister, *J. Mater. Sci.*, 1998; 33: 1431.
- 103.** L. F. C. P. Lima, A. L. E. Godoy, E. N. S. Muccillo, *Mater. Letters*, 2003; 58: 172.

104. K.C. Chan, L.S. Xie, *Scripta Mater.*, 2003; 48: 1147.
105. A.Paul, U. Ramamurty, *Mater. Sci. Eng. A*, 2000; 281: 1.
106. S.Ji, Q. Gu and B. Xia, *J. Mater. Sci.*, 41, 2006; 1757.
107. R. W. Rice, *J. Am. Ceram. Soc.*, 1993; 76(7): 1801.
108. R. W. Rice, *J. Mater. Sci.*, 1996; 31: 1509.
109. A.Hattiangadi and A. Bandyopadhyay, *J. Am. Ceram. Soc.*, 2000; 83(11): 2730.
110. R. W. Rice, *J. Mater. Sci.*, 1996; 31: 102.
111. C. Reynaud, F. Thevenot, *J. Mater. Sci. Letters*, 2000; 19: 871.
112. F. P. Knudsen, *J. Am. Ceram. Soc.*, 1959; 42(8): 376-387.
113. M. Euder, *Powder Metall.*, 1962; 5: 278.
114. S.K. Hyun, K. Murakami, H. Nakajima, *Mater. Sci. Eng. A*, 2001; 299: 241.
115. Y. V. Milman, R. K. Ivashchenko and N. P. Zakharova, *Poroshkovaya Metallurgiya*, 1991; 3(339): 93.
116. S. K. Dutta, A.K. Mukhopadhyay, and D. Chakraborty, *J. Am. Ceram. Soc.*, 1988; 71(11): 942.
117. K. K. Phani and S. K. Niyogi, *J. Am. Ceram. Soc.*, 1987; 70(12): 362.
118. L. Cheng-Feng, Z. Zhen-Gang, *Chin. Phys. Lett.*, 2005; 22(10): 2647.
119. A. P. Roberts, E. J. Garboczi, *J. Am. Ceram. Soc.*, 2000; 83(12): 3041.
120. F. P. Knudsen, *J. Am. Ceram. Soc.*, 1962; 45(2): 94.
121. W. H. Duckworth, *J. Am. Ceram. Soc.*, 1951; 34: 1.
122. R. Spriggs, *J. Am. Ceram. Soc.*, 1961; 44: 628.
123. J. Kováčik, *J. Mater. Sci. Letters*, 2001; 20: 1953.
124. J. Kováčik, *J. Mater. Sci. Letters*, 1999; 18: 1007.
125. J. C. Wang, *J. Mater. Sci.*, 1984; 19: 801.

126. J. C. Wang, *J. Mater. Sci.*, 1984; 19: 809.
127. M. Y. Balshin, *Akad. Sci. USSR*, 1949; 67: 831.
128. M. Tane, T. Ichitsubo, M. Hirao, T. Ikeda and H. Nakajima, *J. Applied Physics*, 2004; 96(7): 3696.
129. K.K. Phani, *Am. Ceram. Soc. Bull.*, 1986; 65: 1584.
130. R. W. Rice, *J. Mater. Sci.*, 2005; 40: 983.
131. R. W. Rice, *J. Mater. Sci.*, 1993; 28: 2187.
132. H. Danninger, G. Jangg, B. Weiss, R. Stickler, *Powder Metall. Intern.*, 1993; 25(5): 219.
133. O. Yeheskel, M. P. Dariel, *Mater. Sci. Eng. A*, 2003; 354: 344.
134. X. Xu, W. Yi, R. M. German, *J. Mater. Sci.*, 2002; 37: 567.
135. G. A. Shoales and R. M. German, *Metall. Mater. Trans. A*, 1998; 29: 1257.
136. A. C. Nyce and W. M. Shaffer, *Inter. J. Powder Met.*, 1972; 15: 171.
137. R. M. German, *Mater. Trans.*, 2001; 42(7): 1400.
138. P. Suri, D. F. Heaney, R. M. German, *J. Mater. Sci.*, 2003; 38: 1.
139. X. Xu, P. Lu, R. M. German, *J. Mater. Sci.*, 2002; 37: 117.
140. A. R. Boccaccini, *J. Mater. Sci. Letters*, 1998; 17: 1273.
141. R. W. Rice, *J. Mater. Sci.*, 1997; 32: 4731.
142. Y. L. Krasulin, V. N. Timofeev, S. M. Barinov, A. B. Ivanov, *J. Mater. Sci.*, 1980; 15: 1402.
143. J. Mizusaki, S. Tsuchiya, K. Waragai, H. Tagawa, Y. Arai and Y. Kuwayama, *J. Am. Ceram. Soc.*, 1996; 79(1): 109.
144. A. K. Mukhopadhyay, K. K. Phani, *J. Mater. Sci.*, 1998; 33: 69.
145. A. K. Mukhopadhyay, K. K. Phani, *J. European Ceram. Soc.*, 2000; 20: 29.

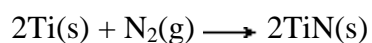
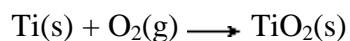
- 146.** E. Andrews, W. Sanders, L. J. Gibson, *Mater. Sci. Eng. A*, 1999; 270: 113.
- 147.** A. E. Simone and L. J. Gibson, *Acta Mater.*, 1998; 46(6): 2139.
- 148.** K. Y. G. McCullough, N. A. Fleck and M. F. Ashby, *Acta Mater.*, 1999; 47(8): 2323.
- 149.** R. Rossi, *J. Am. Ceram. Soc.*, 1968; 51: 433
- 150.** Z. Hashin, *Ceram. Microstr.*, 1968; 14: 313
- 151.** A. R. Boccaccini, G. Ondracek, E. Mombello, *J. Mater. Sci. Letters*, 1995; 14: 534.
- 152.** R.E. Peterson, *Stress Concentration Design Factors*, John Wiley, New York, pp.1, 1953.
- 153.** ASTM F1580-01, Standard Specification for Titanium and Titanium-6Aluminum-4Vanadium Alloy Powders for Coatings of Surgical Implants.
- 154.** ASTM F136-98, Standard Specification for Wrought Titanium 6Al-4V ELI (Extra Low Interstitial) Alloy for Surgical Implant Applications.
- 155.** ASTM B328-92, Standard Test Method for Density, Oil Content, and Interconnected Porosity of Sintered Metal Structural Parts and Oil-Impregnated Bearings.
- 156.** Dong-Geun Lee, Sunghak Lee, Chong Soo Lee, *Mater. Sci. Eng. A*, 2004; 366: 25.
- 157.** M. Guden, E. Çelik, E. Akar, S. Çetiner, *Mater. Characterization*, 2005; 54: 399.
- 158.** S. Malinov, Z. Guo, W. Sha, and A. Wilson, *Metall. Mater. Trans. A*, 2001; 32: 879.

## APPENDIX A

### REACTIONS OF TITANIUM AND MAGNESIUM IN DIFFERENT MEDIUM

#### 1) With air

Titanium metal is coated with an oxide layer that usually renders it inactive. However, once titanium starts to burn in air it burns to form titanium dioxide,  $\text{TiO}_2$  and titanium nitride,  $\text{TiN}$ . Titanium metal even burns in pure nitrogen to form titanium nitride.

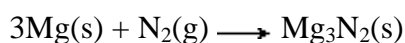
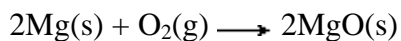


In fact titanium has more than one type of oxide as follows;

**Table A.1** Physical Properties (color) of some titanium oxides

Formula	Color	Melting Point ( $^{\circ}\text{C}$ )
$\text{TiO}$	Dark	1750
$\text{TiO}_2$	White	1800-1843
$\text{Ti}_2\text{O}_3$	Violet	1842
$\text{Ti}_3\text{O}_5$	Black	1777

The surface of magnesium metal is covered with a thin layer of oxide that helps to protect the metal from further attack by air. Once ignited, magnesium metal burns in air with a characteristic blinding bright white flame to give a mixture of white magnesium oxide, MgO and magnesium nitride, Mg<sub>3</sub>N<sub>2</sub>.



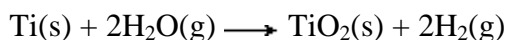
Most common oxides of magnesium are presented in Table A.2

**Table A.2** Physical Properties (color) of some titanium oxides

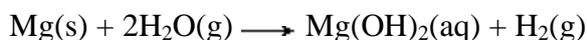
Formula	Color	Melting Point (°C)
MgO	White	2830
MgO <sub>2</sub>	White	100 (decomposition)

## 2) With water

Titanium metal is coated with an oxide layer that usually renders it inactive. However, titanium will react with steam to form dioxide, titanium(IV) oxide, TiO<sub>2</sub>, and hydrogen, H<sub>2</sub>.

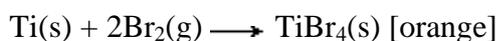
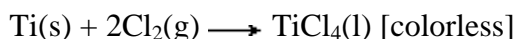
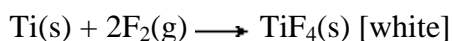


Magnesium does not react with water to any significant extent. It does however react with steam to give magnesium oxide (MgO), or magnesium hydroxide, Mg(OH)<sub>2</sub>, with excess steam) and hydrogen gas (H<sub>2</sub>).

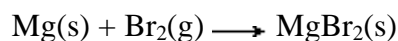
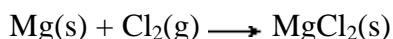


### 3) With the halogens

Upon warming titanium forms titanium(IV) halides. The reaction with fluorine requires heating to 200°C. So, titanium reacts with fluorine, F<sub>2</sub>, chlorine, Cl<sub>2</sub>, bromine, Br<sub>2</sub>, and iodine, I<sub>2</sub>, to form titanium(IV) fluoride, TiF<sub>4</sub>, titanium(IV) chloride, TiCl<sub>4</sub>, titanium(IV) bromide, TiBr<sub>4</sub>, and titanium(IV) iodide, TiI<sub>4</sub>, respectively.



Magnesium is very reactive towards the halogens such as chlorine, Cl<sub>2</sub> or bromine, Br<sub>2</sub>, and burns to form the dihalides magnesium(II) chloride, MgCl<sub>2</sub> and magnesium(II) bromide, MgBr<sub>2</sub>, respectively.



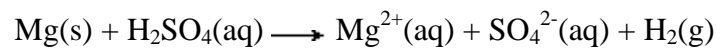
### 4) With acids and bases

Dilute aqueous hydrofluoric acid, HF, reacts with titanium to form the complex anion [TiF<sub>6</sub>]<sup>3-</sup> together with hydrogen, H<sub>2</sub>.



Titanium metal does not react with mineral acids at ambient temperature but does react with hot hydrochloric acid to form titanium(III) complexes.

Magnesium metal dissolves readily in dilute sulphuric acid to form solutions containing the aquated Mg(II) ion together with hydrogen gas, H<sub>2</sub>. Corresponding reactions with other acids such as hydrochloric acid also give the aquated Mg(II) ion.



Titanium and magnesium do not appear to react with alkalis under normal conditions.

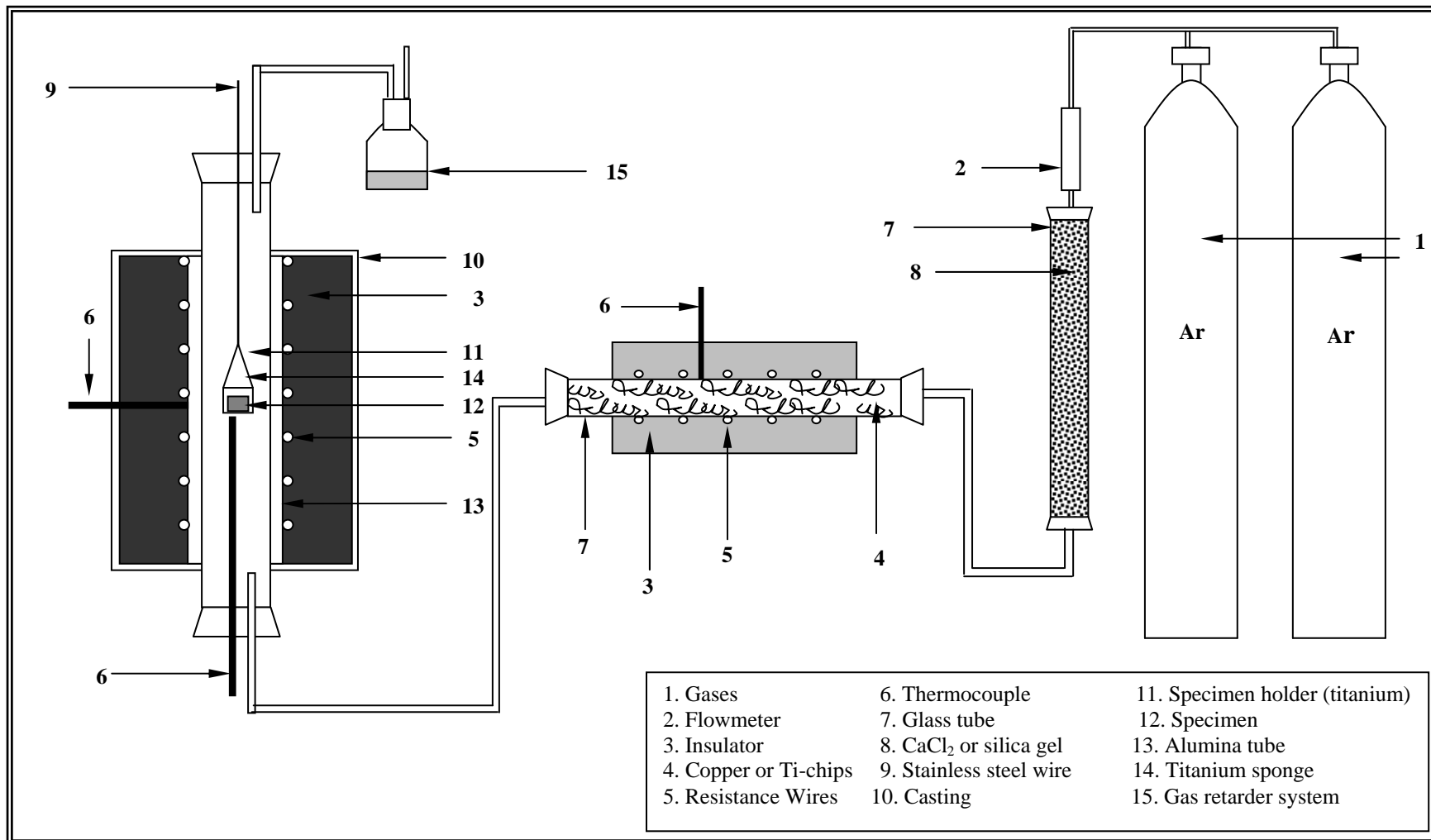


**Figure A.1** Schematic drawing of vertical furnace and its equipment

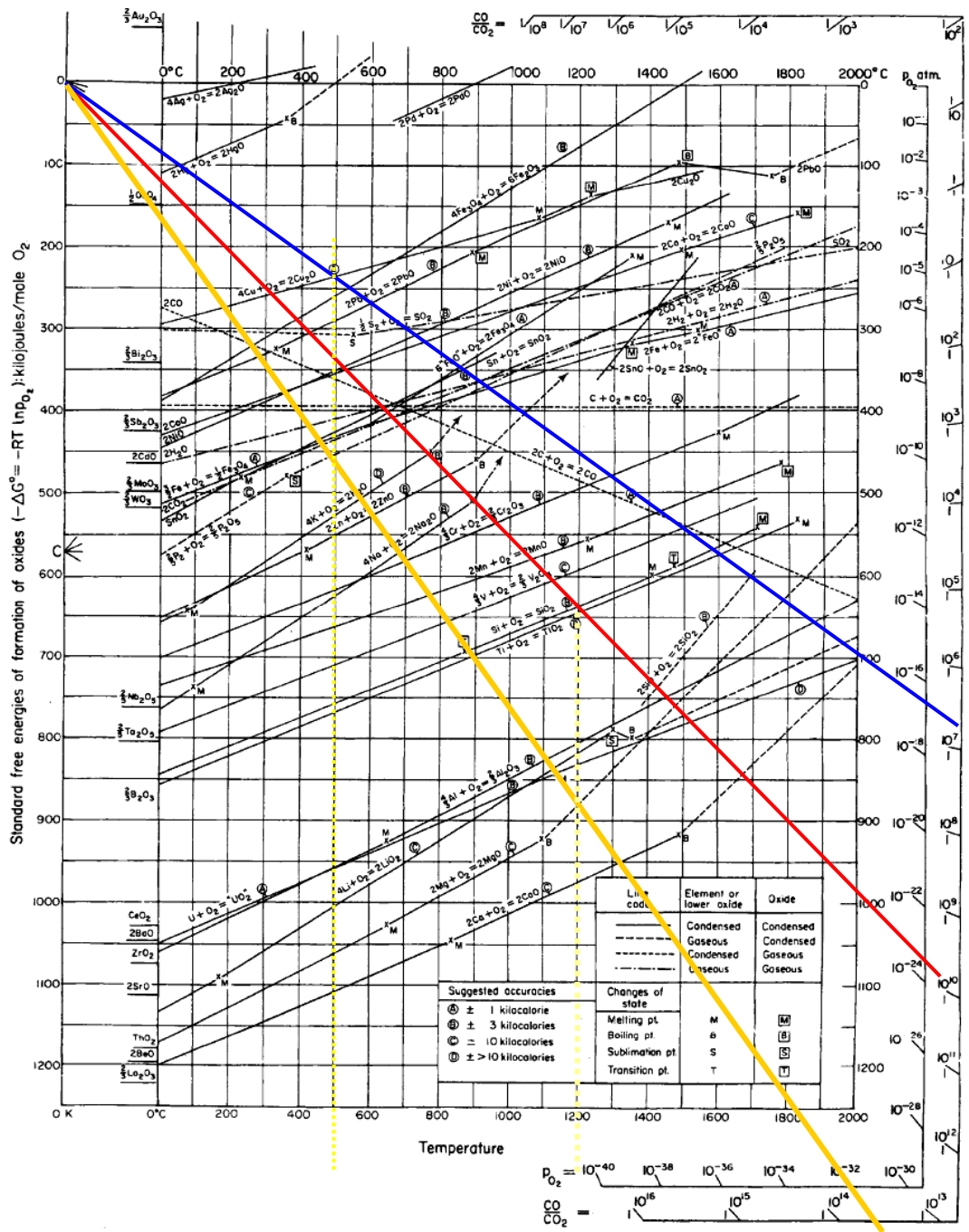


Figure A.2 Ellingham Diagram

## CURRICULUM VITAE

### PERSONAL INFORMATION

Surname, Name : Esen, Ziya  
Nationality : Turkish (TC)  
Date and Place of Birth : 16 September 1975, Bulgaria  
Marital Status : Single  
Phone (home) : -  
Phone (office) : +90 312 210 59 18  
Fax : +90 312 210 25 18  
e-mail : ziaesen@metu.edu.tr  
: ziya.esen@gmail.com

### EDUCATION

<b>Degree</b>	<b>Institution</b>	<b>Year of Graduation</b>
MS	METU Metallurgical and Materials Engineering	2002
BS	METU Metallurgical and Materials Engineering	1999
High School	Eskişehir Anatolian Technical High School, Department of Jet Engines	1994

## WORK EXPERIENCE

Year	Place	Enrollment
1999-2006	METU, Metallurgical and Materials Engineering	Research Assistant
1998 July	FORD-OTOSAN, İnönü/ESKİŞEHİR Heat treatment and Quality Control Department	Intern Engineering Student
1997 July	ERDEMİR, Ereğli/ZONGULDAK Sintering & Blast Furnace	Intern Engineering Student
1994 July	TURKISH AIRLINES, Yeşilköy/İSTANBUL Technical Service	Intern Engineering Student
1993-1994	1.HAVA İKMAL BAKIM MERKEZİ, ESKİŞEHİR Jet Revision Department, J-85	Intern Engineering Student
1992-1993	1.HAVA İKMAL BAKIM MERKEZİ, ESKİŞEHİR Engine Accessories Department	Intern Engineering Student
1991-1992	1.HAVA İKMAL BAKIM MERKEZİ, ESKİŞEHİR GTC Engines Department	Intern Engineering Student

## FOREIGN LANGUAGES

Advanced English

German (Beginner)

## PUBLICATIONS

1. Esen, Z., Ögel, B. ve Bor, Ş. "Bakır Bazlı Şekil Bellekli Alaşımların Toz Metalurjisi Yöntemiyle Üretilmesi" 11. Uluslararası Metalurji ve Malzeme Kongresi, İstanbul, September 2002
2. Esen Z., Tarhan E., Aydınol K., Bor Ş., " Su verilmiş Ti-6Al-4V alaşımında yaşlanma sırasında mikroyapısal gelişim", 12. Uluslararası Metalurji ve Malzeme Kongresi, İstanbul, September 2005
3. Esen Z., Ögel B., Bor Ş., "Cu-Al alaşım sisteminde sinterleme sırasında gözenek oluşumu", 12. Uluslararası Metalurji ve Malzeme Kongresi, İstanbul, September 2005
4. Esen Z., Bor Ş., " Biyomedikal amaçlı gözenekli titanyum ve Ti-6Al-4V alaşımı üretimi", 12. Uluslararası Metalurji ve Malzeme Kongresi, İstanbul, September 2005
5. Esen Z., Bor Ş., " Processing of titanium foams using magnesium spacer particles", Scripta Materialia, 5, 56, 2007, 341-344